Interplay between the conformational dynamics of a transmembrane protein and the mechanical properties of its surrounding membrane

Alicia Damm

Sorbonne Université

Ecole doctorale Physique en Ile-de-France

Laboratoire Physico Chimie Curie — Institut Curie

Interplay between the conformational dynamics of a transmembrane protein and the mechanical properties of its surrounding membrane

Par Alicia Damm

Thèse de doctorat de Physique

Dirigée par Patricia Bassereau et Maxime Dahan

Présentée et soutenue publiquement le 6 décembre 2019

Devant un jury composé de :

Patricia	Bassereau	Directrice de recherche	Directeur de thèse
Thierry	Charitat	Professeur	Examinateur
Daniel	Lévy	Directeur de recherche	Invité
Emmanuel	Margeat	Directeur de recherche	Examinateur
Daniel	Picot	Directeur de recherche	Examinateur
Laurence	Salomé	Directrice de recherche	Rapportrice
Dirk Jan	Slotboom	Professeur	Rapporteur

To Maxime

To my family and friends

"Victoriae mundis et mundis lacrima. Bon, ça ne veut absolument rien dire, mais je trouve que c'est assez dans le ton."

- Kaamelott

Abstract

Cell membranes are composed of a lipid bilayer, crowded with transmembrane proteins that mediate nearly all of the membrane functions, such as detoxification and communication. There is a tight interaction between lipids and transmembrane proteins. Membrane can apply mechanical stress and impact transmembrane proteins shape and function. Reciprocally, the inclusion of a transmembrane protein can bend or stretch the membrane. In particular, this interplay might play a crucial role for proteins that change conformation to mediate cargoes transport.

We study BmrA, a bacterial ABC exporter from *B.subtillis*. ABC (ATP Binding Cassette) transporters represent one of the largest families of membrane proteins. Some ABC exporters lead to a phenotype of multi-drug resistance, such as human P-glycoprotein (P-gp) which transports anti-cancer agents out the cell. BmrA shares high homology with P-gp and is expected to undergo a large conformational change between "open" and "closed" conformations.

The objective is to characterize the interplay between the conformation cycle of BmrA and membrane curvature, at the single molecule level. BmrA is purified in detergent, labelled with dyes suitable for FRET experiments, and incorporated in small liposomes. Conformations of BmrA are probed by single-molecule FRET in TIRF microscopy: a low (resp. high) FRET efficiency corresponds to a protein in open (resp. closed) conformation. Three different liposome sizes are used in order to vary the membrane curvature: diameter 140, 60 and 40 nm. We have found a different protein behavior in 40 nm liposomes as compared to larger ones, indicating an effect of the membrane curvature on BmrA conformations.

Acknowledgement

I would like to express my gratitude to my PhD advisors, Patricia Bassereau and Maxime Dahan, for their guidance and support, their patience also. I have a special thought for Maxime who could not see the present work completed. I am grateful for his trust: he introduced me to the single molecule FRET method (one of his early years beloved technique!) and gave me the opportunity to work on this method from scratch and to eventually make my way through its complexity. To Patricia, I am grateful for taking over this hard project and trusting me to complete it after Maxime passed away. Thank you for your inputs, advice and all the discussions that were always pushing my work forward.

I would like to thank our close collaborator Daniel Lévy for all his help, precious advice and stimulating discussions about the wonders of ABC transporters (in particular in plants!). I am grateful for your involvement in my PhD work.

I want to thank Su Jin Paik (my donor) who has been the best PhD partner ever and who showed so much patience while teaching me all the biochemistry protocols. Thank you for all the time you spent cheering me up at the microscope when smFRET was nothing but working, thanks for your constant support, good mood and friendship.

I want to thank John Manzi for his constant enthusiasm and all his help in purifying BmrA.

I am extremely grateful to Mathieu Coppey and Bassam Hajj who took over the LOCCO team after such a hard time and who managed to allow Maxime's research going forward.

I would like to thank our collaborators: Emmanuel Margeat, for all his inputs and advice on smFRET experiments and analysis, and Michele Castellana, for his interest and curiosity in our data.

I am deeply thankful to all the members of the jury, Thierry Charitat, Emmanuel Margeat, Daniel Picot, Laurence Salomé and Dirk Jan Slotboom, for all the time they put in evaluating my work, for their kindness and interest in my results.

I am grateful to my Thesis Advisory Committee members, David Lacoste and Stéphanie Descroix, for all your support, encouragements and curiosity in the project. Your help

has been precious to me all along my PhD.

I want to thank very warmly all the group members I have been interacting with during this three years, I often had the feeling I was part of three teams and all of you have been of great support and help! A special thank to Bassam Hajj, for all your help with the microscope and your encouragements, to Stéphanie Mangenot, for all your support and the chocolate(!), to Julien Pernier, for your help with the surface treatment, to Elie Balloul, for the crazy time at the microscope and the programming support with Fiji and Matlab, to Manuela Dezi, for the help with ATPase activity measurements, to Aurélie Di Cicco, for the cryo-EM images, and to Cynthia Taveneau, for the BmrA models and the lecture about protein structures!

A warm thank to all the members of the UMR168, you make this unit a pleasant working environment. A very special thank to Oleg Mikhajlov, Stéphanie Mangenot, Feng Tsai, Michael Henderson, Julien Pernier, Thibaut Lagny, Su Jin Paik, Cynthia Taveneau, Elie Balloul, Maud Bongaerts, Laurence Vaslin, Laura Caccianini, Tommaso Galgani, Koceila Aizel, Kotryna Vaidziulyte, Lorena Kolar Znika, Jean-Patrick Vrel, Camille Simon, Antoine Allard, Darine Samandar, Hanane El Manssouri, Anne-Marie Lyne, Thanh Ho-Bouldoires, Louis Verny, I am so grateful to all of you, sometimes without noticing you made my days better! Thank to the Saturday/Sunday market group for being like a little family to meet in the week-ends and share great food: John Manzi, Efe Ilker, Majdouline Aboughali, Remy Kusters, Gert-Jan Both, I love you guys.

Merci à mes amis, pour leur soutien indéfectible, même de loin. En particulier merci à Chloé Felgerolle et Soizic Cossec. Chloé, pour avoir été ma partenaire de combat en 5/2 comme en thèse, dans toutes les épreuves et les bons moments, Soizic, pour avoir si souvent été une bouffée d'oxygène, je vous aime. Merci à Sophie Berceau d'avoir été là depuis si longtemps, et malgré cela d'être toujours là! Merci à Laure-Anne Poutot, Gauthier Stein, Valentin Marchal, Claire Seigneur d'avoir été là pour moi.

Merci à ma famille pour vos encouragements, votre soutien et votre amour, en commençant par mes parents, qui ne m'ont jamais laissé douter que je pourrais aller loin, voir grand, faire de belles choses. Vous avez fait de notre maison de famille un lieu où il y a de la place pour les livres, la musique, le sport et l'art, tout en m'encourageant à poursuivre des études scientifiques. Je vous serai toujours reconnaissante pour tout cela. Merci à mon frère Valentin, à ma sœur Emilie et à leurs petites familles respectives, merci Mathilde, Christophe, Maé (ma croustille) et Cléophée, et à mes cousins Valérie, Michel et Quentin: pour votre soutien sans faille, et surtout pour me garder sur terre et me sortir de mon quotidien scientifique, je vous aime. Merci à mon parrain Jean-Marc qui a suivi et encouragé mon parcours scientifique et académique. Merci à ma petite maman d'avoir été au rendez-vous au téléphone tous les lundis matin et de m'avoir laissé me plaindre!

Une pensée pour ma grand-mère Odette qui aurait été si fière.

Last but not least, a warm thank to my partner, Philipp, who went through the PhD experience hand in hand with me, and who still supports me! For all your encouragements, your patience and your love, thank you.

Abbreviations

- **ABC**: ATP Binding Cassette.
- **Alexa488**: Alexa Fluor 488.
- **ATP**: Adenosine triphosphate.
- **ATP-γ-S**: Adenosine 5'-[γ-thio]triphosphate. Non hydrolysable analog of ATP.
- **AMP-PNP**: Adenylyl-imidodiphosphate. Non hydrolysable analog of ATP.
- **BmrA**: Bacillus multidrug resistance ATP.
- **bp**: Base pair.
- **bPS**: brain Phosphatidylserine.
- **DDM**: n-Dodecyl β-D-maltoside.
- **DM**: Dichroic Mirror.
- **DV**: DualView.
- ***E.coli***: *Escherichia coli.*
- **EPA**: Egg Phosphatidic acid.
- **EPC**: Egg Phosphatidylcholine.
- **LDH**: L-Lactate dehydrogenase.
- **MDR**: Multi-Drug Resistance.
- **NADH**: Nicotinamide adenine dinucleotide.
- **NBD**: Nucleotide Binding Domain.
- **PEG**: Polyethylene glycol.

- **PEP**: Phosphoenolpyruvate.
- **P-gp**: P-glycoprotein.
- **PK**: Pyruvate Kinase.
- **sCy**: sulfo Cyanine.
- **smFRET**: single-molecule Förster Resonance Energy Transfer.
- **TIRF(m)**: Total Internal Reflection Fluorescence microscopy.
- **TMD**: Transmembrane domain.
- **TX**: Triton X-100.
- **Vi**: Orthovanadate.
- **WT**: Wild type.

Contents

List of Figures

List of Tables

Chapter 1

Introduction

Single cells are the most elementary form of living organism as they are able to replicate, migrate, repair from several damages or enter apoptosis (programmed cell death process). Cells are limited by a semi-impermeable membrane composed of a lipid bilayer: the plasma membrane, which allows to form a sort of compartment. Lipid bilayers are also used within the cells to delimit the different organelles, in particular the nucleus. Since membranes are impermeable to most of the molecules, except water and gas such as O_2 or CO_2, complex living organisms have to establish diverse modes of communication between the different cells and between the cell internal compartments. Different mechanisms exist to transfer cargoes regardless of their size, such as endocytosis, exocytosis, and more generally traffic. Some specialized proteins can transport ions (channels, pumps) and other molecules (transporters) across the lipid bilayer. Therefore biological membranes are not simple lipid bilayers but are crowded with membrane proteins that form a complex mixture with different types of lipids and that can move about in the plane of the membrane (Alberts et al. [2017]; Lipowsky and Sackmann [1995]). A scheme of the cell plasma membrane is proposed on figure 1.1 (Kusumi et al. [2012]).

Lipid bilayers are involved in cells compartmentalization and protection, and membrane proteins mediate nearly all of the other membrane functions (Alberts et al. [2017]). In particular, transmembrane proteins are involved in all major cellular processes such as homeostasis, adhesion, signalling, transmembrane potential establishment, cell detoxification and cell-cell communication. Therefore, their dysfunction can lead to severe pathologies. Common efforts have been made in biology and biophysics to investigate the structures and functions of transmembrane proteins. These proteins are embedded in the lipid bilayers of cells and research works have also aimed at better understanding the tight interaction between lipids and transmembrane proteins (see Lee [2003] for a review). Indeed there can be reciprocal mechanical stresses between the protein and the surrounding lipids. Importantly, the shape of a protein is tightly related to its function

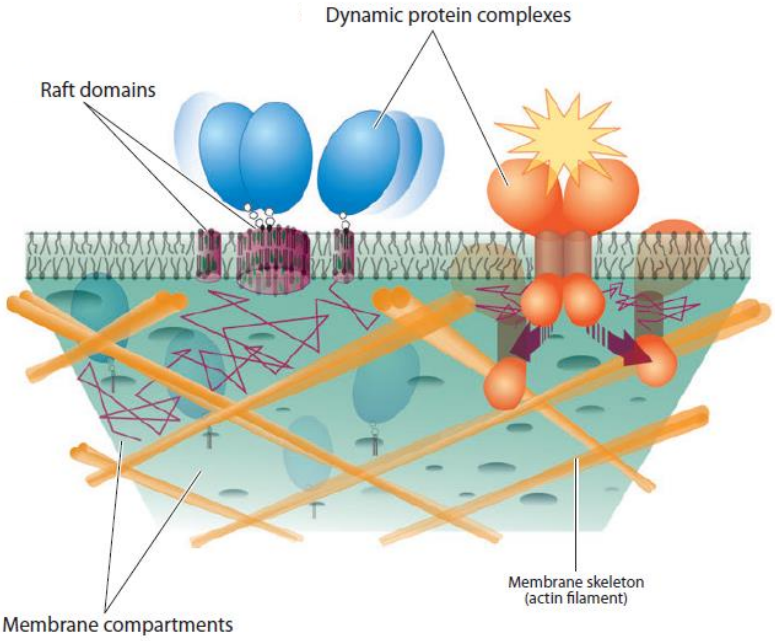

Figure 1.1: Plasma membrane organisation. From Kusumi et al. [2012]. The cell plasma membrane is a dynamic lipid bilayer crowded with protein complexes that are responsible for adhesion, signalling, trafficking. Some proteins are involved in cell migration and membrane deformation by mediating the cytoskeleton anchoring on the membrane.

and any mechanical stress that can impact the protein shape also influences its function. This is the case, for instance, for proteins that change conformation to mediate cargoes transport. Single molecule methods have been widely used to explore in detail this tight interaction between proteins and their lipid environment.

The objective of the present work is to understand and characterize the interplay between the conformation cycle of a transmembrane protein and the mechanical properties of its surrounding membrane, at the single molecule level. We study BmrA, a bacterial ABC (ATP Binding Cassette) transporter from *Bacillus subtillis*, which is expected to undergo a large conformational change.

ABC transporters represent one of the largest families of membrane proteins. All living organisms from bacteria to human have several ABC transporters : 79 were found in *E.coli*, 133 in rice and 49 in human (see figure 1.2, Hwang et al. [2016]). They ensure, in an ATP-dependent manner, transport of various compounds across membranes: some of them are responsible for import of nutrients and other necessary molecules, and other ABCs are exporters. Some ABC transporters are known as multidrug efflux pump and to play a crucial role in some pathologies (the phenomenon of multi-drug resistance will be detailed in 3.1).

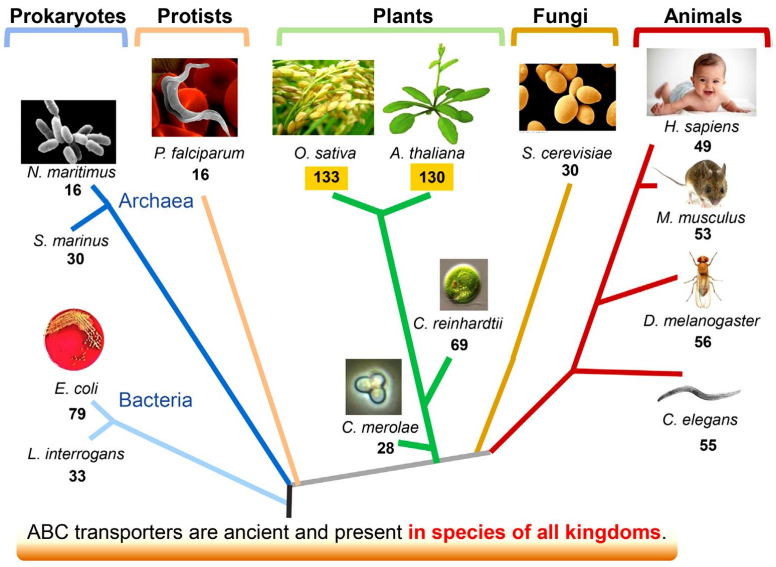

Figure 1.2: ABC transporters: a super family of proteins, present in all living organisms. From Hwang et al. [2016]. Numbers below species indicate the number of ABCs in the organism.

Our approach for studying the interplay between BmrA conformations and its lipid environment relies on two methods:

- BmrA conformations are probed by single-molecule FRET (Forster resonance energy transfer). This method allows measuring distances from 1 to 10 nm. For that, purified BmrA is labelled with a couple of fluorophores suitable for smFRET experiments.

- Purified and labelled BmrA is incorporated into proteo-SUVs, at a very high dilution that ensures the presence of a single protein per liposome. The membrane curvature is controlled by using vesicles with a well-defined size distribution. The size of the liposomes can be tuned by parameters such as lipid composition and reconstitution temperature. Three different liposomes populations will be studied.

In chapter 2, I give an introduction on lipid membranes and transmembrane proteins, followed by an overview of a commonly used method to probe proteins conformations, single-molecule FRET. A general presentation of the ABC transporters family is proposed in chapter 3 with a focus on our protein of interest, BmrA. The assay used for this study will be presented in chapter 4, as well as the set-up and analysis method used for smFRET studies. The system was carefully calibrated and smFRET results obtained for BmrA incorporated in different liposomes populations will be described in chapter 5 and discussed in 6.

Chapter 2

Lipid bilayer and transmembrane proteins

In this introduction chapter, I am going to present an overview of lipid membranes and their properties, of current knowledge on transmembrane proteins interaction with lipid bilayers and finally of some single molecule methods that are commonly used to study transmembrane proteins conformational changes.

2.1 Biophysics of membranes

2.1.1 Lipids

Cell membranes are made of a lipid bilayer, quasi-impermeable to most hydrophilic molecules and of large amounts of membrane proteins either bound to one of the lipid leaflets or fully embedded in the bilayer. The lipid bilayer allows a good separation and compartmentalization between exterior and interior of the cell, and of the subcellular structures. The lipid part of these membranes is mainly composed of amphiphilic phospholipids and sphingolipids, characterized in general by two hydrophobic fatty acid chains and a hydrophilic head group. The main four lipids composing mammalian plasma membrane are depicted on figure 2.1. Some lipids such as cholesterol present a very different structure, also shown on figure 2.1C. The amphiphilic property allows them to form bilayers (as depicted on figure 2.1A), an assembly that minimizes the exposure of the hydrophobic tails to water and therefore minimizes the entropic cost (Israelachvili [1992]). The hydrocarbon core of the membrane acts as a barrier. Small molecules such as water, O_2 or CO_2 can cross (water permeability was found $\sim 10^{-5}$ m/s in phosphatidylcholine

(PC) vesicles, Rawicz et al. [2008]) but most hydrophilic molecules and ions cannot.

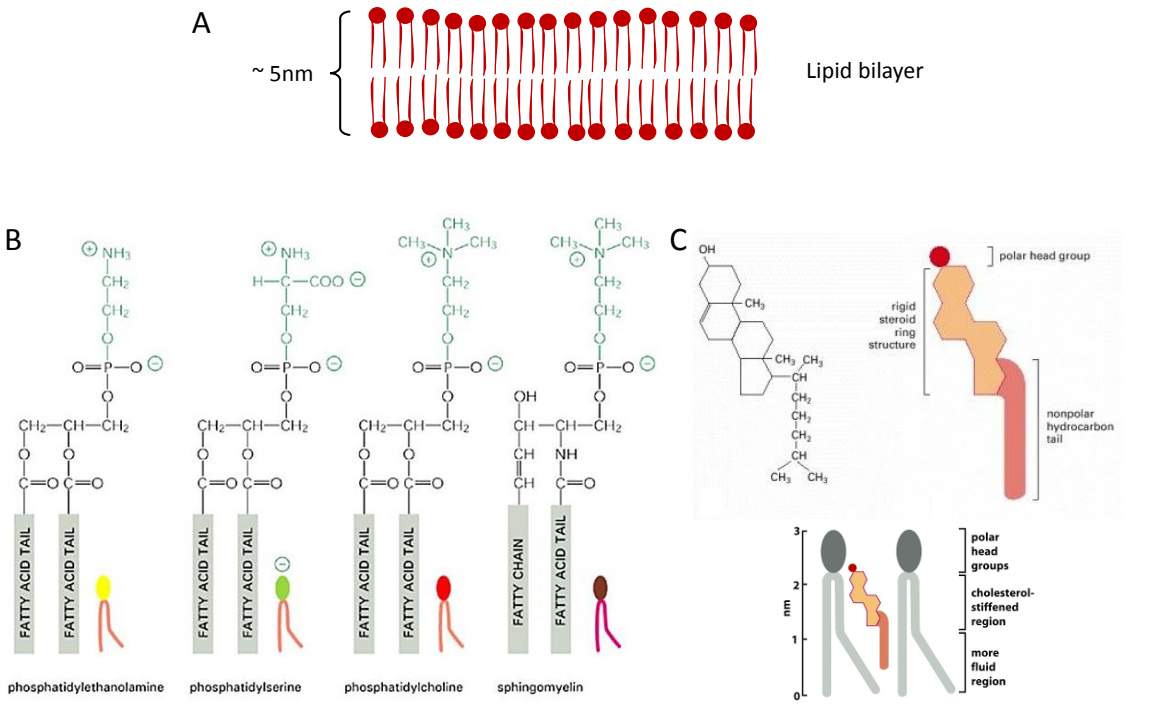

Figure 2.1: Main lipids present in cell membranes. (B) and (C) adapted from Alberts et al. [2017]. **(A)** Membranes consist in an assembly of lipids forming a bilayer of typical thickness ~ 5 nm. **(B)** From left to right: PE, PS, PC, SM. They all have a polar head group and two fatty acid tails. **(C)** Cholesterol has a different structure with a polar head and only one hydrocarbon chain. Cholesterol is positioned and interacts in a specific way within a phospholipids leaflet.

The overall shape and properties of this lipid assembly highly depends on the lipid form itself, as sketched on figure 2.2 (Israelachvili [1992]). Thousands of different lipids are generated in eukaryotes and bacteria with specific properties. Lipids characteristics (such as head group size, length and degree of unsaturation of acyl chains) determine whether the lipid has an inverted-conical, cylindral or conical shape and if the lipids can induce respectively a positive, zero or negative membrane curvature (this concept is introduced in part 2.1.3). Figure 2.2B shows the convention adopted for the curvature sign. The precise lipid composition determines the bending rigidity and the elasticity of the bilayer.

For instance, Phosphatidylcholine (PC) (the main eukaryotic membrane lipid) and Phosphatidylserine (PS) have a cylindrical shape and will favor a flat bilayer (see figure 2.2B). Phosphatidylethanolamine (PE) has a small head group and presents a conical shape which induces (negative) membrane curvature and favors an organisation in inverted cylindrical micelles, as depicted on figure 2.2C (Cullis et al. [1986]). Detergent molecules have a single acyl chain which gives them an inverted-conical shape and leads

to micellar organization, as shown on figure 2.2A.

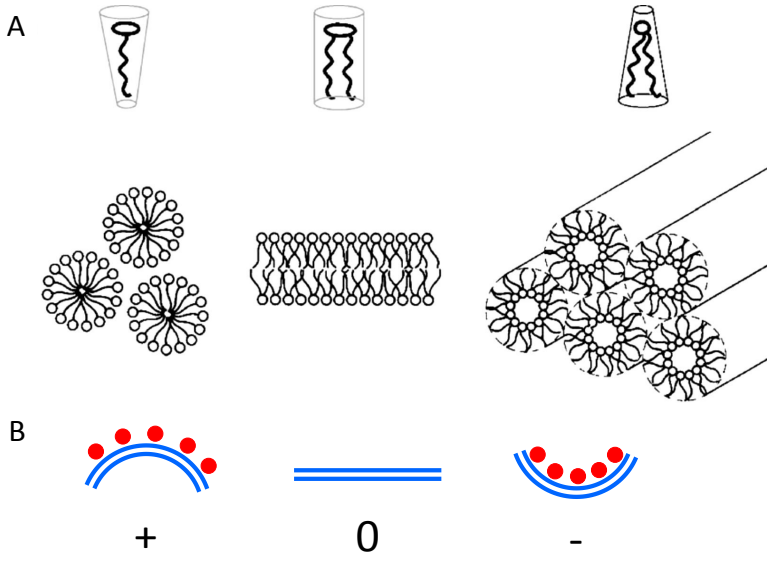

Figure 2.2: Lipids shape and membrane organization. (A) Lipid polymorphism leads to different types of lipid organization. From left to right: molecules with an inverted-conical shape (detergent for instance) form structures with a positive curvature, such as micelles; cylindrical-shaped lipids preferentially form bilayer structures (flat); conical-shaped lipids form negative curvature structures, such as hexagonal phases (Israelachvili [1992]; Van Den Brink-Van Der Laan et al. [2004]). **(B)** Convention of the sign of curvature of a membrane interacting with particles.

2.1.2 Cell membrane

Membrane cells are composed of a large variety of lipids and sterols but also of many membranes proteins, that will be described further in part 2.2 (they typically represent 50% of the membrane in mass). The precise lipid composition highly differs according to the organism (eukaryotes or bacteria) and also depends on the organelle in eukaryotes, as shown on figure 2.3 (Van Meer et al. [2008]). Moreover, lipid composition is asymmetric between the two leaflets of the bilayer, in particular at the plasma membrane (Van Meer and De Kroon [2011]). Finally, a last stage of lipids organisation in membrane is the formation of subdomains. Sphingolipids and sterols form lipid rafts together with their associated proteins, resulting in membrane subcompartments associated with specific function (Lingwood and Simons [2010]). In summary, the lipid composition is not homogeneous within a cell.

Moreover, it has been shown that cellular processes involving membrane remodelling can lead to lipid sorting, membrane protein sorting and to spontaneous formation of

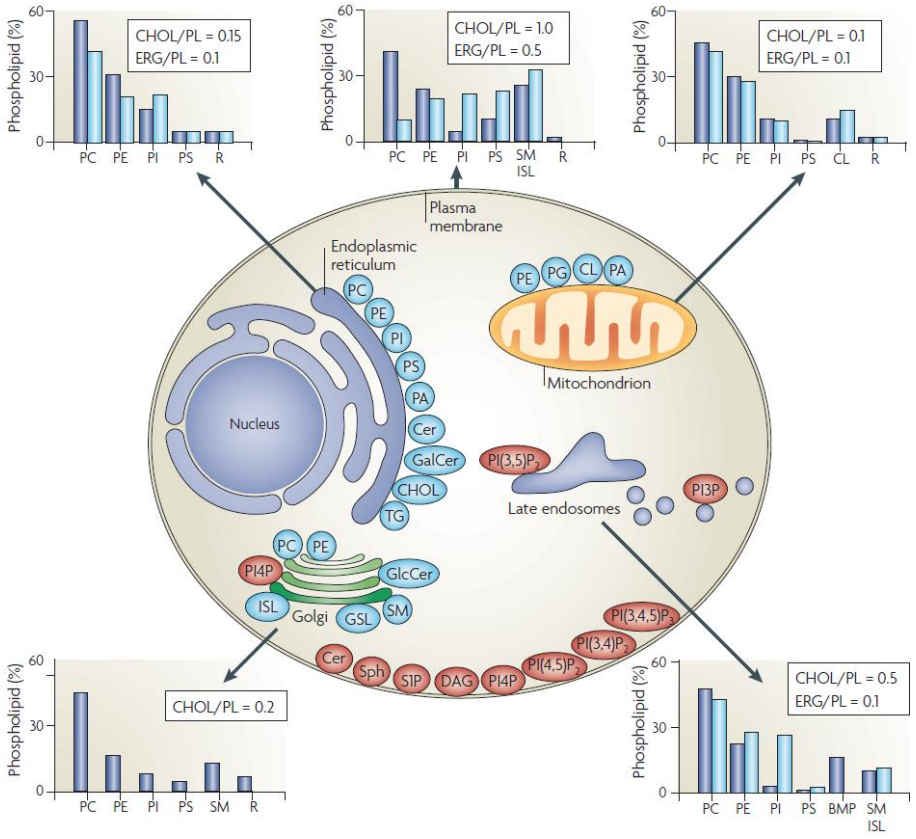

Figure 2.3: Lipid composition of cell membranes. Sketch from Van Meer et al. [2008]. The lipid composition of membrane varies throughout the cell. The lipid composition data (shown in graphs) are expressed as a percentage of the total phospholipid (PL) in mammals (blue) and yeast (light blue). The figure shows the site of synthesis of the major phospholipids (blue) and lipids that are involved in signalling and organelle recognition pathways (red). CHOL = cholesterol, ERG = ergosterol.

domains according to the lipids and/or proteins shape (Callan-Jones et al. [2011]). Membrane composition is a dynamical feature that gets adjusted together with other membrane properties (curvature and tension) during cell life processes such as division, migration, endocytosis and exocytosis (McMahon and Boucrot [2015]; McMahon and Gallop [2005]). Figure 2.4 shows the main mechanisms of membrane remodelling and the type of molecules involved. We can already appreciate the implication of membrane proteins in reshaping lipid bilayers.

Due to membrane dynamics and active regulation, it is hard to precisely control membrane characteristics and properties in cells. In studies aiming at investigating the role of specific membrane parameters, it is relevant to use an in vitro membrane system where its properties can be better controlled. In the next paragraphs, membrane elastic properties will be described, followed by an introduction of commonly used in vitro model membranes.

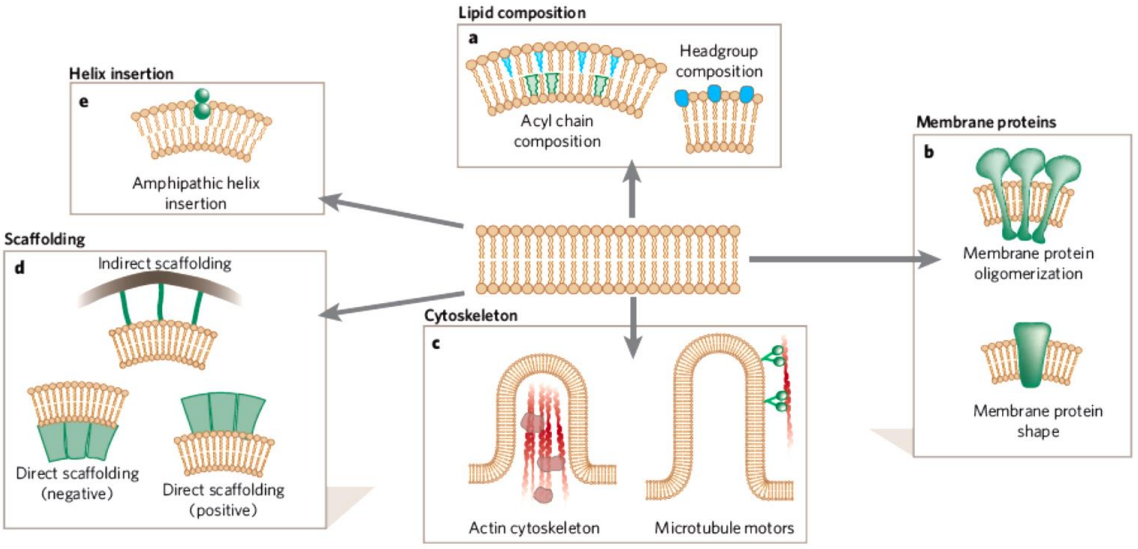

Figure 2.4: Mechanisms of membrane deformation. Sketch from McMahon and Gallop [2005]. The lipid bilayer remodelling is done via many different mechanisms resulting from individual or collective behaviours.

2.1.3 Membrane mechanical properties

Theoretical description of lipid membranes was initiated by Helfrich and Canham (Canham [1970]; Helfrich [1973]). Lipid bilayers are described as elastic sheets, with typical thickness ~ 5 nm. Two main modes of deformation, shown on figure 2.5, are possible: membrane stretching and bending.

Membrane stretching.

Membrane stretching, i.e. extension or compression of the bilayer, is associated to an energy cost (per unit area) that reads, for an elastic material,

$$E_{stretch} = \frac{1}{2}\kappa_s \left(\frac{\Delta A}{A}\right)^2, \tag{2.1}$$

where κ_s is the area-stretching modulus of the bilayer, and $\dfrac{\Delta A}{A}$ is the relative variation in area. The membrane tension σ in elastic regime is defined so that

$$\sigma = \frac{\partial E_{stretch}}{\partial A}. \tag{2.2}$$

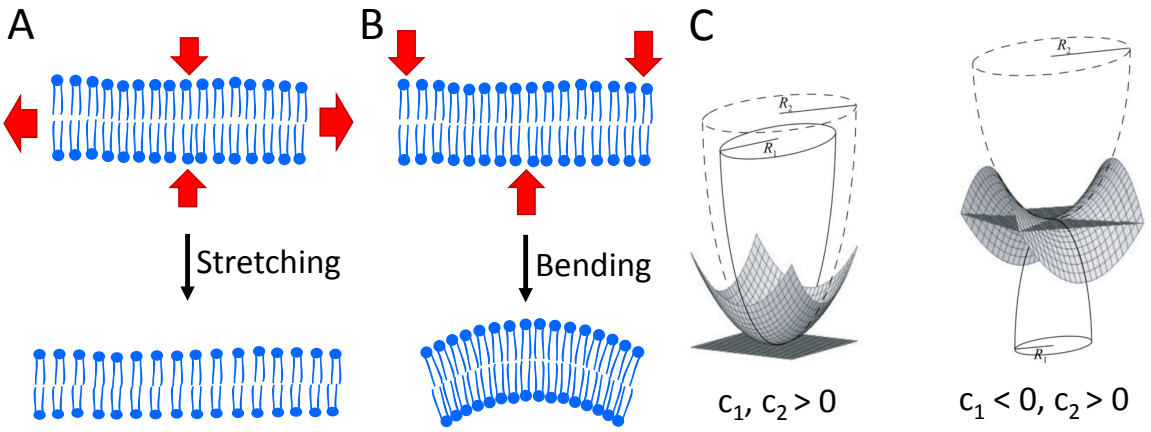

Figure 2.5: Membrane deformations. Two deformation modes are possible. **(A)** Membrane stretching leads to an increased membrane area, with a greater distance between the lipids and a decreased thickness of the bilayer. **(B)** Membrane bending requires to stretch one leaflet (upper) and to compress the other (lower). **(C)** Surface bending is characterized by two curvatures c_1 and c_2.

Using (2.1), we find

$$\sigma = \kappa_s \left(\frac{\Delta A}{A} \right). \tag{2.3}$$

Note than a change in membrane area is not only associated to a lateral stress but also to a modification in membrane thickness Δh as the lipid tails are mostly incompressible. Typical value of κ_s for PC membranes was found around 75 kT/nm^2 (300 mN/m) and highly depends on the lipid composition, such as the presence of cholesterol for instance that increases the value of κ_s (Rawicz et al. [2008]). At low tension, another regime exists, purely of entropic origin and related to membrane thermal fluctuations (Evans and Rawicz [1990]).

Membrane bending.

Membrane can also undergo bending i.e. out-of-plane deformations. The spontaneous curvature c_0 is the energetically preferred curvature of the membrane. A membrane with a spontaneous curvature c_0 is bent and reaches a local profile characterized by two principal curvatures c_1 and c_2, as introduced on figure 2.5B. The energy cost associated (per unit area) is

$$E_{bend} = \frac{1}{2}\kappa_c \left(c_1 + c_2 - c_0\right)^2 + \kappa_G c_1 c_2, \tag{2.4}$$

where κ_c is the bending rigidity modulus and κ_G the Gaussian curvature modulus. κ_c value depends on the lipid composition of the bilayer and typical values in PC lipids membrane are between a few kT to 100 kT (Marsh [2006]). κ_G contributes to the local

energy of the membrane only if the topology changes during the deformation.

Membrane spontaneous deformation can come from the presence of a transmembrane protein for instance, this will be discussed in part 2.2. Membrane inclusions lead to lateral membrane compression, to expansion or compression of the bilayer thickness (Phillips et al. [2009]) and impose a certain curvature to the direct surrounding membrane.

2.1.4 In vitro systems

In vitro membrane systems are convenient models to address specific biophysical questions. Over the years, many different systems have been developped and extensively used, see figure 2.6. Here is a non-exhaustive list of such systems (Bagatolli and Sunil Kumar [2009]): SUVs (Small Unilamellar Vesicles, typical size between 10 and 100 nm), LUVs (Large Unilamellar Vesicles, with diameter between 100 nm and 1 μm), GUVs (Giant Unilamellar Vesicles, with diameter over 1 μm, typically $\sim 10 - 50$ μm), nanodiscs, PSM (planar supported membrane, bilayer), Langmuir films (LF, lipid monolayer at air water interface).

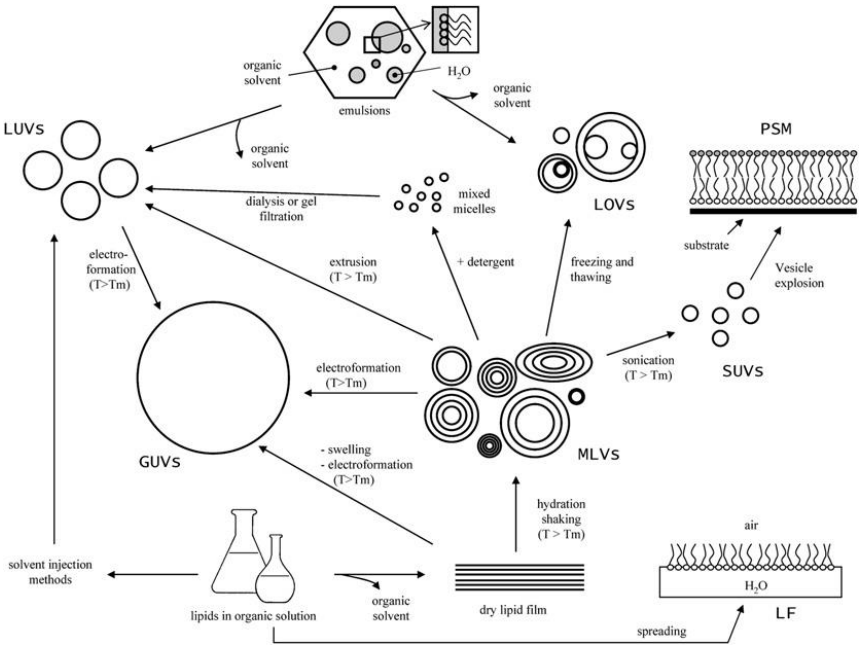

Figure 2.6: Different model membrane systems used in Biophysics. From Bagatolli and Sunil Kumar [2009]. Abbreviations: SUVs, LUVs, GUVs (Small/Large/Giant Unilamellar Vesicles), MLVs (Multilamellar Vesicles), LOVs (Large Oligolamellar Vesicles), PSM (Planar Supported Membranes), LF (Langmuir Films).

Membrane mechanical properties in model systems.

These model systems have been designed to control specific membrane properties. LFs, for instance, allow to control surface pressure.

Controlling SUVs size provides well-defined membrane curvature conditions. It was previously reported in Lévy et al. [1990] that, with detergent removal vesicles formation, liposomes size distribution can vary according to lipid composition and to reconstitution protocol. For instance, smaller vesicles are formed after faster detergent removal. Techniques have been developed in particular in the lab of Dimitrios Stamou to relate liposomes size to fluorescence intensity of a lipid marker (Lohr et al. [2009]). It is then possible to measure individual liposomes diameter without controlling precisely the size distribution of the whole sample (Hatzakis et al. [2009]).

GUVs can be aspirated with a suction micropipette allowing to control the membrane tension (Evans and Rawicz [1990]). Tube-pulling experiments have been developed to pull a nano-tube from a GUV with a fine control on the radius i.e. curvature (radius down to 10 nm can be reached at a high controlled tension) (Phillips et al. [2013]; Sorre et al. [2009]).

Protocols for SUVs and GUVs formation.

SUVs are usually formed by sonication and extrusion. However, in order to ensure unilamellarity of the bilayer and/or to incorporate membrane proteins (formation of proteo-SUVs), another method is preferred. SUVs are formed from a mixture of lipids and detergent, forming micelles, by progressively eliminating the detergent molecules (Rigaud et al. [1995]). Detergent removal is done by successive addition of Biobeads (hydrophobic adsorption onto polystyrene beads) and allows progressive formation of lipid bilayers and liposomes organisation. Figure 2.7a shows the stepwise solubilisation of liposomes. The black arrow indicates the increase of detergent concentration and two critical values are identified: one concentration for which the solubilisation starts and one over which the lipids solubilisation is total. Forming vesicles requires to take detergent concentration below these two critical values. This method provides 100% of unilamellar liposomes.

Different protocols can be used to prepare GUVs (Garten et al. [2015]). One of the most useful is the platinum-wire mediated GUVs electroformation, since it can also be used to obtain giant proteo-liposomes containing transmembrane proteins. A solution of SUVs (or proteo-SUVs when proteins need to be incorporated) is partially dried on a platinum wire, forming stacks of membrane, and then rehydrated under an AC electric field which leads to the GUVs growth, as depicted on figure 2.7b.

Referring to the main objectives of the present study, proteo-SUVs are selected as model system since they allow to work easily at the single molecule level and to investigate the effect of curvature on a transmembrane protein. The main advantage of SUVs as compared to nanotubes pulled from GUVs is first, that the protein is in an isotropic system. Secondly, the protein is localized in a curved membrane and cannot diffuse out of the tube to the GUV (Aimon et al. [2014]).

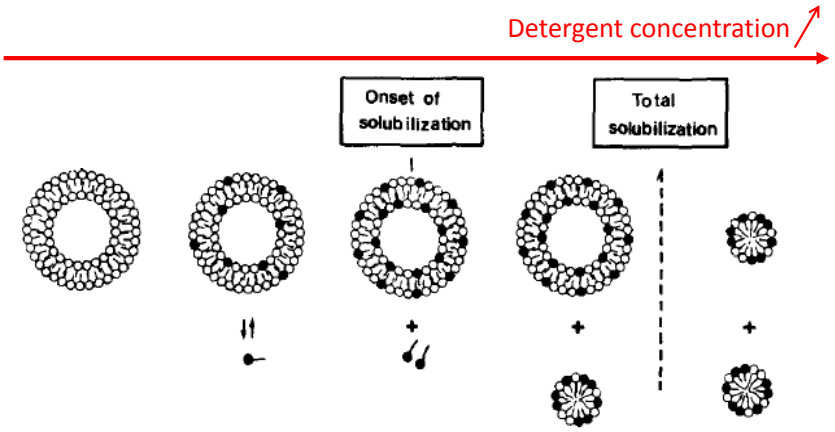

(a) Formation of liposomes by solubilization (Rigaud et al. [1995]). White heads show lipids, black heads show detergent molecules.

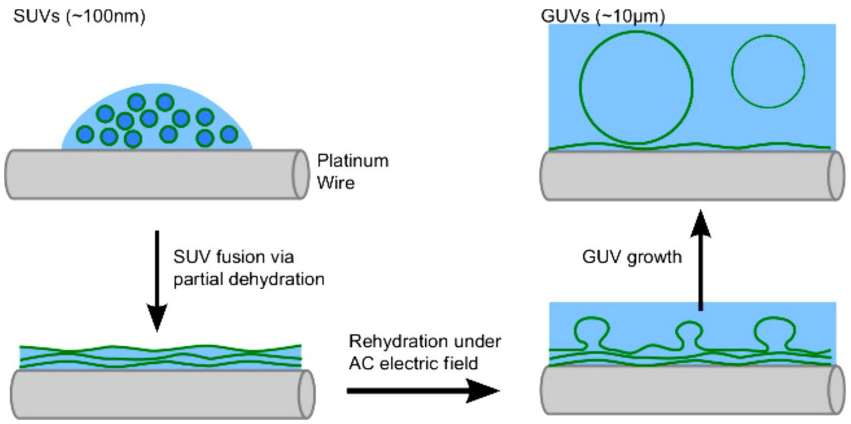

(b) GUVs growth by electroformation on platinum wire (Garten et al. [2015]).

Figure 2.7: Reconstitution methods of SUVs and GUVs.

2.2 Transmembrane proteins and bilayer interactions

Interactions between proteins and membrane can be considered at two different scales:

- at the microscopic scale the molecular interactions play a major part at the lipid-protein interface, such as hydrophobic effects, hydrogen bonds and charge interaction (at this scale, the precise type of lipids composing the membrane is crucial, as well as the structure of the transmembrane domain of the protein),
- at the mesoscopic scale the "global" properties of the membrane such as curvature, tension and thickness can produce mechanical stresses on the protein and reciprocally.

In this part, I will review more precisely (though non exhaustively) what is known about the interplay between transmembrane proteins and their membrane environment at both scales, and about the structure-function relationship for proteins.

2.2.1 A wide variety of transmembrane proteins

Cellular membranes are crowded with proteins (typically 50% in mass for the plasma membrane). These transmembrane proteins carry out a major part in the membrane functions and cellular processes. They are involved in homeostasis, cell adhesion and migration, signalling, cell detoxification and cell-cell communication. A few examples of such proteins are shown on figure 2.8, showing their variety of sizes and shapes. They represent a large fraction of the genome: between 25 and 30%, a proportion that varies very little according to the organism (Stevens and Arkin [2000]). Transmembrane proteins can be discriminated according to their structure: alpha-helical or beta-barrels (Alberts et al. [2017]).

As mentionned, transmembrane proteins represent a large fraction of the genome, and exhibit a wide variety of function, activation-types, topology. In particular, a classification has been established for a sub-family of transmembrane proteins, the transporters (Busch and Saier [2002]; Saier et al. [2006]). They are divided in five categories or classes, depending on the transporter type, the energy cost of the transport (energy arising from a chemical gradient or released by a chemical reaction, such as hydrolysis of a diphosphate bond or oxydoreduction), the transport mode (passive diffusion or active transport) and the exact function of the transporter. Figure 2.9 shows the five main classes of transporters (corresponds to the first digit) and the corresponding sub-classes (corresponds to the letter in second position). For instance, voltage-gated ions channels like KvAP are part of the class 1, bacteriorhodopsin is in category 3.E and finally ABC transporters in 3.A.

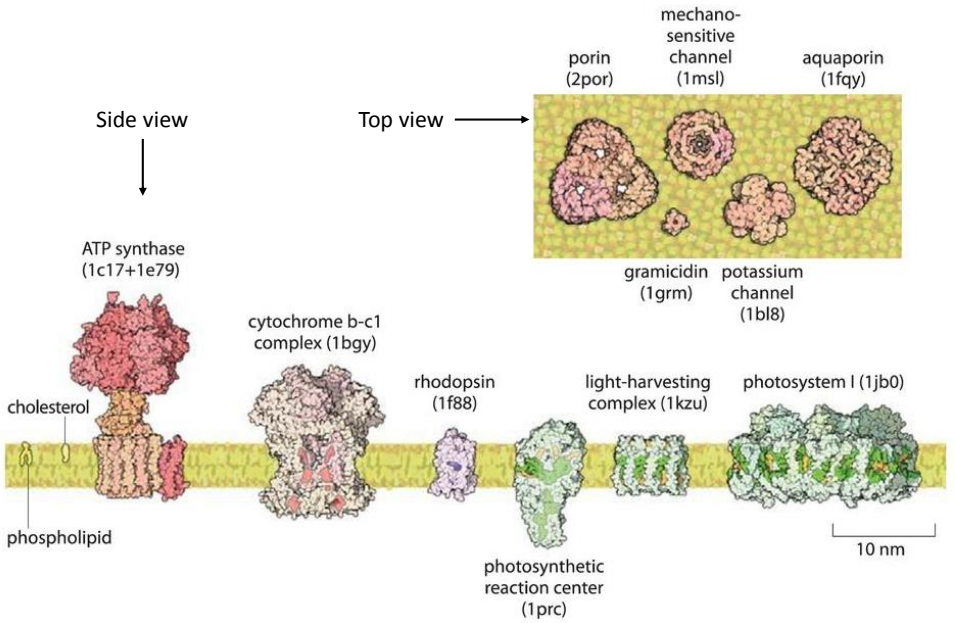

Figure 2.8: Variety of transmembrane proteins in sizes and shapes. From Milo and Phillips [2016]. Top and side views of some notable transmembrane proteins.

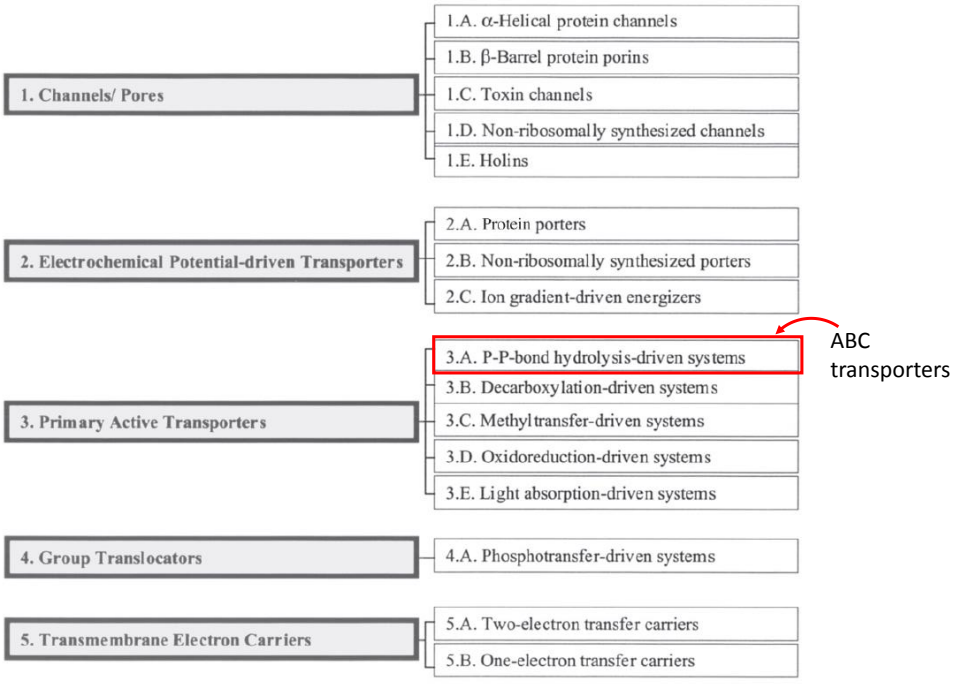

Figure 2.9: The transporter classification system. From Busch and Saier [2002].

2.2.2 Studying transmembrane proteins *in vitro*

To study such proteins in a less complex environment than the native membranes, they are usually expressed in a heterologous system (*E.coli*, yeast or insect cells for instance) and purified after solubilisation of membrane by detergent. Therefore, they can be purified

in large amouts, solubilised in detergent and then incorporated in model membranes such as SUVs or GUVs. Two main methods can be used to incorporate membrane proteins in small liposomes (Rigaud and Lévy [2003]; Rigaud et al. [1995]). Direct incorporation in pre-formed liposomes can be achieved by adding the minimum concentration of detergent that starts lipid solubilisation and that enables the inclusion of the protein (see figure 2.10A). This protocol allows to control the orientation of the protein within the membrane. The second method consists in reconstituting proteoliposomes from proteins in detergent and micelles of detergent/lipids (figure 2.10B). Detergent is removed by BioBeads and lipids form bilayers integrating the proteins.

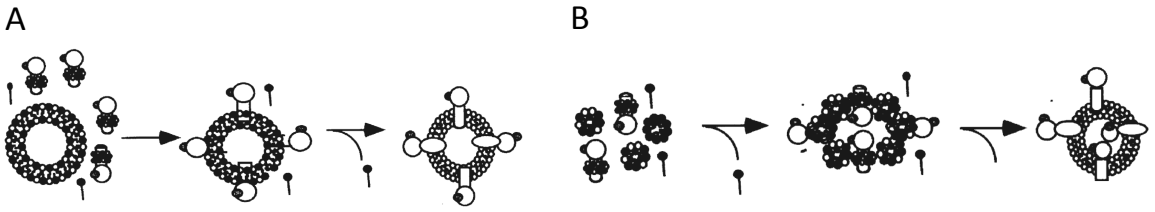

Figure 2.10: Formation of proteoliposomes. From Rigaud and Lévy [2003]. Reconstitution of membrane proteins in proteoliposomes: **(B)** by direct incorporation and **(C)** from micelles of lipids and proteins in detergent. White heads show lipids, black heads show detergent molecules. Transmembrane proteins are depicted as white bodies in figure B and C.

To incorporate proteins in GUVs, similar protocol of growth as presented in part 2.1.4 can be followed starting from proteo-SUVs (Garten et al. [2015]). Single molecule regime can easily be reached with high dilution of the proteins (Quemeneur et al. [2014]) but it is also possible to work at high density of proteins for some applications.

Transmembrane proteins are embedded in the lipid bilayer and their inclusion has a mechanical impact and an energy cost for the membrane.

2.2.3 Protein inclusion: a curvature and hydrophobic matching

Theoretical description.

The first theoretical description of intercalated molecules within a lipid bilayer was proposed by Leibler [1986]. The interaction between these intercalated molecules and the membrane was taken into account in a modified Helfrich Hamiltonian via a coupling parameter. This model predicts that molecules inclusion leads to membrane shape changes and to "curvature instabilities".

More precisely, proteins have a global envelope in membranes referred to as "protein shape": it can be cylindrical or more or less conical, as depicted on figure 2.11. The shape

of the protein is characterized by the parameter c_p called protein intrinsic spontaneous curvature. Membrane proteins inclusion results in interactions between the lipids and the transmembrane domain of the proteins. For a membrane with no topological change, the bending energy is (see equation (2.4))

$$E_{bend} = \frac{1}{2}\kappa_c \left(c_1 + c_2 - c_0\right)^2 . \tag{2.5}$$

The inclusion of membrane proteins, occupying a membrane area fraction ϕ, can be modelled by defining the membrane spontaneous curvature in the presence of proteins (Campelo et al. [2008]) by

$$c_0 = c_p \phi. \tag{2.6}$$

The protein intrisic spontanous curvature c_p can also be seen as the protein inclusion ability to curve membrane: it would be the curvature of an unstressed membrane that is saturated with the protein of interest. Cylindrical proteins exhibit a zero spontenous curvature since they do not bend the membrane, whereas conical-shaped proteins locally bend the surrounding lipid bilayer and have a non-zero c_p.

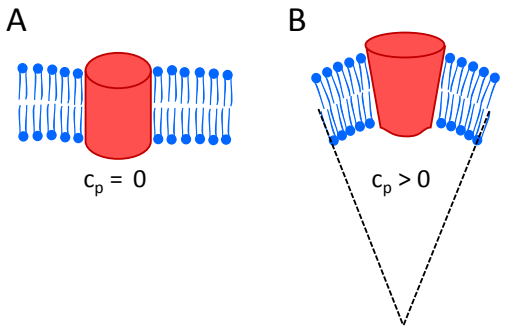

Figure 2.11: Protein spontaneous curvature and membrane bending. (A) Cylindrical-shaped protein does not deform its surrounding membrane out of the plane and has a zero spontaneous curvature. **(B)** Conical-shaped protein bends the lipid bilayer, resulting in a non-zero curvature of its surrounding membrane, defined as the protein spontaneous curvature.

Mesoscopic scale: curvature matching.

Insertion of conical proteins into membrane can either induce a membrane deformation or a redistribution of proteins into curved areas of the membrane: this can be defined as a curvature matching between proteins and the lipid bilayer. Experimental evidences of this curvature matching are available: for instance, experiments with nanotubes pulled from a proteo-GUV allow to measure the protein sorting between a flat membrane (GUV) and a curved membrane (tube) (Callan-Jones and Bassereau [2013]). It was shown that

the conical-shaped protein KvAP is enriched in nanotubes (its spontaneous curvature was found to be $1/25$ nm^{-1}) while the cylindrical-shaped water channel AQP0 does not exhibit any preference for curved or flat membrane indicating a zero spontaneous curvature (Aimon et al. [2014]). This curvature matching was also highlighted in living cells by studying sorting of three Gprotein-coupled receptors (GPRCs) (the neuropeptide Y receptor Y2, the β1 and β2 adrenergic receptors) according to membrane curvature (Rosholm et al. [2017]). Finally, it has been shown on mechanosensitive channels in proteo-SUVs, that the inclusion of a protein in a bilayer leads both to a change of the protein shape (change in the cross-sectional shape was measured) and to a change of the membrane curvature (Marsh [2007]). The effect of the protein shape and of the membrane curvature is thus reciprocal.

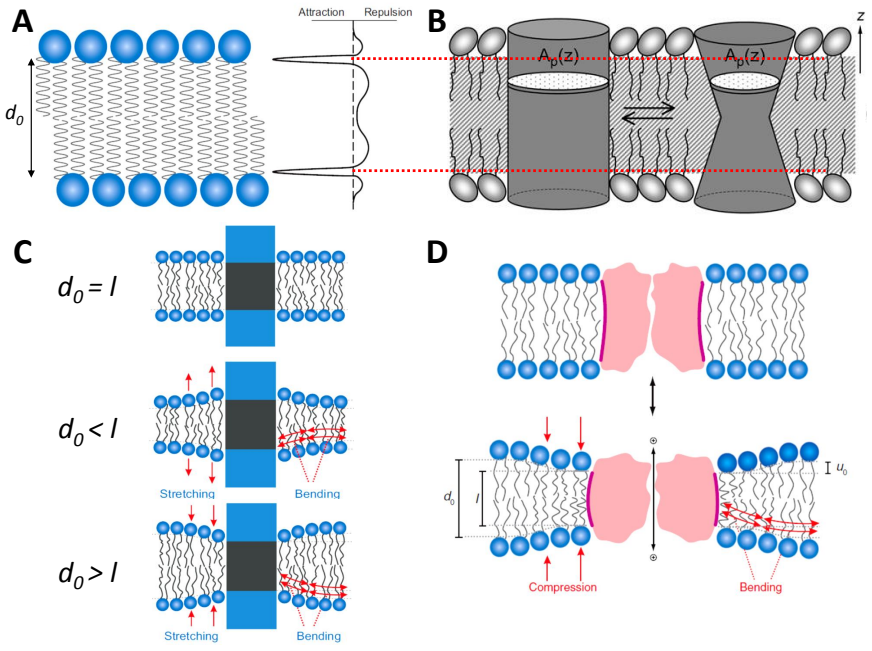

Figure 2.12: Hydrophobic matching between bilayer and transmembrane proteins. (A), (C), (D) are adapted from Andersen and Koeppe [2007], (B) from Marsh [2007]. **(A)** Lateral pressure profile of the lipid bilayer with areas associated with repulsion and attraction indicated (its hydrophobic thickness d_0 is represented). **(B)** Membrane proteins can change their cross section A_p in response to the pressure profile of the membrane. **(C)** Membrane inclusions are shown with the non-polar residues in dark gray and the polar residues in blue. l is the protein hydrophobic thickness, and d_0 is the one of the unperturbed bilayer. When $d_0 = l$ the hydrophobic parts match without exerting extra stress and the bilayer remains unperturbed. When $d_0 < l$ or $d_0 > l$, hydrophobic matching leads to membrane bending with respectively membrane extension and compression (i.e. stretching). **(D)** Effect of a transmembrane protein conformational change on its hydrophobic coupling with the bilayer. Hydrophobic boundaries are depicted with thick purple lines. If the conformational change results in a reduction of the hydrophobic parts, this causes a local membrane deformation.

Microscopic scale: hydrophobic matching.

Not only a curvature matching (mesoscopic scale) is necessary for proteins inclusion in membrane, but also a hydrophobic matching (microscopic scale). The inclusion of a transmembrane protein results in close interactions at the interface between protein transmembrane domain and the lipids. This is massively driven by hydrophobic interactions as the protein is in close contact with the lipid tails (Marsh [2007]). More generally, interactions within the lipid bilayer result from attraction and repulsion integrated over the bilayer thickness. This is the lateral pressure profile of the lipid bilayer, depicted on figure 2.12A. This shows a very specific interaction pattern where the hydrophilic lipid heads repel each other, and the hydrophobic part of the bilayer (formed by lipid tails) also forms a repulsive area of thickness d_0. Lipid head-tail interface shows an attractive contribution to this profile.

Membrane proteins sense the lateral pressure profile as a force exerted on a cross sectional slice of the transmembrane domain of the protein. The average thickness of the hydrophobic domain of a transmembrane protein is about 29 Å (Lee [2003]). Therefore an hydrophobic mismatch between the lipid bilayer and the protein leads to two effects:

- membrane stretching with a compression or extension of the direct surrounding bilayer. Figure 2.12C shows that it results in a local bending of the membrane and therefore to lipids reorganisation within the lipid mixture, since conical-shaped lipids preferentially move to bent areas (Brown [2012]).
- membrane proteins cross section change, in response to the pressure profile of the membrane, as depicted on figure 2.12B.

Membrane deformation models.

Proteins inclusion results in membrane deformations that arise from the lateral pressure profile of the bilayer and from the shape of the protein. Models for two different protein-related membrane deformations have been proposed (Phillips et al. [2009]) and are summarized on figure 2.13:

- Thickness deformation: hydrophobic matching at the protein-bilayer interface induces a compression or expansion of the membrane thickness.
- Midplane bending: curvature matching leads to membrane midplane being tilted by the protein, producing a local membrane curvature.

These concepts are crucial to understand the reciprocal effect of membrane and protein when conformational change occurs. If the conformational dynamics of the protein results

in a reduction or raise of its hydrophobic part, it will induce a membrane deformation as shown on figure 2.12C (Andersen and Koeppe [2007]).

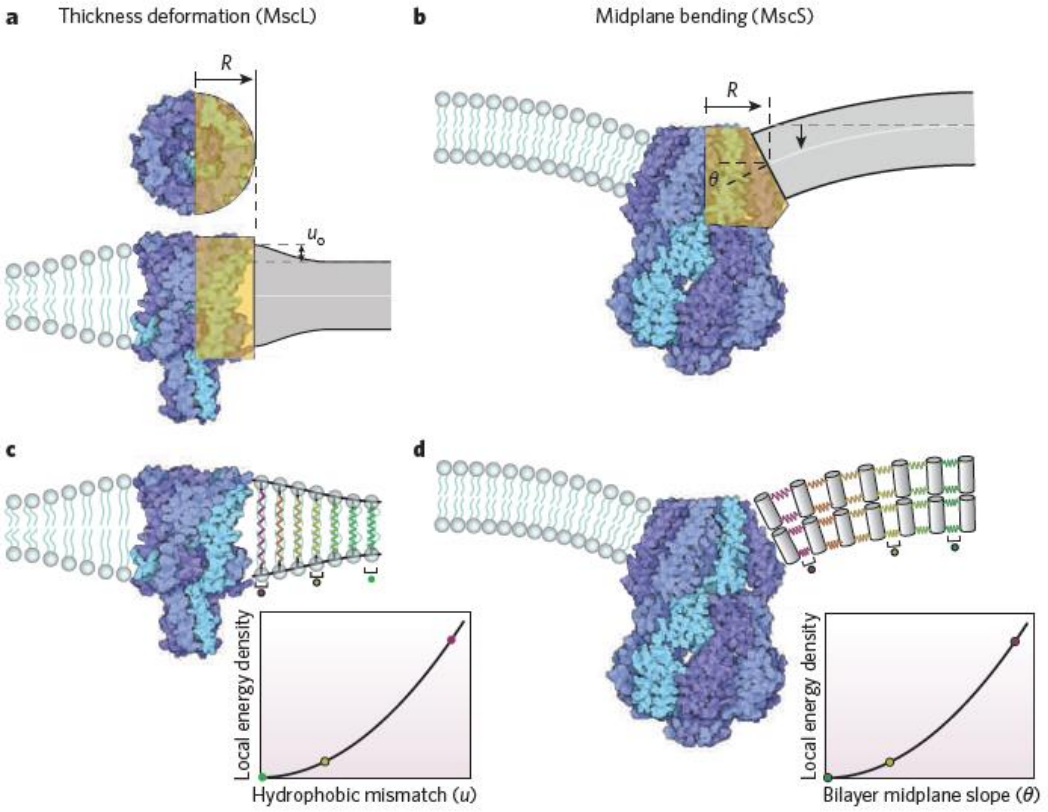

Figure 2.13: Model of the protein-related membrane deformations. From Phillips et al. [2009]. Two mechanosensitive channels are represented: MscL with cylindrical transmembrane domain and MscS with conical transmembrane domain. Hydrophobic mismatch leads to membrane extension for the first channel and the lipid-protein interface results in a membrane bending for the second channel. The corresponding membrane distortion is represented. Membrane can be described as a continuous elastic medium and the elastic response of lipids to membrane deformation is represented by coloured springs on figures c and d. In both cases the local energy density increases when getting closer to the protein.

2.2.4 Protein function and membrane

Functional lipids.

Some specific lipids appear to be of crucial importance for some transmembrane proteins. They are called functional lipids, since depleting them affects the protein function.

Some channel structures have been resolved (see for instance Laganowsky et al. [2014]) revealing a tight binding of some specific lipids that increases the stability of the protein and modulates its function. Similar results were found in Bechara et al. [2015], suggesting that an invariant subset of annular lipids tightly binds to the ABC transporter TmrAB

and is involved in the ATP hydrolysis i.e. in the conformational cycle. This unique set of annular lipids has been fully characterized for ten membrane proteins (including the human ABC transporter P-gp) using molecular dynamics simulations in Corradi et al. [2018]. For the purine transporter UapA, the presence of specific lipids was shown to maintain the stability of the functional dimer while the abundance of monomers increases with delipidation (Pyle et al. [2018]).

Finally, activity measurements on some transporters proved that the presence and nature of lipids affect the activity i.e. transport function of the protein. Schmidt and collaborators found that the activity of the voltage-dependent K^+ channel KvAP depends on the negative charge of phospholipids (Schmidt et al. [2006]). In Pignataro et al. [2015], activity measurements of the solubilised P-type Ca^{2+}-ATPase revealed a maximum activity for a specific molar ratio between PC lipids and detergent. This activity boost in the presence of negatively charged lipids has also been shown by Su Jin Paik on bacterial ABC transporter BmrA (Paik [2018]). Moreover, the activity of BmrA was found systematically increased in lipid/detergent micelles as compared to detergent only, and to depend on the lipid composition.

Effect of curvature and tension.

The stresses (curvature and tension, defined in part 2.2.3) exerted by the membrane have been shown to affect the function of transmembrane proteins. Proteins such as mechano-sensors, ion channels, pumps, and transporters use some energy source (mechanical stretch, electric potential, ATP hydrolysis) to change conformation, and therefore change their shape, their spontaneous curvature and/or hydrophobic thickness. The conformation change of these proteins is tightly linked to their function and has a non-trivial contribution to membrane mechanical properties, and reciprocally.

Different examples show the coupling between protein function and membrane mechanical properties. The mechano-sensor channel MscL is stabilized in its fully open conformation when membrane curvature is increased by addition of conical-shaped lipids (the gating function is affected) (Perozo et al. [2002]). In this study the authors also proved that tuning the hydrophobic mismatch was unable to force and maintain the gate opening. The addition of conical-shaped lipids (PE) was found to increase the "downhill" transport of lactose molecules of the lactose permease LacY compared to membranes containing cylindrical PC lipids (Bogdanov et al. [2010]). Similarly, the activation of the voltage dependent potassium channel depends on the curvature of the membrane (Schmidt and MacKinnon [2008]). As a final example we can cite the work from Tonnesen et al.

[2014] on the bacterial pore α-hemolysin. The authors managed to optically report on the transport activity of α-HL reconstituted in single-molecule regime in SUVs with varying size (diameter between 50 and 400 nm). High membrane curvature was found to reduce the pore permeability by four orders of magnitude indicating a strong regulation of α-HL function by membrane curvature. For a review of the effect of membrane curvature and tension on various transmembrane proteins see Andersen and Koeppe [2007].

2.2.5 Protein-protein interaction

Over the last decade, with a growing interest and curiosity for this interplay between protein and membrane properties, not only the function of single integral proteins has been investigated but also lateral interactions mediated by membrane.

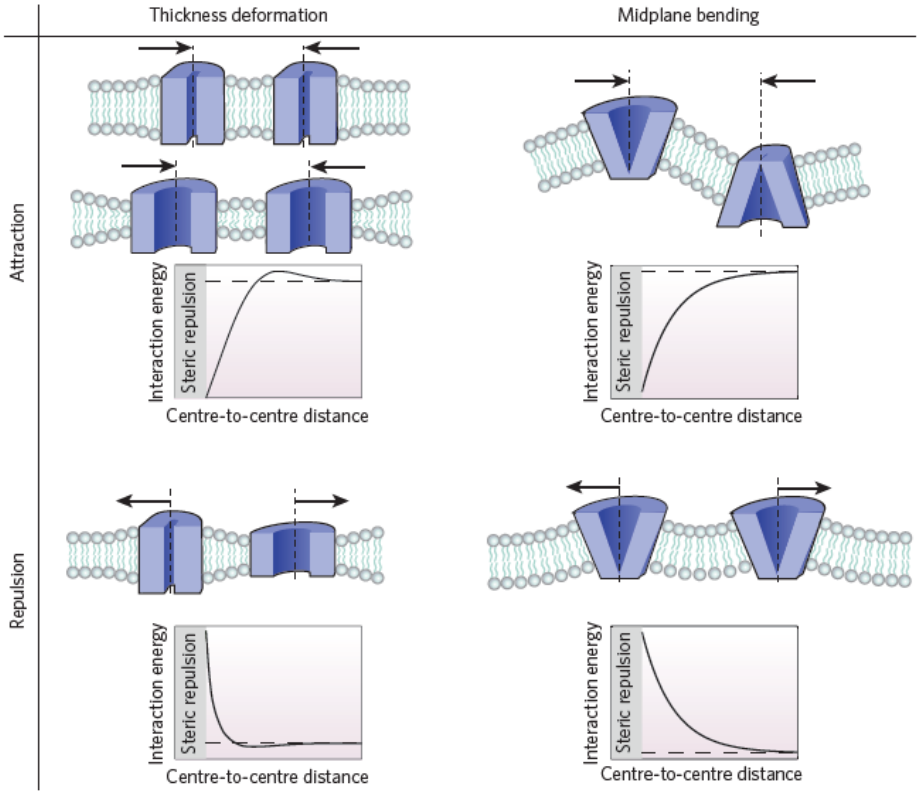

Figure 2.14: Effect of protein conformation (shape) on interaction and cooperativity. From Phillips et al. [2009]. The shape of a protein (cylindrical or more or less conical) results in different membrane deformation (thickness deformation -left- or midplane bending -right). At high density, these membrane deformations affect protein-protein interaction, leading to attraction or repulsion depending on the proteins' shape and orientation.

It has been reviewed in Phillips et al. [2009] how the protein-protein interaction highly depends on their conformation. The ability of a single protein to deform the membrane

(spontaneous curvature and hydrophobic matching) and the spatial extension of this deformation determine if the membrane-mediated interaction is attractive or repulsive, as depicted on figure 2.14. Unfortunately, no experimental work exists so far testing these predictions.

Nevertheless, coarse-grained membrane simulations were done by Schmidt and Weiss [2010] to investigate the effect of hydrophobic mismatch on protein clustering in a flat bilayer. Protein experimenting a hydrophobic mismatch with the membrane were found to cluster. Furthermore, when proteins with different thicknesses of their hydrophobic part were computed, some segregation was observed: proteins with similar mismatch tend to co-localize and get segregated from proteins with different mismatch.

2.2.6 Protein mobility and membrane

The interaction between transmembrane proteins and lipid bilayer results in a modification of the protein mobility according to its shape and to the membrane tension. In Quemeneur et al. [2014] single particle tracking experiments were done on GUVs (flat membrane) while tuning the membrane tension with micropipette aspiration. Two proteins with different shapes were reconstituted at low density and observed: the potassium channel KvAP (conical shape with $C_p = 0,04$ nm^{-1}) and the aquaporin AQP0 (cylindrical shape). It was found that lowering the membrane tension decreases the diffusion coefficient of KvAP but does not affect the one of AQP0 (see figure 2.15). As both proteins share the same diameter, their diffusion coefficient is equal at high tension. Unlike AQP0, KvAP creates a local membrane deformation, that increases when membrane tension drops. Due to intra-bilayer drag forces (frictions) the diffusion coefficient of a conical shaped protein decreases in a low tension membrane (where its deformation is higher) compared to a high tension membrane (quasi-flat deformation).

To summarize part 2.2, some efforts have been made to understand finely the interaction between transmembrane proteins and their lipidic environment. In particular the interactions between protein function and lipid composition, or between protein mobility and membrane mechanical properties are progressively more documented. However, the effect of tension and curvature on functional properties have not been studied for transporters. In general, very few proteins have been studied as compared to the diversity of existing proteins.

In addition, development of single molecule tools like FRET (Förster Resonance Energy Transfer) has allowed to resolve the function and conformation dynamics of some

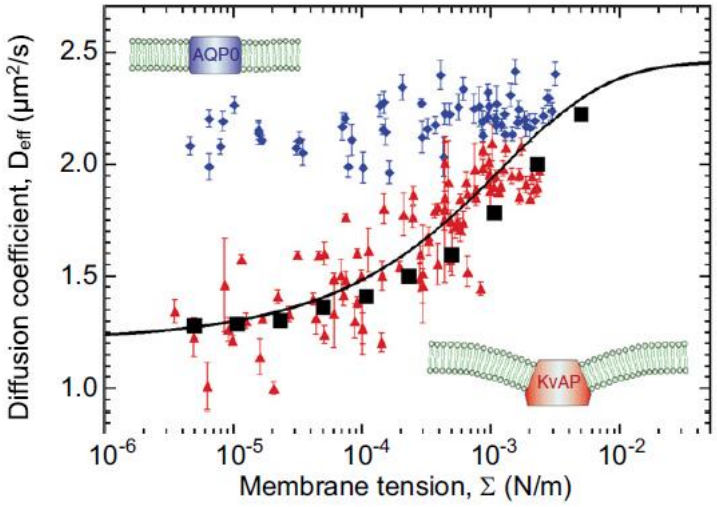

Figure 2.15: Effect of membrane tension and protein shape on its mobility. Single particle tracking shows that lowering membrane tension decreases the diffusion coefficient for conical shaped proteins (KvAP) and does not affect cylindrical ones (AQP0) (from Quemeneur et al. [2014]).

transmembrane proteins. But it has not been investigated yet how the conformational dynamics and kinetics of such proteins depend on membrane mechanical properties.

2.3 Probing single protein conformation: smFRET

Over the past twenty years, Förster Resonance Energy Transfer method (FRET) has been more and more used on biological systems. The first experimental evidences of FRET were found in the 20's by Franck and Cario, who established the concept of energy transfer in vapor phase molecules. From the 40's on Förster characterized and gave a theoretical frame to this phenomenon, which is now named after the scientist (Förster [1960]). FRET was progressively more and more used for ensemble measurements but the first experiments of FRET using a single Donor and a single Acceptor (smFRET) were done by Ha and coworkers on DNA molecules (Ha et al. [1996]). This technique combined two state-of-the-art methods: single-molecule detection allowed not to average on an ensemble but to access the heterogeneity of a system, and FRET provided nanometer scale measurements (typical distances between 1 and 10 nm), acting like a "molecular ruler". Since then, smFRET has been widely used to address biological and biophysical questions such as for close distance interacting partners (intermolecular FRET) or conformation change of proteins (intramolecular FRET) (see part 2.3.3). For instance it

was used to investigate the bending of DNA due to binding of the transcriptor factor TATA-binding protein (Gietl et al. [2014]).

In this part, I will present the fundamental theory of smFRET, the methods to implement it experimentally and how this methods evolved progressively over the last twenty years. Finally I will review non exhaustively some FRET studies made on transmembrane proteins.

2.3.1 Principles of FRET

This paragraph is summarized from Bräuchle et al. [2009]. Förster Resonance Energy Transfer is related to a dipole dipole interaction between a Donor fluorophore (always represented in green in this thesis) and an Acceptor one (represented in red). More precisely the energy transfer occurs between the excited state S1 of the Donor and the ground state S0 of the Acceptor (see figure 2.16A). This transfer of energy depends on three parameters:

- the distance R between the Donor and Acceptor fluorophores. As shown on figure 2.16.C, the transfer is higher, or more efficient, at short distance, and vanishes when the distance increases;

- the spectral overlap between the Donor emission and the Acceptor excitation spectra (integral depicted in light green on figure 2.16.B), characterized by the spectral overlap integral J, intrinsic to each Donor/Acceptor couple;

- and the 3D relative orientation of the two dipoles, taken into account with the orientational factor κ^2 (we use $\kappa^2 = 2/3$, the value found by averaging over all possible orientations).

The energy transfer is characterized by the parameter E called FRET efficiency. E is defined as the probability that energy coming from an excited Donor gets transferred to an Acceptor. FRET efficiency E reads

$$E = \frac{R_0^6}{R_0^6 + R^6}. \tag{2.7}$$

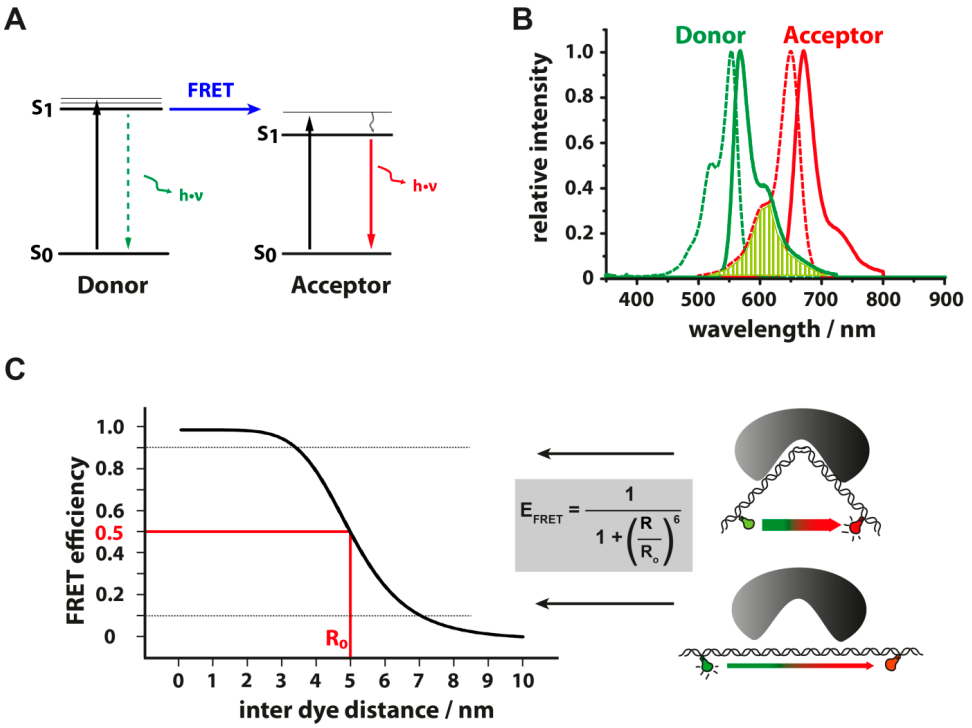

Figure 2.16: Principles of FRET. (Adapted from Gust et al. [2014]). **(A)** Energy levels of Donor and Acceptor fluorophores with a ground state S0 and an excited state S1. FRET corresponds to the energy transfer from the Donor in S1 that brings the Acceptor in S1 (if the Acceptor is in close distance range, from 1 to 10 nm). The acceptor can return to S0 by the emission of a photon. **(B)** Excitation (dashed lines) and Emission (plain lines) typical spectra for a Donor (green lines) and an Acceptor (red lines). FRET can occur only if there is an overlap between the emission spectrum of the Donor and the excitation spectrum of the Acceptor. The overlap area is depicted in light green. **(C)** FRET efficiency E plotted according to the Donor-Acceptor distance. The Förster radius R_0 is indicated in red. An example of biological application is shown on the right: the TATA-binding protein (TBP) can fold DNA which brings the two fluorophores closer together. When TBP binds the DNA, a higher value of E is observed as compared to TBP-free DNA case (Gietl et al. [2014]).

The variation of E with R is plotted on figure 2.16C. R_0 is the Förster radius which depends on the parameters J and κ^2 mentionned above, on the quantum yield of the Donor fluorophore ϕ_D and on the refractive index of the sample n. R_0 is given by

$$R_0 = \left(\frac{2.07 \kappa^2 \phi_D J}{128 \pi^5 N_A n^4} \right)^{1/6}, \tag{2.8}$$

where N_A is the Avogadro number. As shown on figure 2.16C, for $R = R_0$ the FRET efficiency is equal to 50%. When $R > R_0$, E drops and it increases when $R < R_0$. The sensitivity of the FRET is maximum at R_0 but drops quickly: the detection of FRET changes is better for interdye distances close to R_0. This value fully characterizes the fluorophores Donor and Acceptor as a FRET couple (Khadria and Senes [2015] provided a table with R_0 values for commonly used fluorophores). Therefore, in experiments, the

fluorescent dyes should be chosen carefully by selecting them according to their Förster radius and comparing it with the distance range expected in the system of interest in order to maximize the FRET change observed.

In practice, the FRET efficiency E is measured from the drop of fluorescence intensity of the Donor in presence of the Acceptor. The fluorescence intensity of both the Donor I_D and the Acceptor I_F are measured and E is calculated according to the following equation

$$E = \frac{I_F}{I_F + I_D}. \tag{2.9}$$

Practically, depending on the set of optical filters used for the Donor and Acceptor detection, some contributions participate to the apparent intensity in the FRET channel that are not coming from the energy transfer: Donor crosstalk in the FRET channel and Acceptor direct excitation at the Donor wavelength. These extra contributions can be corrected (details will be provided in methods chapter 4).

2.3.2 Methods for FRET measurements

Since the first experiment of FRET with single fluorophores (Ha et al. [1996]), several methods have been developed and widely used. For smFRET measurements two different approaches are possible: measurements in solution or on immobilized molecules, with two different illumination systems: single-illumination at the Donor excitation wavelength or alternating-laser excitation (ALEX) both at the Donor and Acceptor excitation wavelengths.

Solution FRET measurements.

In solution, the molecules diffuse freely and are detected when they enter the excitation beam. The fluorescence is detected in bursts. Single molecule detection requires a small excitation volume, low amount of fluorescing molecules (to limit sources of background) and high-efficiency detectors (see Weiss [1999] for a review of spectroscopy methods). The residence time of the molecules in the beam is short (typical residence time from 1 to 10 ms), i.e. too short to detect conformational changes for instance. However this technique allows to measure distributions of conformational states: this was for example done by Deniz and coworkers on DNA molecules while varying the interdye distance in a controlled manner (Deniz et al. [1999], see figure 2.17). They showed in particular that it

was possible to detect subpopulations within a group of biomolecules using smFRET, as shown on figure 2.17C.

Zander et al. [1996] showed that it is possible to extract information about fluorophore lifetime from the fluorescence bursts. This analysis technique can provide information about the lifetime of conformational states (with 100 ps lifetime temporal resolution). Techniques as fluorescence (cross) correlation spectroscopy (FCS/FCCS) are often used in combination with FRET since they allow to reveal intramolecular fluctuations (see Sahoo and Schwille [2011] for a review).

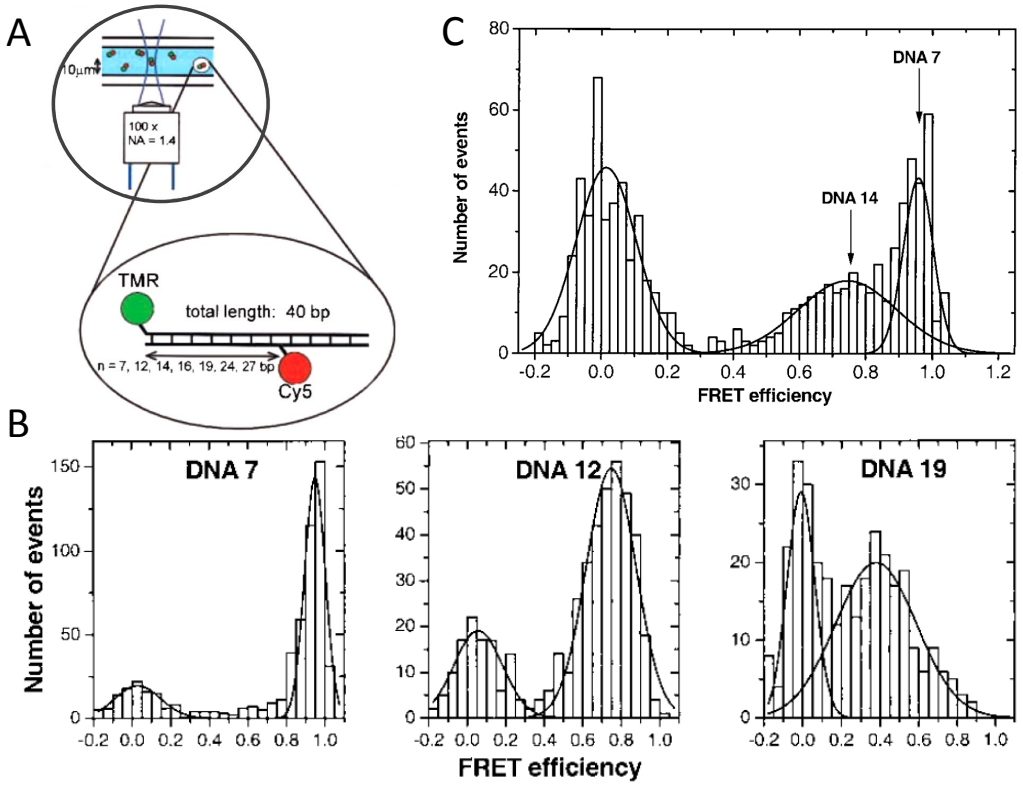

Figure 2.17: Solution-based FRET measurements. (From Deniz et al. [1999]). **(A)** General scheme of the experiment. The system used is a double-stranded DNA labelled with Tetramethylrhodamine TMR (= Donor) and sCy5 (= Acceptor) at different interdye distances (indicated in base-pair bp, betzeen 7 and 27). DNA freely diffuses in the sample solution and is detected when it enters the excitation beam. **(B)** FRET efficiency histograms measured for interdye distances 7, 12 and 19 bp. First peak round $E = 0$ corresponds to Donor leakage and is called "zero peak". With increasing interdye distance the main FRET peak shifts from $E \simeq 1$ to $E \simeq 0,4$. **(C)** Histogram of a $1:1$ mixture of DNA 7 and 14 (interdye distances in bp) where two subpopulations can be detected.

Immobilized molecules FRET measurements.

Immobilized molecules experiments were rapidly developed as solution measurements have a very limited timescale over which a single particle can be observed. Immobilized molecules observation allows measurement on single particles over a long time (limited

by photobleaching). Breakthrough and advanced techniques from physics and chemistry were crucial. Immobilization of biomolecules was required to be robust, specific and not altering their functionality.

Several surface treatment protocols using BSA or NHS-PEG or PLL-PEG and biotin-streptavidin-biotin strong binding or His-tag groups were adopted to anchor specifically DNA, free proteins and liposomes (Roy et al. [2008]; Selvin and Ha [2008]). Figures 2.18A, B and C show some examples of possible immobilization methods.

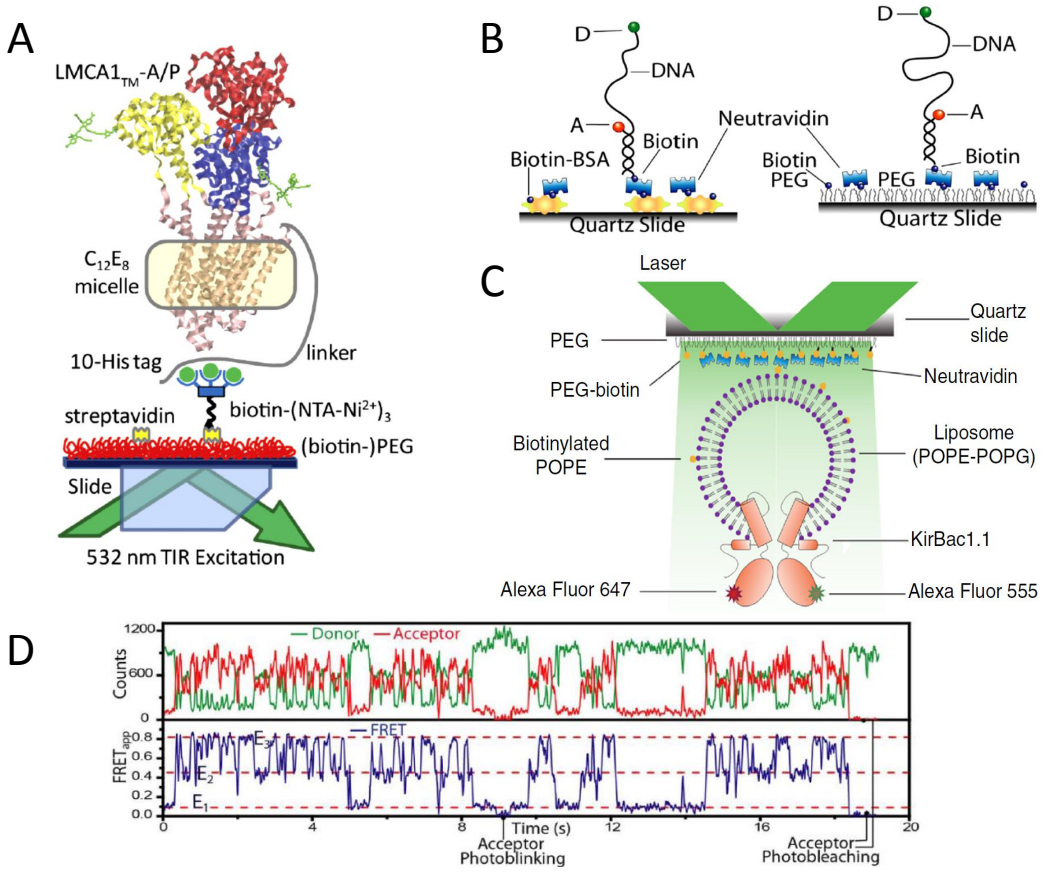

Figure 2.18: Immobilized molecules FRET measurements. Some surface immobilization strategies are shown: **(A)** for proteins in detergent, using a His-tag (Dyla et al. [2017]), **(B)** for DNA using biotin-streptavidin-biotin binding on a surface covered with PEG or BSA molecules (Roy et al. [2008]), **(C)** for liposomes containing a transmembrane protein (Wang et al. [2015]). **(D)** An example of intensity measured over for the Donor and the Acceptor and the corresponding FRET efficiency (Roy et al. [2008]). Some events such as photoblinking or photobleaching are indicated.

Total Internal Reflection Fluorescence (TIRF) microscopy is used in order to reduce background signal (as the evanescent wave has a depth of 100 to 200 nm). The spatial and temporal resolution limits of this techniques are documented in Holden et al. [2010].

Finally, the observation time is limited by photobleaching and blinking of fluorophores. It has been found that dioxygen plays a major part in these reactions and that the use of an oxygen-scavenging solution can enhance drastically the photostability and life-time

of the dyes Rasnik et al. [2006]; Aitken et al. [2008]. Figure 2.18D shows an example of FRET trace that can be observed.

Alternating laser excitation *versus* single-laser excitation.

One of the latest and greatest breakthrough for smFRET experiments was the introduction of alternating laser excitation (ALEX) (Kapanidis et al. [2004]). The principle is explained below. The main difficulty in smFRET comes from the diversity of populations often present in biophysical samples. This heterogeneity can be due to the coexistence of differently labelled populations (Donor only, Acceptor only, doubly labelled), inactive molecules (therefore not providing any FRET signal) or to free molecules (when studying ligand interaction for instance).

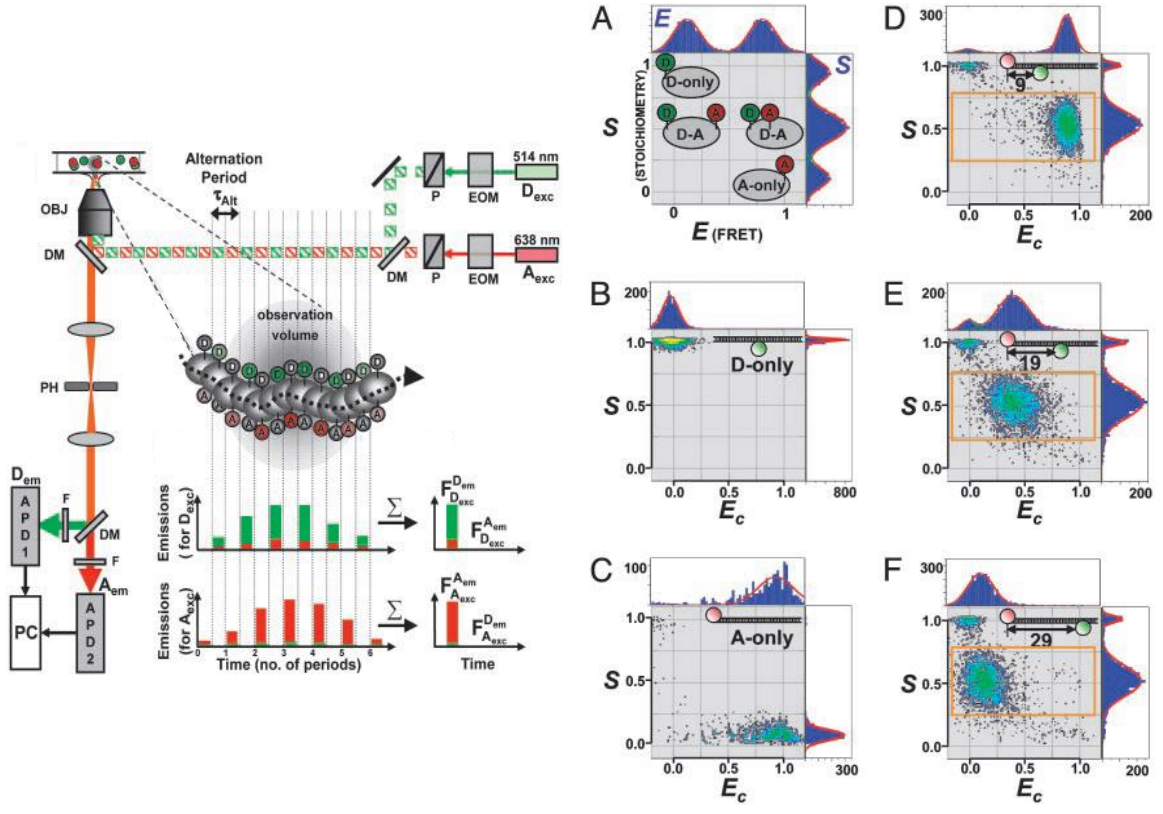

Figure 2.19: ALEX optical system and analysis. From Kapanidis et al. [2004]. **(Left)** Illumination scheme with alternating laser excitation. When a molecule crosses the observation volume, three emission intensities are detected in bursts: $F_{D_{exc}}^{D_{em}}$ (corresponding to I_D in the main text), $F_{D_{exc}}^{A_{em}}$ (I_F) and $F_{A_{exc}}^{A_{em}}$ (I_A). **(Right)** From these intensities, efficiency E and stochiometry S are measured and plotted in 2D histograms. **(A)** schematizes typical sorting of Donor only, Acceptor only and doubly labelled populations. **(B-F)** A double stranded DNA system was used with different labelling (Donor is TMR and Acceptor is Alexa647): **(B)** Donor only, **(C)** Acceptor only, **(D)** Donor/Acceptor with interdye distance 9 bp, **(E)** Donor/Acceptor with interdye distance 19 bp and **(F)** Donor/Acceptor with interdye distance 29 bp.

With single-laser measurements, only one fluorescent ratio is calculated, the FRET efficiency E. Populations can be identified when a clear difference in E is observed between peaks. However, for low FRET efficiency population we cannot distinguish what comes from Donor only-labelled molecules (exhibiting leakage in the FRET channel which typically gives an E value around 0,05 to 0,15), from doubly labelled molecules but that are inactive or exhibiting a very low FRET signal. The data interpretation (associating efficiency peaks with biomolecules populations) is particularly delicate for unknown structure proteins for instance. ALEX system provides a method to better sort molecules within a biological sample.

The principle is summarized on figure 2.19 (Kapanidis et al. [2004]). Two lasers are used for illumination, corresponding to the excitation of donor and acceptor reciprocally. It consists in switching rapidly between donor and acceptor excitation lasers to collect both informations for each single particle, instead of detecting only at Donor excitation wavelength. Three intensities are measured for each "particle": the Donor and Acceptor fluorescence intensity when excited at Donor excitation wavelength, respectively I_D and I_F, and the Acceptor fluorescence intensity when excited at Acceptor excitation wavelength, I_A. Using the ALEX scheme, two fluorescence ratios can be measured: the FRET efficiency E (equation (2.9)) which reports on interdye distance, and the stochiometry S which provides the molecules identity and reads:

$$S = \frac{I_D + I_F}{I_D + I_F + I_A}. \tag{2.10}$$

As depicted on figure 2.19 (right), for Donor only population $S \sim 1$, for Acceptor only $S \sim 0$ and for doubly labelled S will have a value between $0,3$ and $0,7$. Plotting 2D histograms of E and S allows a good identification of the biological sample populations and improves data interpretation.

Quantitative and accurate distance measurements.

With the growing number of smFRET techniques and users, many efforts have been made lately in order to homogenize smFRET studies and especially distance measurements. In fact extracting quantitative and accurate distances from the efficiency distributions is not trivial.

In Hellenkamp et al. [2018], a worldwide comparison of FRET measurements has been made by 20 labs on the same standard DNA samples. Two fluorophores couples were systematically studied, for each two different inter-dye distances were provided (respectively 5,8 and 8,3 nm). Collaborators were performing either solution measurement (confocal

microscopy with ALEX system) or immobilized molecules measurements (observed with TIRFm) with or without ALEX scheme. The compiled results, shown on figure 2.20, are very consistent throughout the labs.

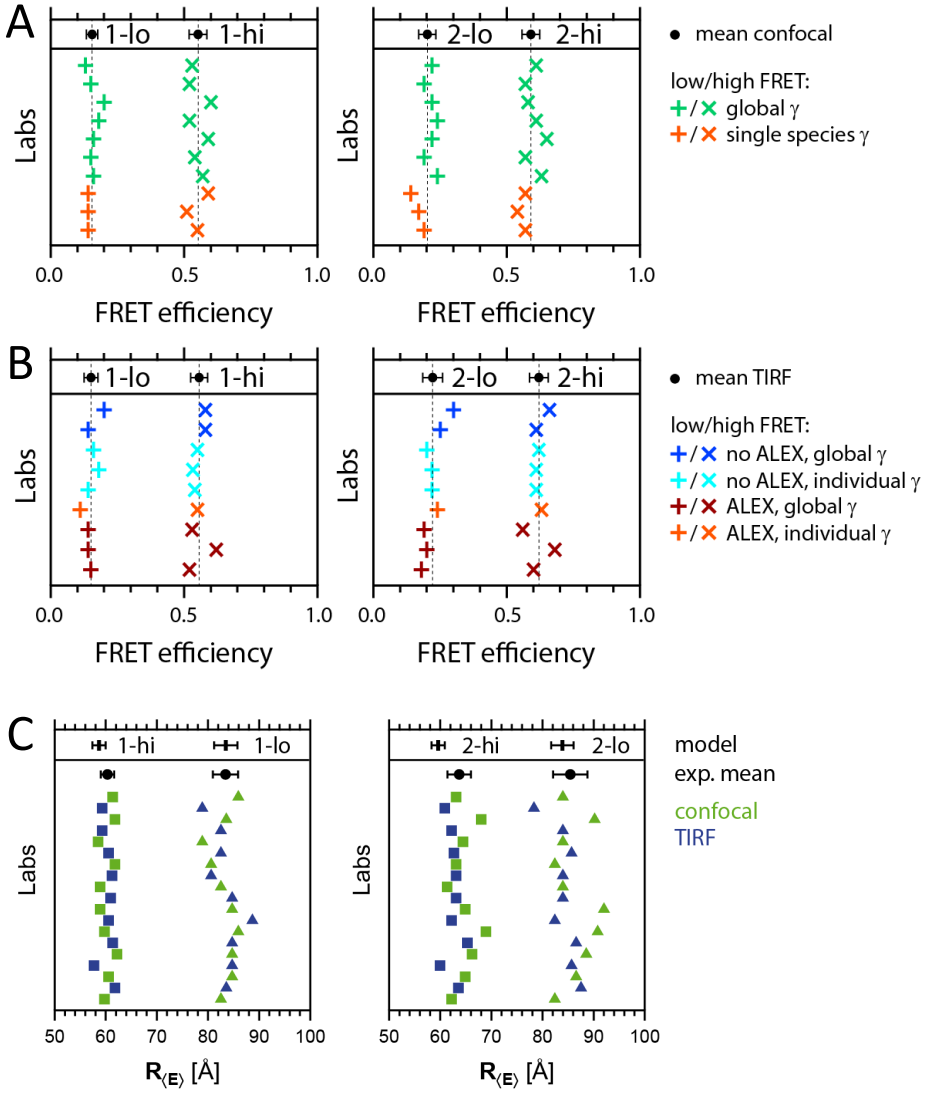

Figure 2.20: Comparison of FRET efficency and interdyes distance by different labs. (From Hellenkamp et al. [2018]). For two different DNA samples (1 and 2, labelled with different dyes), two interdye distances are investigated (low and high). **(A)** Mean FRET efficiency measured in solution with confocal microscopy. **(B)** Mean FRET efficiency measured on immobilized molecules with TIRF microscopy (with or without ALEX system). (Different correction schemes can be used for the detection correction factor γ). **(C)** Mean interdye distances determined by inverting equation (2.7) from mean efficiency plotted in (A) and (B).

Great efforts were made that all the collaborators analyze and correct their data in a

standardized manner. This study proves that a more systematic and better defined analysis method is crucial to homogenize and compare FRET data from different labs. With the corrected FRET efficiency and the Förster radius also determined in a standardized way, equation (2.7) is inverted to measure the inter-dye distance, plotted on figure 2.20C.

Quantifying distances with smFRET methods is not straightforward. However, Hellenkamp and collaborators are paving the way for analyzing smFRET data in a systematic and standardized manner in order to measure and interpret accurate distances and to be able to compare FRET data worldwide.

2.3.3 Biological applications

smFRET has turned more and more popular over the last twenty years and has already been widely used to study biological systems. As a first example the work of Abbondanzieri et al. [2008] can be mentionned. Intermolecular smFRET was used to probe the interaction between the HIV reverse transcriptase (RT) (labelled with Donor) and nucleic acid substrate (labelled with Acceptor). They found asymmetric RT orientation depending when it binds to a DNA or RNA primer. Additionally they showed that addition of Nevirapine (an anti-HIV drug) destabilize the polymerase-competent orientation of RT.

Since our study is focussed on transmembrane proteins, I will give a brief overview of what has been achieved on transmembrane proteins thanks to smFRET measurements on immobilized molecules, indicating that this method is a suitable conformation detector.

smFRET experiments can supplement usual methods such as crystallography, cryo-EM, NMR, DEER (double electron-electron resonance), in structure resolution and provide a dynamical view of proteins' structure. It was successfully achieved in Zhao et al. [2010] on a neurotransmitter transporter homologue LeuT by first confirming the existence of two distinct conformations of the transporter, by showing that the transition between these two states is ligand-dependent and finally by highlighting the role of Na^+ ions in stimulating binding and transport.

smFRET was also used to investigate the rigidity of protein domains. By labelling the tetrameric potassium channel KirBac1.1 at different positions (different constructs with extracellular, transmembrane or cytoplasmic domains labelled), Wang and coworkers revealed rigid (extracellular) and flexible (transmembrane and cytosplasmic) parts of the channel while changing conformation (Wang et al. [2015]).

Finally FRET methods is extensively used to propose transport-related dynamics models: understanding how the different parts of a transporter arrange together to allow

transport (this raises the question of the transition between strong affinity to bind the substrate in the protein cavity to low affinity to release the molecule), identifying new intermediates that cannot be isolated in crystallography, and establishing the temporal relationship between protein motion and substrate transport. This was done on the aspartate transporter Glt_{Ph} reconstituted in a lipid bilayer. It is composed of three subunits that were found to change conformation and allow transport independently from each other in presence of aspartate (Erkens et al. [2013]) with an elevator-like motion within each subnit (Akyuz et al. [2015]). A kinetic model was proposed for the transport cycle in Akyuz et al. [2015].

This application of smFRET technique is particularly interesting for learning more about ATPases transport (Dyla et al. [2017]) and in particular ABC-transporter super family is extensively studied with this method. I mention here a few articles that report great breakthroughs in ABC transporters knowledge and that will be detailed in next chapter 3 dedicated to this protein family: Husada et al. [2018]; Verhalen et al. [2012]; Goudsmits et al. [2017]; Zarrabi et al. [2014].

2.3.4 Alternative methods to FRET

Some alternative methods to FRET exist to study distance changes (in the range of 1 to 10 nm), either in ensemble or at the single molecule level.

Luminescence Resonance Energy Transfer (LRET) is a close derivative of FRET technique for ensemble measurements. Instead of using a conventional organic dye molecule as in FRET, the Donor fluorophore is replaced by a lanthanide series cation such as chelated terbium (Dolino et al. [2014]). Chelated lanthanides contain multiple sharp emission peaks, compared to organic dyes that have one large emission spectrum. Main advantages of this method over FRET are: a longer emission lifetime of the donor, several emission peaks of Donor allow the use of multiple acceptor fluorophores and the emission peaks sharpness results in no bleed-through from Donor emission. The main limitation is the need for low-noise detectors. LRET technique has been successfully used in the group of Guillermo Altenberg to study two ABC transporters MsbA and P-gP (Cooper and Altenberg [2013]; Zoghbi et al. [2017]; Zoghbi and Altenberg [2018]).

A derivative technique of single-molecule FRET consists in using a dark quencher instead of an organic Acceptor dye. Dark quenchers are chromophores that can be excited upon photon absorption and go back to the ground state nonradiatively, i.e. without

emitting photon. When used as an Acceptor for FRET experiments, this property results in an energy transfer visible thanks to the decreasing Donor signal without any background contribution coming from the Acceptor. It was shown in the group of Achillefs Kapanidis that dark quenchers can be succesfully used in multichromophore systems to probe multiple interactions and distances (Le Reste et al. [2012]).

Finally double electron-electron resonance (DEER) technique can be used in a very similar manner on spin-labelled proteins to probe conformational transitions and to measure nanometric distances in ensemble. The electron-electron interaction is measured with electron paramagnetic resonance (EPR) spectroscopy. The distance distribution is deduced from spins dipole-dipole interaction (see McHaourab et al. [2011]). This technique has been used on P-gp in Verhalen et al. [2017] to map the distances over the whole transporter and how they change under addition of ATP, substrate and/or inhibitor.

As a summary of part 2.3, crucial breakthroughs have been done over twenty years on FRET and its use at single-molecule regime. It is a precious tool to probe nanometric distance changes on single transmembrane proteins, as shown by many different labs on various proteins. In our study, we focus on a specific type of transmembrane proteins, ABC transporters, that are described in next chapter.

Chapter 3

ABC transporters

In this chapter, I want to give a general introduction on ABC (ATP Binding Cassette) transporters and then focus on our protein of interest: BmrA, a bacterial ABC exporter. I will conclude this part by giving the main motivations and goals of this work.

3.1 General introduction on ABC transporters

3.1.1 Diversity of cellular functions

ABC transporters are essential in cells life as they are involved in processes such as homeostasis, cell detoxification and nutrient uptake. Three functional categories of ABCs can be distinguished (Davidson et al. [2008]). (i) Importers are mainly involved in the uptake of nutrients, and present only in prokaryotes. They can transport saccharides, ions, amino acids, metals among others. (ii) Exporters can transport lipids, peptides and are actors of cell detoxification by extruding out of cells hydrophobic drugs and toxins. (iii) Last category is nontransport involved proteins.

The plant ABC transporter ABCG5/PDR5 is involved in the defense against wounding, fungal pathogen and herbivore. Damages caused by herbivore result in production of substrates that, once translocated out of cells by ABCG5/PDR5, will limit feeding and protect leaves from herbivore (Bienert et al. [2012]; Pierman et al. [2017]).

Many mammalian ABCs are expressed in crucial organs and tissues (brain, testis, placenta, liver, kidney) to protect them from toxins as well as the full organism (Gottesman et al. [2002]).

The human transporter associated with antigen processing (TAP), located at the endoplasmic reticulum, effluxes antigenic peptides that load onto the major histocompatibility complex I (MHC I) and participate to immune response (Gaudet and Wiley [2001]).

Apart from their detoxification and defense role in normal physiology, they are also involved in diseases and chemoresistance (figure 3.1a summarizes these two roles played by ABCs). Some ABC transporters are responsible for a multidrug resistance phenotype (MDR) which is ubiquitous and confers bacteria, fungi, plants and humans resistance to antibiotics, antifungals, herbicides and anticancer drugs respectively.

In particular for cancer, many different causes lead to drug resistance as shown on figure 3.1b, but there are strong evidences for ABCs involvement as very efficient drug efflux pumps. Three human ABC exporters (P-glycoprotein P-gP, MDR-associated protein MRP1 and breast cancer resistance protein ABCG2) were identified as main MDR actors in cancer cells, where they are over-expressed compared to normal physiology. They are able to interact with (and to translocate) a broad range of drugs and anti-cancer agents (Sharom [2008]), although it has been shown that ABC transporters play a larger role in treatment resistance than simply anti-cancer agents efflux (see Fletcher et al. [2010] for a review and Robey et al. [2018]). Multidrug resistant cells (i.e. with over-expressed ABC transporters) survive when tumour is exposed to chemotherapy and then proliferate, leading to recurrent incurable tumours, as sketched on figure 3.1b (Dean et al. [2005]).

Some clinical trials using MDR transporters regulators, to try to inhibit the activity of such proteins, have been done in the last years but so far no real benefit was shown (Fletcher et al. [2010]).

3.1.2 Structure and topology of ABCs

To investigate the structure, organization and dynamics of ABC transporters, proteins were purified out of native membranes. They can then be studied in pure detergent, micelles detergent/lipids or in model membranes such as nanodiscs or liposomes.

Topology and organization of ABC transporters.

All ABC transporters exhibit the same minimal organisation core composed of two solvent-exposed nucleotide binding domain (NBD) and two transmembrane domain (TMD) that are bound via a coupling helix (see scheme 3.2A). Within one organism, several subfamilies of ABCs were identified: for instance the 49 human ABC transporters are categorized in seven families (from A to G) (Vasiliou et al. [2009]). Each family shares specific

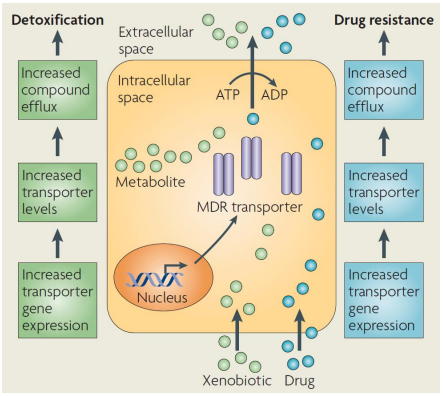

(a) Transporters able to export out of cells materials recognized as toxic (xenobiotics or drugs) can lead either to cell detoxification under normal physiology or to drug resistant tumour (scheme from Fletcher et al. [2010]).

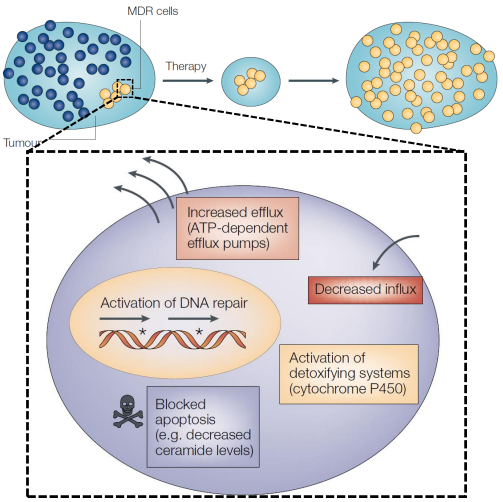

(b) Drug-resistant cells in a tumour will survive chemotherapy and proliferate, leading to a recurrent and resistant tumour (Dean et al. [2005]). Different cellular factors result in drug resistance and are listed on the cell's scheme. ABC transporters are largely responsible for the increased efflux of drug out of the cells (Gottesman et al. [2002]).

Figure 3.1: Cell detoxification *versus* drug resistance phenotype.

topology, substrates and subcellular localization (Neumann et al. [2016]). There are various topologies: some ABCs work as a full transporter (2 TMD and 2 NBD, they can be hetero- or homodimeric), others can function as a half transporter (1 TMD and 1 NBD) and finally some have an additional transmembrane domain. Some of the most studied ABC transporters are the human ABC P-glycoprotein (P-gp) which is a full transporter, and the bacterial homodimeric transporter MsbA.

The NBDs are the cytosolic parts of the transporter where ATP molecules bind and hydrolyse, and drive conformational change in the attached transmembrane domains. NBDs are highly conserved subunits among the ABC family (see figure 3.2B). In full transporters, NBDs form dimers that can be in a compact form or with a separation of several angströms. When the NBDs are in close contact, this forms two sites for the binding of ATP molecules and therefore this conformation is crucial in the hydrolysis process and protein activity. Note that homodimers have two ATP hydrolysis sites while heterodimers contain only one site as the other is degenerated.

One TMD is composed of 6-10 helices (so between 12 and 20 for a full transporter, most exporters have 12). The two TMDs will form a cavity in the lipid bilayer that contains the substrate binding sites. Whereas NBS are highly conserved, there is a diversity of folds

of the TMDs. Figure 3.2B shows the TMD folds for different transporter types: B-family exporters, type 1, 2 or ECF-type importers.

Importers of type 1 and 2 have an additional substrate-binding domain (SBD) or substrate-binding protein (SBP) depicted in red on figure 3.2B which is responsible for capturing the substrate and deliver it to the TMDs.

In the ABC exporters, two main conformations have been identified. "Open" refers to the conformation of the protein where the NBDs are separated and the substrate cavity is open to the cytoplasm, and is also called "inward-facing" conformation or "apo" state. "Closed" refers to the conformation where the NBDs dimerize and the cavity is open towards the extra-cellular matrix, and is also called "outward-facing" conformation or "post-hydrolytic" state.

The size of the opening is a matter of debate since 2003. It was believed that a larger opening results in a larger cavity allowing larger substrates translocation. However data were highly contradictory. It is also debated whether the NBDs are in contact or not in open conformation. With cryo-electron microscopy data, it emerges that for bacterial ABCs, NBDs are not in contact and that there are different conformations in the apo state with variable openings. This will be discussed in detail in the next paragraph and along the manuscript.

Structures of ABC exporters.

ABC transporters conformations have been studied for over 40 years and very contradictory data were obtained, raising questions about the different species and the different accessible conformations. In the next paragraphs, I try to summarize the pre-consensus that arises for a few years, especially thanks to cryo-EM data.

Structures of ABC transporters are widely investigated by X-ray crystallography and cryo-electron microscopy where proteins can be in micelles of detergent and lipids or in detergent alone or in membrane (nanodics) (Manolaridis et al. [2018] and Hofmann et al. [2019] gave new insights respectively about ABCG2 and TmrAB substrate-bound structures using cryo-EM). The first full structure of ABC exporter has been resolved by Dawson and Locher [2006] for Sav1866 followed by many other ABC exporters structures (Locher [2016]).

For ABC exporters two main conformations can be identified, although a wide distribution of NBDs separation is observed and is still under discussion.

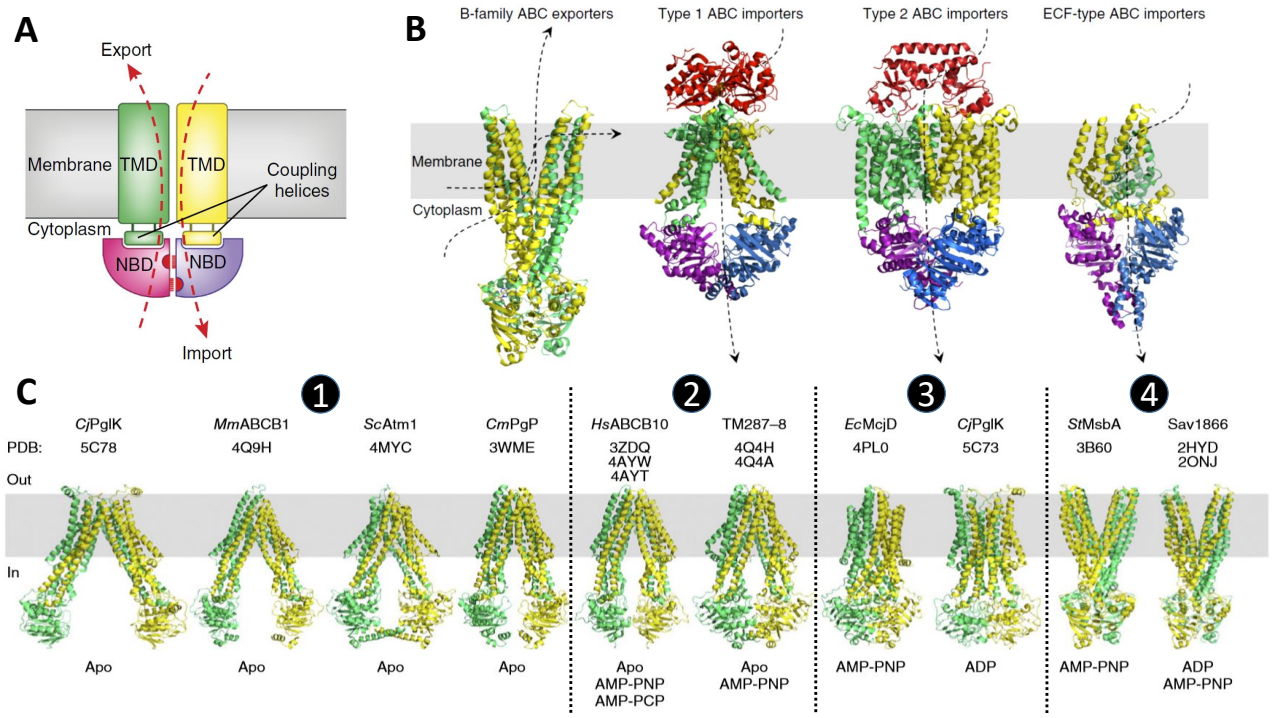

Figure 3.2: ABC transporters structures. Adapted from Locher [2016]. **(A)** Sketch of the four core domains common to most of ABC transporters: NBDs and TMDs. Dashed red arrows indicate the import and export paths orientation. Red areas in the NBDs show the ATP binding sites. **(B)** Structures according to ABC transporter type. Dashed arrows indicate the known or suspected substrate path. Yellow and green parts represent the TMDs (they are fused with NBDs for exporter type, which are also depicted in green and yellow). Purple and blue domains are the NBDs, and red parts are the substrate binding domain (SBD). **(C)** Diversity of conformations in the B-family ABC exporters. The name of the corresponding exporter is indicated on top. Bottom row indicates the nucleotide state (i.e. conformation). When several states are indicated, there was no significant change observed in the NBDs separation. ① States with NBDs apart from each other. ② NBDs separation is not different upon addition of ATP. ③ Occluded states. ④ States with bound-NBDs.

In the absence of ATP, NBDs are separated from each other and the substrate cavity is opened towards the cytoplasm and accessible for molecules: the protein is in apo (or inward facing) conformation. As shown on figure 3.2C the separation between NBDs can vary according to the conformation (structures labelled ①) indicating that the proteins can explore a wide conformational space in apo. It has been observed by Moeller and coworkers, in single particle Electron Microscopy, that MsbA and P-gP can explore a broad variety of states with different NBDs separation (Moeller et al. [2015]).

The presence of ATP, or a mixture ATP-ADP, or a non-hydrolysable form AMP-PNP (that acts as an inhibitor of the protein acivity), results in a nucleotide-bound state where separation between NBDs is generally smaller than in apo form. Again, a range of conformations is observed in this condition (see figure 3.2C). For some conformations (④), a tight binding of the NBDs is observed as well as a rearrangement of the TMDs

with substrates cavity opened towards the extra-cellular space: it is referred at as the outward facing conformation. Other conformations exhibit an occluded state with the NBDs closer but neither opening of the TMDs towards the outside nor the inside of the cell (③). Finally some conformations show no different NBDs separation in the inward or outward facing form (②).

In the latest published study, Hofmann and collaborators identified by cryo-EM eight structures of the heterodimeric exporter TmrAB, mapping its full functional cycle (Hofmann et al. [2019]). This is presented on figure 3.3 where both transport ("useful") and futile cycles are considered.

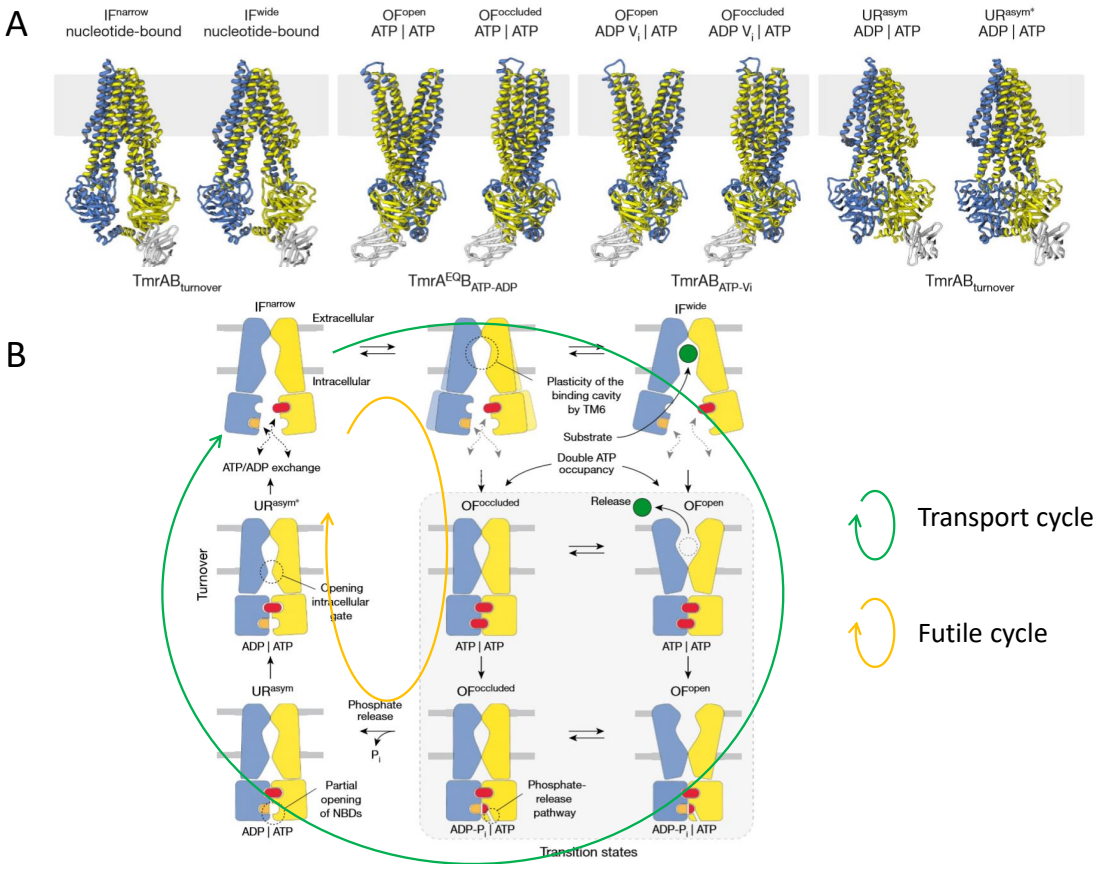

Figure 3.3: ABC transporters functional cycle. Adapted from Hofmann et al. [2019]. **(A)** Conformational space of TmrAB. TmrA is in blue, TmrB is in yellow, and cytoplasmic nanobody (forming a complex with TmrB NBD) is shown in light grey. Two inward-facing (IF) conformations were found with narrow and wide opening, in ATP-bound state and in vanadate-trapped state two sets of outward-facing (OF) conformations were dominating with open and occluded TMDs organisation. Finally two unlock-returned (UR) states were identified with dimerized NBDs and tightly sealed extra-cellular gates. **(B)** Translocation cycle proposed after the eight structures of TmrAB. Both transport and futile cycles are proposed.

This shows ABC transporters have a certain flexibility and that each conformation corresponds to a specific step within the functional cycle. Upon addition of ATP, exporters undergo a kinetic cycle between the inward facing and the outward facing conformations.

Therefore investigating their dynamics, the kinetics of conformational changes and substrate transport is crucial to fully embrace their function.

3.1.3 Dynamics of ABC exporters

Many structures of ABC transporters (we here focus only on exporters) are now available, showing a variety of conformations. However techniques such as crystallography and EM provide only snapshots of conformations, although cryo-EM can now solve the different conformations of an ABC present in solution. Therefore, the kinetics of conformations change and transport mechanism remain unclear. Dynamics start to be investigated with methods mentioned in part 2.3: FRET (single molecule), LRET and DEER (ensemble). The use of inhibitors (such as vanadate (Vi) or AMP-PNP) is common to measure a reference value as the protein is expected to be locked in outward-facing state. The effect of the presence of substrates can also be investigated with these techniques.

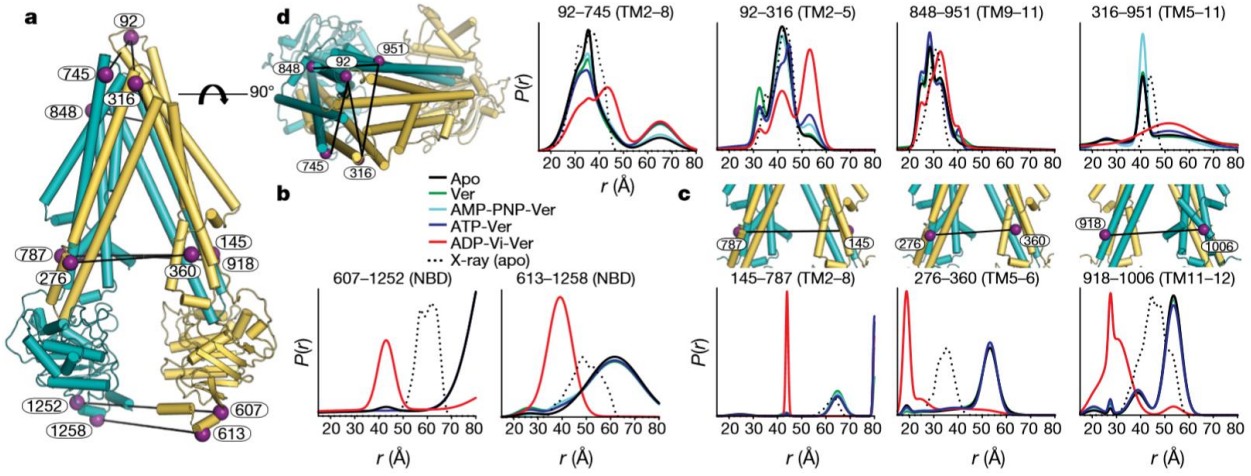

Figure 3.4: Dynamics of P-gp studied with DEER. From Verhalen et al. [2017]. **(a)** Several positions of P-gp are successively labelled with spins to perform DEER measurements. **(b), (c), (d)** Distance changes measured respectively in the NBDs, in the intracellular domains (ICDs) and in the TMDs. Conformation change is observed only upon addition of ADP-Vi-Verapamil.

Using DEER method, Verhalen and collaborators systematically measured distances between different positions on P-gp in 5 chemical conditions (Verhalen et al. [2017]). Their results are shown on figure 3.4. They found a large distance change in the NBDs (positions 613-1258) upon addition of ATP and vanadate (red lines): from 65 to 40 Å. The TMDs also undergo distance changes: close to the NBDs (figure 3.4c) and at the extremity (figure 3.4d 316-951). No difference is detected under addition of ATP only.

DEER was also used on MsbA to observed distance change between apo conformation and in the presence of ATP vanadate (Zou et al. [2009]).

LRET technique was used on P-gp and MsbA with interesting outcome (Zoghbi et al. [2017]; Zoghbi and Altenberg [2018]). Figure 3.5.A shows structure of P-gp with red beads indicating the labelled residues (positions 607-1252) (similar labelling position was used on MsbA, 561). For P-gp reconstituted in nanodisc, they found more proteins with bound NBDs when adding ATP and even more when adding vanadate compared to apo condition (3.5B). However they measured smaller distance for P-gp than previously reported at the same labelled positions, with a switch from 45 to 33 Å. Similar results were found on MsbA in nanodisc (3.5D).

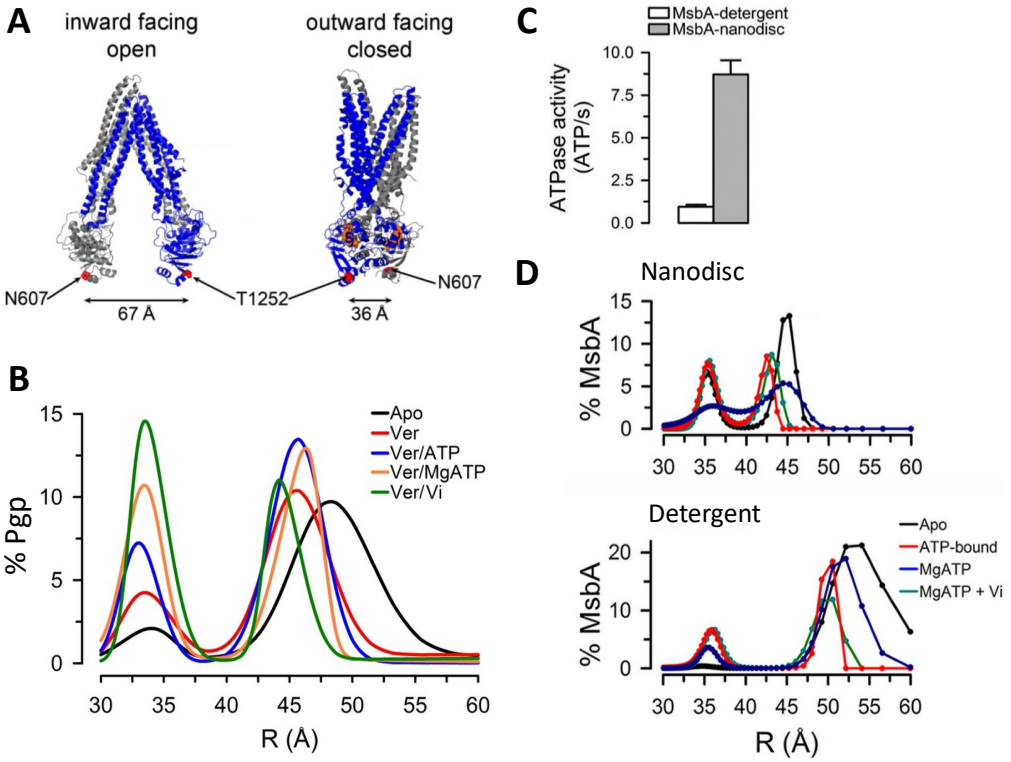

Figure 3.5: Dynamics of P-gp and MsbA studied with LRET. From Zoghbi et al. [2016, 2017]. **(A)** P-gp inward- and outward-facing structures. Red dots indicate the position labelled for LRET experiments. Equivalent positions were used on MsbA. **(B)** Distance distribution in P-gp calculated from LRET measurements in 5 chemical conditions. **(C)** ATPase activity of MsbA in detergent or in nanodics. **(D)** Distance distribution for MsbA in nanodisc (up) or in detergent (down) in 4 chemical conditions.

It was also proved that the presence of a membrane around the exporter MsbA results in a smaller distance between NBDs in the apo conformation: 45 Å when the protein is incorporated in nanodiscs as compared to $\simeq$ 55 Å measured in detergent (see figure 3.5D) (Zoghbi and Altenberg [2018]).

Using these methods, supplemented by cryo-EM observations, many efforts are currently made to propose a model for the full transport cycle (Verhalen et al. [2012]; Husada et al. [2018]; Hofmann et al. [2019]; Mishra et al. [2014]).

3.1.4 Substrates translocation models

There is a consensus about the major steps of transport mechanism: substrate binding in the TMDs cavity, ATP-dependent NBDs dimerization which drives the TMDs switch from inward- to outward-facing, ATP hydrolysis, release of substrate, release of phosphate and ADP that eventually brings the TMDs back to inward-facing conformation (Wilkens [2015]). It is unclear in what precise order all these steps occur and what are the intermediates. Also, in homodimeric exporters, two ATP sites are available and it is unclear if hydrolysis of two molecules is simultaneous or consecutive.

Three main model mechanisms have been proposed for the substrate transport of ABC exporters: alternating access model (or "switch"), the outward only mechanism and the constant contact model. Note that models also exist for ABC importers and are reviewed in Locher [2016] and Jones and George [2013].

Alternating access model.

The alternating access model is mainly based on the observation of large NBDs separation for ABC exporters (Moeller et al. [2015]). This mechanism (sketched on figure 3.6a) involves that the NBDs have to totally dissociate after the substrate is released to allow the cycle to start all over again from inward facing conformation (Higgins and Linton [2004]). ATP binding leads in NBDs dimerization and TMDs switch to outward-facing state (potentially via an occluded state), it is hydrolysed in ADP and phosphate which, when released, dissociate the NBDs and drag the TMDs back to inward-facing (possible NBDs mechanism is shown on figure 3.7a).

This model is also very relevant with a switch of substrate affinity to the cavity. The structure of the inward-facing state favours substrate affinity and hydrophobic molecules can bind from the cytoplasm or from the inner lipid leaflet. The rearrangement of the helices during TMDs switch leads to a change of cavity surface and to a chemical mismatch with the substrate which results in its release. It is particularly relevant for lipid translocation, as an orientation change of the substrate is necessary to "flip" (180^o rotation) the lipid from the inner to outer leaflet (Neumann et al. [2016]). The switch of TMDs and their rearrangement allow a 180^o rotation of lipids. Such a mechanism is very relevant in regard to observations on many ABC exporters (Husada et al. [2018]; Verhalen et al.

[2012, 2017]; Cooper and Altenberg [2013]; Zoghbi and Altenberg [2018]).

However, there are some evidences that ATP is hydrolyzed in a constant alternating manner, while NBDs with empty ATP sites is suggested as a step in the alternating access model. Additionally, physiological conditions can also be discussed since ATP is always present in the cytoplasm and has a high affinity with the ATP empty site in NBDs (NBDs affinity for ATP is typically 0,5 to 1 mM, up to 2 mM in cells). In a dynamical vision where the ATP molecules would subsequently be hydrolysed and ADP molecules release would not be simultaneous but alternating, NBDs could remain in close contact over the cycle. For these reasons and also since the physiological relevance of the inward-facing conformation is under discussion (Locher [2016]), other models have been proposed.

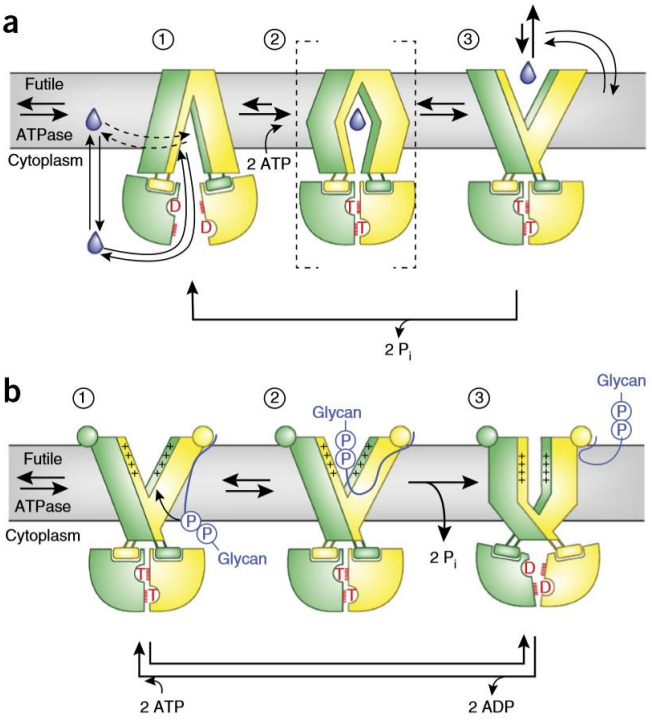

Figure 3.6: Alternating access and outward only models. From Locher [2016]. Transport mechanism models proposed for ABC exporters. **(a)** Alternating access model with a switch between inward-facing conformation ① to outward-facing ③ potentially via an occluded intermediate ②. **(b)** "Outward only" model proposed for the LLO flippase PglK.

"Outward only" model.

The "outward only" mechanism was proposed for the LLO flippase PglK (Perez et al. [2015]), without any inward-facing state involved. The cycle (depicted on figure 3.6b) starts in outward-facing state with NBDs already dimerized with bound-ATP. The lipid phosphate-glycan headgroup binds in the outward-facing cavity via electrostatic interactions. ATP hydrolysis drives the NBDs slightly apart and the TMDs together to

form an occluded state. Finally the substrate is released to outer leaflet, and ADP is exchanged with ATP to restart the cycle. This mechanism would also be suitable for transport of large substrates for steric reasons.

Constant contact model.

The constant contact model proposes an alternating hydrolysis between the two ATP sites of ABC exporters (Jones and George [2013]). ATP binds to one site and is hydrolyzed in ADP plus phosphate. The second empty site has a high affinity for ATP which binds. Phosphate is released from the first site followed by ADP which leaves a site with high affinity for ATP. New molecule of ATP binds there while ATP is hydrolysed in site 2 with release of phosphate and ADP, and the cycle starts again as shown on figure 3.7b.

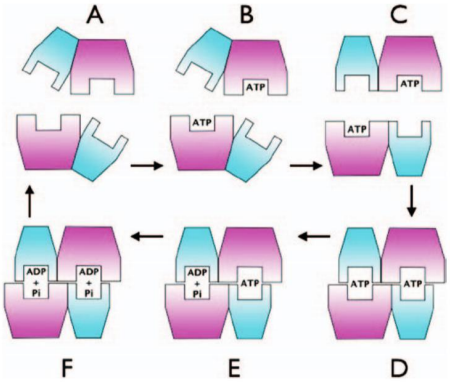

(a) In the alternating access model. A is the configuration for the resting state (apo), and D-F correspond to the bound state. Releasing ADP and phosphate brings the protein back to apo conformation.

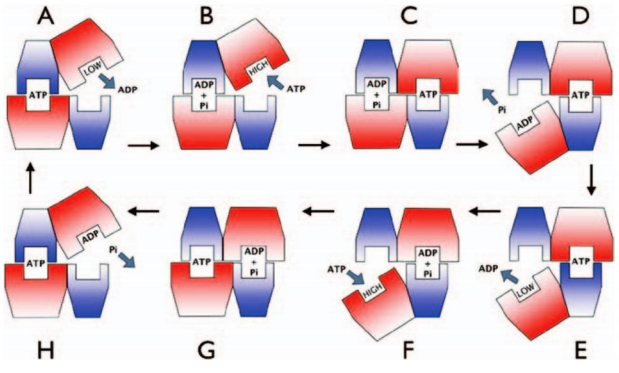

(b) In the constant contact model. At least one ATP site is always bound to an ATP molecule. The hydrolysis on the two sites is made in an alternative manner and the NBDs remain in close contact.

Figure 3.7: ATP hydrolysis cycle at the NBDs level in two transport models. From Jones and George [2013].

There are experimental evidences on P-gp proving the relevance of this model. The use of non-hydrolizable ATP-γ-S to occlude one ATP site showed that NBDs remain in close contact during the catalytic cycle. The substrate fixation was not affected by one ATP-γ-S occluded site, showing that transport remains possible in this model (Siarheyeva et al. [2010]; Sauna et al. [2007]). This model was also suggested for heterodimeric exporters (Mishra et al. [2014]) as they have one degenerate site over two. Last, but not least, it was shown by Verhalen and Wilkens [2011] that crosslinking the two NBDs doesn't affect ATPase activity of P-gp and the drug stimulation of activity.

To conclude, although these three models are very different and still under discussion, it should not be excluded that an exporter can function according to several mechanisms depending on the substrate (Zoghbi et al. [2017]). It is worth mentioning that chemical activity (hydrolysis of ATP), mechanical activity (physical conformation change) and substrate transport are distinct and not all inter-dependent. On one hand, conformation change can occur without translocation of substrate, hydrolysis of ATP does not systematically lead to TMDs switch but to a so-called "futile" cycle (Husada et al. [2018]). On the other hand the substrate transport is ATP-dependent and it has been shown that the ATPase activity of the protein is boosted in the presence of substrate molecules.

3.1.5 ABC transporters and membrane

In part 2.2 the different interactions between transmembrane proteins and surrounding membrane were presented: the presence of functional lipids around the protein, the changes induced by proteins on membrane curvature and thickness, the protein-protein interaction, and the protein mobility. Here I want to give a brief overview on what is known about ABC transporters interactions with their membrane.

ABC transporters and lipid composition.

The role of surrounding membrane on ABC transporters has mainly been studied through the function modulation of the proteins by specific lipids and substrates. Many detergents drive a total loss of activity of the transporter P-gp by depleting the functional lipids that stabilize the protein (Sharom [2014]). Similar result was found on MsbA by Zoghbi et al. [2016]: the activity of MsbA is increased nearly 10 times when reconstituted in nanodics compared to detergent (see figure 3.5C). The presence of a lipid bilayer around ABC transporters has a crucial effect. Moreover, the composition of this lipid bilayer matters. It was found that cholesterol stimulates ATPase activity of P-gp (Eckford and Sharom [2008]). Replacing PE lipids by PC alters transport of P-gp (Gustot et al. [2010]) and inhibits the activity of LmrP (Hakizimana et al. [2008]).

Lipid composition can not only modify the activity of the protein but can also alter the overall structure of the transporter (Gustot et al. [2010]; Hakizimana et al. [2008]).

Coarse-grained simulations performed by Corradi et al. [2018] showed that lipids arrange in a specific pattern around P-gp, both in the upper and lower leaflet, depending on interactions with the interface area of the protein (see figure 3.8.A). They form the so-called annular (or functional) lipids of P-gp.

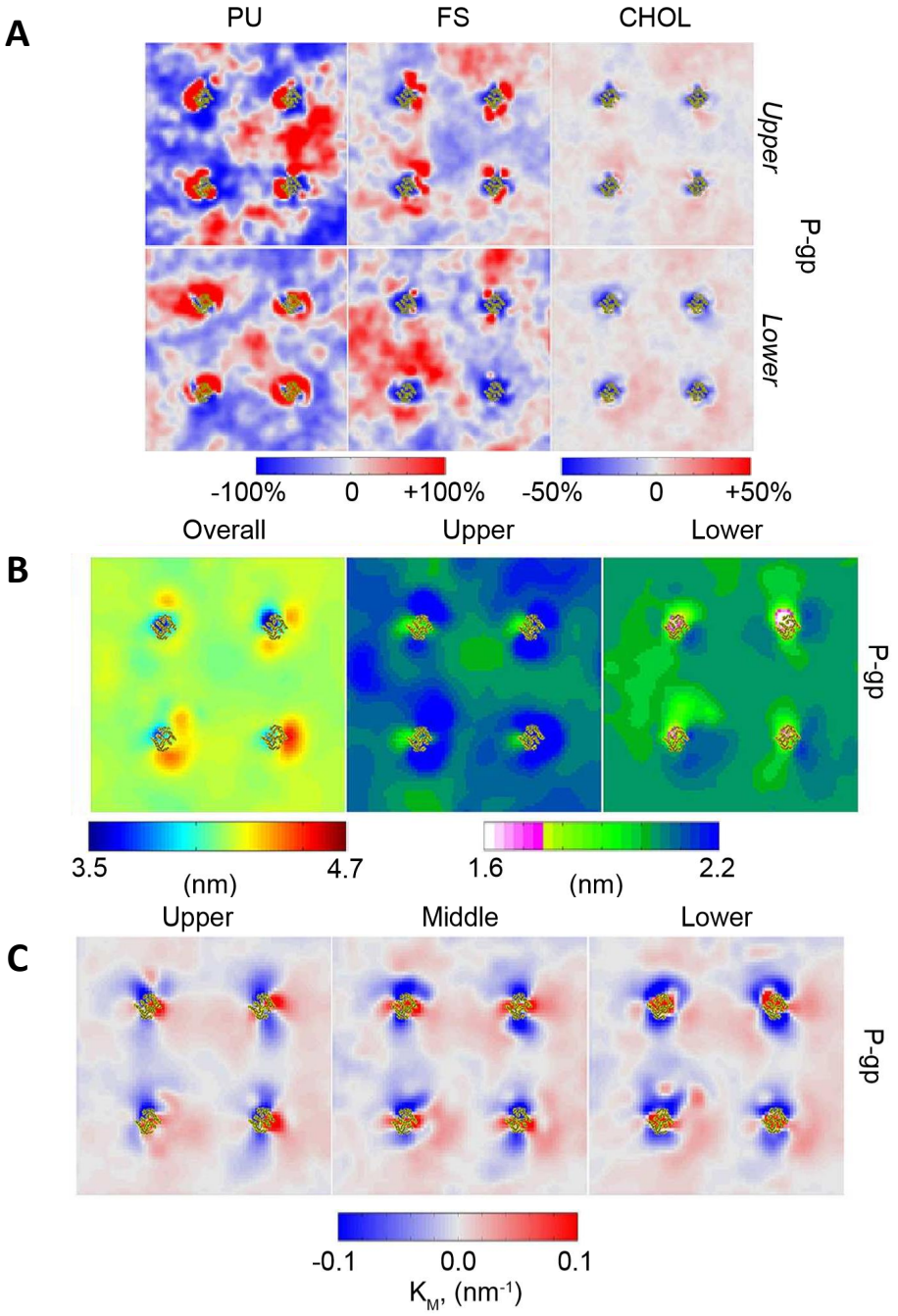

Figure 3.8: Lipid core and membrane properties around P-gp. From Corradi et al. [2018]. The maps were done with 4 copies of P-gp within the membrane. **(A)** Lipid density map in the upper and lower leaflet: PU, FS and CHOL stand for poly-unsaturated lipids, fully saturated and cholesterol. Red areas are enriched, blue are depleted. **(B)** Membrane thickness (in nm) calculated from the upper to lower leaflet (Overall), from the upper leaflet to middle plane (Upper) and from the middle place to the lower leaflet (Lower). **(C)** Mean curvature K_M (in nm^{-1}) calculated in the upper leaflet, middle plane and lower leaflet. Red areas are positively curved, blue are negatively curved.

ABCs substrates interact with membrane.

The transport function of ABCs can be altered by membrane interactions. Most of ABC exporters' substrates are hydrophobic and therefore localize at the membrane (at the

lipid tails layer) before they are translocated out of the cell. Enrichment of cholesterol may modify the hydrophobic substrates partition within the membrane and therefore lower the uptake rate of the exporter (Eckford and Sharom [2008]).

Some ABCs were also identified as lipid transporters (Neumann et al. [2016]), which adds complexity to the overall picture. The presence of such a transporter can change the lipid partitioning and the properties of the bilayer. Some studies aim at better understanding lipid transport process, such as the work of Barreto-Ojeda et al. [2018] who used molecular dynamics simulations to map the lipid pathways inside P-gp cavity.

ABC transporters conformation in lipid bilayers.

It has been shown that the overall shape of ABC transporters is different when incorporated in a membrane (nanodiscs or liposomes) than in micelles of detergent. For instance, the conformations and distances were measured for MsbA in Zoghbi et al. [2016] (detergent *vs* nanodics) and for McjD in Husada et al. [2018] (micelles detergent/lipids *vs* liposomes). This suggests a structural role of the rigidity of the hydrophobic environment of the protein.

ABC transporters and membrane mechanical properties.

ABC transporters are highly flexible proteins which can access a wide range of conformations with different cavity opening and NBDs separation (Moeller et al. [2015]; Ward et al. [2013]). These proteins can still undergo large conformational changes (and fluctuations) when embedded in a lipid bilayer. This strongly suggests that there is a crucial interplay between protein's shape or conformation and mechanical properties of the membrane.

Simulations done by Corradi et al. [2018] on P-gp show that membrane mechanical properties such as thickness and spontaneous curvature are altered and non uniform around the inclusion. P-gp creates a strong negative curvature on the lower leaflet (close to the NBDs) and also affects the bilayer thickness (see figures 3.8B and C).

These simulations have provided precious informations about interplay between transmembrane proteins and membrane physical properties but experimental systematic studies are still lacking. A first observation of the interaction between protein conformational change and membrane curvature was proposed by the lab of Daniel Lévy. They studied BmrA, a bacterial ABC exporter from *Bacillus subtillis*, first in cryo-EM (Fribourg et al. [2014]), and then with ATPase activity measurements (Paik [2018]).

3.2 BmrA : a bacterial ABC exporter

3.2.1 Presentation of BmrA

BmrA (*Bacillus* Multidrug Resistance ATP, formerly named YvcC) is a bacterial ABC exporter from *Bacillus subtillis*. It is a half transporter of $\sim$ 65 kDa that functions as a homodimer (Dalmas et al. [2005]). BmrA presents a high sequence homology with the bacterian transporter MsbA, and with both halves of human P-gp (Steinfels et al. [2004]). BmrA, P-gp and MsbA share common drugs as substrates, such as reserpine, vinblastine, verapamil, doxorubicin or Hoechst 33342, and inhibitors such as vanadate (Steinfels et al. [2002, 2004]).

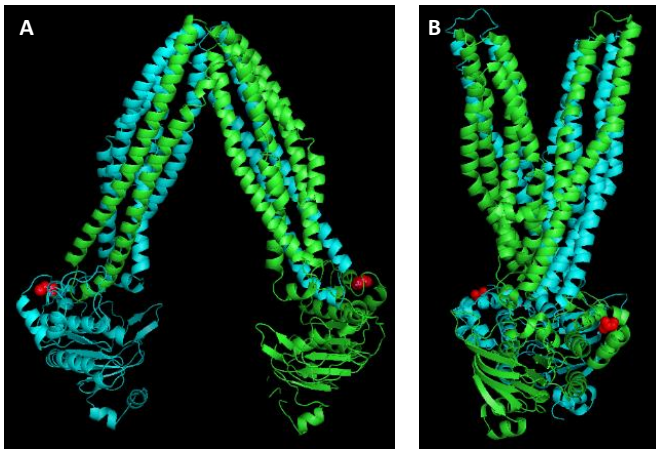

Figure 3.9: Model structure of BmrA conformations. The models are based respectively on MsbA structure (PDB: 3B5W) and SAV1886 (PDB: 2HYD). **(A)** Inward-facing or apo conformation. **(B)** Outward-facing conformation. Half transporters are represented in blue and green and form a homodimer. The red beads mark the native cysteins C436 that will be used for fluorescent labelling in this study. The distance between the two cysteins is measured on these models: 80 Å in apo and 40 Å in closed conformation.

BmrA was identified as a multidrug resistance actor: it is involved in the reserpine-sensitive efflux of ethidium bromide out of bacteria (Steinfels et al. [2004]). However the physiological substrates and role of BmrA is still under discussion, since its expression is not modulated by the presence of drugs and because deletion of Bmra in *B.subtillis* has no significant effect on the physiology of bacteria. This is a common feature for ABCs, that could be explained by the fact that one species generally has many ABC transporters and that they can compensate the deletion of one of them. In addition, in the case of bacterial ABC transporters, the MDR role is not clearly established since this phenotype is mainly performed by other proteins family such as RND proteins.

Additionally, the structure of BmrA remains unknown. Models, shown on figure 3.9, are inferred from homologs MsbA (PDB: 3B5W) and SAV1886 (PDB: 2HYD) (for which 3D structures have been solved). Both inward- and outward-facing conformations are shown here, indicating that the protein is expected to undergo a large conformational change. BmrA can be trapped in both conformations: in inward-facing in the absence of ATP (although its conformation could fluctuate), in outward-facing in the presence of ATP and vanadate; or can switch upon catalytic cycle when adding ATP. In this study, single molecule FRET will be performed by labelling the cystein residues (indicated in red on 3.9) with Donor and Acceptor fluorophores. The models provide the following distance between the cysteins: 80 Å in apo conformation and 40 Å in NBD-bound state.

3.2.2 Biochemical studies of BmrA

BmrA can be purified in high amounts when expressed in *E. coli* (Steinfels et al. [2002]). It was shown that BmrA ATPase activity depends on the detergent type and is systematically increased in presence of lipids (Steinfels et al. [2004]), in particular negatively charged lipids (Paik [2018]). The activity is even greater when BmrA is incorporated in SUVs and is significantly higher in *E.coli* lipids vesicles than in PC based vesicles (see figure 3.10). This shows that lipid composition has an impact of the ATP hydrolysis rate of the protein.

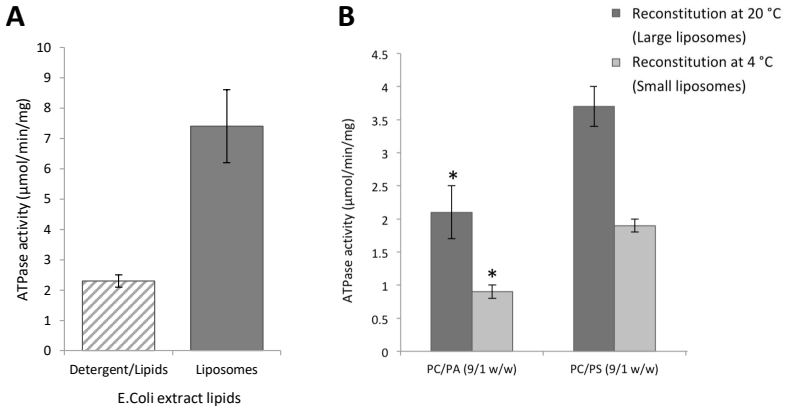

Figure 3.10: ATPase activity of BmrA. From Paik [2018]. **(A)** Measurements show a higher activity of BmrA incorporated in liposomes than in a mixture detergent/lipids (*E.coli* extract lipids). **(B)** Activity measured in small liposomes is significantly lower than in big liposomes (done for two lipid composition: PC/PA and PC/PS 9/1 w/w). * Measurement was done at 25^{o}C instead of 37.

Moreover, the activity was measured in vesicles sharing same lipid composition but with two different sizes: this was done by changing the reconstitution temperature from

20 to 4^{o}C for two compositions PC/PA (9/1 w/w) and PC/PS (9/1 w/w). The diameter of the vesicles reconstituted at 20^{o}C is on average 140 nm while it is 40 nm at 4^{o}C. The activity of BmrA is decreased by a factor 2 in small liposomes compared to large ones, indicating that membrane curvature impacts chemical activity of the transporter.

3.2.3 Dynamics and structural studies of BmrA

Studies using hydrogen/deuterium exchange (HDX), electron microscopy (EM) and cryo EM bring experimental evidences for the following statements:

- both inward- and outward-facing conformations of BmrA are observable,
- addition of ATP, ATP-vanadate and/or substrates affect the protein conformation,
- there is an interplay between BmrA and the surrounding membrane at high protein density.

Mehmood and collaborators used HDX method to investigate the conformations of BmrA in membrane, or purified in detergent (Mehmood et al. [2012]). For both conditions they find significantly less HD exchange when the protein is inhibited with vanadate compared to apo conformation (or resting state), indicating that the protein is in a closed state with NBDs tightly bound. Additionally, the intra-cellular domains of the protein are found more flexible in the open conformation than in the bound state. This indicates that in the resting apo state, several NBDs separation (i.e. conformations) are accessible for the protein.

Cryo EM studies confirmed the V-shaped apo conformation of BmrA and allowed to build a 3D model of the protein embedded in a lipid membrane (Chami et al. [2002]; Fribourg et al. [2014]).

When BmrA is reconstituted in lipid membrane (with detergent to lipid ratio 1:1 molar) at high protein density, the dimers arrange in ring shape as shown on figure 3.11A (cryo EM image), 3.11B (3D model of the ring). In these ring structures, of external diameter $\sim$ 40 nm and containing 24 homodimers, the overall shape of BmrA is a V-shaped conformation with NBDs separated from 3 nm (inner parts of the NBDs) and 9 nm (outer parts of the NBDs) (see figure 3.11C).

Further detergent removal leads to membrane tubes and sheets formation with BmrA embedded. Two population are observed: thin membranes sheets with similar BmrA

arrangement than in the rings (same separation of the NBDs was found) and thicker membranes tubes with a greater distance between protein' NBDs. Figures 3.11D-F show negatively-stained EM images of respectively rings, thin and thick membrane tubes. These results highlight that at least two V-shaped conformations of BmrA exist (confirming a certain flexibility of the apo form) and that they alter the overall shape of the membrane, indicating a strong interaction between protein and membrane shapes.

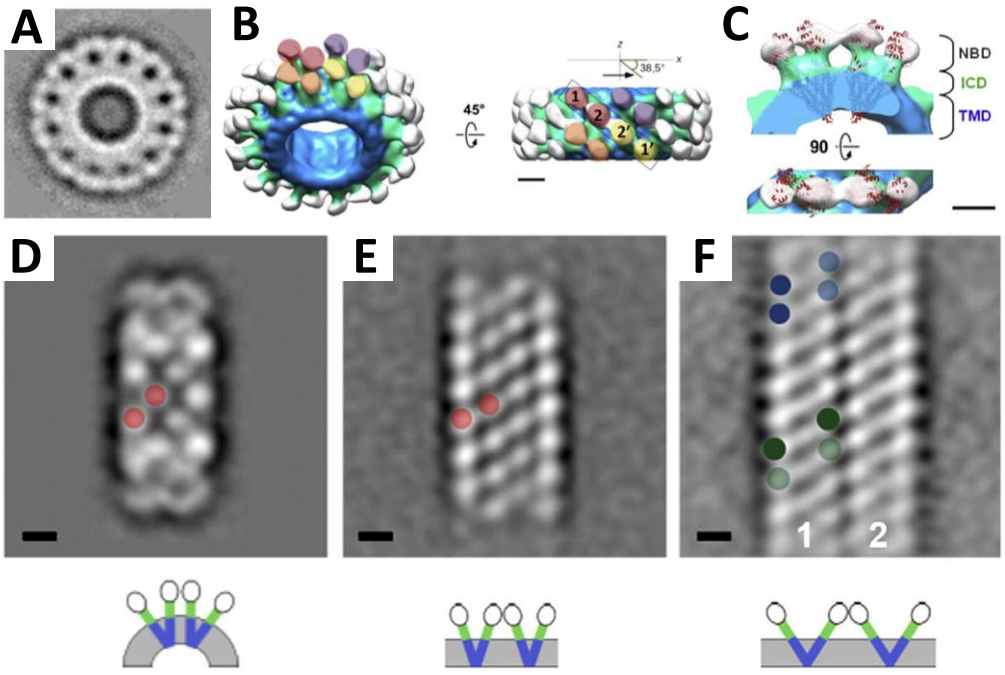

Figure 3.11: BmrA shape in membrane. From Fribourg et al. [2014]. **(A)** Cryo-EM image of ring shape structure of BmrA in membrane at high protein density (detergent lipid ratio 1:1). **(B)** 3D model of the ring shows how BmrA homodimers are positioned within the ring. **(C)** Side view of the homodimers in the ring. **(B, C)** TMDs are shown in blue, intracellular domains (ICDs) in green and NBDs in white. Scale bars are 5nm. **(D, E, F)** Negatively-stained images respectively of BmrA rings, thin tubes and thick membrane sheets, show two different aperture of the V-shaped apo conformation. Scale bars are 5 nm.

Finally, addition of Mg-ATP or of ATP-γ-S (non-hydrolysable form) leads to dissociation of the ring-shaped structures, indicating that the protein is still active in the rings and undergoes conformational change that change membrane organization (Orelle et al. [2008]). This change in membrane shape was further investigated in the lab of Daniel Lévy. Adding ATP and vanadate to apo BmrA rings results in a flattening of the membrane as shown on figure 3.12 (Paik [2018]). Moreover, when BmrA was reconstituted in membrane trapped in closed conformation by ATP-vanadate, homodimers do not arrange in highly curved membrane such as rings, tubes or ribbons, but in flatter surfaces (not shown here, see Paik [2018]). This highlights preference of V-shaped apo BmrA for highly

curved membranes and of ATP-bound state for flat membranes. Finally, the presence of substrate was also found to modulate the membrane shape.

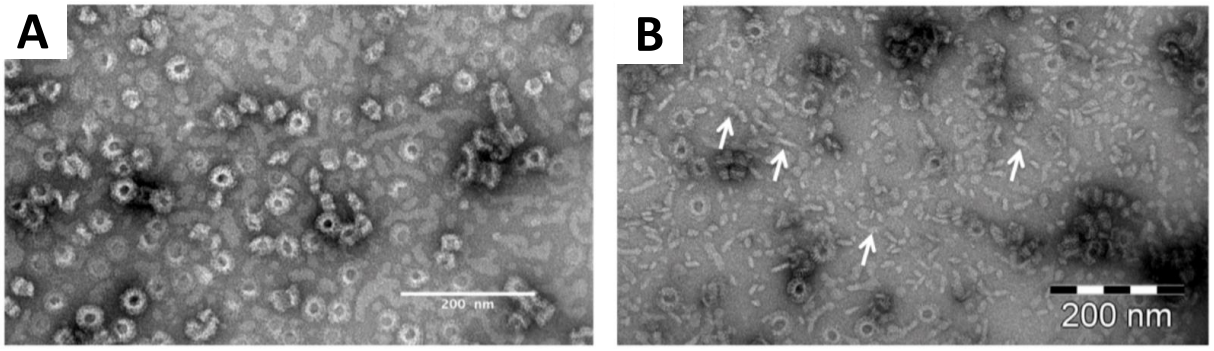

Figure 3.12: Conformation change effect on membrane shape. From Paik [2018]. Negatively stained images of BmrA reconstituted in membranes. **(A)** Homodimers form ring shape in the absence of ATP. **(B)** Addition of ATP and vanadate brings the protein to NBD-bound state and results in flattening of membrane (flat membrane fragments are pointed with white arrows).

All these results put together indicate a strong interplay between BmrA conformation and membrane properties. My PhD work aims at further investigating this interplay.

3.3 Objectives of the project

Multiple evidences are now available for a strong interaction between ABC transporters and membrane mechanical properties such as curvature and tension. ABC exporters have two main conformations with specific shape: a V-shaped inward-facing (open form, apo form) and an outward-facing conformation (closed form, post-hydrolysis form). The function of such proteins, i.e. ATP-dependent substrate translocation, relies on a conformational cycle between open and closed conformations. The change in the protein shape that occurs during the cycle may affect the membrane properties and reciprocally we can ask whether changing membrane mechanical properties would impact the conformational change. However, systematic experimental method is still lacking to investigate this mutual effect. Most of single molecules studies were achieved in micelles of detergent/lipids, or in nanodiscs or in liposomes with minimal size of 150 nm. In this project, we propose a method to investigate highly curved membrane systems and to address the following biophysical questions:

- What is the effect of membrane properties on protein conformations (static study)?

- What is the effect of membrane properties on protein conformational cycle (dynamic study)?

The ABC exporter BmrA has been chosen for this study as it is expected to undergo a large conformational change, as shown on figure 3.9. Moreover interesting preliminary data show that BmrA interacts with its surrounding membrane.

Since single molecule methods are suitable for probing protein conformations, smFRET technique has been used on immobilized molecules to record individual protein conformation change. Labelling of BmrA with fluorophores suitable for FRET was previously established (Paik [2018]). First task has been to implement smFRET method in the lab, calibrate the FRET efficiency and optimize data analysis.

Membrane curvature could be tuned by using small liposomes with different sizes. Lipid composition and reconstitution conditions can be modified to vary the liposomes' size and therefore control membrane curvature. Single BmrA have been incorporated in vesicles and immobilized on a glass surface. Second task was to measure FRET efficiency of the protein according to membrane curvature and to chemical condition: apo conformation, ATP-vanadate (static bound-state) and ATP (dynamic cycle). Our method have given interesting results about the strong impact of highly curved membrane on the transporter BmrA.

Chapter 4

Materials and Methods

In this chapter the methods used first to purify BmrA from *E.coli*, label it and reconstitute it into small proteoliposomes are presented. Secondly the protocol to anchor the liposomes in observation chambers so that we can record fluorescent signal for a few seconds is described. Finally the FRET technique is fully explained both by spectroscopy and by fluorescence microscopy, including the description of the set up and the analysis performed.

4.1 Protein purification, labelling and characterization

The expression, purification and labelling of BmrA (WT and mutants) was optipmized by Su-Jin Paik and John Manzi, adapting the previously reported method (Steinfels et al. [2004, 2002]; Wiseman et al. [2014]).

4.1.1 Wild-type BmrA and mutants.

The expression of BmrA in *E.coli* and the membrane fraction preparation were carried out by John Manzi from plasmids provided by Jean-Michel Jault (IBCP, Lyon). The protein batches used during this thesis were purified and labelled by Su-Jin Paik (see Paik [2018]). BmrA purification was done using the histidine tag present at its C-terminal and in detergent DDM at $0,05\%$ (weight). Su-Jin Paik designed several mutants during her thesis so that we could observe the FRET signal with different dyes positions on the NBDs (see figure 4.1):

- M1: C436S, cystein-less mutant
- M2: C436S / T444C, the cystein is moved to a close position compared to WT (blue position on figure 4.1),

- M3: C436S / T559C, the cystein is placed on a loop at the bottom of the NBD, a way more accessible position (yellow position on figure 4.1).

The choice of these mutants was motivated by reported studies of FRET and LRET on BmrA homologs, MsbA and PgP (Cooper and Altenberg [2013]; Verhalen et al. [2012]; Zoghbi et al. [2017]). The purification and labelling protocols are similar between the WT and the mutants.

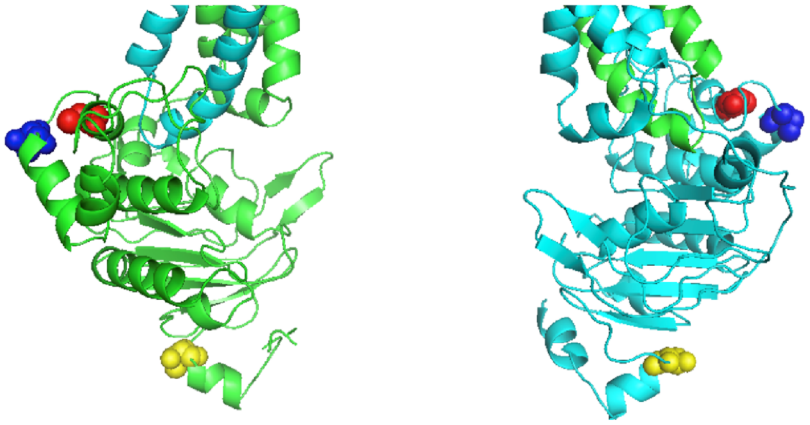

Figure 4.1: Position of the cystein residue on WT, M2 and M3. The figure shows the NBD region in a putative model of BmrA, based on *E.coli* Apo MsbA structure (PDB: 3B5W). The native cystein position is shown in red and the mutated cystein residue of M2 and M3 are shown respectively in blue and yellow.

4.1.2 Protein purification and labelling with fluorescent probes.

Only a summary of the purification and labelling procedures is provided here. The complete protocol is available in appendix A. The full protocol is summarized on figure 4.2. BmrA is purified in detergent DDM at 0,05%.

BmrA is expressed in *E.coli* and membrane fractions are collected after cell lyse and solubilized in detergent (DDM 1%). After centrifugation, the non solubilized pellet forms a brown stain at the bottom of the tube and the solubilized protein remains in solution. The supernatant is incubated with Ni-NTA agarose beads, that bind selectively with BmrA via its histidine tag. The resin (with BmrA anchored) is collected after centrifugation, loaded on a column and washed with a solution containing imidazole, in order to elute the proteins. The concentration of the protein fractions is measured by Bradford method. At this step, the protein in detergent (DDM 0,05%) can be frozen in small aliquots (5 to 10 μL) in liquid nitrogen and stored at -80^{o}C. For this project, the protein is systematically labelled in order to perform FRET experiments.

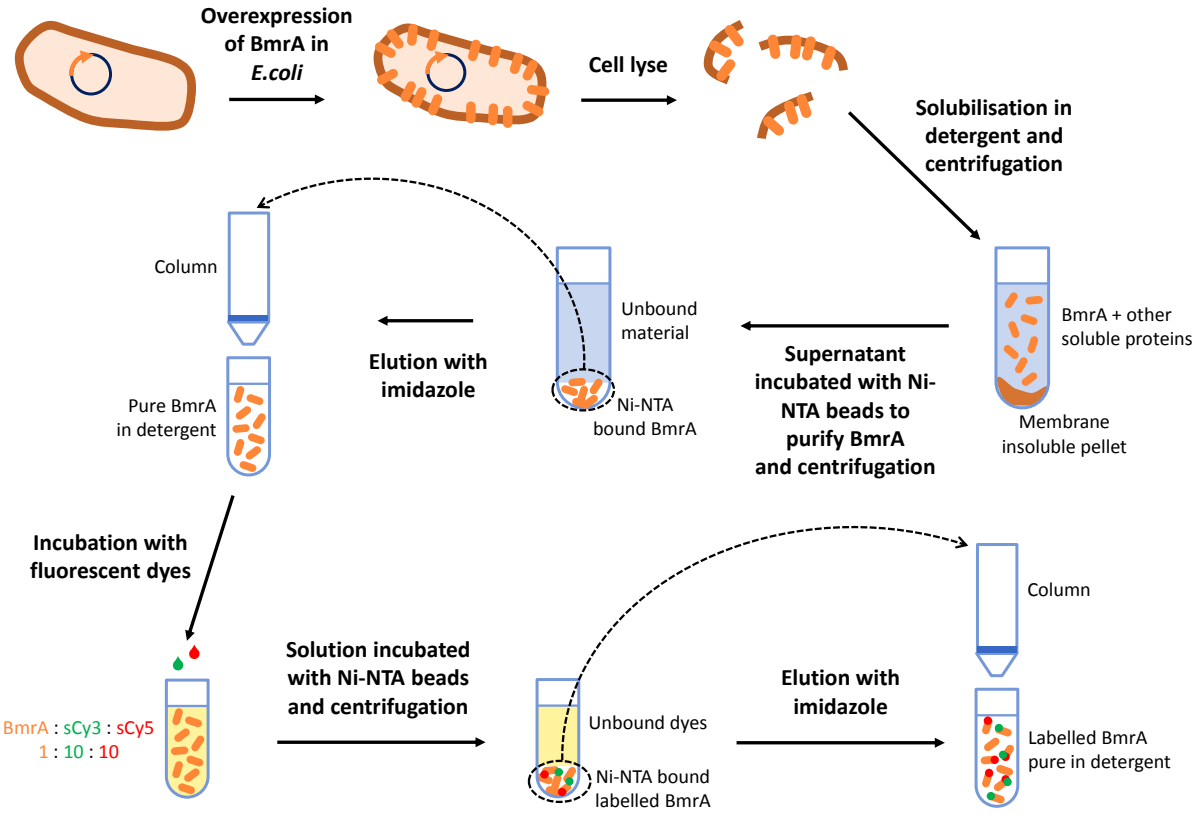

Figure 4.2: BmrA purification and labelling protocols.

Each NBD carries a single cystein residue C436 (for the WT), that are labelled with fluorescent maleimide dyes. The labelling step is performed on the purified protein in detergent at pH 7.0 (in order to avoid non specific labelling of other residues such as lysines and arginines). BmrA is labelled with sulfo-cyanine 3 maleimide (sCy3 = Donor) and sulfo-cyanine 5 maleimide (sCy5 = Acceptor), which characteristics are given in table 4.1.

The protein is incubated over night with sCy3 and sCy5 at ratio 1:10:10 mol/mol/mol for Protein:Donor:Acceptor. The unbound dyes are eliminated using the specific affinity of BmrA histidine tag to Ni-NTA beads just as before. Therefore, the solution is incubated with the beads, that are collected after centrifugation and loaded on a column to elute the protein. The concentration of the protein fractions is measured by Bradford method. The concentration of fluorescent dyes is measured by absorbance. The rate of labelling is the ratio between dyes and protein concentrations. The labelled protein, in detergent (DDM 0,05%), is frozen in small aliquots (5 to 10 μL) in liquid nitrogen and stored at -80^{o}C.

Each step of the purification process is analyzed on a 12 or 15% SDS-Page and using fluorescence. An example is provided on figure 4.3: a band at 65 kDa corresponding to

Dye	Donor or Acceptor	Molar extinction coefficient ϵ ($cm^{-1}.M^{-1}$)	Maximum Exc/Em wavelength (nm)	MW ($g.mol^{-1}$)	Company
sulfo-Cyanine 3 Maleimide (sCy3)	Donor	162000	548/563	777	Lumiprobe
sulfo-Cyanine 5 Maleimide (sCy5)	Acceptor	271000	646/662	803	Lumiprobe

Table 4.1: Fluorescent dyes. The following dyes are used in my project to perform FRET experiments.

BmrA is visible in row 7 and 10, before and after labelling respectively, and is also visible by fluorescence.

4.1.3 ATP, inhibitors and susbtrates of BmrA

BmrA function as an homodimer (dimerization of half transporters): there are two ATP hydrolysis sites where ATP molecules bind and bring the two NBDs together (closed conformation). At the end of the conformational cycle, at least two molecules of ATP are consumed and ADP and phosphate are released. Different inhibitors are known like AMP-PNP, ATP-γ-S or orthovanadate. AMP-PNP and ATP-γ-S are non-hydrolysable form of ATP (the hydrolysis rate is very low) while vanadate molecules compete with phosphate groups and replace them after a phosphate gets released, preventing from the reopening of the NBDs. In this study, orthovanadate was mostly used in order to lock the protein in its NBDs-bound state (or post-hydrolysis conformation).

ATPase activity measurements were performed on BmrA in previous work (Paik [2018]), using an NADH assay (the full procedure is presented in appendix A).

Stock of ATP.

ATP disodium salt (from Sigma) is in solution at 100 mM, aliquoted at 10 μL and kept at -20^{o}C.

Preparation of orthovanadate.

Orthovanadate (from Sigma) was prepared by Su-Jin Paik at 100 mM in water. pH is adjusted to 10 with HCl and the solution is aliquoted and stored at -20^{o}C. Orthovanadate is boiled at least 5min just before use and is kept at room temperature during all the

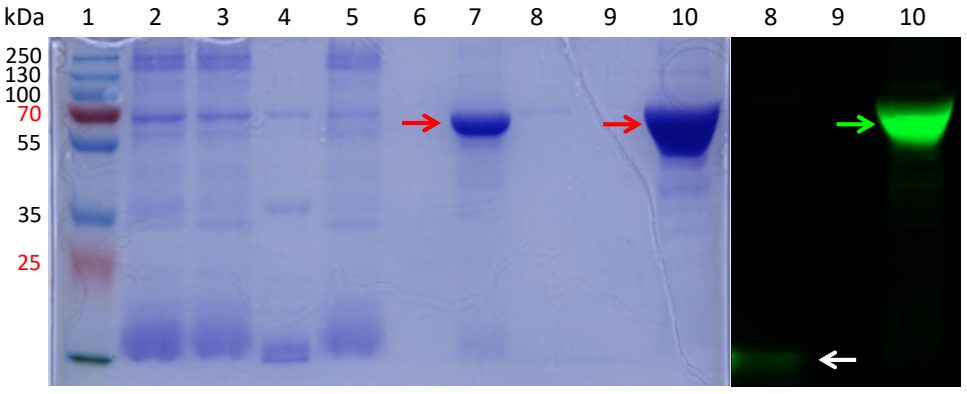

Figure 4.3: Example of SDS Gel for BmrA purification and labelling. Row 1 shows the molecular weight marker, with 70 and 25 kDa highlighted in red. Rows 2 to 4 show the membrane solubilization. Rows 5 to 7 show the purification of BmrA. Rows 8 to 10 shows the second step of purification after BmrA labelling. Rows 5 and 8 show the Ni-NTA beads supernatant, meaning the unbound proteins. Rows 6 and 9 show the beads washing solutions. Rows 7 and 10 show the beads elution. The red arrows point the purified BmrA proteins (with a molecular weight of 65 kDa, we found bands between 70 and 55 markers). The green arrow shows the purified protein labelled with fluorescent dyes (here, given as an example, Alexa488). The white arrow shows the free fluorescent dyes that remain in the supernatant.

time of the experiment. ATPase activity of BmrA is inhibited up to 80% by addition of orthovanadate.

BmrA substrates.

BmrA is able to interact and possibly transport various substrates in particular drugs such as reserpine, vinblastine or verapamil (Steinfels et al. [2004]). It has been shown that the activity of the protein is not much stimulated (20%) by the presence of these substrates (Paik [2018]). For this reason, generally no substrate was added to observe the conformational dynamics of BmrA. Only some assays were done using Verapamil at 50 μM (presence of substrate will be mentioned).

4.1.4 Sample summary

BmrA WT was labelled with sCy3/sCy5 fluorophores in order to perform single molecule FRET. The purified and labelled protein batch has the following characteristics:

- the rate of labelling is 31,5% for sCy3 and 38,7% for sCy5 (24,4% of doubly labelled proteins in theory),
- the activity is conserved at 79,8% as compared to the unlabelled WT BmrA (the activities of unlabelled WT in different lipid compositions are shown on figure 3.10).

4.2 Reconstitution of proteoliposomes and characterization

Referring to our main objectives, a fine control of mechanical properties is required in this study. In practice, the radius of proteo-SUVs cam be changed, provided a control of membrane curvature. In previous work in the lab of Daniel Lévy, it was reported that the liposomes size can be finely tuned by three important parameters: the lipid composition, in particular the presence of anionic lipids (that are conical-shaped lipids), the reconstitution temperature and the detergent removal speed during SUVs preparation(Paik [2018]; Lévy et al. [1990]; Rigaud et al. [1995]). Indeed, micelles must coalesce to form vesicles and the intermediate steps are crucial in determining the size of future vesicles. In this work, three different liposomes populations are used corresponding to two different lipid composition and three distributions of size. In this part, the reconstitution protocol and the liposomes characterization are described.

4.2.1 Lipids

The lipids are purchased from Avanti Polar Lipids (USA) in chloroform or in powder. The powder is resuspended in chloroform and all the lipids stock solutions are kept in glass vials under argon gas at -20^{o}C. Note that biotinylated lipids were systematically used in order to immobilize the liposomes on a glass coverslip for single molecule FRET observation (see part 4.3). For this work, two different lipid compositions were mainly used:

- *E.coli* / DSPE-PEG2000-Biotin 99,5/0,5 % w/w;
- EPC / PS / DSPE-PEG2000-Biotin 90/9,5/0,5 % w/w.

For small volumes (eg. a 100 μL at finale concentration 2 mg/mL in lipids), proteoliposomes are reconstituted starting from a mix of lipids in chloroform allowed to dry under vacuum for at least two hours.

In order to prepare larger volumes of liposomes in a controlled manner, I prepare a stock of liposomes in water. A dried lipid film is rehydrated at 5 mg/mL in water, sonicated for 1min with a tip sonicator, aliquoted and stored at -20^{o}C.

For visualizing the membrane, 0,1% of DHPE Texas Red lipids or 0,01% of Bodipy FL lipids is added to the previous solutions for some experiments.

4.2.2 Detergents and formation of liposomes

The dried lipid film obtained is then rehydrated under magnetic stirring in buffer A (50 mM MOPS pH 7,5, 150 mM NaCl) with detergent Triton X-100, so that the weight of detergent is 2,5 × the weight of lipids in solution.

Starting from the frozen stock of liposomes, buffer A is mixed with water and detergent Triton X-100 (2,5 × lipids weight) before to add the liposomes at a finale concentration of 2mg/mL.

In both cases, we allow the solution to hydrate under magnetic stirring for 15 min. At this step the protein can be added to the solution (see next section 4.2.3). The lipids are forming mixed micelles with the detergent, which is then removed by successive additions of biobeads (from Bio-Rad).

Preparation of the biobeads.

The biobeads are washed in methanol under stirring during 30 min. The methanol is removed and the beads are rinsed three times 10 min in milliQ water under stirring. Biobeads are kept at 4^{o}C for one month. Then we prepare a new batch of biobeads with the same protocol.

Detergent removal.

The amount of biobeads added to the lipid solution and the temperature of reconstitution will set the rate of detergent removal (Rigaud et al. [1995]). It has been shown that the size of liposomes is highly dependent on the lipid composition and on the detergent removal rate (see part 4.2.4). Therefore the liposomes size distribution can be experimentally tuned. For this work, I mainly used three different liposomes populations obtained under the following experimental conditions (see part 4.2.4 for the size measurement method):

- *E.coli* liposomes, reconstituted at 20^{o}C with successive additions of biobeads with a ratio biobeads/detergent 10 w/w for 2 h, then 10 w/w for 1 h and finally 20w/w for 1 h : a well defined size population centered on 60 nm diameter is obtained,

- EPC/PS liposomes, reconstituted at 20^{o}C with successive additions of biobeads with a ratio biobeads/detergent 10 w/w for 2 h, then 10 w/w for 1 h and finally 20w/w for 1 h : a wide size distribution between 100 nm and 180 nm diameter is obtained,

- EPC/PS liposomes, reconstituted at 4^{o}C with successive additions of biobeads with a ratio biobeads/detergent 30 w/w for 2 h, then 30 w/w for 1 h and finally 60w/w for 1 h : a well defined size population at 40 nm diameter is obtained.

At the end of the detergent removal, the liposomes solution is collected, by taking good care that all the biobeads are removed, and stored at 4^{o}C for one to two days. We generally prepare 100 μL at 2 mg/mL lipids that are kept in the fridge for one night or that is used on the very same day.

4.2.3 Incorporation of the protein

To reconstitute BmrA into proteoliposomes, the purified protein is first diluted in a buffer B containing detergent (50 mM MOPS pH 7,5, 150 mM NaCl, 0,05% DDM). The protein is then added to the hydrated lipid mixture under magnetic stirring for 20 min.

The protein can be incorporated in its apo conformation or trapped in post-hydrolysis state. To trap BmrA in closed conformation, the solubilization buffer A must contain 1 mM of $MgCl_2$ (equimolar with ATP). At this step 1 mM of orthovanadate is added to the lipid/protein mixture and left under stirring for 20 min. 1 mM of ATP is added just before loading the biobeads and starting the reconstitution.

Lipid/protein ratio (LPR).

Single molecule study requires that at most one protein is incorporated per liposome. The theoretical Lipid/Protein Ratio (LPR) can be calculated from the mean radius R of the liposomes distribution (see part 4.2.4) and the surface occupied by one lipid, which is on average $S_{lipid} = 65$ Å^2 (Kučerka et al. [2011]).

The surface of the bilayer is

$$S = 4\pi R^2, \tag{4.1}$$

and the number of lipids in a liposome is

$$N_{lipid} = \frac{S}{S_{lipid}}. \tag{4.2}$$

The number of protein per liposome is $N_{protein}$ (note that BmrA is a monomer but works as a homodimer, so the number of homodimer per liposome simply corresponds to $\frac{N_{protein}}{2}$). $N_{protein}$ is the targeted number that should be taken lower than 1 to guarantee single molecule regime. One monomer of BmrA has a molecular weight of 65 kDa and the lipids have an averaged molecular weight of 800 Da. Finally, the LPR (w/w) is given by the following equation:

$$LPR = \frac{N_{lipid} \times 800}{N_{protein} \times 65000}. \tag{4.3}$$

Figure 4.4 shows the LPR plotted against the liposome's diameter for different targeted value of monomer/liposome $N_{protein}$. Experimentally, $N_{protein}$ was taken between 0,1 and 0,4 monomer per liposome, all the experimental values are available on table 4.2 in part 4.2.5.

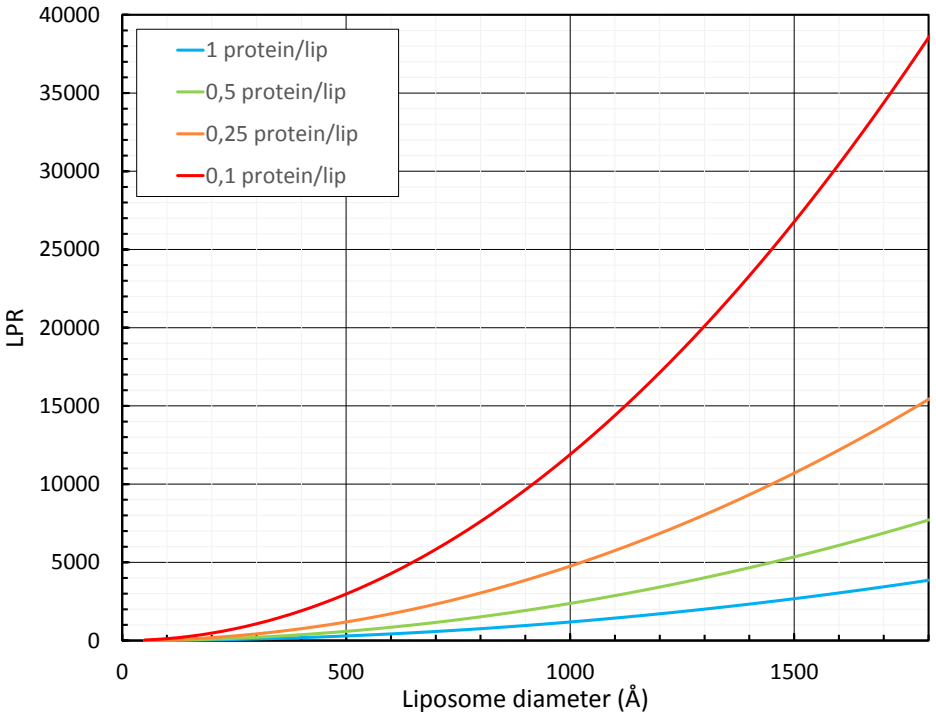

Figure 4.4: [Lipid protein ratio in liposomes. LPR is plotted according to liposome's diameter for different targeted values of monomer per liposome $N_{protein}$. As an example, if one works with 1000 Å diameter liposomes and aims at 0,25 monomer per liposome, the LPR should be 5000 w/w.

Characterization of protein incorporation.

The incorporation and orientation of BmrA incorporated into proteo-SUVs were fully characterized in previous work by Su-Jin Paik:

- The protein incorporation was tested by a flotation assay in a sucrose gradient. It allows to separate the protein properly reconstituted in liposomes, the empty liposomes and the aggregated proteins. 98% of BmrA was found properly incorporated.
- The protein orientation was tested with fluorescently labelled protein. The NBDs carrying the fluorescent dyes can be digested by trypsin. BmrA with NBDs oriented inside the liposome (will not be digested) can be discriminated from proteins with NBDs oriented towards the outside (will get digested by trypsin). In *E.coli* extract liposomes and in PC liposomes (diameter bigger than 100 nm), the protein incorporation was found non-symmetrical with 75% of Apo BmrA with outward-facing NBDs. In small PC liposomes (diameter around 40 nm) 100% of Apo BmrA are incorporated with outward-facing NBDs. The trypsin digestion did not work properly in the post-hydrolytic conformation.

In this work, the number of protein per liposomes was estimated using fluorescence, in order to guarantee single-molecule conditions. Liposomes containing $0,01\%$ Bodipy-FL lipids are prepared with sCy5-labelled BmrA incorporated. The liposomes were immobilized on a glass coverslips (this method is developed in part 4.3). Fluorescent signal is visible in the Bodipy-FL channel when there is a liposome and in sCy5 channel when there is a protein. Co-localization of both signals corresponds to a liposome containing at least one BmrA (see results part 5.3.2).

4.2.4 Liposomes characterization: size and lamellarity

The liposomes population have been fully characterized in term of size and lamellarity by Su Jin Paik and Aurélie Di Cicco, via electron-microscopy imaging.

Figure 4.5 shows cryo-EM images of liposomes with different lipid compositions (reconstituted without protein). Regular and unilamellar vesicles with diameters respectively around 140 nm and 60 nm are observed. Unilamellarity is crucial in our work since we study a transmembrane protein that hydrolyzes ATP. If multilamellar liposomes are used, the proteins in the inner layers would not be accessible under addition of ATP.

Size distributions were measured from the cryo-EM images and 500 liposomes were analyzed for each condition (Paik [2018]). Figure 4.6 show that *E.coli* lipids-based vesicles are homogenous with an average radius of 30 nm while larger distributions of larger liposomes were measured for PC lipids-based vesicles (radius between 40 and 90 nm). *E.coli* is composed of 67% of PE lipids that are conical-shaped and that impose a lower liposomes' size. It was found that PC liposomes are significantly smaller when reconstituted at 4^oC (diameter $\varnothing \sim 40$ nm) than at 20^oC ($\varnothing \sim 140$ nm).

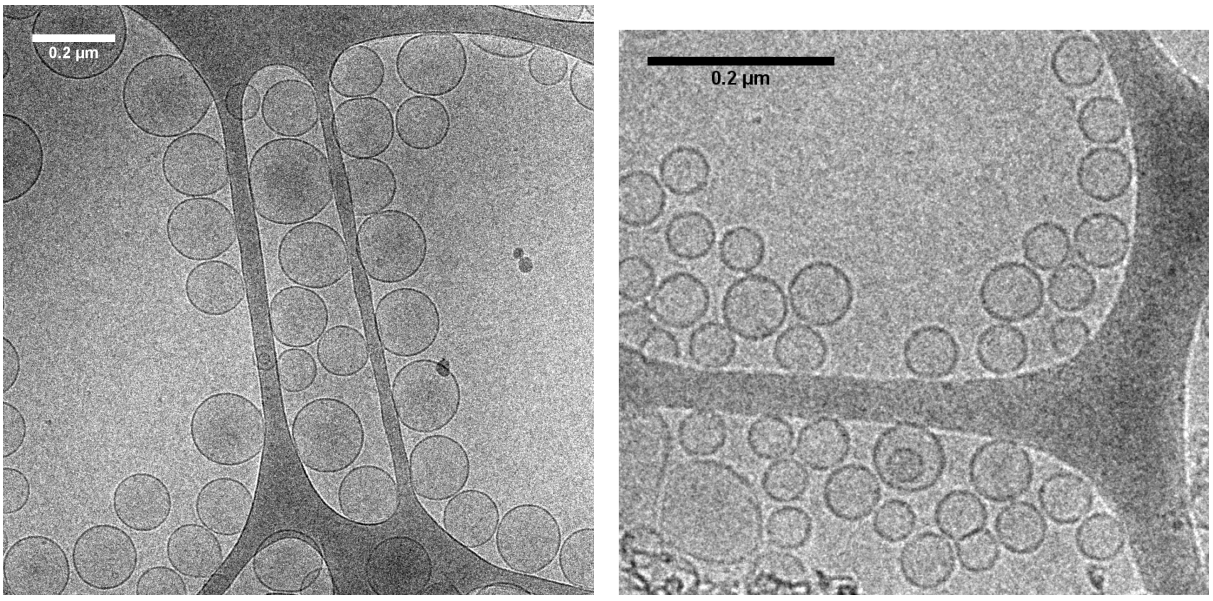

(a) EPC/bPS 9/1 w/w 20^{o}C liposomes. **(b)** *E.coli* 20^{o}C liposomes.

Figure 4.5: Liposomes characterization in terms of size and lamellarity. Scale bars are equal to 200 nm.

This provides different sets of unilamellar SUVs with precise characteristics that can be used to address our biophysical questions. Note that in this study we only have access to the mean radius for each batch of vesicles. Each condition will be considered to have a specific curvature and we will discuss their effect qualitatively.

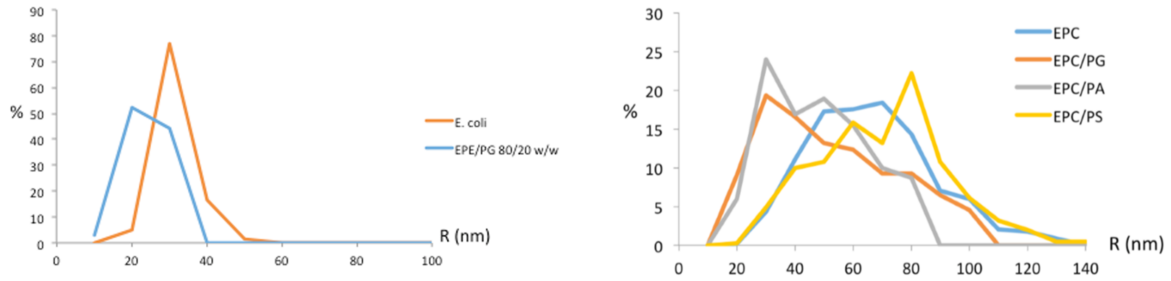

(a) Homogenous small liposomes distribution with *E.coli* lipid extract or EPE/PG 8/2 w/w (20^{o}C).

(b) Heterogenous liposomes distribution with EPC lipids added with different negatively charged lipids : PG, PA, PS (20^{o}C).

Figure 4.6: Liposomes size distributions for different reconstitution conditions. Between 500 and 1500 liposomes were analyzed for each condition (Paik [2018]).

4.2.5 Samples summary

Table 4.2 summarizes the three liposomes populations used in this study with the experiment LPR used and the mean size measured by cryo-EM imaging.

Lipids Lipids	Reconstitution temperature (^{o}C)	Liposomes average diameter (nm)	Experimental LPR (w/w)	Number of protein/lip
E.coli	20	60	2000	0,21
EPC/bPS	20	140	6000	0,4
EPC/bPS	4	40	700	0,27

Table 4.2: Experimental LPR used in the different liposomes samples. And the corresponding number of protein per liposome calculated with equation 4.3.

In the three lipid compositions, BmrA is systematically observed in the four following conditions:

- the protein is incorporated and observed in its Apo form (referred to as **Apo**),
- the protein is trapped with vanadate and ATP (1 mM) before to be incorporated in the vesicles (referred to as **Vi trapped**),
- the protein is incorporated in vesicles in its Apo form and incubated with Vi and ATP (1 mM) (referred to as **ATP Vi**),
- the protein is incorporated in vesicles in its Apo form and incubated with ATP (1 mM) (referred to as **ATP**) (in *E.coli* liposomes, Verapamil was added at 50 μg/mL together with the ATP, referred to as **ATP Ver**).

In conditions **Apo**, **Vi trapped** and **ATP Vi** we expect the conformation of the protein to be "frozen" and not to cycle. In Apo, the protein has a certain flexibility and can therefore fluctuate. In the **ATP** or **ATP Ver** conditions, the protein should cycle and some dynamics should be observable.

4.3 Surface treatment

Single molecule FRET experiments can be performed in two different manners, as introduced in part 2.3.2: solution-based measurements where the particles diffuse freely or with immobilized molecules allowing to resolve signal in time. The immobilized method was selected for our study in order to observe conformational dynamics of BmrA. In this part, the strategies for coverslips cleaning and coating are detailed.

4.3.1 Coverslip cleaning and chamber assembly

For single molecule studies, the observation chambers, the buffers and all the samples used must be highly clean (Selvin and Ha [2008]). Fluorescent contaminants left on coverslips are very similar to the signal given by single fluorophores (see figure 5.1a in chapter 5). Therefore we must limit these contaminants on the surface. It is hard to totally get rid of them, especially at 532 nm excitation, but a suitable protocol that minimizes them is described here. A small channel of roughly 10 μL is built between two coverslips as shown on figure 4.7A. The lower coverslip is round with 25 mm diameter, and the top coverslip is a squared 18×18 mm^2 that is cut to 18×10 mm^2.

Different cleaning strategies were tried among which:

- Water, ethanol, acetone, KOH 1 M, water;
- Water, Hellmanex 2%, water, KOH 1 M, water.

These protocols were not satisfying enough for this study, since a lot of contamination was left on the surfaces. The final protocol is summarized below.

The glass coverslips (Menzel-Gläser, thickness #1) are placed on a Teflon carrier in a glass beaker. They are washed under sonication with the following steps:

- Chloroform during 20min
- Water during 5min
- KOH 1 M during 20min
- rinsed three times in water
- Water during 15min.

The coverslips are dried under a gentle stream of nitrogen and placed for 1,5 min in an air plasma cleaner. A double-sided tape mask is used to sandwich the two coverslips and

form a small channel as shown on figure 4.7A. The channel is loaded by using a pipette tip on one side and aspirating at the other side with a clean towel (Kimwipes).

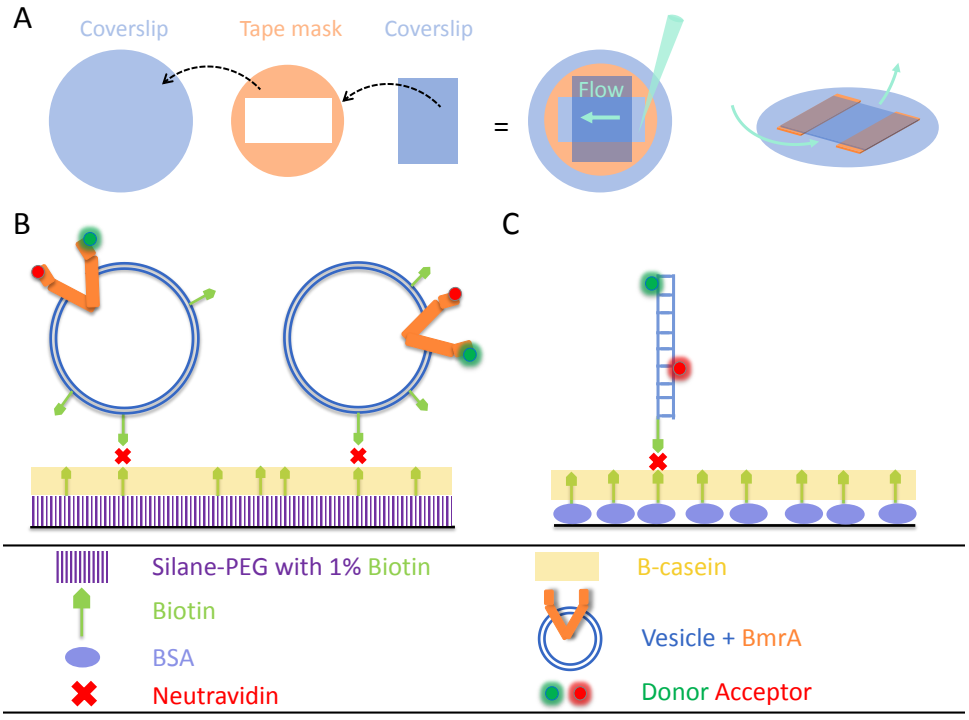

Figure 4.7: Surface treatment and chamber design. (A) Building the microchannel. **(B)** Surface treatment strategy for specific attachment of the liposomes. **(C)** Surface treatment strategy for specific attachment of double stranded DNA.

4.3.2 Coating strategies

Protocol for liposomes' attachment

Attaching strongly and specifically the liposomes (and proteoliposomes) on the glass coverslip requires a precise surface treatment.Different strategies were tested, among which:

- PLL-PEG with 1% PLL-PEG-Biotin, neutravidine
- Tris NTA PEG coverslips sent by collaborators (J. Piehler, Universität Osnabrück).

The strategy finally selected is summarized on figure 4.7B. The chamber is incubated with a solution of silane-PEG with 1% of silane-PEG-biotin at 5 mM during one hour. The solutions of silane-PEG2000 and silane-PEG3400-biotin (LaysanBio) are prepared from powder in DMSO at 5 mM and kept at room temperature. The solution is washed away and the chamber is rinsed by injecting 100 μL of buffer A (50 mM MOPS pH 7,5, 150 mM NaCl), i.e. 10× the volume of the chamber.

A solution at 20 μg/mL of neutravidin is incubated during 5 to 10 min, and the surface is then rinsed with 100 μL of buffer A. 40 μL of each surface treatment solution are generally flowed through the chamber, i.e. approximately 4$\times$ the volume of the chamber. Neutravidin (Sigma) solution is prepared from powder in ultra-pure water at 2 mg/mL, filtered with 0,2 μm pore size filter, aliquoted at 10 μL and kept at -20^{o}C. The stock solution is diluted at 20 μg/mL in buffer A.

A solution of β-casein at 1 mg/mL is incubated at least 10 min to fully passivate the coverslip and to fill holes in the silane coating. The chamber is again rinsed with 100 μL of buffer A. The β-casein (Sigma, from bovine milk $\geqslant$ 98%) solution is prepared at 1 mg/mL from powder in a solution of 0.1 M Tris-HCl at pH 7.5, filtered with 0.2 μm pore size filter, aliquoted at 1 mL and kept at -20^{o}C.

Finally the solution of liposomes is injected at a concentration :

- 5.10^{-3} mg/mL in lipids for small proteoliposomes : *E.coli* 20^{o}C and EPC/bPS 4^{o}C,
- 5.10^{-2} mg/mL in lipids for larger proteoliposomes : EPC/bPS 20^{o}C,

during 5 to 10 min just before to start the observation at the microscope. We rinse with 100 μL of buffer A.

At this step, more reagents can be added to the chamber at the required concentration: oxygen scavenger, ATP, inhibitors (we then use buffer A complemented with $MgCl_2$ equimolar, usually 1 mM).

Protocol for DNA attachment

In order to calibrate the smFRET set-up, a double-stranded DNA sample (carrying a biotin) was used (see part 4.4.1 for the description of the system). Attaching specifically DNA requires a different strategy than for the liposomes. Buffer TE (10 mM Tris-HCl pH 8, 400 mM NaCl, 1 mM EDTA) was systematically used for DNA sample, both for the hybridization and the observation. A solution of biotinylated BSA at 1 mg/mL is incubated in the chamber for 5 min and rinsed with 100 μL of buffer TE. The surface is coated with neutravidin at 20 μg/mL for 5 min, rinsed with 100 μL of buffer TE, incubated with β-casein at 1 mg/mL for 10 min (in order to fully passivate the surface, note that BSA could have been used here) and rinsed with 100 μL of buffer TE. Just before observation, the DNA sample is loaded at 30 pM for 2 min and rinsed with 100 μL of buffer TE. The strategy is summarized on figure 4.7C.

4.3.3 Characterization of the surfaces

The liposomes/DNA attachment with biotin was carefully characterized in terms of specificity. To do so, chambers were prepared as described in part 4.3.2 without the neutravidin step. The samples are then loaded in a similar way in order to quantify the amount of non-specifically interacting molecules. Range of neutravidin and biotin concentrations have been tested to optimize the coating protocol.

The liposomes' integrity conservation was also tested in order to see whether they remain intact after immobilization on the surface. Liposomes containing 0,1% of DHPE Texas Red lipids were used for this test. A soluble fluorescent dye was also added inside the liposomes: 300 μM of pyranine. The fluorescent lipids allowed detecting the surface of the liposomes and the pyranine solution allowed visualizing their inner volume. Detecting pyranine signal informs whether the liposomes are intact on the surface or if they are damaged when binding to the coverslip.

4.4 smFRET calibration system

Before presenting the set-up, acquisition settings and the analysis method used for smFRET study, the sample used to calibrate and optimize our experiments is described here.

4.4.1 smFRET calibration with double-stranded DNA

Oligonucleotides' description.

In order to calibrate the single-molecule FRET signal observed with the set-up, a 40 base pair (bp) long double-stranded DNA was used, with similar sequence as in Deniz et al. [1999]. FRET method can be seen as a "nanometric ruler" and the goal of this calibration is to assess what FRET efficiency is reached according to the relative distance between the Donor and the Acceptor. One strand carries a Donor fluorophore and the complementary strand is labelled with an Acceptor dye. Three different samples were used with various known distances between Donor and Acceptor.

The oligonucleotides were ordered from Eurofins. The DNA stock solutions at 50 μM were kept at -20^{o}C. The oligo 1 (or Up) has the following sequence : 5'-CTC TTC AGT TCA CAG TCC ATC CTA TCA GCC GCT TGC CTT C-3'. The oligo 2 (or Down) has the complementary sequence. Different modifications are made to the oligonucleotides. The strand Up carries a Biotin in 3', to allow us to anchor it specifically to glass coverslips

as explained in part 4.3.2. The strand Up is also modified in 5' with a Donor fluorescent dye and four different oligonucleotides Up are ordered labelled with Alexa488, sCy3, TMR and no dye in 5'. The Down oligonucleotides were designed to have three different distances between the fluorescent dyes: an sCy5 dye is added on a T-base at 19, 12 and 7 bp distance from the Donor dye (i.e. from its 3' end). A dye-free Down strand is also ordered. The different modifications are summarized on figure 4.8.

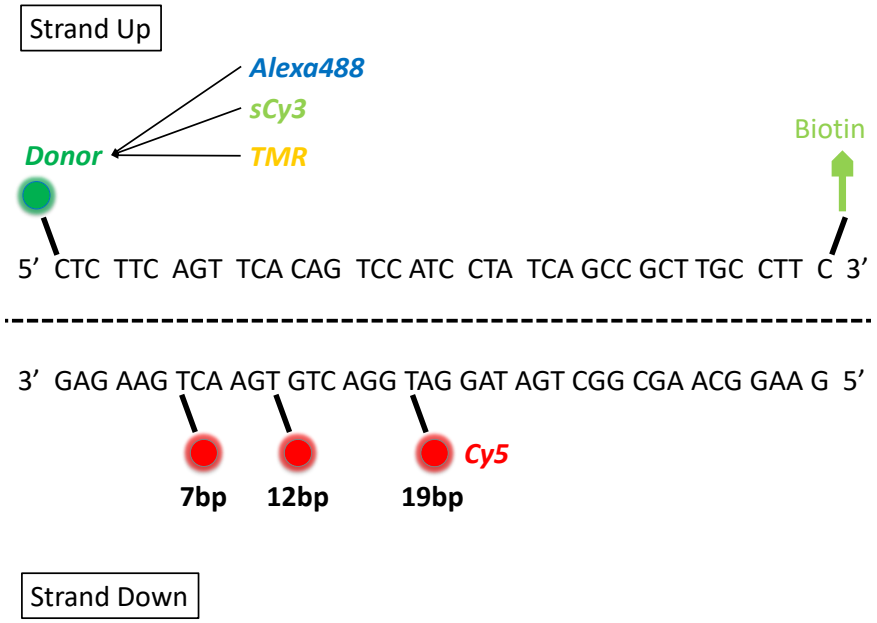

Figure 4.8: Scheme of double stranded DNA used for FRET calibration. All the modifications are indicated.

Double stranded DNA.

The oligonucleotides Up and Down are hybridized in buffer TE (10 mM Tris-HCl pH 8, 400 mM NaCl, 1 mM EDTA). A stock of buffer TE×3 is prepared. The oligonucleotide stocks are at 50 μM. 30 μL of double stranded DNA solution at concentration 15 μM of each oligo are obtained by mixing: 9 μL of oligo Up, 9 μL of oligo Down, 10 μL of buffer TE×3 and 2 μL of ultra-pure water. The solution is brought to 84,6^{o}C (melting temperature of the DNA strand + 10) during 10 min. The sample is allowed to cool down to room temperature. DNA solutions are then diluted to the desired concentration in buffer TE×1.

FRET system calibration with DNA samples.

The FRET calibration was done in three steps. (i) We first checked the FRET efficiency in bulk for all the samples with fluorescence spectroscopy (this is presented in part 4.4.3). (ii) The samples were also observed in bulk with our microscope (see part 4.5.4).

(iii) Finally, they were observed with a single molecule detection by anchoring them on glass surface as explained in part 4.3.2. The acquisition was done with the exact same parameters used for BmrA and that are presented in next part 4.5.3.

4.4.2 Inter-dye distance helical model.

A model was proposed in Deniz et al. [1999] to calculate the theoretical distance R between the Donor and Acceptor dyes on a double stranded DNA: the inter-dye distances–helical model of DNA. The DNA double helix can be described as a cylinder of radius 10 Å. Each base pair makes a rise of 3,4 Å and 10 bp correspond to one full turn. The Donor and Acceptor dyes are positioned on different base pair on this cylinder as shown on figure 4.9. The inter-dye distance R has a parallel component R_a and a perpendicular component R_b that read

$$R = \sqrt{R_a^2 + R_b^2}, \tag{4.4}$$

$$R_a = 3,4(n-1) + L, \tag{4.5}$$

$$R_b = a^2 + d^2 + 2ad\cos\theta, \tag{4.6}$$

where n is the base pair separation between Donor and Acceptor, L is the distance between the dyes for $n = 1$, a and d are the Acceptor and Donor distances from the cylinder axis (as shown on figure 4.9), θ is the angle between the dyes and reads :

$$\theta = 36(n-1) + \phi \tag{4.7}$$

with ϕ the inter-dye angle at $n = 1$. Similar parameters values as reported in Deniz et al. [1999] were used here: $a = d = 15$ Å, $L = 5$ Å, $\phi = 225°$. In our case, R was calculated for $n = 19, 12$ and 7 bp corresponding to 66,6, 46,7 and 34,1 Å respectively.

4.4.3 Spectroscopy measurement

Fluorimetry is a common technique to have access to ensemble FRET efficiency of the sample. It allows to scan samples quickly and estimate the different FRET levels in different experimental conditions. Spectrosocopy was used for the calibration of DNA samples.

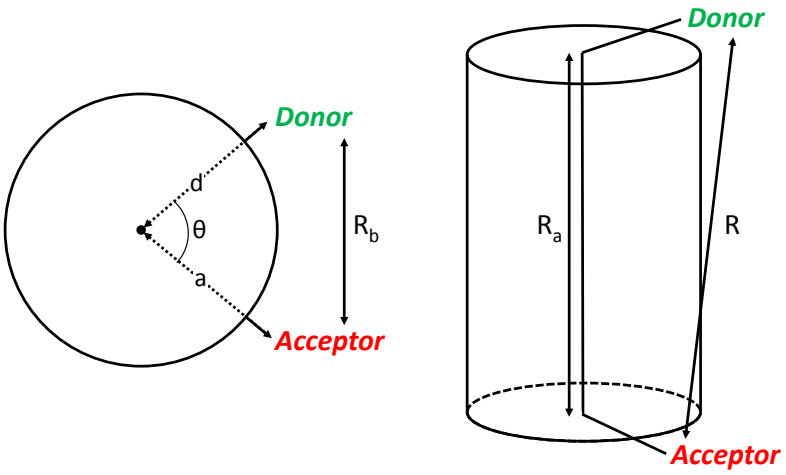

Figure 4.9: Inter-dye distances helical model. Scheme made from Deniz et al. [1999]. The DNA double helix is represented by a cylinder. The Donor and Acceptor dyes are positioned on two different nucleotides. Right scheme shows a side view where we can see the parallel component R_a between Donor and Acceptor. Left scheme shows a top view where we can see the perpendicular component R_b.

The measurements are performed on Cary Elipse Fluorescence Spectrophotometer (Agilent Technologies) in a quartz cuvette 10×2 mm (Hellma Analytics). A blank is done with buffer TE. 100 μL of the sample is loaded in the cuvette to obtain a final concentration of 0,5 μM for each fluorescent dye (it may change the total concentration of DNA in the cuvette depending on the observed sample). Emission spectrum is obtained with an excitation wavelength a bit lower than the maximal excitation wavelength of the fluorescent probe (to avoid bleed through of the excitation in the emission spectra).

Three FRET couples of fluorescent dyes were used on DNA samples: Alexa488/sCy5, sCy3/sCy5 and TMR/sCy5 (Tetramethylrhodamine). The parameters used at the spectrophotometer for each dye are summarized in table 4.3.

4.4.4 Spectroscopy analysis

We first measure the spectra for the Donor/Acceptor couple when exciting it at the Donor wavelength and then at the Acceptor wavelength. An example for the FRET couple sCy3/sCy5 is provided on figure 4.10A. From the spectra, the fluorescence intensity of the Donor F_D, Acceptor F_A and FRET signal F_{FRET} are measured. For that the fluorescence is integrated over a 20 nm wide interval around the maximum emission wavelength

Fluorescent probe	Donor or Acceptor	Excitation wavelength (nm)	Emission wavelength interval (nm)
Alexa488	Donor	470	480 - 800
sCy3	Donor	520	530 - 800
TMR	Donor	530	540 - 800
sCy5	Acceptor	620	630 - 800

Table 4.3: Experimental observation parameters for spectroscopy. For each fluorescent dye we used a different excitation wavelength and a specific range of emission wavelength.

of the Donor for F_D and of the Acceptor for F_{FRET} and F_A. In this paragraph, "Donor channel" refers to the measurement around the Donor maximum emission when excited at the Donor excitation wavelength, "FRET channel" refers to the measurement around the Acceptor maximum emission when excited at the Donor excitation wavelength and "Acceptor channel" to the measurement around the Acceptor maximum emission when excited at the Acceptor excitation wavelength.

The FRET signal F_{FRET} is corrected for two effects: the leakage of the Donor probe emission in the FRET interval, and the direct excitation of the Acceptor dye at the Donor excitation wavelength. We measure spectra for a sample containing only Donor and only Acceptor in the same conditions (dye concentration and spectrophotometer parameters) as before. An example for sCy3 alone and sCy5 is shown on figure 4.10B and C. The fluorescence intensities $A1$, $A2$, $A3$ and $A4$ defined on the figure, are measured by integrating the signal over a 20 nm wide interval. $A1$ is the fluorescence intensity of the Donor only in the Donor channel, $A2$ is the fluorescence intensity of the Donor only in the FRET channel, $A3$ is the fluorescence intensity of the Acceptor only in the Acceptor channel and $A4$ is the fluorescence intensity of the Acceptor only in the FRET channel. The correction ratio for Donor leakage $R_1 = A1/A2$ and for Acceptor direct excitation $R_2 = A3/A4$ can then be computed. The corrected FRET signal is defined as follow:

$$F_{FRET}^{corr} = F_{FRET} - \frac{F_D}{R_1} - \frac{F_A}{R_2}. \tag{4.8}$$

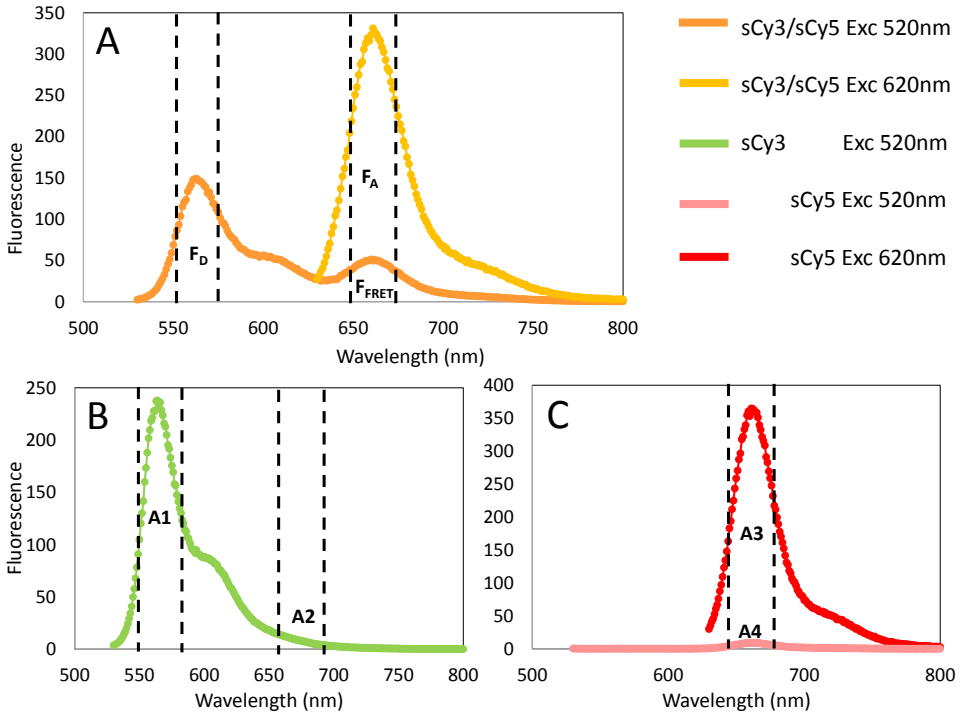

Figure 4.10: Example of spectra measured for the couple sCy3/sCy5. (A) Spectra for sCy3/sCy5 couple. F_D, F_{FRET} and F_A are respectively the Donor, FRET and Acceptor fluorescence integrated on a 20 nm wide interval around the maximum emission wavelength of the Donor for F_D and of the Acceptor for F_{FRET} and F_A. **(B)** Spectrum for sCy3 only (Donor only). $A1$ and $A2$ are the Donor fluorescence integrated on a 20 nm wide interval around the maximum emission wavelength of the Donor for $A1$ and of the Acceptor for $A2$. **(C)** Spectra for sCy5 only (Acceptor only). $A3$ and $A4$ are the fluorescence integrated on a 20 nm wide interval around the maximum Acceptor emission wavelength in the Acceptor channel for $A3$ and in the FRET channel for $A4$.

The FRET efficiency is then calculated with:

$$E = \frac{F_{FRET}^{corr}}{F_{FRET}^{corr} + F_D} \tag{4.9}$$

4.5 Single-molecule FRET measurement : set-up

4.5.1 Microscopy : techniques and characterization

I have used a TI-Eclipse microscope from Nikon equipped with an auto-focus module and a Nikon TIRF arm. During my thesis I added to the microscope different elements to perform single-molecule FRET imaging: lasers, a DualView system with different filters and dichroic mirrors, a sCMOS Camera, and I have used Metamorph Software to pilot them.

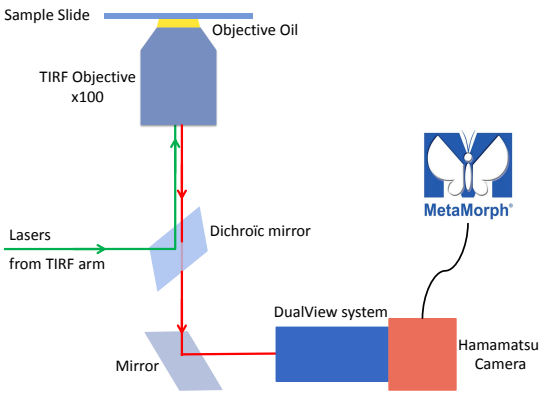

(a) General scheme of the microscope set-up.

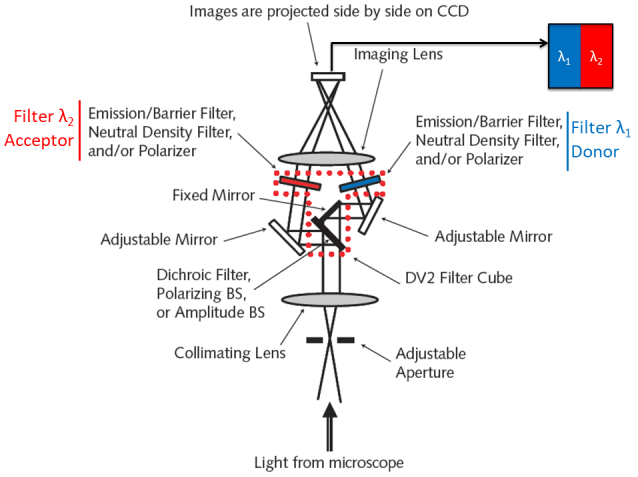

(b) Scheme of the DualView system used to visualize both the Donor and Acceptor signal on one image. Image adapted from the technote of the DualView.

Figure 4.11: Microscope set-up used for single-molecule FRET imaging.

Lasers.

The three lasers (Oxxius), 488 nm, 532 nm and 638 nm, enter the same optical fiber connected to the TIRF arm module of the microscope. The optical fiber head is adjusted to give the higher power for the three lasers out of the fiber. The lasers are controlled via a DAC (Digital to Analog Converter): thereby the laser power is controlled in voltage from 0 to 5 V by 0,01 V steps, in the software Metamorph. A microscope slide power sensor out of the objective (from Thorlabs) was used for measuring laser power (with deposition of a drop of oil on the objective). It has a large power sensor and it allowed to measure the laser power directly out of the objective. The calibration of the laser power received by the sample according to the voltage sent by the DAC is shown figure 4.12. The laser power profiles are pretty linear but at voltage close to 0 and 5 V. In this manuscript, 'power 3/5' (reads 3 out of 5) stands for the laser power at voltage 3.

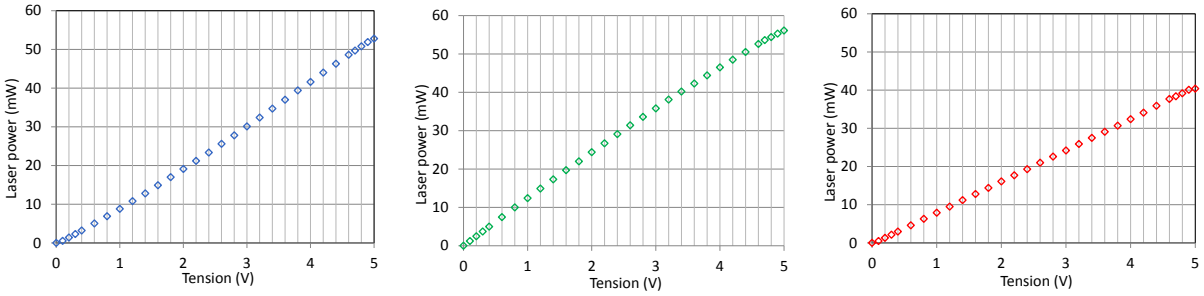

(a) Laser 488 nm. **(b)** Laser 532 nm. **(c)** Laser 638 nm.

Figure 4.12: Laser power calibration according to the voltage sent by the DAC.

Motorized TIRF arm.

The microscope is equipped with a Nikon TIRF module and an extra lens that allows to focus further the laser beam (and therefore to increase the surface power, see figure 4.13). The head of the optical fiber sets is screwed at the entrance of the module. Four screws allow to orientate properly the beam through the arm and the microscope. A fluorescent sample is visualized at the camera while setting the screws so that the illumination beam is more or less centered on the camera as shown on figure 4.13. It can be useful to reach higher surface power for single-molecule studies but in this project it was more advantageous to work with a wider and more homogeneous illumination.

TIRF microscopy is widely used for observing samples directly at the surface of the coverslip since it creates a very thin illumination field. The laser beam arrives at the coverslip with an angle greater than the critical angle for which there is total internal reflection of the beam. This creates an evanescent wave inside the sample medium. The penetration depth of this evanescent wave depends on the laser wavelength, on the refractive index of the sample medium and of the "outer medium" (oil is deposited on the objective) and on the incident angle of the beam. This microscopy technique allows the user to lower dramatically the noise coming for the sample medium by illuminating only a thin depth above the coverslip. The penetration depth depends on the incident angle and is generally around 200 nm.

The TIRF angle can be set with a manual screw for one direction and is motorized in the perpendicular direction. The manual screw was initially set to have a perpendicular beam out of the objective and then is not moved anymore. The TIRF module is connected to Metamorph which allows to control the motorized screw via the software. Since the TIRF angle depends on the laser wavelength we create different illumination settings for each laser with the required TIRF angle for each. The TIRF angles were set with a fluorescent sample: the angle is increased until no detection is possible and then decreased until the fluorescen is back and to reach an illumination as uniform as possible over the image.

Dichroic mirrors.

Initially a quadband dichroic mirror was (405-488-532-640, from Chroma) to provide high flexibility in the system and to allow to later set-up an ALEX system (Alternating Laser EXcitation). In multi-band dichroic the bandpasses are not as sharp as for single band. Therefore one single-band dichoic mirror is used in this study, for each laser: 491 nm, 532 nm and 640 nm (Chroma).

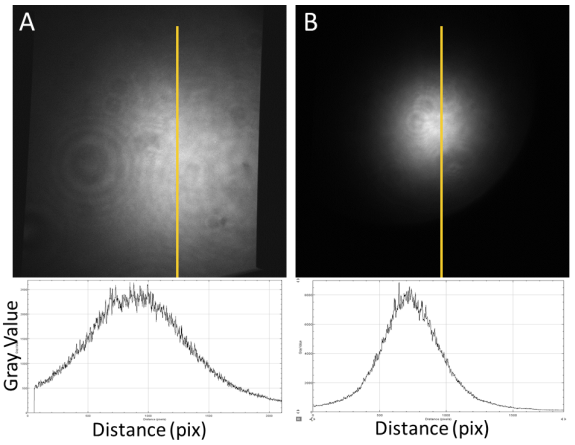

(a) Image taken with the camera **A.** without the extra lens and **B.** with the focusing lens, and intensity profiles plot along the yellow line.

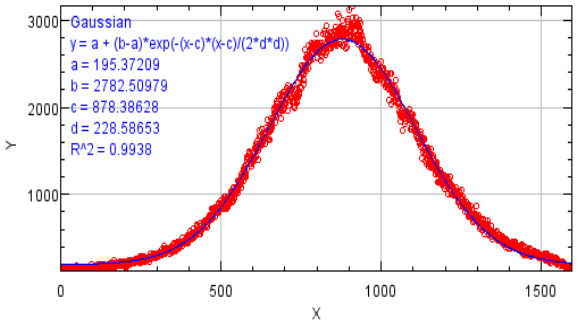

(b) Gaussian fit of laser intensity profile.

Figure 4.13: Laser profile on the camera.

Objective.

A TIRF oil objective ×100 with a high Numerical aperture equal to 1,45 is used.

DualView system and filter set.

To perform smFRET, it is necessary to observe on the same image signal coming from the Donor dye and from the Acceptor dye. It requires a DualView system which splits in two the light coming from the sample and leads it through two different filters: one for the Donor emission and one for the Acceptor emission. The DualView is positioned between the microscope and the camera. The principle of the DualView system is shown on figure 4.11b. The red dots highlight the removable part where the two filters and the dichroic mirror can be changed depending on the FRET couple that are used. The filters and dichroic mirrors are summarized on table 4.4.

Camera.

An ORCA-Flash4.0 V3 Digital CMOS camera (Hamamatsu) is used. The size of the detector is 2048×2048 pixels with a pixel size of 6,5μm. With the ×100 objective the conversion: 1 pix = 65 nm must be used.

Using a fluorescent sample as on figure 4.13a, the laser beam width can be measured in order to calculate the surface power of the lasers. The surface power is the laser power divided by the surface of the laser beam on the sample. Measuring the surface power and optimizing it is crucial in single molecule studies. For single molecule observation, not only a high laser power is required but also the way the laser beam distributes in the focal plane matters.

Fluorescent dye	Donor or Acceptor	Laser (nm)	DM in the microscope (nm)	DM in the DV (nm)	Emission filter in the DV (nm)
Alexa488	Donor	488	491	633	525/30
sCy3	Donor	532	532	633	593/40
sCy5	Acceptor	638	640	633	684/24

Table 4.4: Filter set for each fluorescent dye used as a Donor or an Acceptor in the DualView system (DV). DM stands for Dichroic Mirror.

For each laser, the beam profile is measured with the camera (without and with the extra lens) and the intensity profile along two lines is plotted: a vertical and a horizontal lines. The intensity profiles can be fit by a gaussian $y = a + (b - a) \times e^{-(x-c)^2/(2d^2)}$ as shown on figure 4.13b (where a, b, c and d are the fitting parameters). The full width at half maximum is calculated by $\Delta x = 2 \times \sqrt{2ln(2)} \times d$. For each laser we then get Δx_h for the horizontal profile and Δx_v for the vertical profile, and we calculate the average $\Delta x_m = (\Delta x_h + \Delta x_v)/2$. Since the profile is Gaussian 68% of the total laser power are collected in the disk of diameter Δx_m (the integral of a gaussian function at its full width at half maximum is equal to 68% of its total integral). The final surface power is given by:

$$P_s = \frac{68}{100} \frac{P_{laser}}{\pi(\Delta x_m/2)^2}. \tag{4.10}$$

P_{laser} is taken equal to the maximum laser power measured (i.e. at voltage 5/5) and thus provides us with the maximum surface power we can reach. Table 4.5 shows the surface power measured for the three lasers with and without the lens. The focusing lens increases the surface power by 4.

Acquisition Software.

All the devices (lasers via the DAC, microscope, motorized stage and camera) are controlled in Metamorph. Writing journals allows automatization for a systematic acquisition of data (both snapshots and movies) over the full surface of the sample. The settings used for acquisition will be summarized later in part 4.5.3.

Laser (nm)	488		532		638	
	No lens	With lens	No lens	With lens	No lens	With lens
Δx_m (μm)	68,6	33,6	58,6	35,1	58,9	32,0
P_s (kW.cm^{-2})	0,97	4,04	1,42	3,94	1,01	3,41

Table 4.5: Surface power measurement. P_s values are calculated with the maximum power of each laser (voltage 5/5) : $P_{488} = 52,8$ mW, $P_{532} = 56,1$ mW and $P_{638} = 40,4$ mW

4.5.2 Oxygen Scavenging system

Photostability of fluorescent dyes can be greatly improved using an oxygen scavenging cocktail. It prevents from fast photo-bleaching and can lower blinking that are due to oxygen solubilized in the sample buffer (Aitken et al. [2008]). The oxygen scavenger system consists of 4 mg/mL D-glucose (Sigma), 1 mg/mL glucose oxidase (Sigma) and 0,04 mg/mL catalase (from bovine liver, MP Biomedicals) (Selvin and Ha [2008]). The chemical reaction is depicted on figure 4.14. Two molecules of D-glucose react with two molecules of dioxygen and glucose oxidase in presence of catalase and the total reaction consumes one molecule of dioxygen.

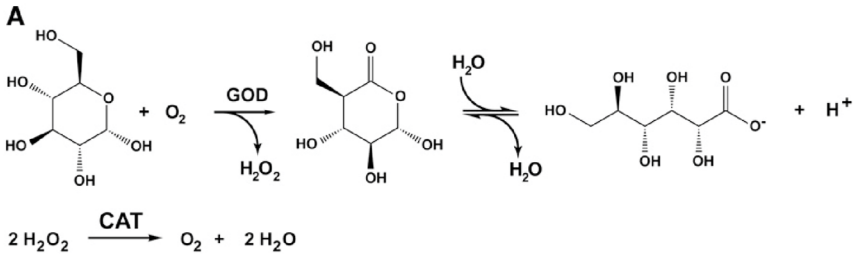

Figure 4.14: Oxygen scavenger chemical reaction. Image from Aitken et al. [2008]. A molecule of D-glucose reacts with dioxygen in presence of glucose oxidase (GOD) which releases a molecule of H_2O_2. 2 molecules of H_2O_2 react with catalase (CAT) to release a molecule of dioxygen. The total reaction consumes one molecule of dioxygen.

This oxygen scavenger is complemented with Trolox (Sigma), a triple-state quencher which further improves the photostability of the dyes. Trolox is added at a final concentration higher than 0,5 mM (better higher than 1 mM). The oxygen scavenger solution is always prepared at the last minute before the observation at the microscope and is kept in dark on ice in a closed vial. The solution can also contain ATP or other reagents that are necessary for the experiment.

Stock of buffer A×2 at 8 mg/mL D-glucose.

A stock of buffer A×2 additionned with D-glucose can be prepared in advance since it can be stored long term at -20^{o}C. The composition of the buffer A×2 is: 100 mM of MOPS pH betwen 7.5 and 8.0 (Oxygen Scavenger reaction generates acid so it is important to buffer the solution), 300 mM NaCl, (2 mM $MgCl_2$ to work with ATP), 8 mg/mL D-glucose. The solution is filtered with 0,2 μm pore size filter, aliquoted at 1 mL and kept at -20^{o}C.

Stock of "gloxy" solution.

A mixture of catalase and glucose oxydase is prepared: it is the "gloxy" ×100 stock solution. The catalase is diluted in buffer A (50 mM MOPS, 150 mM NaCl) to a final volume of 100 μL. 10 mg of glucose oxydase is added to the solution and we mix by tapping (no vortexing). We centrifuge 1min and collect the supernatant which can be stored at 4^{o}C up to several months.

Stock of Trolox.

A Trolox stock solution is prepared at more than 1 mM. 40 mg of Trolox are dissolved in 10 mL of ultra-pure water. The solution is vortexed for several minutes (it is hard to fully solubilize the powder). We filter with a 0,2 μm syringe filter. We measure the absorption at 290 nm (ϵ = 2350 $M^{-1}.cm^{-1}$) and use the Beer Lambert law to estimate the concentration. pH is adjusted to 7.5 with NaOH. We filter again at 0,2 μm and we store the solution in the dark at 4^{o}C up to two weeks.

4.5.3 smFRET acquisition settings

The data acquisition for smFRET is done mainly in two different ways: a) by taking sequential snapshots with long exposure time t_{exp} at λ_{Donor} and at $\lambda_{Acceptor}$, b) by acquiring movies at shorter exposure time at λ_{Donor} (see figure 4.15). In both cases an area on the detector of 300×2048 pix^2 is selected and centered on the maximum of the laser profile. Journals in Metamorph allow to take many different snapshots and to record movies while scanning the sample.

The snapshots taken at λ_{Donor} and at $\lambda_{Acceptor}$ between 150 and 250 ms exposure time allow to select data points corresponding to molecules with both a Donor and an Acceptor dyes and to measure the FRET signal for these pairs. The intensities and thus the FRET efficiency are averaged values over t_{exp}. However with these data the bleaching of the molecules cannot be detected. We can vary the laser power or the exposure time to limit

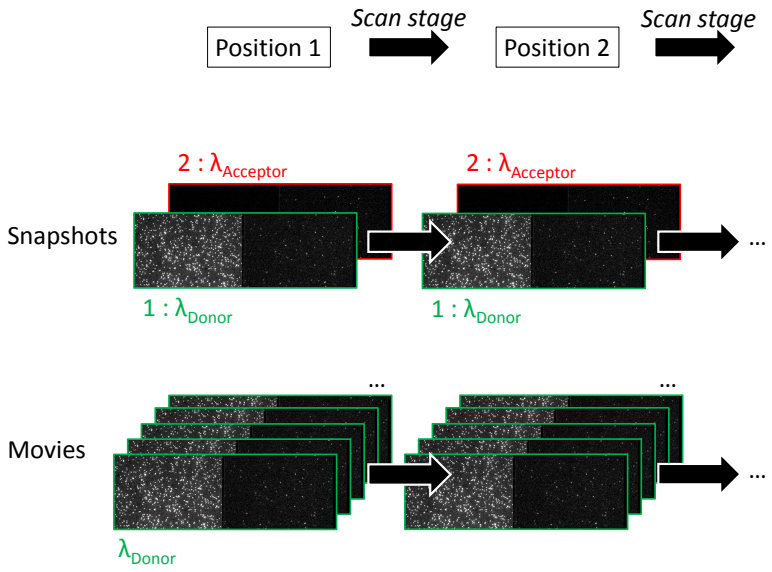

Figure 4.15: Scheme of our two acquisition methods.

the bleaching of molecules: it appears that the laser power has greater influence on the bleaching. At 150 ms exposure time and laser power 3/5 there are still more than 70% of fluorescent molecules after the snapshot acquisition. These data will later be referred to as "Snapshots data".

The movies taken at λ_{Donor} with a 50 ms exposure time allows us to observe traces, to detect bleaching events and to identify clear FRET signature. I generally record 100 images per movie. These data will later be referred to as "Movies data".

100 images of an empty observation chamber were also systematically recorded in the same acquisition conditions (laser power and exposure time).They are averaged in order to subtract the background from the images.

Table 4.6 summarizes the different settings used for both acquisition types.

4.5.4 Calibration with DNA samples.

The double stranded DNA used for calibration was presented in part 4.4.

The FRET calibration was done in three steps. We first checked the FRET efficiency in bulk for all the samples with fluorescence spectroscopy, presented in part 4.4.3.

The samples were also observed in bulk with our microscope to have a rough idea of the FRET efficiency changes in our experimental conditions. Practically, a drop of concentrated DNA solution (500 nM) is deposited on a glass coverslip and images of the bulk are taken at 50 ms exposure time with the following illumination conditions:

Type	Exposure time (ms)	Laser λ_{Donor} (nm) and power	Laser $\lambda_{Acceptor}$ (nm) and power
Snapshots	150	488 or 532 3/5	638 3/5
Movies	50	488 or 532 3/5 or 4/5	×

Table 4.6: Acquisition parameters used for smFRET studies (double-stranded DNA calibration and BmrA observation).

- for Alexa488: laser 488 nm at power 1/5,
- for sCy3: laser 532 nm at power 0,5/5,
- for TMR: laser 532 nm at power 1/5,
- for sCy5: laser 638 nm at power 0,5/5.

For each sample I take one image at the Donor excitation wavelength and one at the Acceptor wavelength. We calculate the FRET efficiency by averaging the intensity of the Donor and FRET channels :

$$E = \frac{I_{FRET}^{avg}}{I_{FRET}^{avg} + I_{D}^{avg}}. \tag{4.11}$$

We also observe in the bulk samples with Donor only and Acceptor only so that we can correct the FRET efficiency from the Donor leakage and the Acceptor direct excitation (this is explained in part 4.4.3). Note that this experiment was done early in my PhD without Oxygen Scavenger solution.

Finally, the DNA samples were observed with a single molecule detection by anchoring them on glass surface as explained in part 4.3.2. The acquisition was done with the exact same parameters we used for BmrA and that are summarized in paragraph 4.5.3.

4.6 Single-molecule FRET measurement : analysis

All the analysis are performed under Matlab and imageJ for background subtraction.

4.6.1 Preliminary image treatment

Before analyzing the FRET signal the background is subtracted from all the images. 125 snapshots are generally acquired for each sample, corresponding to 7000-30000 single molecule data points (depending on the concentration of liposomes). Between 25 and 40% of these data points are doubly-labelled proteins (with both Donor and Acceptor). A 100 movies are generally acquired for each sample.

As explained in part 4.5.3 100 images of an empty observation chamber are taken and averaged. This creates the background image that is subtracted from all the other data.

4.6.2 Efficiency and Stochiometry

From the intensities of the Donor and Acceptor excited at λ_{Donor} (I_D and I_F) and of the Acceptor excited at $\lambda_{Acceptor}$ (I_A) of each data point, two values are calculated: the Efficiency (E) also called proximity ratio and the Stochiometry (S) with the following equations

$$E = \frac{I_F}{I_D + I_F}, \tag{4.12}$$

$$S = \frac{I_D + I_F}{I_D + I_F + I_A}. \tag{4.13}$$

The efficiency provides information about the energy transfer between the dyes and thus about the protein conformation. The stochiometry provides information about the labelling of the protein: "Donor only" exhibit S $\sim$ 1 (higher than 0,8 roughly), "Acceptor only" give S $\sim$ 0 (lower than 0,3 roughly) and doubly labelled objects are in-between.

For the "Snapshots" data, acquisition is made in the Donor, FRET and Acceptor channels. Therefore both FRET efficiency E and stochiometry S can be measured for each data point. Stochiometry allows to select the efficiency values of population of interest: doubly labelled or Donor only. $S = 0,8$ is the limit value used to discriminate between these two populations (see part 5.3.3 for details).

For the "Movies" data, only signal in Donor and FRET channels is acquired. It is not possible to discriminate between the "Donor only" and the "doubly labelled" populations by using S. However we have a signal resolved in time and therefore E is measured over time for each data point. Two histograms are plotted: (i) one collecting all the instantaneous E values at every time point and (ii) the time-averaged E value, E_{mean}, for each

particle.

4.6.3 Corrections on E and S

Being quantitative requires to correct these raw values of E and S. Several corrections are made: the detection correction (with the factor γ), the Donor leakage in the FRET channel (with the correction factor α) and the direct excitation of the Acceptor at λ_{Donor} (with the correction factor β).

Detection correction factor γ.

The factor γ compares the quantum yield of the Donor and Acceptor fluorophores (ϕ_D and ϕ_A) and the difference in the detection efficiencies of Donor and Acceptor emission channels (η_{Dem} and η_{Aem}):

$$\gamma = \frac{\phi_A \eta_{Aem}}{\phi_D \eta_{Dem}}. \tag{4.14}$$

γ is hard to determined experimentally and is here taken equal to 1. Different methods exist with the ALEX system or with single-color excitation system (articles Lee et al 2005 and Ha et al 1999).

Donor leakage correction factor α.

The factor α is measured with Donor only (Do) labelled proteins with the same acquisition conditions at λ_{Donor} using the formula

$$\alpha = \frac{I_F^{Do}}{I_D^{Do}} \tag{4.15}$$

where I_F^{Do} and I_D^{Do} are the intensities of the Donor only respectively in the FRET and in the Donor channels when exciting at λ_{Donor}.

With two-color systems, α can also be determined with the Efficiency/Stochiometry graph by selecting the population of Donor only (high S). The efficiency histogram is centered on mean value $\langle E^{Do} \rangle$ (between 0,05 and 0,1 usually) and α is calculated with

$$\alpha = \frac{\langle E^{Do} \rangle}{1 - \langle E^{Do} \rangle}. \tag{4.16}$$

Acceptor direct excitation correction factor β.

The factor β is measured with Acceptor only (Ao) labelled proteins with the same

acquisition conditions at λ_{Donor} and $\lambda_{Acceptor}$ using the formula

$$\beta = \frac{I_F^{Ao}}{I_A^{Ao}}. \tag{4.17}$$

where I_F^{Ao} is the intensity of the Acceptor only in the FRET channel when exciting at λ_{Donor} and I_A^{Ao} is the intensity of the Acceptor only in the Acceptor channel when exciting at $\lambda_{Acceptor}$.

With two-color systems, β can also be determined with the Efficiency/Stochiometry graph by selecting the population of Acceptor only (low S). The stochiometry histogram is centered on mean value $\langle S^{Ao} \rangle$ and β is calculated with

$$\beta = \frac{\langle S^{Ao} \rangle}{1 - \langle S^{Ao} \rangle}. \tag{4.18}$$

Corrected FRET intensity.

The intensity I_F measured at λ_{Donor} in the FRET channel is the sum of three contributions: the real FRET signal I_F^{corr}, the leakage of the Donor dye and the direct excitation of the Acceptor dye at λ_{Donor}. We can then calculate I_F^{corr} by

$$I_F^{corr} = I_F - \alpha \times I_D - \beta \times I_A. \tag{4.19}$$

This value I_F^{corr} is then used to calculate the FRET efficiency E and stochiometry S.

With a one-color excitation system we do not have access to I_A for every particle and we cannot correct for the direct excitation of the Acceptor.

In our study we systematically correct from the Donor leakage but we could not correct from the Acceptor direct excitation (see part 5.3 in next chapter).

4.6.4 iSMS software

The smFRET data are analysed with the software iSMS developed in the group of Victoria Birkedal (Single-molecule Biophotonics group, Aarhus University), available in Matlab (Hildebrandt et al. [2015]). I summarize in this paragraph the main steps of analysis for the different kinds of dataset acquired. In all cases the selection of a Region Of Interest (ROI) is the same. The images taken with the DualView system are shared in two: the left part is the Donor channel (the light is collected through the Donor emission wavelength filter) and the right part is the Acceptor channel (the light is collected through the Acceptor emission wavelength filter). A square is selected in the Donor channel. The same size frame is automatically drawn in the Acceptor channel. These ROI are selected

in the center of each channel to get closer to an homogeneous illumination area (still not perfect because of the gaussian profile). The ROI in the Donor channel is aligned with the square in the Acceptor channel in order to have co-localization of Donor and Acceptor data points. Since this alignment can be hard on FRET data I did a calibration by using fluorescent beads and I used these images to align systematically the Donor and Acceptor signals.

Analysis of the "Snapshots" data.

I select the *excitation scheme*: "Alternating Laser EXcitation (ALEX)". We define the peak thresholds for Donor and Acceptor (the values 100 for D and 130 for A are suitable for the "Snapshots" data) and then the program automatically finds the Donor and the Acceptor points and associates them in pairs (with a maximum peak separation of 3pix). In the *Peak-finder settings* two options exist:

- "Put a D at every A position", this option allows to detect high FRET or Acceptor only data points,

- "Put an A at every D position", this option allows to detect low FRET or Donor only data points.

When no option is selected, only points detected as pairs of a Donor and an Acceptor are considered. When selecting both options, all the possible populations are taken into account: doubly-labelled proteins, Donor only, and Acceptor only, which can then be discriminated by calculating the Stochiometry (see the definitions in part 4.6.2).

We have access to the intensities of each data point in the different channels: Donor, FRET and Acceptor, in a new window (*FRET Pairs Window*). The data are saved for each FRET pair as a table containing among other: the pair position on the image, the mask used for measuring the intensities, the Donor, FRET and Acceptor intensities, the Efficiency and Stochiometry values.

The Efficiency and Stochiometry histogram are plotted in a new window in iSMS (*S-E Histogram Window*) and it is then possible to make a specific data selection, for instance plotting the FRET Efficiencies corresponding to a Stochiometry between 0,3 and 0,7 (corresponding to doubly labelled molecules). This is a useful tool to select the different populations as explained in part 4.6.2.

For most of the histograms presented in this thesis I wrote a Matlab program to plot, select and correct the data (see 4.6.3).

Analysis of the "Movies" data.

I select the *excitation scheme*: "Single color Excitation". In this case, we have measured the signals of Donor and FRET channels only. We do not have access to the Acceptor positions and intensities and therefore we do not measure Stochiometry. For this analysis I select the option "Put an A at every D position" so that we do not miss low FRET data. We use a lower Donor peak threshold here (40) and we plot the data point traces (in *FRET Pairs Window*). We have traces in time for the Donor and the FRET signal as shown on figure 4.16. At this step I operate manually a selection of the data:

- I eliminate the traces with several bleaching steps showing this is not single molecule,
- I set the time intervals of the blinking and bleaching events with the software dedicated function (on figure 4.16b, the blinking time appears as a dark green colored interval, and the bleaching time is colored in light green for Donor and light red for Acceptor as shown on figures 4.16),
- these data as saved as a single file, containing data from Donor only proteins and from doubly labelled proteins,
- I then select only the traces that present a clear FRET signature (Donor intensity increases as Acceptor gets bleached, as shown on figures 4.16c and 4.16d),
- these data are saved as a separate file, containing only data from proteins with a FRET signal.

With this selection we can discriminate the FRET efficiency which comes from the Donor only population (an example is shown on figure 4.16a) and the one of the FRET pairs. The data are saved again as a table which contains the bleaching and blinking times previously defined manually in the software. I wrote a Matlab code to calculate FRET efficiency at every time point out of the blinking and bleaching intervals, and I can plot, select and correct the data (see 4.6.3).

Note that all the histograms plotted in this work are normalized.

(a) Traces of a Donor only protein.

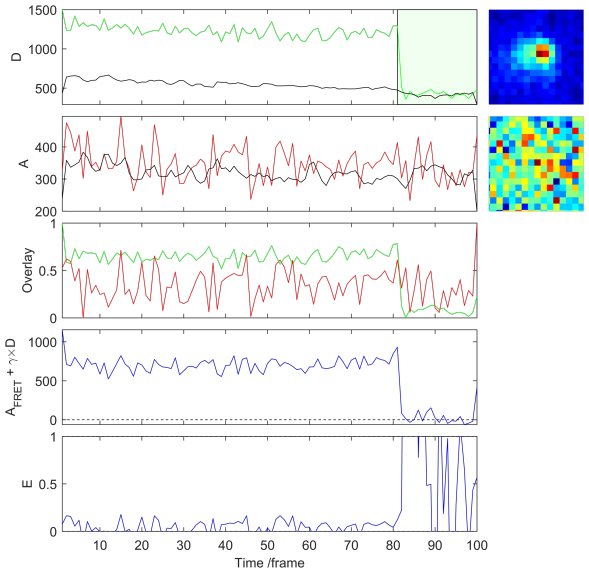

(b) Traces of a dye exhibiting blinking.

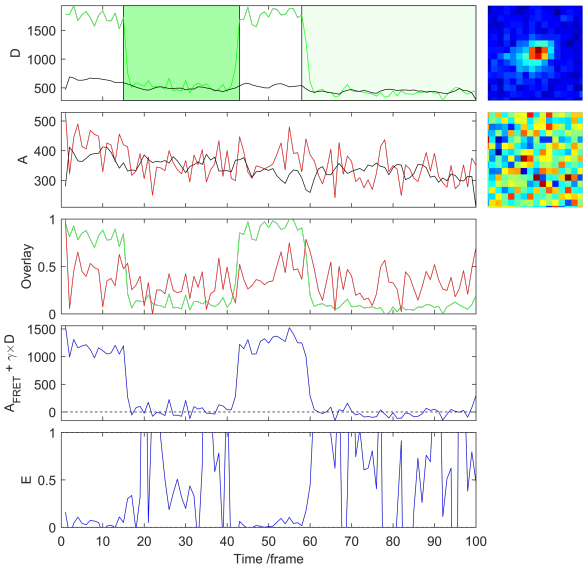

(c) Traces of a doubly labelled protein exhibiting a clear FRET signature.

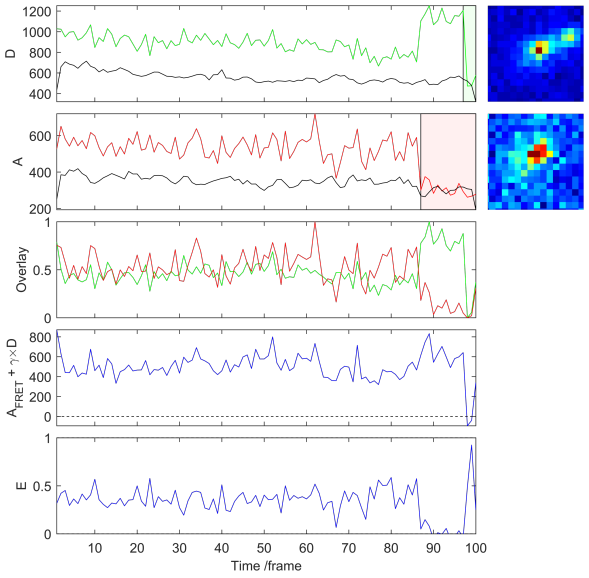

(d) Traces of a doubly labelled protein exhibiting a clear FRET signature.

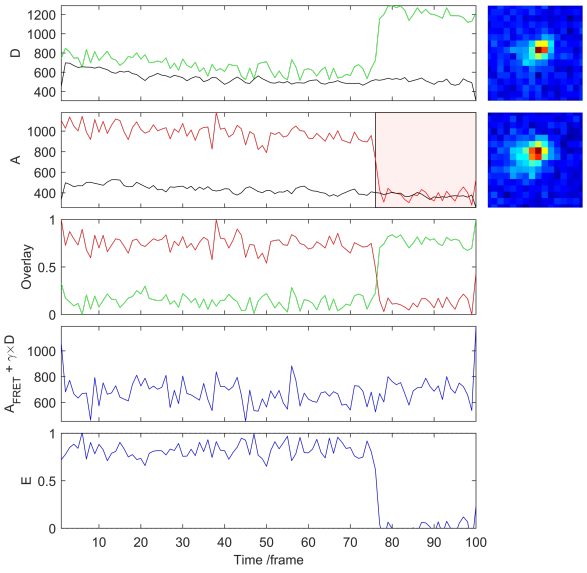

Figure 4.16: Example of traces obtained with the software iSMS for a movie. In all cases presented, the traces plotted are (from top to bottom) : the Donor intensity (D), the FRET intensity (A), the overlay of normalized traces, the sum of intensities A+D (here the correction factor $\gamma = 1$) and the FRET efficiency (E). The black curves show the background level. The small images on the right show the data point in the Donor and Acceptor channels. On the x-axis : 1 frame = 50 ms. The dark green box shows a blinking interval of the Donor dye. The light green and red box show the bleaching event respectively for the Donor and the Acceptor.

Chapter 5

Results

5.1 Surface characterization

We have performed TIRF experiments on single BmrA proteins incorporated in small liposomes, tethered to a glass surface. Before detailing the FRET results, several issues had to be tackled concerning the glass surfaces and the interaction of liposomes with them.

5.1.1 Cleaning process

Importantly, FRET studies at the single-molecule scale require very clean glass coverslips to avoid any contamination of the FRET signal. Indeed, the signal from fluorescent contaminants is often similar to that of the molecules of interest, as shown on figure 5.1a.

Several protocols (detailed in 4.3) have been tested for cleaning the glass coverslips. After the surface was treated with PEG-silane, neutravidin and β-casein, no pollution was visible for excitation wavelengths 488 nm and 638 nm (figures B.1a, B.1b and B.1d are shown in appendix B part B.1). Same imaging settings were used as for the samples containing FRET couples Alexa488/sCy5 and sCy3/sCy5.

However, some contamination dots remain visible on the surface at excitation 532 nm. We put efforts at improving the protocol to limit them but we could not totally get rid of them. However these fluorescent contaminants are observed only in the Donor channel (figure 5.1b) and not in the FRET channel (figure 5.1c, indicating that FRET signal does not get polluted.

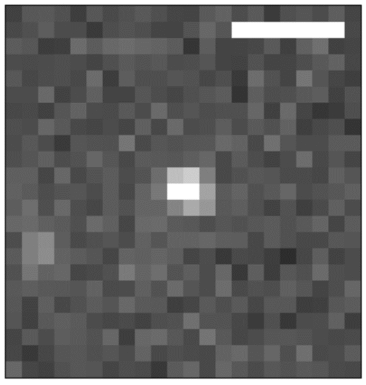

(a) Fluorescent contaminant observed at excitation wavelength 532 nm. Scale bar = 1 μm.

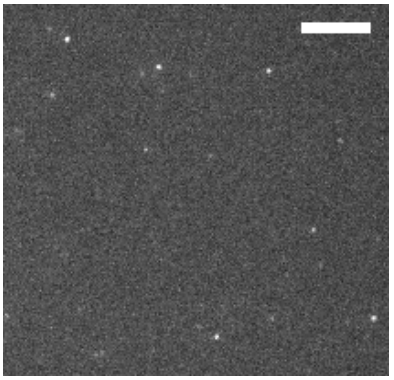

(b) Donor channel. Scale bar = 5 μm.

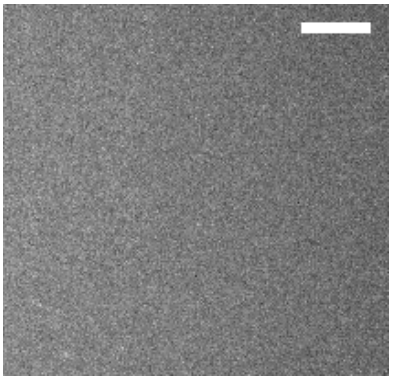

(c) FRET channel. Scale bar = 5 μm.

Figure 5.1: Fluorescent contamination on glass surface. An empty chamber is observed after surface cleaning and treatment protocols have been completed. Images are taken at 532 nm excitation wavelength with laser power 4/5 at 250 ms exposure time with the filter set for the FRET couple sCy3/sCy5 (see table 4.4).

5.1.2 Specificity of DNA and liposomes attachment

The anchoring of samples on glass surfaces is carefully tested whether it is specific or not. To do so, samples are incubated on coverslips that are not treated with neutravidin (the other treatment steps are similar). This control was done for all the different samples studied: DNA strands and small liposomes.

Attachment specificity of DNA.

DNA is anchored on neutravidin coated surface in a specific manner as shown on figure 5.2. A few dots remain when the surface is not coated with neutravidin, but the specificity is very satisfying. The average number of points per image (averaged on 10 images) is: 495 on neutravidin-coated surfaces and 27 on neutravidin-free surfaces. It represents 5% of non specific DNA strands attached on the surface per image.

Note that the concentration of DNA used here is 50 pM but image 5.2b shows that it leads to a high points density. For single-molecule observation, concentration will be decreased down to 30 pM with shorter incubation time in order to better distinguish single dots.

Attachment specificity of liposomes.

The attachment of the liposomes is also found to be very specific, as shown on figure

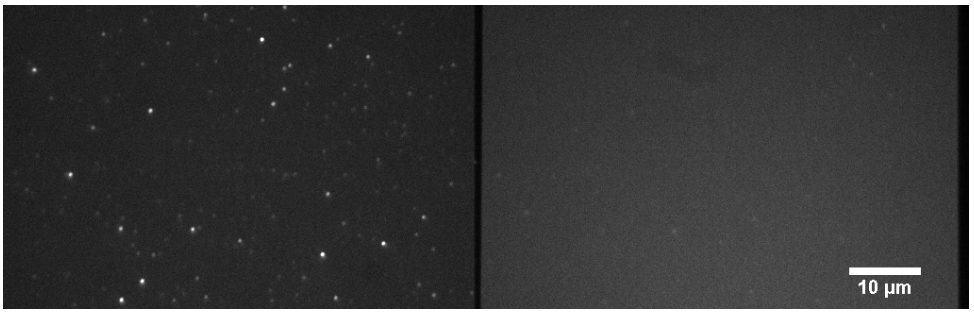

(a) Surface without neutravidin incubated with 50 pM DNA and rinsed.

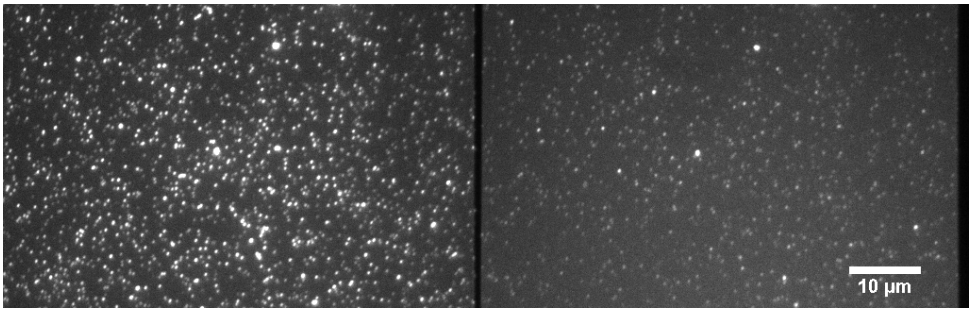

(b) Surface with neutravidin incubated with 50 pM DNA and rinsed.

Figure 5.2: DNA specific attachment. The DNA sample used here is Up sCy3/ Down sCy5 with distance 12 bp. Images are taken with laser 532 nm power 4/5 at 250 ms exposure time with the filter set for the FRET couple sCy3/sCy5 (see table 4.4). Left half is the Donor channel, right is the FRET channel.

5.3. The sample used here consists of *E.coli* liposomes containing DHPE Texas-Red lipids. Texas-Red maximum excitation wavelength is 594 nm. As the microscope is not equipped with the corresponding laser, 532 nm wavelength laser is used. Regarding the spectrum width of Texas-Red and the high concentration of dye used, this laser is suitable to visualize the liposomes with a good signal. We can see on image 5.3a that very few dots are left when we incubate the liposomes on non neutravidin-coated surface. The average number of dots per image (averaged on 10 images) is: 86,2 on neutravidin-coated surfaces and 0,3 on neutravidin-free surfaces. It represents 0,3% of non specific attachement on the surface, which is very low.

A range of neutravidin concentration was tested (on a surface coated with 1% of Biotin-PEG-silane) in order to count the number of liposomes attached to the surface. Figure 5.3c shows the number of liposomes (averaged over 20 images) for neutravidin concentration from 0 to 20 μg/mL. Note that this experiment was done in different conditions as compared to figures 5.3a and 5.3b (density of liposomes cannot be compared). The number of liposomes decreases when lowering the concentration of neutravidin, consistent with a specific attachment of the vesicles. Neutravidin concentration 20 μg/mL is chosen for single-molecule studies since the vesicles are numerous and distinguishable in this condition.

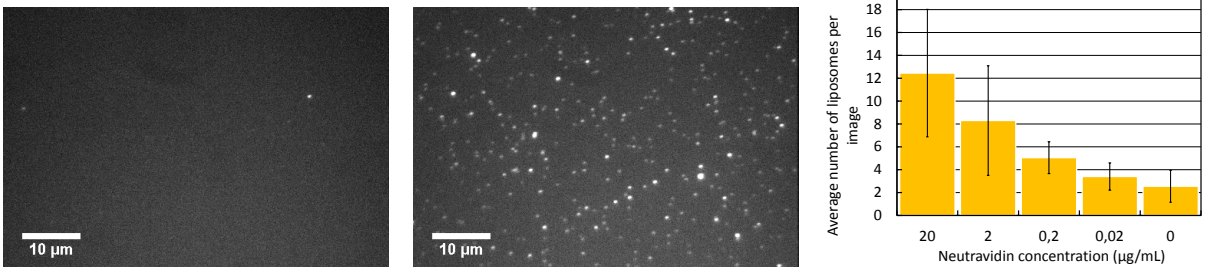

(a) Surface without neutravidin incubated with Texas-Red liposomes (concentration 2×10^{-3} mg/mL of lipids) and rinsed.

(b) Surface with neutravidin incubated with Texas-Red liposomes (concentration 2×10^{-3} mg/mL of lipids) and rinsed.

(c) Liposomes counting on surfaces incubated with 1% of Biotin-PEG-silane and different neutravidin concentrations (from 0 to 20 μg/mL).

Figure 5.3: Liposomes specific attachment. The *E.coli* liposomes contain DHPE Texas-Red lipids that allow us to visualize them at 532 nm at 100 ms exposure time. Quantification on figure 5.3c is done on 20 images per condition.

Liposomes' integrity preservation.

Strong adhesion of vesicles to a surface can lead to their rupture (Bernard et al. [2000]). In fact, this property is widely used to form supported lipid bilayers from fusing small liposomes to a subtrate (Keller et al. [2000]). Therefore, the next test to be done was checking whether the vesicles remain intact after binding to the neutravidin-coated glass. Two different dyes were used: Texas-Red lipids to detect the membrane of vesicles and soluble pyranine (green dye) in the inner volume of vesicles to check for their rupture (see part 4.3.3). If co-localisation of pyranine and Texas-Red signals is observed, then the liposomes are not damaged. Not observing pyranine indicates the membrane opens when in contact with the surface and releases the soluble fluorophore. Images were taken for the pyranine and for the Texas-Red signals and the amount of intact liposomes was measured.

Figure 5.4a shows the number of "membrane" (in Red) and the number of "internal volume" (in Green) data points (averaged over 20 images). Different concentrations of biotin-PEG-silane in the PEG-passivated surface were tested (0, 1, 2,5 and 10%). The concentration of neutravidin was 50 μg/mL. The number of vesicles per image is quasi-constant when varying the biotin fraction between 10% and 1% suggesting that the surface is already saturated with liposomes at 1%. The amount of vesicles drops for 0% of biotin-PEG-silane, consistent with specific attachment.

The percentage of intact vesicles, calculated as the ratio between the number of pyranine points and the number of Texas-Red points, is shown on figure 5.4b. The fraction of

intact liposomes increases as the percentage of Biotin decreases (see figure 5.4b). Interestingly, for 0% of biotin, a very low density of liposomes is observed but nearly 90% of them are intact.

It has been shown in Bernard et al. [2000] that the interaction strength between the membrane and the surface depends on the lipid composition (presence of negatively charged lipids for instance) and on the surface coating. The interaction strength, if too high, can lead to membrane rupture. Our results are consistent since increasing the concentration of biotin on the surface leads to a higher number of links (i.e. biotins) between the liposomes and the surface. Therefore, this explains why the interaction strength between the vesicles and the surface, and the fraction of membrane rupture both increase with biotin fraction (figure 5.4b).

1% of biotin fraction provides with over 80% of intact vesicles and therefore was used for the final protocol.

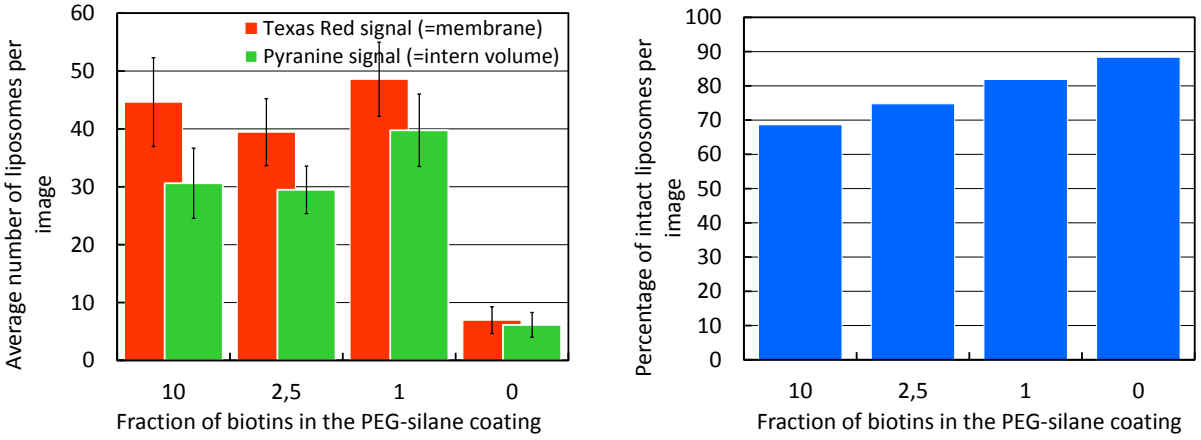

(a) Average number of Texas-Red dots and pyranine dots per image.

(b) Fraction of intact liposomes per image.

Figure 5.4: Liposomes' integrity conservation. Small liposomes are reconstituted with DHPE Texas-Red, allowing to visualize membrane, and pyranine soluble dye, allowing to detect vesicles' inner volume. One dot in Texas-Red signal is counted as one liposome. Co-localisation with pyranine signal indicates an intact liposome. Fraction of intact liposomes is the ratio between the number of pyranine dots and Texas-Red dots. Four fractions of biotin in the PEG-silane surface coating were tested. Quantification is done on 20 images per condition.

Part 5.1 : conclusions.

- A protocol for cleaning glass coverslips was successfully established and allows to get rid of most fluorescent contaminants on the surface.
- A protocol to anchor specifically molecules on glass coverslips was also developed: for double strand DNA (used for FRET calibration) and liposomes, by using biotin-neutravidin interaction on passivated substrate.
- Finally the liposomes remain intact up to 80% even when tethered to the surface through biotin-neutravidin interaction. This validates the cleaning and attachment protocols that have been established.

5.2 FRET calibration with DNA samples

In this part, the assessment of the FRET signal observable on the microscope and the optimization of acquisition parameters are presented. A double stranded DNA labelled with fluorescent dyes is used as described in part 4.4.1, inspired from Deniz et al. [1999]. For each dye couple, three samples were available with different interdye distances: 19, 12 and 7 base-pairs, corresponding to 66.6, 46.7 and 34.1 Å respectively. Since the energy transfer decreases with higher interdye distance, different FRET efficiencies are expected for each sample. Since the distance between Donor and Acceptor fluorophores is perfectly known, these samples allow to calibrate the system (like a "ruler") and thus to correlate the FRET efficiency to the distance between fluorophores.

The three DNA constructs have been selected in order to investigate the range of distances expected for BmrA in different conformations (see figure 5.5). The closer distance between BmrA NBDs is expected in the NBDs bound state i.e. closed conformation when the compaction is maximal. Using the model for BmrA's closed conformation (from SAV1886), the distance between the two cystein residues C436 (where the fluorophores are labelled) was measured to be 39 Å. In the apo conformation, the distance between the dyes is found around 80 Å. However the protein is expected to have some flexibility in its open conformation and a range of distances could be observed. Thus, it is crucial to have the largest possible change in FRET efficiency between 40 Å and 80 Å, and to calibrate it.

The FRET efficiency was first measured in bulk experiments (in cuvette and with TIRF microscopy), and eventually single-molecule experiments were performed with TIRF.

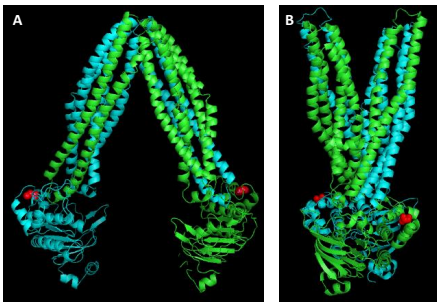

Figure 5.5: Model structure of BmrA conformations. The models are based respectively on MsbA structure (PDB: 3B5W) and SAV1886 (PDB: 2HYD). **(A)** Inward-facing or Apo conformation. **(B)** Outward-facing conformation. The red beads mark the native cysteins C436 that are used for fluorescent labelling. The distance between the two cysteins is measured on these models: 80 Å in apo and 40 Å in closed conformation.

5.2.1 Ensemble FRET measurement by fluorescence spectroscopy

Ensemble FRET was first measured in cuvette with the spectrometer (see part 4.4). Data are systematically corrected from the Donor leakage and the direct excitation of the Acceptor. Figure 5.6 shows the spectra for the couples Alexa488/sCy5, sCy3/sCy5 and TMR/sCy5. We can see that as the interdye distance decreases the FRET fluorescence F increases and the Donor fluorescence F_D decreases as expected.

	Interdye distance (Å)	Alexa488/sCy5 E_{corr}	sCy3/sCy5 E_{corr}	TMR/sCy5 E_{corr}
19 bp	66,6	0,04	0,20	0,19
12 bp	46,7	0,17	0,49	0,51
7 bp	34,1	0,49	0,83	0,72

Table 5.1: Corrected FRET efficiency measured by fluorescence spectroscopy.

The corrected FRET efficiency values are calculated with equations (4.8) and (4.9) (see part 4.4.4) and are summarized on table 5.1. We can observe clearly a trend with increasing E when distance decreases. A larger FRET efficiency change is found according to distance for the couples sCy3/sCy5 and TMR/sCy5 as compared to Alexa488/sCy5. We calculated the Förster radius for Alexa488/sCy5, found equal to $R_0 = 55$ Å. Therefore, the E values obtained at 12 bp and 7 bp are surprisingly low and were expected to be

higher than 0,5. No satisfying explanation was found for this observation. The values measured for sCy3/sCy5 and TMR/sCy5 are relevant with their Förster radius both equal to $R_0 = 53$ Å(Stein et al. [2011]; Deniz et al. [1999]). For further investigation and in order to test the microscope, the different DNA samples were observed first in ensemble and then at the single-molecule level with the corresponding excitation parameters and set of filters.

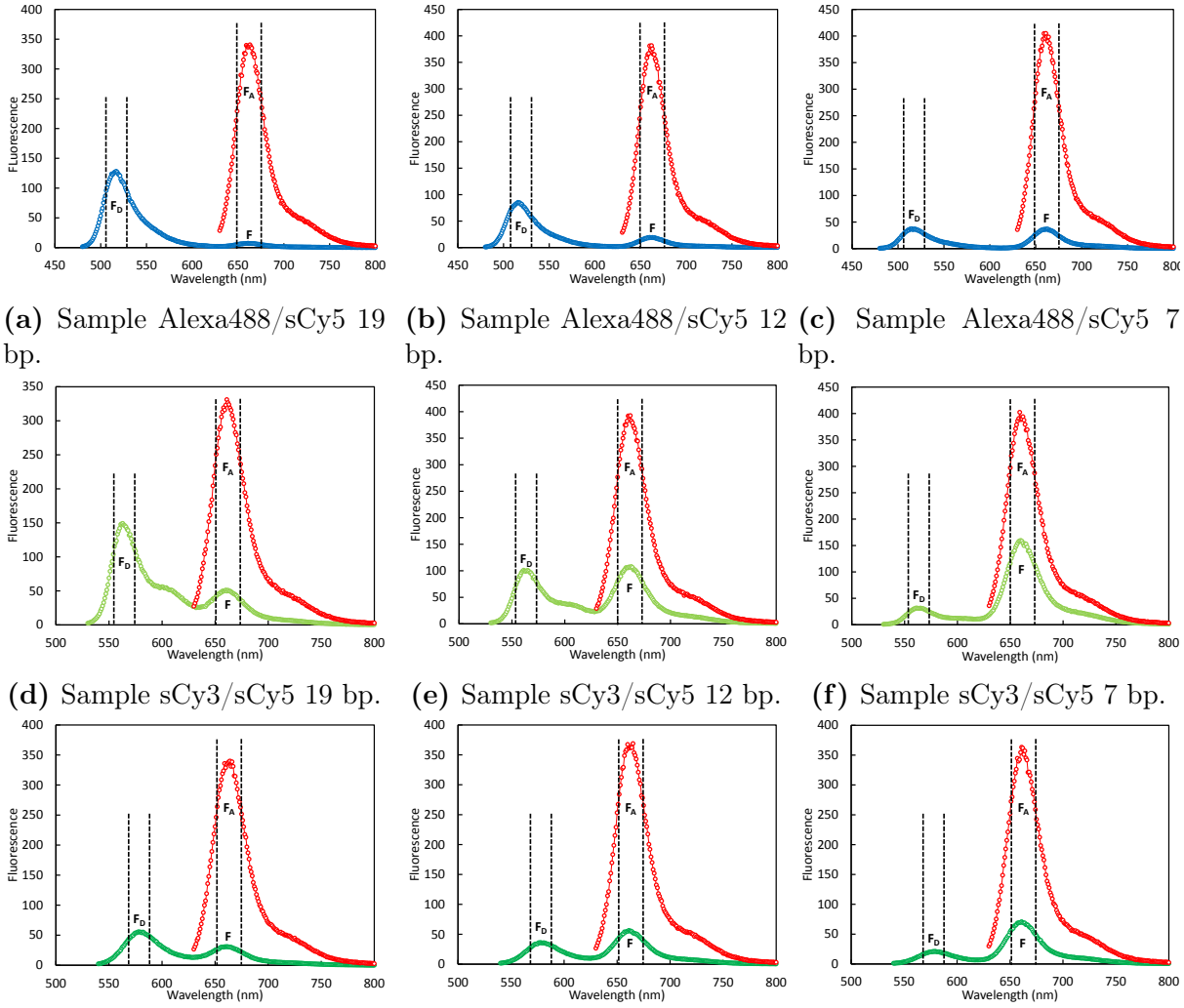

(a) Sample Alexa488/sCy5 19 bp. **(b)** Sample Alexa488/sCy5 12 bp. **(c)** Sample Alexa488/sCy5 7 bp.

(d) Sample sCy3/sCy5 19 bp. **(e)** Sample sCy3/sCy5 12 bp. **(f)** Sample sCy3/sCy5 7 bp.

(g) Sample TMR/sCy5 19 bp. **(h)** Sample TMR/sCy5 12 bp. **(i)** Sample TMR/sCy5 7 bp.

Figure 5.6: Ensemble FRET calibration for Alexa488/sCy5 (a,b,c), sCy3/sCy5 (d,e,f) and TMR/sCy5 (g,h,i). In blue, light green and dark green the respective emission spectra at Donor wavelength excitation, in red the emission spectra at Acceptor (sCy5) wavelength excitation. The corresponding interdye distance is indicated in base-pair (bp) in the graph subtitle. F_D, F and F_A are the fluorescence in the Donor, FRET and Acceptor channels respectively. They are measured by integration on a 20 nm interval around maximum emission wavelength, depicted by the dashed lines. These fluorescence values are used to calculate the corrected FRET efficiency E with equations (4.8) and (4.9) (see part 4.4.4).

5.2.2 Bulk measurement with the microscope

It took some time to fully optimize the protocol for DNA attachment to the glass substrate and the imaging conditions. Thus the DNA molecules were first observed in bulk at the microscope in order to extract averaged efficiency data. The protocol and acquisition conditions are described in part 4.4.1. Table 5.2 shows the FRET efficiency values measured with the microscope: the raw values E_{raw} and those corrected from Donor leakage and direct Acceptor excitation E_{corr}.

For the three couple of dyes we see that the FRET efficiency increases as their relative distance decreases. The values measured are noticeably different from the results with the spectrometer. This is mainly due to the use of dichroic mirrors and optical filters in the microscope that pre-select the wavelengths band detected on the camera. Values found for Alexa488/sCy5 and sCy3/sCy5 are consistent with their Förster radii although a bit low for 12 bp. The values measured for TMR/sCy5 are surprisingly low. For 7 bp they should be similar to those obtained with the other fluorophores since their R_0 are in the same range.

These preliminary FRET experiments show that we are able to detect on our microscope three different values of FRET efficiency for distinct distances. However, the FRET efficiencies found with the spectrometer and in bulk with the microscope were not taken as reference and single molecule measurements were performed to be in the same conditions as in the experiments with BmrA.

Interdye distance (Å)		Alexa488/sCy5		sCy3/sCy5		TMR/sCy5	
		E_{raw}	E_{corr}	E_{raw}	E_{corr}	E_{raw}	E_{corr}
19 bp	66,6	0,147	0,101	0,236	0,066	0,233	0,065
12 bp	46,7	0,374	0,342	0,476	0,365	0,459	0,340
7 bp	34,1	0,663	0,623	0,729	0,663	0,565	0,462

Table 5.2: FRET efficiency measured in bulk at the microscope. Raw and corrected values are shown.

5.2.3 Couple of fluorescent dyes for smFRET

The two main candidates tested to perform FRET with BmrA were the couples Alexa488/sCy5 and sCy3/sCy5. The final choice was to work with sCy3/sCy5 labelling for the physical and biochemical reasons detailed below.

As shown in part 5.1.1 protocols have been established in order to obtain very clean surfaces with a very low fraction of signal contaminants, even at 532 nm excitation. Therefore both couples were potentially suitable. However, based on the ensemble FRET calibration (see part 5.2.2), we considered that the sCy3/sCy5 couple is more interesting since it offers a larger range of efficiency E over the same interdye distance than Alexa488/sCy5 and thus, more chance to distinguish between different conformations of BmrA.

Moreover, the activity of BmrA was measured on the WT and on labelled batches to see if the activity of the protein was preserved after labelling. Table A.3 in appendix A shows the characteristics of each batch. The labelling yield was good for both couples but the protein activity was slightly better conserved with sCy3/sCy5 than for Alexa488/sCy5.

Therefore, all the final single-molecule FRET experiments and analysis were performed with sCy3/sCy5 WT BmrA in liposomes. Single molecule FRET calibration was then performed only with the DNA sample labelled with sCy3/sCy5.

5.2.4 smFRET measurement

As mentionned above, I had different issues to solve for visualizing properly the double stranded DNAs on the surface. In the first experiments, the strand "Up", which carries the biotin and the Donor dye, was detected on the surface. However the complementary strand with the Acceptor dye was not visible. One explanation is that DNAs were not properly hybridized and that the biotinylated strand was bound to the surface while the complementary strand got washed away by rincing. Another possible explanation is that the Acceptor dye quickly bleached as the oxygen-scavenger mix was not optimized yet. Without anti-bleaching solution, the photostability of sCy3 and Alexa488 is much better than that of sCy5 which bleaches very rapidly. This could explain why we were able to observe Donor signal but no Acceptor.

After optimization of the oxygen-scavenger system (see part 4.5.2), I could observe good signal in both Donor and Acceptor channels (raw images are shown in appendix B, figure B.2, where the FRET signal clearly increases when the interdye distance changes from 19 to 7 bp). Only experiments on the sCy3/sCy5 couple were performed since these

fluorophores were selected for smFRET experiments with BmrA (see part 5.2.3). Both types of data "Snapshots" and "Movies" are analyzed (see part 4.5.3 for the acquisition settings and part 4.6 for the analysis methods).

Results for the "Snapshots".

Snapshots are acquired at 150 ms exposure time with one image taken at 532 nm excitation followed by an image at 638 nm excitation wavelength. For the analysis, following the process explained in part 4.6.4, both options "put an A at every D position" and "put a D at every A position" are selected. Thereby, it provides information on every possible population: "Donor only", doubly-labelled and "Acceptor only". The efficiency values are corrected from Donor leakage (see part 4.6.2): the Donor leakage correction factor α is calculated for each sample and indicated on figure 5.7. The E histograms are fitted with a double gaussian function to measure the mean position and the width of the peaks. The quality of the gaussian fit is shown on figure 5.7d for the 12 bp DNA sample and the other fits are shown in appendix B (figure B.9 in part B.4). The values from the fits are shown on table 5.3.

	Interdye distance (Å)	Population in %		Mean position $\langle E \rangle$		Standard deviation	
Gaussian		1	2	1	2	1	2
19 bp	66,6	66,7	33,3	0,001	0,124	0,029	0,086
12 bp	46,7	59,8	40,2	0,001	0,346	0,035	0,077
7 bp	34,1	69,2	30,8	0,001	0,614	0,045	0,094

Table 5.3: FRET efficiency data from two gaussian fit, on "snapshots" data. A two gaussian fit is applied to the **corrected** E histograms. For each gaussian (i.e. peak) the table summarizes: the population (in percentage), the mean position $\langle E \rangle$ and the standard deviation.

Figure 5.7 shows the 2D efficiency (corrected) and stochiometry histograms plotted for the three interdye distances. For the three samples, a first peak centered on $\langle E \rangle = 0$ corresponding to a population of stochiometry 1 is systematically observed. This is the "Donor only" population. Interestingly we do not detect any "Acceptor only" population here (expected at $S = 0$). Practically, when hybridized, the DNA strands are labelled

with Donor and Acceptor at 1 : 1. The strand that carries the biotin, for binding to the substrate, is the "Donor" strand. Due to the passivation of the surface, "Acceptor" strand cannot bind alone, thus no "Acceptor only" signal was detected. This explains why we observed "Donor only" when the hybridization did not occur or doubly-labelled population. The two gaussian fit reveals that the proportion of "Donor only" and doubly-labelled populations are respectively 2/3 and 1/3.

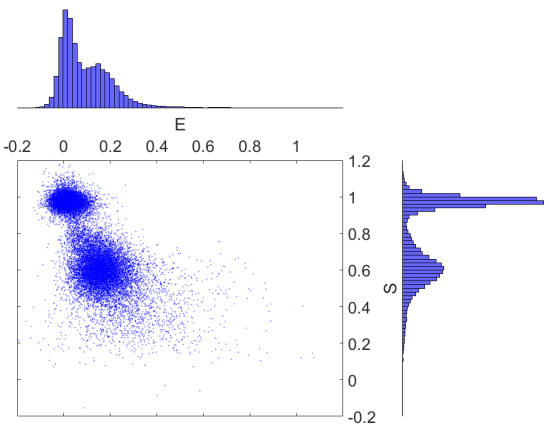

(a) Distance of 19 bp ($\alpha = 0,061$).

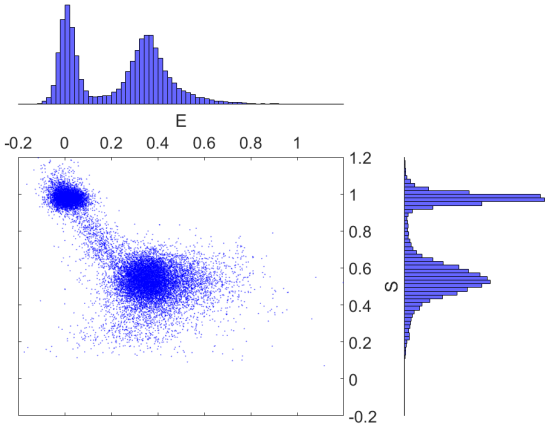

(b) Distance of 12 bp ($\alpha = 0,068$).

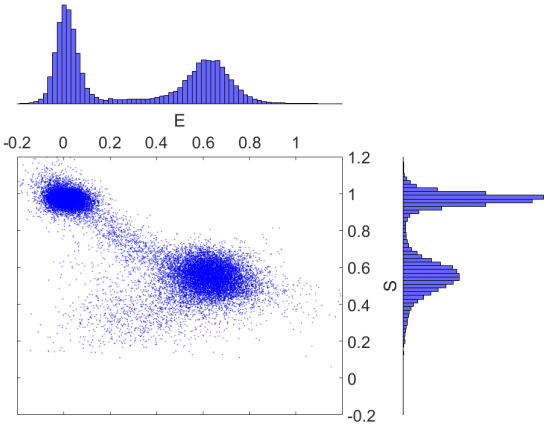

(c) Distance of 7 bp ($\alpha = 0,064$).

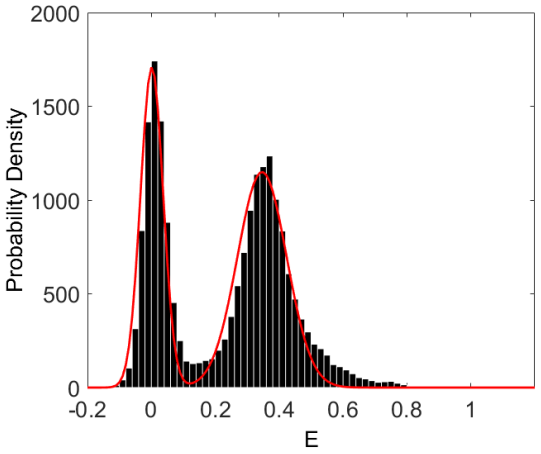

(d) E distribution for 12 bp fitted by a double gaussian.

Figure 5.7: FRET efficiency and stochiometry histograms for sCy3/sCy5 labelled DNA from "snapshots" data. Top histogram is the corrected FRET efficiency E, right histogram is the stochiometry S. The number of data points plotted is : (a) 23863 particles, (b) 19682 particles, (c) 25695 particles. Figure (d) shows the E distribution for 12 bp DNA fitted by a double gaussian.

A second population is visible with a stochiometry mean value around 0,5 or 0,6, that corresponds to the doubly-labelled DNAs. This population gives a FRET efficiency at $\langle E \rangle = 0,124$ for 19 bp distance, $\langle E \rangle = 0,346$ for 12 bp and $\langle E \rangle = 0,614$ for 7 bp (see

table 5.3). These corrected values corresponds to those found in bulk with the microscope and reported in table 5.2.

Note that there is a continuum of data points on figure 5.7 between the two clearly distinguished populations ($S = 1$ and $S = 0,5 - 0,6$). They correspond to events where the Acceptor dye bleaches or blinks during the acquisition time and thus the efficiency and stochiometry values are intermediate between both populations.

Results for the "Movies" data.

Acquiring movies should allow in principle to resolve conformational changes of BmrA with time. In order to compare later with data obtained with proteins, I recorded movies at 50 ms exposure time (20 images per second). Long lasting intensity traces can be acquired: two examples are shown on figure 5.8, proving that the oxygen-scavenging system is efficient.

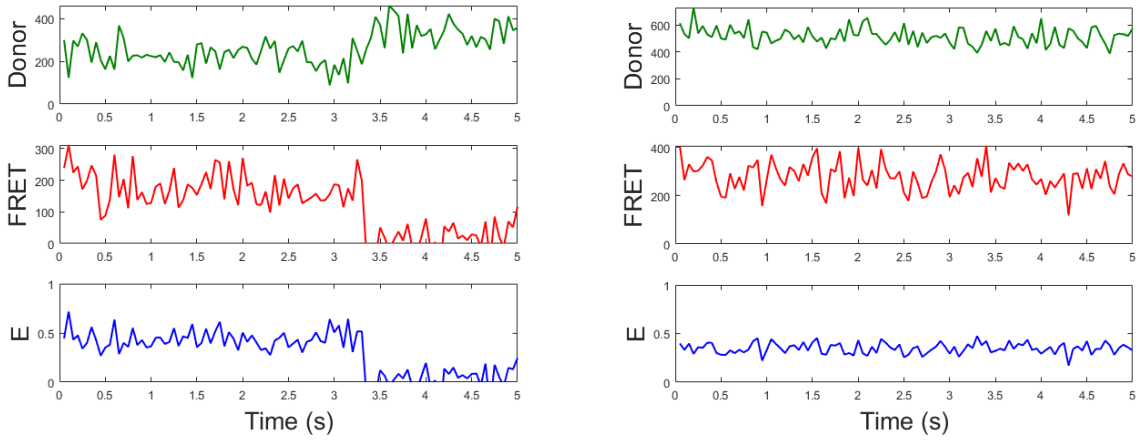

(a) Example where Acceptor bleaching event is observed. Donor intensity then increases and FRET efficiency drops to 0 at $t \sim 3,5$ s.

(b) Example of a long lasting time trace.

Figure 5.8: Time traces of Donor intensity (green), FRET intensity (red) and efficiency (blue) on sCy3/sCy5 labelled DNA (12 bp). Acquisition speed is 20 images per second.

With "movies" data, no signal is collected from the "Acceptor only" population. Donor dots are paired with corresponding dots in the FRET channel. Following the process explained in part 4.6.4, both options "put an A at every D position" and "put a D at every A position" are selected, in order not to miss the extreme cases where Donor intensity or FRET intensity is zero. Thereby, it gives access to all data points including very low or high FRET efficiencies. Bleaching and blinking intervals are set in order to retain time

points with both Donor and Acceptor emitting.

Three types of analysis were plotted:

- the distribution of all instantaneous E values for all molecules (for each molecule, about 100 values of E are recorded during the time course of the movie) (figure 5.9a, d, g);

- the distribution of all instantaneous E values limited to molecules exhibiting FRET signal (figure 5.9b, e, h);

- the distribution of time-averaged E values (E_{mean}) only for molecules exhibiting FRET signal (figure 5.9c, f, i).

All the efficiency values are corrected from Donor leakage with the correction factor $\alpha = 0,0469$ (measured from a control with "Donor only" samples, see part 5.4.1). The E and E_{mean} histograms of FRET molecules are fitted with a single gaussian function to measure the mean position and the width of the peaks. The fits are shown in appendix B (figure B.10 in part B.4) and the values from the fit are shown on table 5.4.

	Interdye distance (Å)	Mean position $\langle E \rangle$		Standard deviation	
Distribution		E	E_{mean}	E	E_{mean}
19 bp	66,6	0,148	0,131	0,114	0,029
12 bp	46,7	0,356	0,346	0,141	0,058
7 bp	34,1	0,894	0,928	0,172	0,090

Table 5.4: FRET efficiency data from one gaussian fit, on "movies" data. A gaussian fit is applied to the **corrected** E and E_{mean} histograms for FRET molecules. For each fit, the table summarizes: the mean position $\langle E \rangle$ and $\langle E_{mean} \rangle$ of the maximum and the standard deviation.

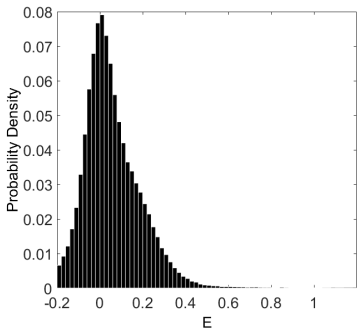

(a) 19 bp, E for all data (226747 time points for 2305 particles).

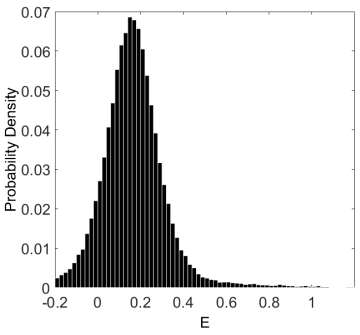

(b) 19 bp, E for FRET data (69022 time points for 712 particles).

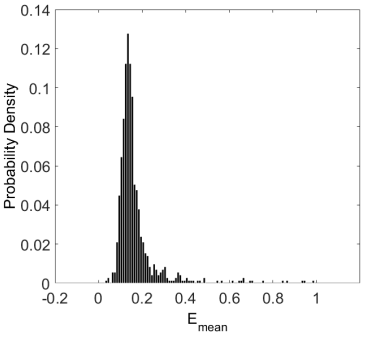

(c) 19 bp, E_{mean} for FRET data (712 particles).

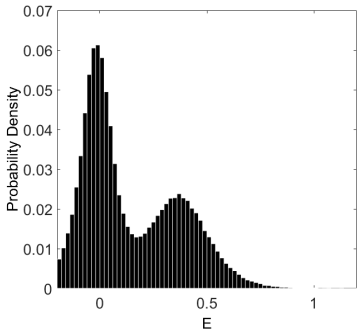

(d) 12 bp, E for all data (236373 time points for 2465 particles).

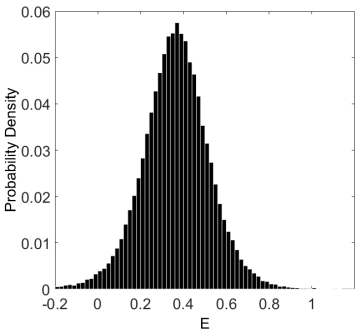

(e) 12 bp, E for FRET data (95940 time points for 1030 particles).

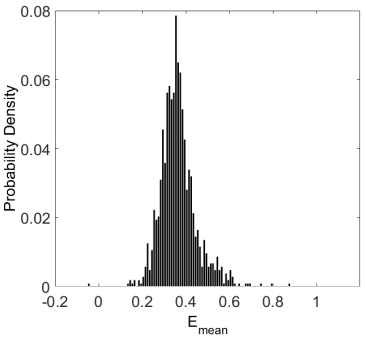

(f) 12 bp, E_{mean} for FRET data (1030 particles).

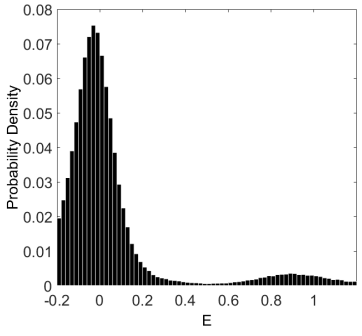

(g) 7 bp, E for all data (302931 time points for 3065 particles).

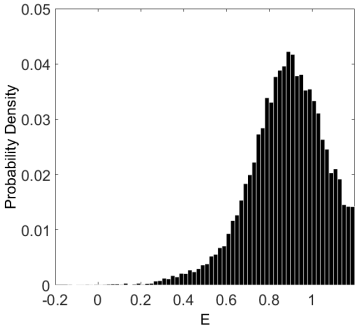

(h) 7 bp, E for FRET data (25024 time points for 258 particles).

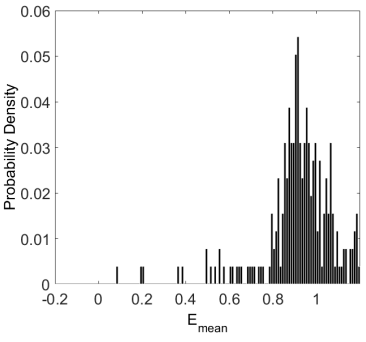

(i) 7 bp, E_{mean} for FRET data (258 particles).

Figure 5.9: FRET efficiency histograms for sCy3/sCy5 labelled DNA from "movies" data. (a),(d),(g): E distribution at all time for all the data. (b),(e),(h): E distribution for the particles exhibiting FRET signal. (c),(f),(i): time averaged efficiency E_{mean} distribution for all the particles exhibiting FRET signal. Number of data points is indicating under each graph. All the data are corrected from Donor leakage.

On figure 5.9.a, d and g, a first peak is visible centered on $\langle E \rangle = 0$, corresponding to the "Donor only" population. For an interdye distance of 19 bp, a shoulder is visible at low FRET ($E < 0,2$). For the 12 bp and 7 bp data, a clearly distinguishable FRET peak

is present respectively at $E \simeq 0,4$ and $E \simeq 0,9$. When only data exhibiting a clear FRET signal are manually selected (figure 5.9.b, e and h), the FRET peak is better visible, as expected. A clear shift of the FRET population is observed when the interdye distance decreases: the mean peak position equals $\langle E \rangle = 0,15$ for 19 bp distance, $\langle E \rangle = 0,36$ for 12 bp and finally $\langle E \rangle = 0,89$ for 7 bp. Similar values are found when fitting the time averaged E_{mean} distribution as shown in table 5.4. The values obtained are in agreement with those measured on the "Snapshots" data and in bulk (see respectively tables 5.3 and 5.2). However the 7 bp data exhibits a slightly higher $\langle E \rangle$ in "movies" measurements than previously found. One possible reason is the bleaching events occurring that cannot be subtracted from "Snapshots" or bulk data and that lowers the FRET efficiency.

These single-molecule measurements confirm that we are able to detect change in FRET population according to the distance between Donor and Acceptor dyes. This "ruler-type" calibration will very useful for interpreting the FRET experiments done with BmrA in different conformations (see figure 5.10).

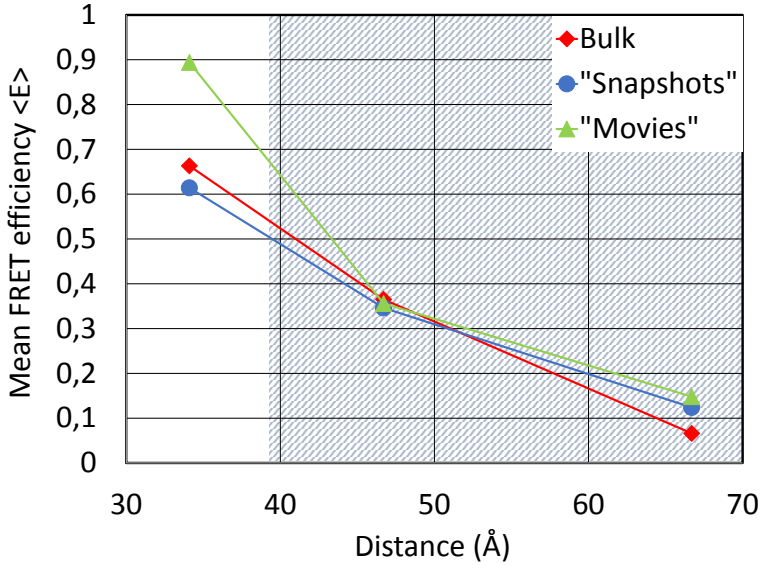

Figure 5.10: FRET efficiency calibration for the different types of measurements. The grey zone indicates the conformational spaces of BmrA, based on the models and assuming a certain flexibility of NDBs opening.

Part 5.2 : conclusions.

- Bulk experiments (with fluorescence spectroscopy and with the microscope) have shown an increase of FRET efficiency as the distance between Donor and Acceptor dyes decreases (this was done for the three couples of dyes : Alexa488/sCy5, sCy3/sCy5 and TMR/sCy5).
- DNA labelled with sCy3/sCy5 has been studied in single-molecule with the microscope: the FRET population also shifts towards higher values with decreasing distance between the fluorophores. This was observed both for "snapshots" and "movies" data. sCy3/sCy5 is the couple that will be used for smFRET study on BmrA.
- The table below and figure 5.10 summarize the corrected mean efficiency values $\langle E \rangle$ measured by gaussian fit for the sCy3/sCy5 labelled DNAs using the microscope (bulk, "snapshots" and "movies" data). Since the distances probed should be in the same range as the experiments with BmrA, our acquisition parameters should be suitable to observe a change in the FRET efficiency with the protein.

	Interdye distance (Å)	Bulk	"Snapshots"	"Movies"
19 bp	66,6	0,066	0,124	0,148
12 bp	46,7	0,365	0,346	0,356
7 bp	34,1	0,663	0,614	0,894

5.3 SmFRET with BmrA: establishment of conditions for observation and analysis

From the DNA-ruler experiments, we know the acquisition and analysis parameters are suitable to observe FRET efficiency change with dyes distant 3 to 7 nm. In this part the observation of BmrA in immobilized liposomes at single-molecule regime is first presented. The analysis process is then detailed, in particular the corrections applied for Donor leakage and Acceptor direct excitation.

5.3.1 Single molecule observation of BmrA in immobilized liposomes

sCy3/sCy5 labelled WT BmrA was reconstituted in liposomes in three different lipid compositions as summarized in table 4.2 in chapter 4. Figure 5.11 shows raw images of sCy3/sCy5 WT BmrA incorporated in EPC/bPS liposomes (at 20^{o}C = 140 nm diameter) and immobilized on glass coverslips. Many Donor and Acceptor data points are visible respectively in the left and right channels, and FRET signal is detected in the middle channel when both Donor and Acceptor colocalize.

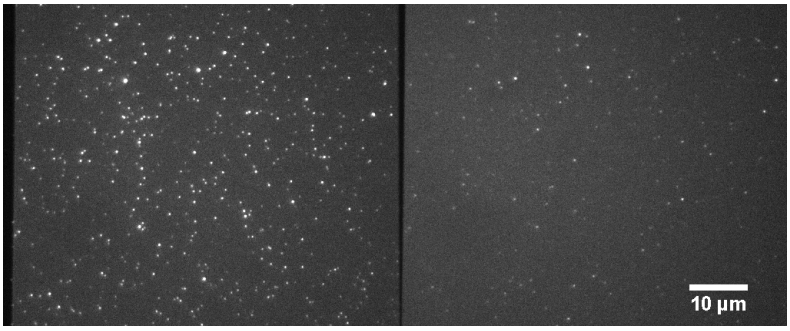

(a) Dual View image at excitation 532 nm: Donor channel on the left, FRET channel on the right.

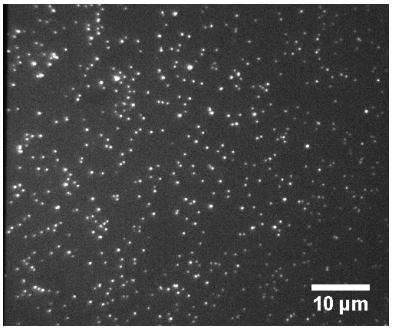

(b) Image at excitation 638 nm: Acceptor channel.

Figure 5.11: smFRET image of BmrA reconstituted in EPC/bPS liposomes at 20^{o}C (140 nm diameter). Images acquired at 150 ms exposure time, with laser power 3/5 both at 532 and 638 nm excitation.

5.3.2 Single molecule calibration

Since the liposomes' diameter varies according to lipid composition, it was necessary to adapt the Lipid/Protein ratio w/w (LPR) in order to reach single-molecule regime. Indeed, LPR, given by equation (4.3) (part 4.2.3), depends on the liposomes' diameter and of course on the targeted number of proteins per liposome.

Our goal was to quantify the LPR to guarantee there is a single BmrA per vesicle. Two different lipid compositions were tested together with several values of LPR that should all insure single-molecule regime:

- *E.coli* liposomes with LPR = 1200 or 7000,
- EPC/bPS liposomes at 4^{o}C with LPR = 500 or 2500.

Table 5.5 shows the corresponding number of proteins theoretically expected per liposome $N_{protein}$ (calculated by inverting equation (4.3)).

Lipid composition	Diameter (nm)	$N_{protein}$ for LPR = 500	$N_{protein}$ for LPR = 1200	$N_{protein}$ for LPR = 2500	$N_{protein}$ for LPR = 7000
EPC/bPS (4^oC)	40	0,38		0,08	
E.coli (20^oC)	60		0,35		0,06

Table 5.5: Expected number of proteins per liposome. Two LPR were used respectively for EPC/bPS vesicles (reconstituted at 4^oC) and *E.coli* liposomes. For each LPR, the corresponding number of protein expected per liposome ($N_{protein}$) is indicated (calculated by inverting equation 4.3).

Following the protocol described in part 4.2.3, the incorporation of BmrA was tested by observing sCy5-labelled BmrA in vesicles containing 0,01% Bodipy-FL lipids. Two different lipid concentrations were tested in the observation chamber: 5.10^{-3} and 5.10^{-4} mg/mL. The solution was incubated 5min and then rinsed. Images were acquired at 100ms exposure time with the following parameters:

- Bodipy-FL liposomes: excitation laser 488 nm at power 3/5, emission filter 525/30 nm,
- sCy5 labelled protein: excitation laser 638 nm at power 3/5, emission filter 684/24 nm.

125 images were acquired and analyzed. A fluorescent dot in the bodipy-FL channel is counted as one liposome. If it colocalizes with sCy5 signal, the liposome contains at least one protein. A single image was acquired and not a movie, therefore no bleaching events can be detected on an intensity time trace. Counting the bleaching events on a time trace would have been a method to test whether vesicle contain at most one protein. However, BmrA being a homodimer, it can be labelled with one or two sCy5 fluorophores. Thus, we could not discriminate between vesicles containing one doubly-labelled protein or two singly-labelled BmrA. Only the distinction between "empty" versus "full" liposomes (i.e. containing at least one protein) is made.

The total number of liposomes and the number of vesicles containing a protein are measured. Figure 5.12 shows the fraction of "full" liposomes. For EPC/bPS 4^oC (figure 5.12a), we find between 31 and 40% of "full" vesicles for LPR = 500, consistent with the 38% expected, and we measure less than 5% for LPR = 2500 when we expect 8. For *E.coli* (figure 5.12b), between 22 and 25% of "full" liposomes are observed for LPR =

1200 which is even lower than the theoretical value of 36% and we obtain around 5% for LPR = 7000, in good agreement with the 6% expected. In conclusion, our results are in agreement with the values calculated with equation 4.3 and prove that single molecule regime is reached for these conditions. The final LPRs, shown in table 4.2, were chosen accordingly with these results: LPR = 2000 for *E.coli*, LPR = 700 for EPC/bPS 4^{o}C and LPR = 6000 for EPC/bPS 20^{o}C.

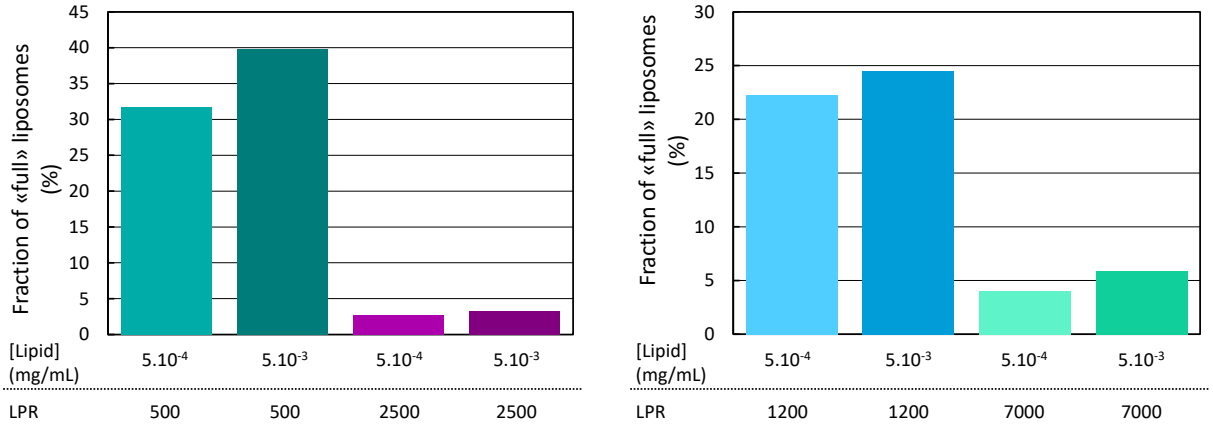

(a) EPC/bPS liposomes reconstituted at 4^{o}C. **(b)** *E.coli* liposomes reconstituted at 20^{o}C.

Figure 5.12: Fraction of vesicles containing at least one BmrA in two different lipid compositions.

5.3.3 Correction process on "snapshots" data

The raw signal observed in the FRET channel has different contributions: the energy transfer itself but also effects called "Donor leakage" and "Acceptor direct excitation". Figure 5.13 sketches the principle of these two effects: sCy3 emission and sCy5 excitation spectra are plotted, the excitation wavelength of the laser is indicated (green arrow at 532 nm) and the position of the sCy5 band-pass filter is marked by dashed lines. Some signal coming from sCy3 emission can be collected by the Acceptor filter: this is Donor leakage in the FRET signal. sCy5 can be slightly excited by 532 nm wavelength laser: this is the Acceptor direct excitation that contributes to the raw FRET signal. In order to correct for these effects, control experiments were performed with BmrA labelled only with the Donor dye (sCy3) and only with the Acceptor fluorophore (sCy5) respectively.

"Donor only" control with "snapshots" data.

sCy3-labelled BmrA was reconstituted (in Apo form) in EPC/bPS liposomes at 20^{o}C and observed on coverslips with similar acquisition parameters as doubly labelled proteins

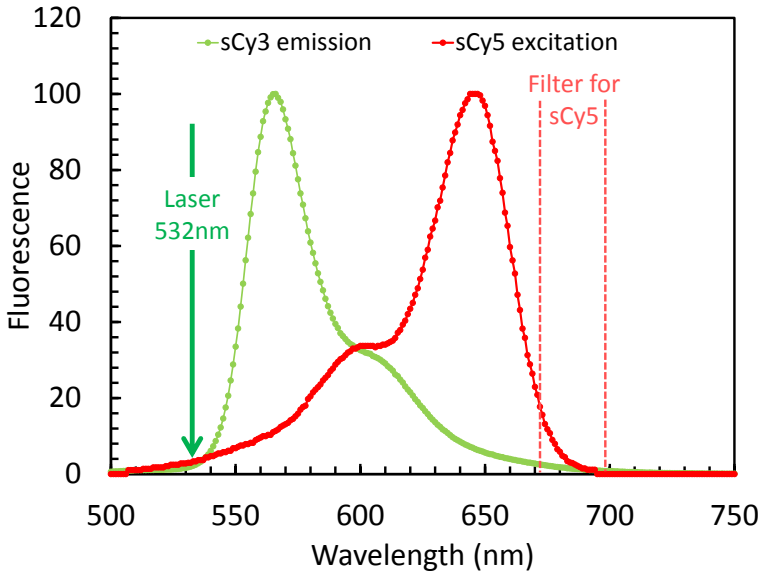

Figure 5.13: Principle of Donor leakage and Acceptor direct excitation. sCy3 emission and sCy5 excitation spectra are plotted in light green and red respectively. The laser excitation wavelength is indicated in green at 532 nm. The band of the sCy5 filter is marked with dashed red lines (filter 684/24).

(see table 4.6). Here, "snapshots" data are analyzed, using the option "Put an A at every D position". This implies that all Donor-only particles are analyzed and it allows to measure the FRET signal coming from the leakage of the "Donor only" population. Figure 5.14a shows the 2D E/S histogram for efficiency and stochiometry. A single population is observed with $S \simeq 1$ and E close to 0, corresponding to this "Donor only" population.

Figure 5.14b exhibits the efficiency histogram for data points with $S > 0,8$. 3148 over 3153 data points have a stochiometry higher than 0,8. $S = 0,8$ will be used in the rest of this work as the limit value to separate "Donor only" and doubly-labelled populations. Indeed because BmrA is a homodimer with two labelling sites and due to our labelling strategy, we have a mixture of six populations: $\varnothing - \varnothing$, $\varnothing-$ sCy3, $\varnothing-$ sCy5, sCy3-sCy3, sCy5-sCy5, sCy3-sCy5. Only the last population is doubly-labelled and can give FRET signal. In theory, 24,4% of BmrA should be doubly-labelled.

The efficiency distribution of the "Donor only" is not exactly centered on 0 because of the Donor leakage in the FRET channel and this effect can be corrected. The efficiency histogram of the "Donor only" population (Do) is centered on a value $\langle E^{Do} \rangle$, measured by fitting the histogram 5.14b with a normal distribution: $\langle E^{Do} \rangle = 0,0685$. The Donor leakage correction factor α is calculated for each experiment with equation (4.16): here $\alpha = 0,0736$. The corrected FRET efficiency is then calculated with the corrected FRET intensity I_F^{corr} introduced in equation (4.19) (with $\beta = 0$ as we do not correct from the

Acceptor direct excitation):

$$E^{corr} = \frac{I_F - \alpha I_D}{I_F + (1-\alpha) I_D}. \tag{5.1}$$

Figure 5.14c shows the efficiency histogram corrected from the Donor leakage: it is now centered on $E = 0$.

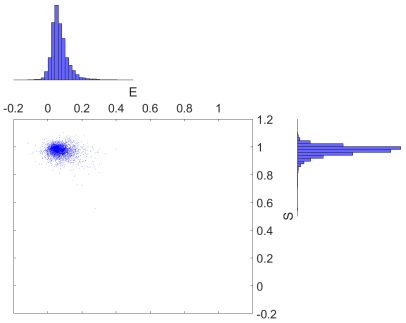

(a) 2D histogram with efficiency E (top) and stochiometry S (right). We observe a single population with $S \simeq 1$ (3153 data points).

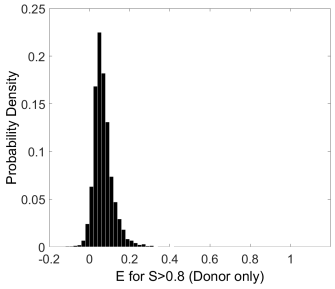

(b) Efficiency E histogram obtained by selecting data with $S > 0,8$ (3148 data points).

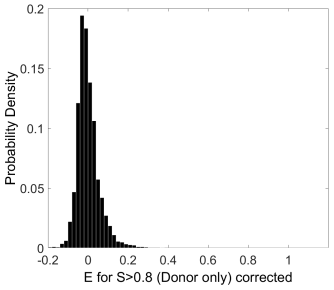

(c) Efficiency E histogram obtained by selecting data with $S > 0,8$ and by correcting from the Donor leakage with the correction factor $\alpha = 0,0736$.

Figure 5.14: Control for the Donor only with sCy3 labelled BmrA ("snaphots" data). sCy3 labelled BmrA is reconstituted in single molecule regime in EPC/bPS liposomes at 20^{o}C. The analysis is done with the option "Put an A at every D position" in iSMS program (see Part 4.6.4).

"Acceptor only" control with "snapshots" data.

sCy5 labelled BmrA was reconstituted (in Apo form) in EPC/bPS liposomes at 20^{o}C and observed on coverslips with the same parameters as doubly labelled proteins (see table 4.6). Here, "snapshots" data are analyzed, using the option "Put a D at every A position". This implies that all Acceptor-only particles are analyzed and it allows to measure the contribution of the Acceptor direct excitation to the FRET signal. Figure 5.15a shows the 2D E/S histogram for efficiency and stochiometry. A large distribution of stochiometry is observed while we would expect a narrower distribution with $0 < S < 0,3$. One possible explanation is that the Acceptor bleaching events enlarge the S distribution towards higher values. This effect makes it difficult to separate the doubly labelled population (expected around $S = 0,5$) from the Acceptor only. Finally, the FRET efficiency E of "Acceptor only" population presents a wide distribution close to 0,4. This is in agreement

with the expected value $E \sim 0,5$, since both intensities I_D and I_F both close to zero and thus $I_D \simeq I_F$.

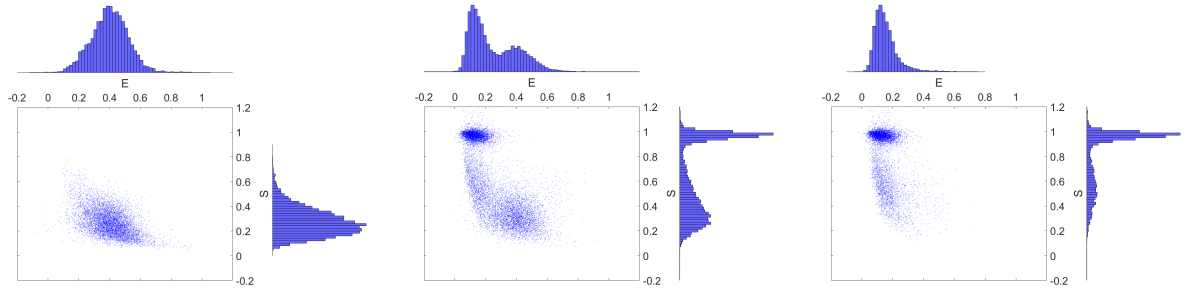

(a) sCy5-labelled BmrA. We observe a wide population both in S and E (7705 data points).

(b) sCy3/sCy5-labelled BmrA. Three populations are analyzed: Donor only, doubly labelled and Acceptor only (11661 data points).

(c) sCy3/sCy5-labelled BmrA. Only two populations are analyzed: Donor only and doubly labelled (7181 data points). Same data set as for figure (b).

Figure 5.15: Control for the Acceptor only with sCy5 labelled BmrA and comparison of analysis methods for sCy3/sCy5 labelled BmrA ("snaphots" data). sCy5 labelled BmrA and sCy3/sCy5 labelled BmrA are reconstituted in single molecule regime in EPC/bPS liposomes at 20^{o}C. 2D E/S histograms are shown when (a): the analysis is done with the option "Put a D at every A position" in iSMS program (see Part 4.6.4), (b): the analysis is done with both options "Put an A at every D position" and "Put a D at every A position", (c): the analysis is done only with the option "Put an A at every D position".

These observations are confirmed if we compare two different ways of analyzing data on sCy3/sCy5 labelled BmrA. sCy3/sCy5 labelled proteins (note that a mixture of six populations is present) were reconstituted (in Apo form) in EPC/bPS liposomes at 20^{o}C and observed immobilized on coverslips (similar observation parameters, see table 4.6). "Snapshots" are analyzed in two different ways. In one case, both options "put an A at every D position" and "put a D at every A position" were selected, resulting in detection of the three populations: "Donor only", doubly-labelled and "Acceptor only". The E/S histogram is shown on figure 5.15b. In the second case, only the option "put an A at every D position" was selected, providing the "Donor only" and the doubly labelled populations. The histogram is shown on figure 5.15c. Figure 5.15b shows that it is very hard to separate the doubly-labelled population from the "Acceptor-only" as it has a wide S distribution. For our study, it seems more relevant and accurate to do the analysis as on figure 5.15c (with only "put an A at every D position" applied). This analysis method should not eliminate any interesting data as only detection and colocalization of a Donor and an Acceptor dyes can provide FRET signal. Therefore we cannot correct for the Acceptor direct excitation effect (with the method explained in 4.6.3) as a distinct "Acceptor only" population is required.

To summarize, data are corrected only for the Donor leakage and not for the Acceptor direct excitation on the "snapshots" data.

5.3.4 Correction process on "movies" data

In "movies" data, signal is recorded in the Donor and FRET channels only but not in the Acceptor channel. Therefore, data cannot be corrected for the Acceptor direct excitation.

"Donor only" control in "movies" data.

sCy3 labelled BmrA was reconstituted (in Apo form) in *E.coli* liposomes at 20^{o}C and observed on coverslips with the same parameters as doubly labelled proteins for "movies" data type (see table 4.6). Analysis is made with the option "Put an A at every D position" so that we have access to the "Donor only" population. Figure 5.16a shows the efficiency E histogram. As for the "snapshots" data, a single peak is visible with E close to 0.

Correction for the Donor leakage on "movies" data is done the same way as previously on "snapshots" data. Fitting the histogram with a normal distribution gives $\langle E^{Do} \rangle = 0,0448$. The Donor leakage correction factor α is calculated with equation (4.16): $\alpha = 0,0469$. Equation (5.1) gives the corrected values of E. The corrected histogram is shown on figure 5.16b and is centered on 0.

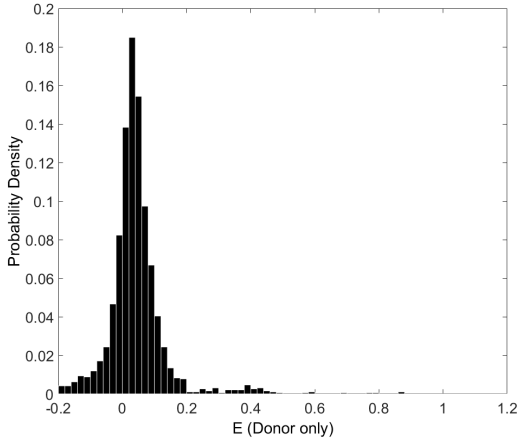

(a) Efficiency E histogram on sCy3 labelled BmrA, not corrected from Donor leakage.

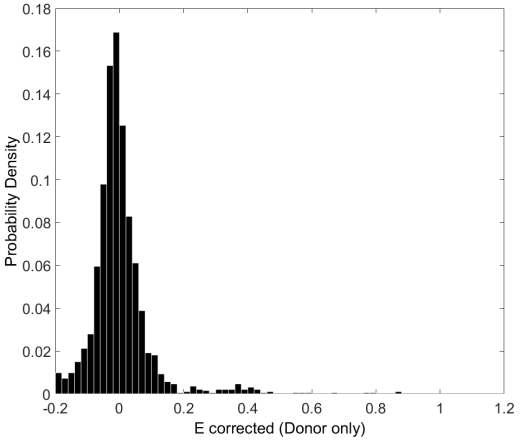

(b) Efficiency E histogram on sCy3 labelled BmrA, corrected from Donor leakage.

Figure 5.16: Control for the Donor only with sCy3 labelled BmrA ("movies" data). sCy3 labelled BmrA is reconstituted in single molecule regime in *E.coli* liposomes at 20^{o}C. Images are acquired at 50 ms with the same parameters as for the "movies" data (see part 4.5.3).The analysis is done with the option "Put an A at every D position" in iSMS program (see part 4.6.4). The number of particles analyzed is 48, and we have a total of 1931 time points.

The main difference with the "snapshots" data is that, with the "snapshots", we are able to correct for each sample independently as we can select the "donor only" population using stochiometry. In the rest of this study all the "movies" data will be corrected using the same correction factor: $\boxed{\alpha = 0,0469}$.

Part 5.3 : conclusions.

- BmrA is successfully reconstituted in single-molecule regime in liposomes. The vesicles containing BmrA are immobilized on a glass surface, FRET signal can be observed and both "snapshots" and "movies" data are acquired.
- The controls on 1-color labelled proteins shows that FRET efficiency E can be systematically corrected for the Donor leakage but not for the Acceptor direct excitation. This is true for "snapshots" and "movies" data.
- For "shapshots" data, the correction is made for each distribution individually using the "Donor only" population ($S > 0,8$) and calculating the corresponding factor α.
- For "movies" data, the same correction factor measured from Donor only control is used: $\alpha = 0,0469$.
- As we do not have the ALEX system, both "snapshots" and "movies" data contain complementary information. In the first case we can select the "doubly labelled" population using S but the signal is not resolved in time. In the second case we have access to traces over time but not to the direct emission from the Acceptor and therefore S cannot be calculated.

5.4 Single-molecule FRET results in three different conditions

In this part smFRET results obtained for sCy3/sCy5 WT BmrA are presented in three different conditions. The lipid composition and the liposomes size vary: EPC/bPS reconstituted at 20^{o}C (⌀ 140 nm), EPC/bPS reconstituted at 4^{o}C (⌀ 40 nm) and *E.coli* reconstituted at 20^{o}C (⌀ 60 nm). For each liposome type, four conditions of BmrA are observed:

- the protein is incorporated and observed in its Apo form (referred to as **Apo**),
- the protein is trapped with vanadate and ATP (1 mM) before to be incorporated in the vesicles (referred to as **Vi trapped**),
- the protein is incorporated in vesicles in its Apo form and then incubated with Vi and ATP (1 mM) (referred to as **ATP Vi**),
- the protein is incorporated in vesicles in its Apo form and then incubated with ATP (1 mM) (referred to as **ATP**) (in *E.coli* liposomes, verapamil was added at 50 μg/mL together with the ATP, referred to as **ATP Ver**).

In conditions **Apo**, **Vi trapped** and **ATP Vi** we expect the conformation of the protein to be "frozen" and not to cycle. In Apo, the protein has a certain flexibility and can therefore fluctuate. In the **ATP** or **ATP Ver** conditions, the protein should cycle and some dynamics should be observable.

In all these conditions, both "snapshots" and "movies" data are analyzed and presented here.

5.4.1 Liposomes EPC/bPS of 140 nm diameter

These liposomes are the largest population we investigate. Experiments were performed twice (for Apo, Vi trapped and ATP Vi) with similar results found. The results of only one experiment are presented here.

Results from "snapshots" data.

Figure 5.17 shows the E histograms measured for the four conditions mentionned above. These graphs contain only the doubly-labelled population as only data with $S < 0,8$ were selected. The 2D E/S histograms are available in appendix B, figure B.3. In all conditions, two peaks are observed for the stochiometry: a "Donor only" peak

around $S = 1$ (used for Donor leakage correction) and a wide population around $S = 0,6$ corresponding to the "doubly labelled" population. For the efficiency, the information from doubly-labelled molecules is hidden in the main peak at low E coming from the "Donor only" population. As previously mentionned, BmrA is a homodimer with two labelling sites and we have a mixture of six populations. Only the sCy3-sCy5 population can give FRET signal (in theory 24,4%). Therefore, it is convenient to select the doubly-labelled proteins using stochiometry. The FRET efficiency was systematically corrected for Donor leakage on these histograms and the correction factor α used for each condition is indicated on 5.17.

In all cases, a clear peak at low FRET ($E \simeq 0,1$) is visible, which should correspond to the open conformation, and a long tail on the high FRET values. Surprisingly, no higher FRET population is observed when adding ATP and Vi (5.17c) or just ATP (5.17d) and the distribution remains similar to that of the Apo form (5.17a). A high FRET population is observed at $E \simeq 0,35$ in one condition only: when the protein is trapped by vanadate and ATP before to be incorporated to the vesicles (5.17b).

This proves first that we are able to observe two FRET populations: a low FRET population that corresponds to the open conformation and a high FRET population corresponding to BmrA in closed conformation.

Secondly, no high FRET population is observed in ATP Vi (figure 5.17c), as compared to Vi Trapped (figure 5.17b). We can suppose that either the NBDs are not accessible to the reagents or BmrA cannot "close" in this particular condition. Indeed, one possible interpretation is that when the protein is reconstituted in the liposomes, it cannot "close" and ATP and vanadate cannot lock the protein in post-hydrolytic conformation.

Thirdly, histogram 5.17b shows that, even in Vi trapped condition, only a fraction of the molecules are in a conformation corresponding to high FRET. A two gaussians fit gives 70 and 30% in the low and high FRET population, respectively. A high proportion of BmrA is thus in a low FRET conformation, indicating that either these proteins never were in the closed conformation, or that they re-opened, or that the dyes bleached within the exposure time (150 ms). The first hypothesis would imply that the cycle inhibition by vanadate is not very efficient. However, it was measured by Su Jin Paik that the inhibition in this condition is close to 100%. The second hypothesis would imply that incorporation of the closed proteins in liposomes generates a stress that forces the re-opening of some proteins. This would also be consistent with our observations in ATP Vi condition (5.17b) where no high FRET population is visible. Regarding the last possible explanation, an oxygen scavenger mixture was used to limit the bleaching but on "snapshots" data I cannot take the bleaching into account in the calculation of E. For this reason it is

important to analyse the "movies" data and to observe time traces.

In addition, the "movies" data can also provide useful information on the ATP condition. Graph 5.17d do not exhibit any high FRET population although the protein is supposed to cycle in the presence of ATP and therefore to spend some time in both conformations. One possibility is that BmrA spends more time in the Apo form which prevents us from observing a significant high FRET peak corresponding to the post-hydrolytic conformation in the "snapshots" data. The results from the "movies" data are detailed below.

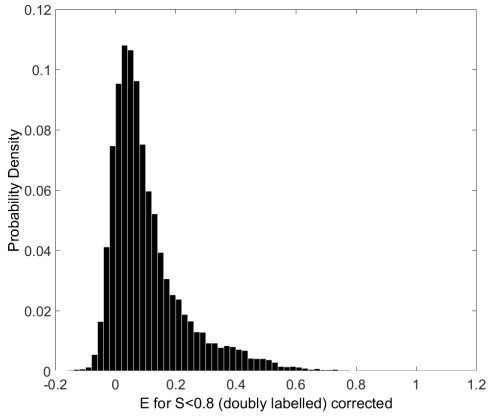

(a) Apo (8117), $\alpha = 0,116$.

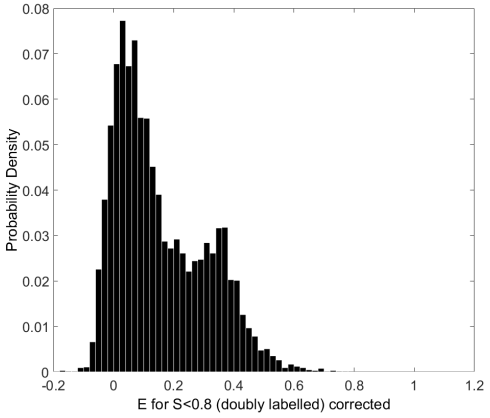

(b) Vi trapped (6509), $\alpha = 0,122$.

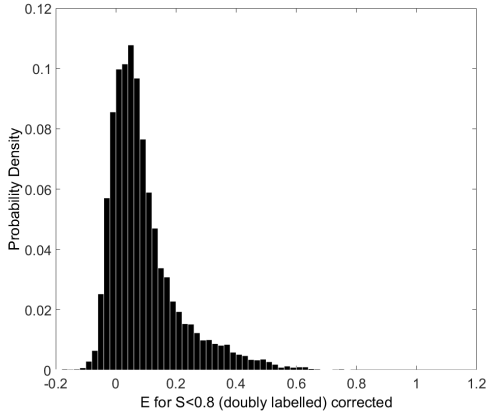

(c) ATP Vi (6977), $\alpha = 0,123$.

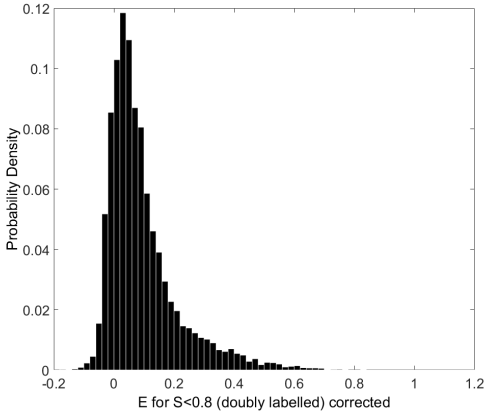

(d) ATP (9117), $\alpha = 0,108$.

Figure 5.17: FRET efficiency histograms for BmrA in EPC/bPS 20^{o}C liposomes from "snapshots" data. Distributions of E are shown for doubly-labelled population only (i.e. for particles with $S < 0,8$). Efficiency is corrected from Donor leakage (factor α is indicated for each). The number of proteins is indicated between brackets, this corresponds to 100 images analyzed.

Results from "movies" data.

Following the analysis process described in part 4.6.4, only proteins with a clear FRET signature were selected, referred to as "FRET population". This guarantees that

the "Donor only" data points are not kept and that only doubly-labelled proteins are considered. The bleaching and blinking intervals were set so that FRET efficiency is measured only when both Donor and Acceptor dyes are photo-active.

Two types of analysis were plotted:

- the distribution of all instantaneous E values limited to molecules exhibiting FRET signal (figure 5.19a, c, e, g, i);
- the distribution of time-averaged E values (E_{mean}) only for molecules exhibiting FRET signal (figure 5.19b, d, f, h, j).

Figures 5.19a, 5.19b, 5.19c and 5.19d show data for sCy3/sCy5 DNA samples with interdye distance $66,6$ and $46,7$ Å respectivelly, as a reference. E and E_{mean} histograms for all data ("Donor only" and doubly-labelled populations) are available in appendix B, figure B.4. The FRET efficiency was systematically corrected for Donor leakage with the correction factor $\alpha = 0,0469$. A gaussian fit was applied to the E distributions: two gaussians were used in order to take into account the main peak and the large distribution tail observed at high FRET. The fits are shown in appendix B, figure B.11. One of the two gaussians was systematically found more populated and its mean position $\langle E \rangle$ is given in table 5.6. The complete set of parameters given by the two gaussians fit are available in appendix B, table B.2.

Table 5.6 summarizes the number of data points we have for each condition and shows that significantly less proteins exhibiting FRET are detected in Apo, ATP Vi and ATP ($\simeq 10\%$) than in Vi trapped condition ($17,6\%$).

Two different distribution profiles are observed. In Apo (5.19e, 5.19f), ATP Vi (5.19i, 5.19j) and ATP (5.19k, 5.19l), the histograms exhibit a wide peak with a maximum around $E = 0,2$ and a large tail at high efficiency values. This long tail is not present on the DNA 19 and 12 bp references, indicating that it does not result from the set-up or the analysis. In Vi Trapped (5.19g, 5.19h), a peak is observed at higher FRET efficiency with a mean at $\langle E \rangle = 0,39$, consistent with the value previously found for "shapshots" data. In Vi trapped, the E and E_{mean} distributions are more similar to the DNA reference, with a such less pronounced tail than in the other conditions.

The results confirm our observations obtained from "snapshots": addition of ATP and vanadate results in a high FRET population only when added before the protein incorporation in the vesicles.

Condition	Total number of particles	Number of particles exhibiting FRET	Ratio (%)	Mean position $\langle E \rangle$ of gaussian fit
Apo	5466	566	10,4	0,19
Vi Trapped	5074	894	17,6	0,39
ATP Vi	2105	191	9,1	0,22
ATP	2226	223	10,0	0,17

Table 5.6: Data points from "movies" data for BmrA in EPC/bPS 20^{o}C liposomes. For each conditions we indicate the total number of particles found, the number of particles exhibiting FRET and the ratio of proteins exhibiting FRET over the total number. A two gaussians fit was applied to the instantaneous E distribution, the mean position $\langle E \rangle$ of the main peak is indicated.

Surprisingly, we do not detect any clear signature of the protein dynamics on the traces when BmrA is incubated with ATP and expected to cycle. Typical time traces obtained in the four conditions are shown on figure 5.18. In Apo (5.18a), Vi trapped (5.18b) and ATP Vi (5.18c), the protein exhibits one single state (high or low FRET) before the Donor or Acceptor bleaches. In the presence of ATP, no anticorrelation is observed with a signal cycling from low to high FRET. Most of the traces show a single low FRET state. Figure 5.18d shows an example where the protein seems to go from closed to open conformation since the FRET signal does not drop to zero. However the FRET signal does not return back to high FRET state within the observation time. Therefore it is hard to discriminate between Acceptor bleaching or protein cycling to explain this drop.

The 50 ms exposure time was chosen to optimize the single-molecule observation and to be compatible with BmrA activity measurements. At 37^{o}C, the activity of BmrA reconstituted at 20^{o}C in EPC/bPS liposomes is 4 μmol per minute per mg of protein (here, one protein means one half transporter = monomer). This corresponds to 4,3 molecules of ATP hydrolyzed per second per monomer. BmrA works as a homodimer and each monomer has to hydrolyze a molecule of ATP to complete a full cycle (i.e. two molecules of ATP for the full transporter). Therefore one cycle lasts 250 ms at 37^{o}C. All our experiments were done at 20^{o}C which means the cycle should last longer in the experimental conditions. Therefore 50 ms exposure time over 5 s observation time should be suitable in principle.

Since no signature of the protein dynamics is observed in the presence of ATP, several hypothesis can be proposed. (i) The closed conformation has a very short lifetime and we need to reduce the exposure time to be able to detect the protein in this conformation. (ii) The dynamics of BmrA is very slow, and the efficiency of the oxygen scavenger cocktail should be improved in order to observe several full cycles on longer traces. (iii) The liposome curvature results in a mechanical stress applied on the protein by the membrane, that prevents the NBDs dimerization and the cycle. This last hypothesis would be consistent with our observations in ATP Vi condition where the protein is not in a closed state.

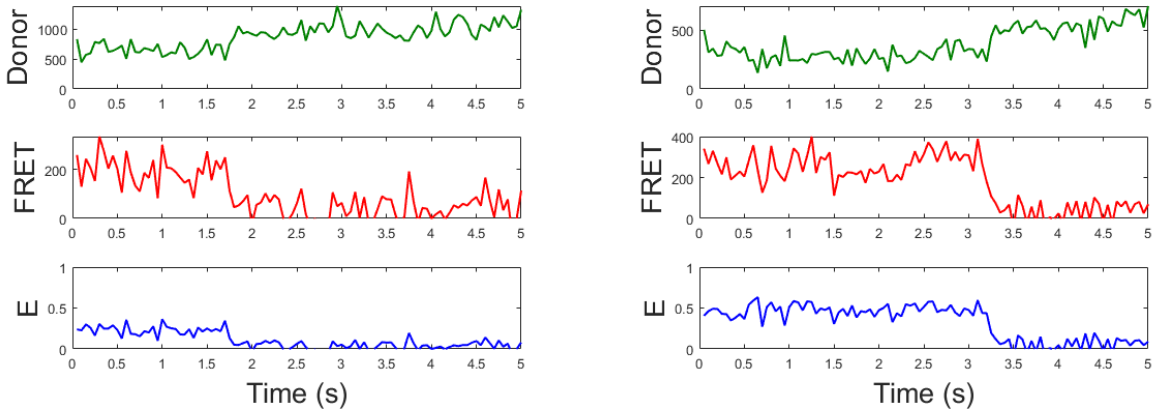

(a) Apo.

(b) Vi Trapped.

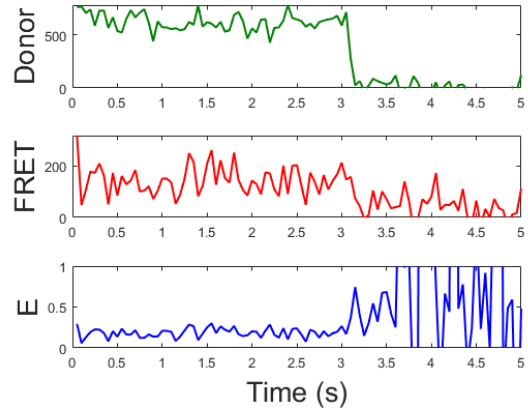

(c) ATP Vi.

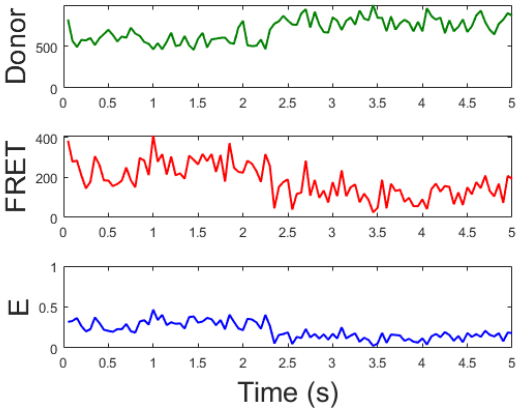

(d) ATP.

Figure 5.18: 5 seconds traces of Donor intensity, FRET intensity and efficiency from BmrA reconstituted in EPC/bPS 20^{o}C liposomes. Typical traces in different conditions are shown. Acquisition speed is 20 images per second. (a),(b): After Acceptor bleaching (occurring at 1,7 s and 3,2 s respectively), the FRET signal and efficiency drop to 0 and the Donor intensity increases. (c): Donor fluorophore bleaching (occurring at 3,1 s) results in the drop of Donor and FRET signals. (d): FRET signal decreases at 2,3 s correlated with an increase of the Donor intensity, but FRET does not seem to drop to zero. This is possibly the signature of the conformation change between closed to open conformation.

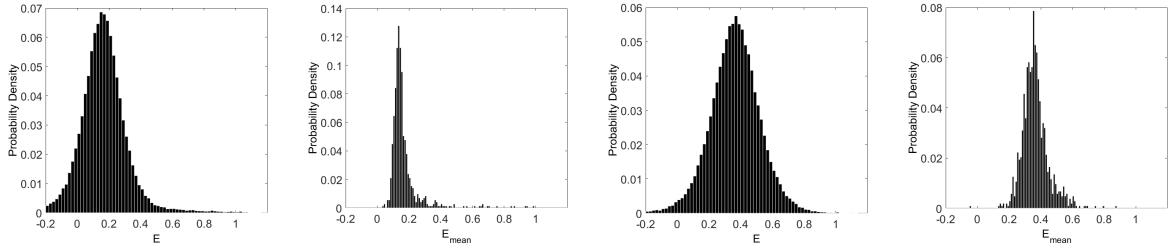

(a) E for DNA 19 bp (66,7 Å) (69022 data points). **(b)** E_{mean} for DNA 19 bp (66,7 Å) (712 data points). **(c)** E for DNA 12 bp (46,7 Å) (95940 data points). **(d)** E_{mean} for DNA 12 bp (46,7 Å) (1030 data points).

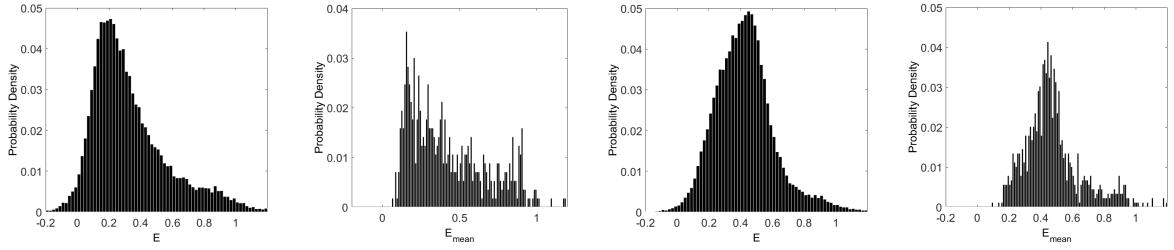

(e) E for Apo (26594 data points). **(f)** E_{mean} for Apo (566 data points). **(g)** E for Vi trapped (40274 data points). **(h)** E_{mean} for Vi trapped (894 data points).

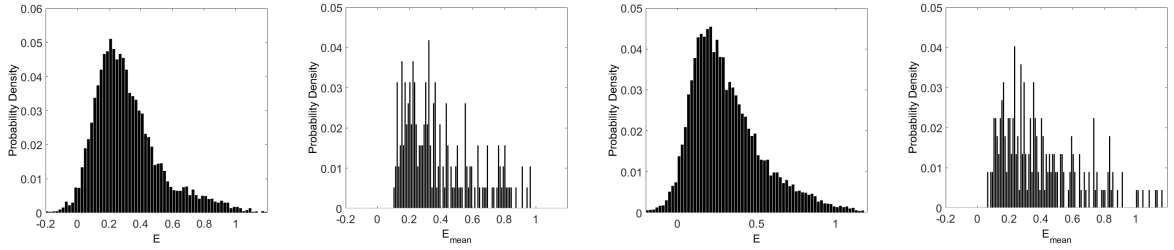

(i) E for ATP Vi (10410 data points). **(j)** E_{mean} for ATP Vi (191 data points). **(k)** E for ATP (11917 data points). **(l)** E_{mean} for ATP (223 data points).

Figure 5.19: FRET efficiency histograms for BmrA in EPC/bPS 20^{o}C liposomes from "movies" data. Only data exhibiting a clear FRET signal, i.e. doubly-labelled population, are shown here. Histograms (a), (c), (e), (g), (i), (k) contain all time data points. Histograms (b), (d), (f), (h), (j), (l) show the time averaged values E_{mean}. FRET efficiency was corrected from Donor leakage with $\alpha = 0,0469$. Histograms (a),(b) and (c),(d) show data from FRET calibration with interdye distance 66,6 and 46,7 Å respectively. These data are used as a landmark. The number of data points is indicated between brackets, this corresponds to 30 to 50 movies analyzed.

Interestingly, the E distribution in Vi trapped condition (5.19g) do not exhibit a low FRET population as the one observed on "snapshots" data (5.17b). This graph suggests that we have about 100% of molecules in a closed conformation corresponding to high FRET. This tends to confirm our third hypothesis (formulated in the "snapshots" data paragraph): 70% of proteins are found in a low FRET state due to bleaching during the acquisition period. With the analysis of the "movies" data, bleaching and blinking intervals are set and we can circumvent this issue.

In conclusion, "movies" data show that two different FRET populations are observed: a low FRET population corresponding to $E \simeq 0,2$ with a very long tail on the high FRET values, and a high FRET population corresponding to $E = 0,4$. The high FRET population is observed only in one condition: when BmrA is locked in post-hydrolytic conformation before to be reconstituted in the lipid membrane. Since "movies" data provide more accurate information about the protein state, only this type of data will be presented in detail for the two next lipid compositions.

5.4.2 Liposomes *E.coli* of 60 nm diameter

E.coli liposomes have a smaller size than those prepared with EPC/bPS at 20^{o}C. It is interesting to explore a different lipid composition, as the protein activity was found twice higher in *E.coli* vesicles as compared to EPC-based liposomes (see part 3.2.2). Globally, the results with *E.coli* are very similar to those obtained in EPC/bPS 20^{o}C reported in part 5.4.1. Note that here, a substrate (verapamil) was added together with ATP, in order to test if ATP cycle is observable in the presence of substrate.

Experiments were performed three times (for Apo, Vi trapped and ATP Vi) with similar results found. The results of only one experiment are presented here.

Results from "snapshots" data.

The histograms for the four conditions of BmrA are shown in appendix B, figure B.5. The observations are the same as for the bigger liposomes in part 5.4.1. A high FRET population is observed only in Vi trapped condition.

Results from "movies" data.

Figure 5.20 shows E and E_{mean} histograms only for the selected proteins exhibiting FRET signal. E and E_{mean} histograms for all data ("Donor only" and doubly-labelled populations) are available in appendix B, figure B.6. The gaussian fits for E distributions are shown in appendix B, figure B.11, as well as the complete set of parameters given by the two gaussians fit on table B.2.

Table 5.7 summarizes the number of proteins exhibiting FRET signature *vs* the total number of data points. It also gives the mean position of the peak $\langle E \rangle$, measured from a two gaussians fit.

First, the fraction of proteins exhibiting FRET is higher in *E.coli* as compared to EPC/bPS 20^{o}C, in all conditions (see table 5.7), potentially due to a higher protein activity although it is not twice higher.

Condition	Total number of particles	Number of particles exhibiting FRET	Ratio (%)	Mean position $\langle E \rangle$ of gaussian fit
Apo	1279	164	12,8	0,20
Vi Trapped	1489	301	20,2	0,38
ATP Vi	1295	182	14,1	0,21
ATP	1232	197	16	0,25

Table 5.7: Data points from "movies" data for BmrA in *E.coli* liposomes. For each conditions we indicate the total number of particles found, the number of particles with a clear FRET behavior and we calculate the ratio of proteins exhibiting FRET over the total number. A two gaussians fit was applied to the E distribution, the mean position $\langle E \rangle$ of the main peak is indicated.

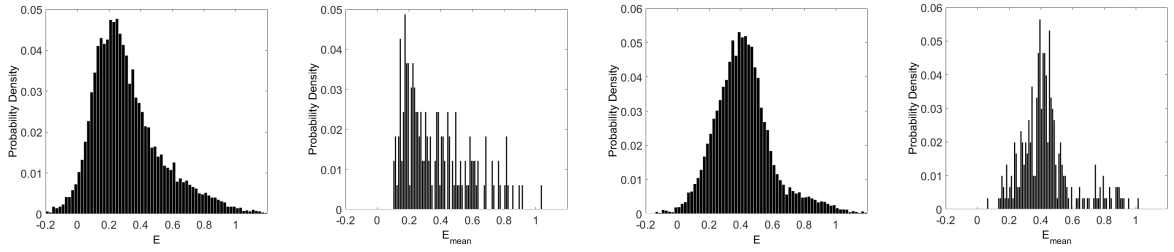

(a) E for Apo (7691 data points). **(b)** E_{mean} for Apo (164 data points). **(c)** E for Vi trapped (13587 data points). **(d)** E_{mean} for Vi trapped (301 data points).

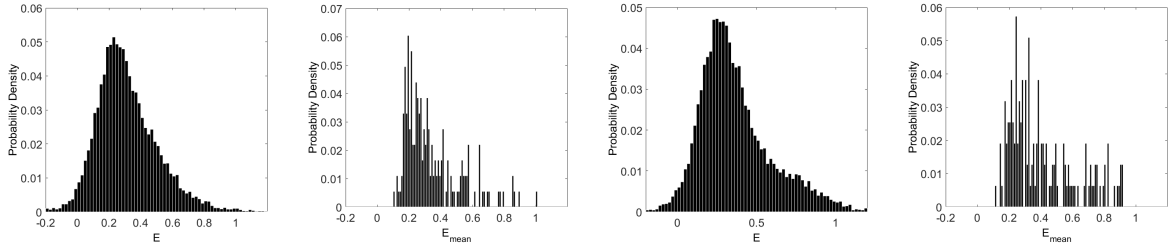

(e) E for ATP Vi (12561 data points). **(f)** E_{mean} for ATP Vi (182 data points). **(g)** E for ATP Ver (8997 data points). **(h)** E_{mean} for ATP Ver (157 data points).

Figure 5.20: FRET efficiency histograms for BmrA in *E.coli* liposomes from "movies" data. Only data exhibiting a clear FRET signal, i.e. doubly-labelled population, are shown here. Histograms (a), (c), (e), (g) contain all time data points. Histograms (b), (d), (f), (h) show the time averaged values E_{mean}. FRET efficiency was corrected from Donor leakage with $\alpha = 0,0469$. The number of data points is indicated between brackets, this corresponds to 50 movies analyzed.

The results are very similar to those obtained for the large liposomes (5.4.1). In three conditions, Apo (5.20a, 5.20b), ATP Vi (5.20e, 5.20f) and ATP Ver (5.20g, 5.20h), the distributions show a wide peak with maximum around $E = 0,2$ and with a long tail in the high FRET values. This confirms that in our experimental conditions, incubating the protein with ATP Vi or ATP Ver has no detectable effect on the conformations probed by BmrA. Moreover, as in the previous lipid composition, no conformational dynamics is visible in the movies when adding ATP/substrate. A high FRET population is observed only in Vi trapped BmrA as shown on figures 5.20c and 5.20d. No pronounced tail at high FRET was observed, similarly to previous case. The E distribution is centered on $E = 0,38$, same value as that found in EPC/bPS 20^{o}C.

5.4.3 Liposomes EPC/bPS of 40 nm diameter

For the same lipid composition as in part 5.4.1, these vesicles are significantly smaller. Moreover, the protein activity was found twice lower in small vesicles as compared to large EPC/bPS liposomes (see part 3.2.2). Experiments were performed only one time. One short term perspective of this work is to repeat this condition.

Results from "snapshots" data.

The histograms for the four conditions of BmrA are shown in appendix B, figure B.7. The observations are very similar to those for the other liposomes conditions in part 5.4.1 and 5.4.2, except for the Vi trapped condition where no high FRET population is detected.

Results from "movies" data.

Figure 5.21 shows E and E_{mean} histograms only for the selected proteins exhibiting FRET signal. E and E_{mean} histograms for all data ("Donor only" and doubly-labelled populations) are available in appendix B, B.8. The gaussian fits for E distributions are shown in appendix B, figure B.11, as well as the complete set of parameters given by the two gaussians fit on table B.2.

Table 5.8 summarizes the number of proteins exhibiting FRET signature *vs* the total number of data points. It also gives the mean position of the peak $\langle E \rangle$, measured from a two gaussians fit.

First, the fraction of proteins exhibiting FRET is lower in EPC/bPS 4^{o}C as compared to the two other liposomes conditions (see table 5.8). This difference is particularly visible in Apo where only 6,5% of particles exhibit a FRET signature instead of 10,4% in the large liposomes. This difference also exists in Vi Trapped and ATP conditions.

Condition	Total number of particles	Number of particles exhibiting FRET	Ratio (%)	Mean position $\langle E \rangle$ of gaussian fit
Apo	1208	79	6,5	0,21 - 0,58
Vi Trapped	1329	197	14,8	0,37
ATP Vi	1076	142	13,2	0,22
ATP	905	80	8,8	0,17

Table 5.8: Data points from "movies" data for BmrA in EPC/bPS 4^{o}C liposomes. For each conditions we indicate the total number of particles found, the number of particles with a clear FRET behavior and we calculate the ratio of proteins exhibiting FRET over the total number. A two gaussians fit was applied to the E distribution, the mean position $\langle E \rangle$ of the main peak is indicated. For Apo, two equivalent populated peaks were found in the fit and both their mean positions are given.

Considering the FRET distribution in Apo, the results differ from those obtained with larger liposomes in part 5.4.1. On figures 5.21a and 5.21b, a very large distribution is observed, wider than for the large liposomes, indicating that the proteins can explore a large range of conformations. In particular, no clear peak at low FRET is visible.

In the three other conditions, similar results are found with small liposomes as compared to large ones. In Vi trapped condition (5.21c, 5.21d), a high FRET population is observed, centered on a similar value as previously reported: $E = 0,38$. This indicates that all the proteins observed in the "FRET" population are locked in post-hydrolytic conformation.

ATP Vi (5.21e, 5.21f) and ATP (5.21g, 5.21h) distributions show a wide peak with maximum around $E = 0,2$ and with a long tail in the high FRET values. However, ATP distribution exhibits a particular shape at high FRET values and it is hard to determine whether we observe a long tail or a second peak at $E \simeq 0,8$. Moreover, as for the large liposomes, no conformational dynamics is visible in the movies when adding ATP.

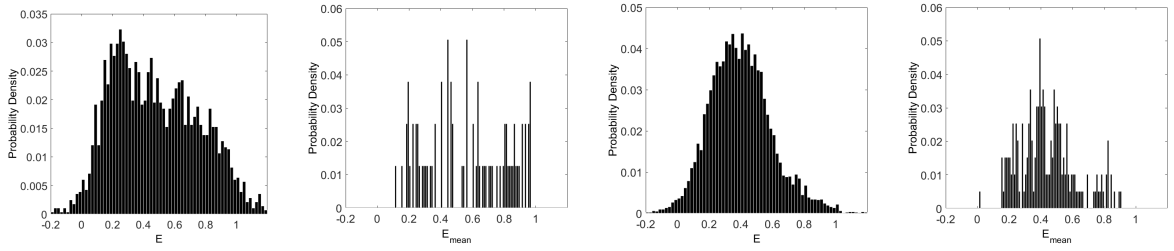

(a) E for Apo (2817 data points). **(b)** E_{mean} for Apo (79 data points). **(c)** E for Vi trapped (8259 data points). **(d)** E_{mean} for Vi trapped (197 data points).

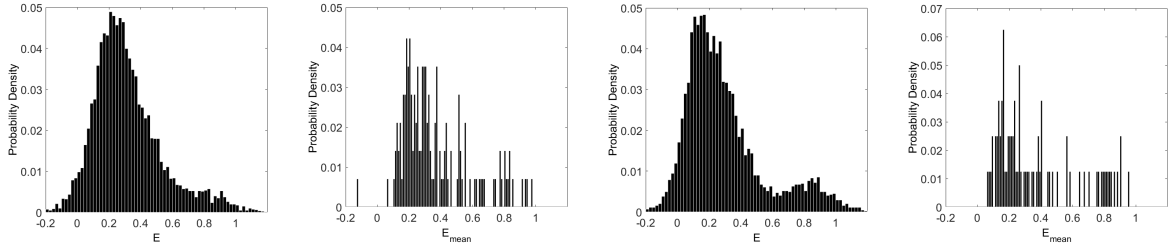

(e) E for ATP Vi (8012 data points). **(f)** E_{mean} for ATP Vi (142 data points). **(g)** E for ATP (4447 data points). **(h)** E_{mean} for ATP (80 data points).

Figure 5.21: FRET efficiency histograms for BmrA in EPC/bPS 4^{o}C liposomes from "movies" data. Only data exhibiting a clear FRET signal, i.e. doubly-labelled population, are shown here. Histograms (a), (c), (e), (g) contain all time data points. Histograms (b), (d), (f), (h) show the time averaged values E_{mean}. FRET efficiency was corrected from Donor leakage with $\alpha = 0,0469$. The number of data points is indicated between brackets, this corresponds to 50 movies analyzed.

Part 5.4 : conclusions.

Three different conditions were investigated for the liposomes: EPC/bPS reconstituted at 20^{o}C (⌀ 140 nm), EPC/bPS reconstituted at 4^{o}C (⌀ 40 nm) and *E.coli* reconstituted at 20^{o}C (⌀ 60 nm). For each we explored four conditions for BmrA : Apo, Vi trapped, ATP Vi and ATP (or ATP Ver).

- The only conditions where we can observe a high FRET population are Vi trapped BmrA. All the other conditions exhibit a low FRET peak with a long tail at high E. It indicates that locking the protein in the post-hydrolytic conformation is effective only when done before BmrA is incorporated in the liposomes.
- When Apo BmrA is reconstituted into proteo-SUVs, similar distribution is observed upon addition of ATP Vi or ATP only as compared to Apo distribution. The closed conformation corresponding to small distances between NBDs is not reached in these conditions.
- We could not detect any effect of the addition of ATP on the FRET traces.
- In the absence of nucleotide, BmrA can exhibit a large variety of conformations. Also, a very flat and large distribution was obtained with Apo BmrA in small liposomes, indicating that a large conformational space is accessible for the protein in curved membrane.

Globally, this suggests that the orientation of the protein (inward- or outward-facing NBDs), and thus accessibility of the NBDs for the reagents, and that membrane curvature might play a role in BmrA conformation.

Chapter 6

Discussion

6.1 Conformational space of BmrA

6.1.1 Distance estimation on BmrA

The FRET calibration, performed on different interdye distances using double-stranded DNA, not only proves that it is possible to detect large changes of FRET efficiency over distance changes of 30 Å (on our set-up and with the selected dyes), but it also provides a reference for the efficiency value according to interdye distance. Figure 6.1a shows a comparison between the experimental data found for DNA samples with 7, 12 and 19 bp separation (blue data) and the theoretical FRET efficiency calculated with $R_0 = 50$ Å and that reads

$$E_{th} = \frac{R_0^6}{R_0^6 + R^6}. \tag{6.1}$$

There is no clear consensus on the Förster radius values for the fluorophores couples since different values are referenced in various publications (see Khadria and Senes [2015] for a review). For sCy3/sCy5 couple, 53 Å was found by Stein et al. [2011] by fitting experimental data, $R_0 = 55$ Å was used in You et al. [2005] and our calculation gives $R_0 = 48$ Å. Therefore, we use $R_0 = 50$ Å for data interpretation, keeping in mind that an absolute calibration is difficult to achieve. Theoretical E curve confirms that the sensitivity of FRET technique is high between 30 and 70 Å, i.e. well adapted to the distance range we aim to probe.

On figure 6.1, circles indicate the position of the mean in the E distribution and the vertical lines represent the standard deviation, measured with a gaussian fit. The efficiency values measured on DNA sample match the theoretical curve E_{th}, except for the 12 bp sample which has a lower value (figure 6.1a).

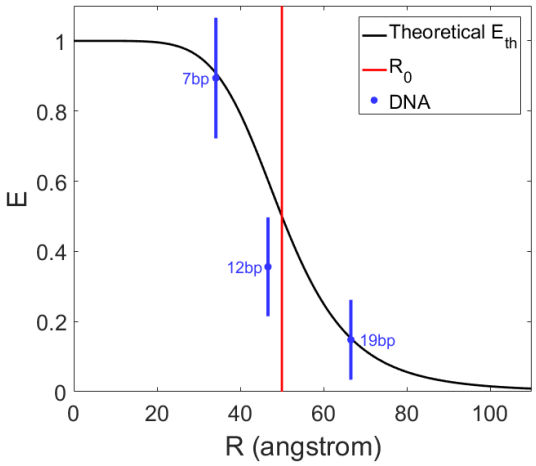

(a) DNA calibration.

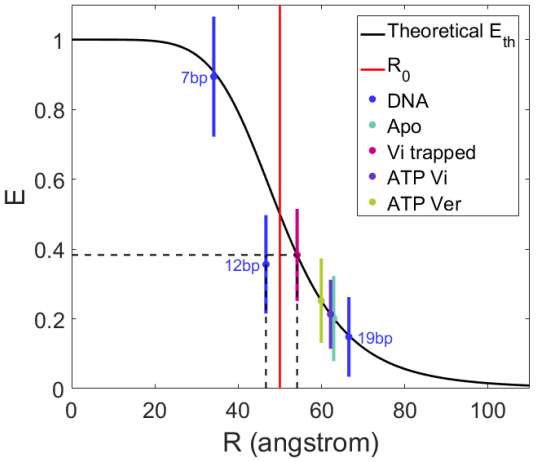

(b) *E.coli* liposomes (⌀ 60 nm).

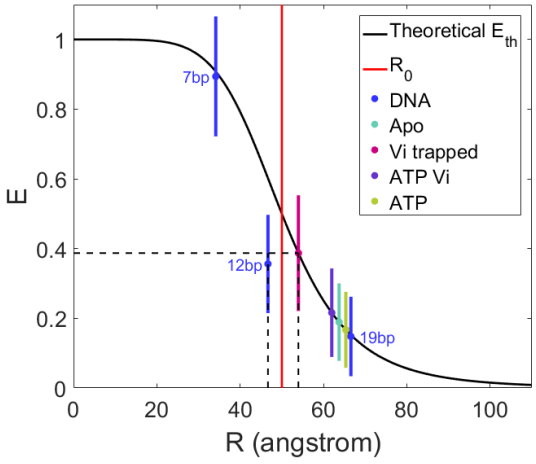

(c) EPC/bPS 20^{o}C liposomes (⌀ 140 nm).

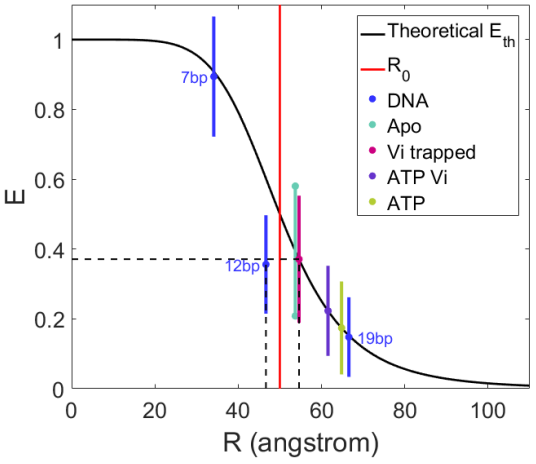

(d) EPC/bPS 4^{o}C liposomes (⌀ 40 nm).

Figure 6.1: BmrA NBDs separation distances. Based on theoretical FRET efficiency (black line) calculated with $R_0 = 50$ Å (red line) and on the FRET efficiency calibration performed with three different interdye distances (light blue data), the distance between BmrA NBDs (positions C436) in the different conditions is estimated. Circles indicate the position of the mean in the E distribution and the bars correspond to the standard deviation, measured from the gaussian fit. For EPC/bPS 4^{o}C liposomes, in the apo conformation, since the distribution did not exhibit a clear maximum, the circles indicate the two mean positions found with a two gaussians fit. The distance R was calculated using the theoretical E_{th} equation (6.1) and $R_0 = 50$ Å for visualisation purpose. The distance estimation is done using the DNA calibration data.

The DNA sample serves as a reference to estimate the NBDs distance of BmrA in the different conditions. Figures 6.1b, 6.1c and 6.1d show similar graphs with theoretical efficiency E_{th}, DNA data and BmrA data for *E.coli*, EPC/bPS 20^{o}C and EPC/bPS 4^{o}C respectively. For *E.coli* and EPC/bPS 20^{o}C liposomes, conditions Apo, ATP Vi, ATP Ver and ATP exhibit similar low FRET efficiencies (around $E = 0,2$) corresponding to a distance between NBDs slightly smaller in average than the 19bp DNA sample, i.e. smaller than 67 Å. Similar values are found for ATP Vi and ATP BmrA in EPC/bPS

4^oC. In contrast, Apo BmrA in EPC/bPS 4^oC exhibits a different E distribution with no clear peak. Therefore, figure 6.1d shows the two mean values found with a two gaussians fit (indicated by circles). The corresponding R distance was calculated from the mean of these two values only for visualisation purpose: a large flat E distribution indicates that the explored distance range is large. Finally, in the three liposomes conditions, Vi trapped BmrA exhibit a FRET efficiency of $E = 0,4$ corresponding to the efficiency of 12 bp DNA sample. Therefore, according to the calibration data, the distance for Vi trapped BmrA is of the order of 47 Å. The conformational space of the protein will now be discussed in the four conditions Apo, Vi trapped, ATP Vi and ATP.

6.1.2 Apo BmrA

Figure 6.2 shows the FRET distributions obtained for Apo BmrA according to liposomes size (same distributions as presented in part 5.4). In the apo conformation, the FRET efficiency distribution exhibits a clear peak around $E = 0,2$ but with a very long tail towards the high values of E. Plotting the time averaged efficiency E_{mean} allows to visualize the average conformation "occupied" by one protein. The distribution E_{mean} also presents a long tail towards the high values of FRET, indicating that there are proteins keeping a high FRET state over the 5 seconds time of the experiments. This proves that the high FRET values do not simply correspond to the thermal fluctuations of the proteins. The long tail indicates a large spectra of inward-facing conformations accessible to BmrA, with various NBD separation distances.

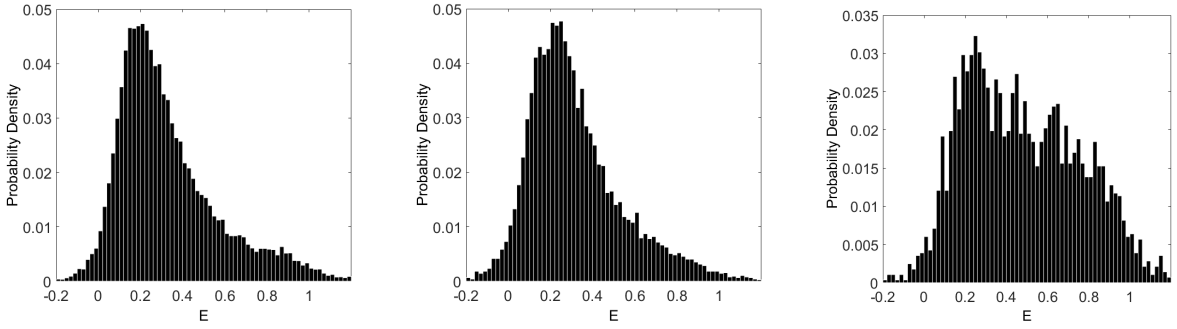

(a) Liposomes ∅ 140 nm (EPC/bPS 20^o). **(b)** Liposomes ∅ 60 nm (*E.coli*). **(c)** Liposomes ∅ 40 nm (EPC/bPS 4^o).

Figure 6.2: FRET distributions of Apo BmrA. E distributions plotted for Apo BmrA reconstituted in three different liposomes populations. Only particles exhibiting FRET signal are plotted.

These observations are in good agreement with the large conformational flexibility

found by Moeller and coworkers for MsbA and P-gp, using single particle Electron Microscopy (EM) (Moeller et al. [2015]). The transporters are embedded in a mixture of detergent and peptides (forming a β sheet peptide assembly) with addition of lipids. This forms bicelles which stabilize integral proteins and maintain their function. Figure 6.3 shows the conformational spaces found for these two proteins in apo, with opening from 40 to 65 Å for MsbA, and from 50 to 75 Å for P-gp. The authors showed that in the absence of nucleotide, P-gp and MsbA are essentially in inward-facing conformation with a large distribution of opening, but more constrained for P-gp than for MsbA.

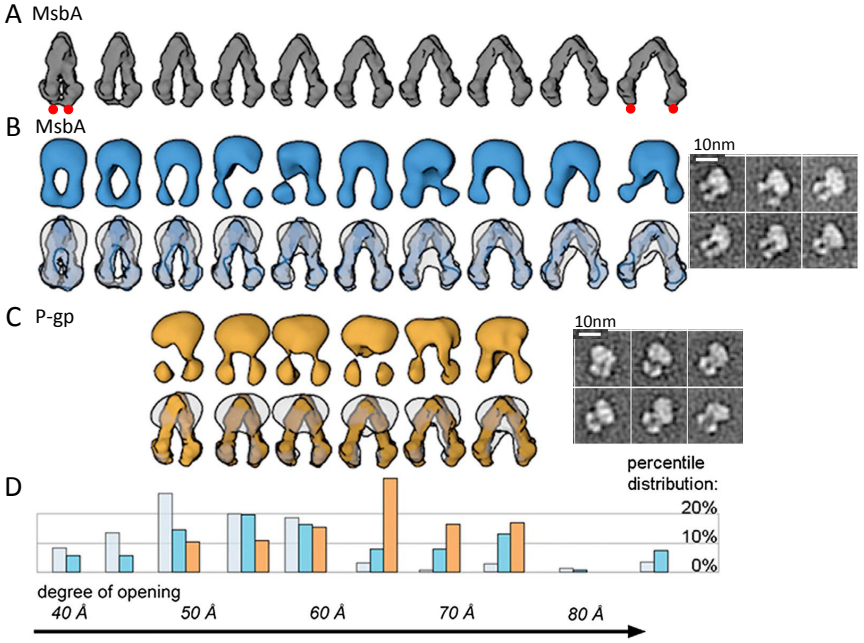

Figure 6.3: Conformational space of inward-facing MsbA and Pgp. From Moeller et al. [2015]. Inward-facing MsbA data is shown in blue, and in orange for P-gp. **(A)** Surface representations from MsbA apo X-ray structure. Red dots indicate the positions T561 on MsbA NBD, where separation distances are measured. Equivalent position is used on P-gp. **(B), (C)** First rows show experimental EM densities from apo proteins, arranged by increasing NBD separation. Second rows show the superposition of EM density with corresponding X-ray structures. Raw EM data are shown on the right. **(D)** NBD separation distance (or degree of opening measured between the red dots) distributions are shown for apo MsbA (light blue), ATP-bound MsbA (dark blue) and apo P-gp (orange).

High FRET (respectively low FRET) values correspond to apo conformations with close distance (respectively large distance) between the NBDs. Our experimental E distributions even exhibit FRET values higher than $0,9$, which corresponds to distances shorter than 34 Å according to our FRET calibration. However, the FRET calibration with a small interdye distance of 34 Å (done with a double-stranded DNA with 7 bp distance) shows that high FRET values go along with a larger peak. We do not have

any satisfying explanation for this observation, but this should be kept in mind when observing the long tail on the E distribution.

For *E.coli* and EPC/bPS 20^{o}C liposomes, the main peak centered on $E = 0,2$ shows that the majority of the proteins exhibit a conformation with a large opening between the NBDs, with a distance around 67 Å according to our calibration. This value is relevant with BmrA model, with cryo-EM data (Fribourg et al. [2014]) and with values found for MsbA and P-gp, both sharing high homology with BmrA (note that on BmrA the distance is measured at a different position (C436) compared to EM study of P-gp and MsbA, see red dots on figure 6.3A, and that we measure distances for BmrA incorporated in a membrane).

For EPC/bPS 4^{o}C liposomes, a different behavior is found. The peak at $E = 0,2$ disappears and the E distribution is very flat. The most populated state is not anymore the open conformation with large NBD separation. The long tail observed in the previous conditions is still present, indicating a large range of conformations that are all occupied with a similar probability. This puzzling result will be discussed further in part 6.4.

6.1.3 Vi Trapped BmrA

BmrA solubilized in detergent was trapped in post-hydrolytic conformation with ATP and vanadate (Vi), before to be reconstituted in liposomes. This protocol should guarantee 100% of proteins in closed conformation i.e. with NBDs in bound-state (high FRET). Figure 6.4 shows the FRET distributions obtained for Vi trapped BmrA according to liposomes size (same distributions as presented in part 5.4). In the three liposomes conditions, the FRET efficiency distribution exhibits a clear peak at $E = 0,4$, and no large tail distribution as for apo or the other conditions. This indicates that the proteins have a fixed conformation under addition of ATP and Vi, in agreement with ATPase activity measurements where 80% of inhibition by vanadate was measured (Paik [2018]).

According to our calibration, this corresponds to a NBD separation slightly smaller than 47 Å. Accordingly, the model for BmrA outward-facing conformation (based on SAV4886, PDB: 2HYD, see figure 3.9) provides a distance of 40 Å between the labelled positions C436. This is in agreement with the value measured with our calibration. However it seems that the NBDs are not in their more compact form. FRET values higher than $0,4$ corresponding to smaller NBD separation, i.e. to more compact conformations, are also accessible but these states are populated only by a low fraction of proteins. This result will be further discussed in part 6.4.

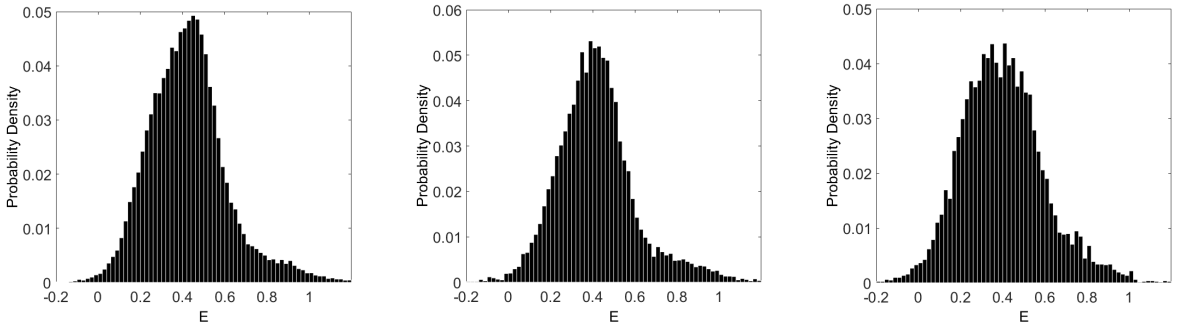

(a) Liposomes ∅ 140 nm (EPC/bPS 20^o). **(b)** Liposomes ∅ 60 nm (*E.coli*). **(c)** Liposomes ∅ 40 nm (EPC/bPS 4^o).

Figure 6.4: FRET distributions of Vi trapped BmrA. E distributions plotted for Vi trapped BmrA reconstituted in three different liposomes populations. Only particles exhibiting FRET signal are plotted.

6.1.4 ATP Vi BmrA

Protein inhibition was performed in another way: BmrA was incorporated in nucleotide-free conformation (i.e. apo) in liposomes and ATP/Vi were added afterwards. Figure 6.5 shows the FRET distributions obtained for ATP Vi BmrA according to liposomes size (same distributions as presented in part 5.4). In the three liposomes conditions, the FRET efficiency exhibits a similar distribution as for Apo BmrA with a clear main peak around $\langle E \rangle = 0,2$ and with a very long tail towards the high values of E. The same large distribution with a long tail was observed in the E_{mean} distribution. This indicates, as in part 6.1.2, that a majority of proteins are in open conformation with NBDs separation around 67 Å while a non-negligible amount have their NBDs closer together.

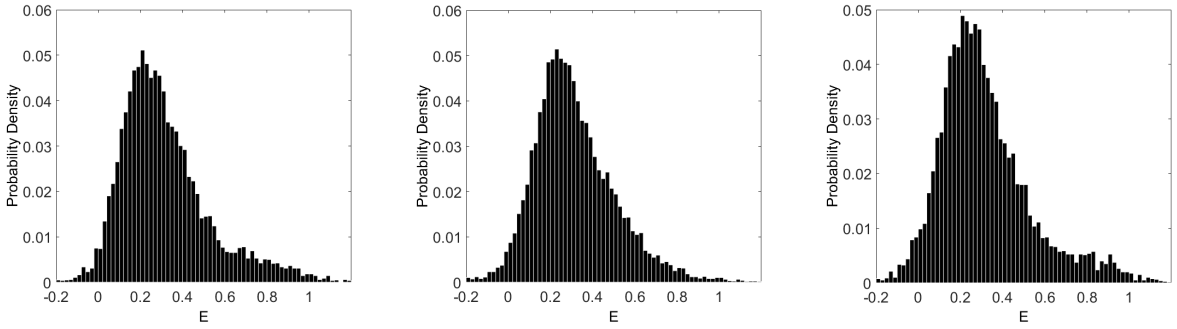

(a) Liposomes ∅ 140 nm (EPC/bPS 20^o). **(b)** Liposomes ∅ 60 nm (*E.coli*). **(c)** Liposomes ∅ 40 nm (EPC/bPS 4^o).

Figure 6.5: FRET distributions of ATP Vi BmrA. E distributions plotted for ATP Vi BmrA reconstituted in three different liposomes populations. Only particles exhibiting FRET signal are plotted.

In our experimental conditions, addition of ATP Vi did not modify the conformational space of BmrA compared to Apo. Importantly, this observation is contradictory with ATPase activity measurements performed on BmrA in *E.coli* liposomes (80% of inhibition by vanadate when added after reconstitution), which proves that the protein should be mostly in NBDs bound-state. Activity assays were performed at high density of proteins, for which it was shown that most of the proteins are oriented with outward-facing NBDs, i.e. accessible to ATP and vanadate molecules (75% for *E.coli* and EPC/bPS 20^{o}C liposomes, and 100% for EPC/bPS 4^{o}C vesicles). In my work, less than one BmrA was incorporated per liposome. The protein orientation was not tested and might be different than that for high protein density. Therefore accessibility of the NBDs to ATP and vanadate molecules is not guaranteed.

Nevertheless, this result is also contradictory with electron-microscopy observation of BmrA: proteins form ring shape structure in apo and addition of ATP and Vi leads to membrane flattening as shown on figure 3.12 (see part 3.2.3). However, these experiments were also done at high protein density. As mentioned above, outward-facing NBDs orientation is obtained in these conditions, and potentially, collective behaviors occur that do not show up in single-molecule regime.

The previous protocol, with BmrA trapped with Vi prior to reconstitution (6.1.3), provided 100% of proteins in closed conformation independently of their orientation in the liposome since the inhibition was done before incorporation. Here, the protein orientation is one possible limitation that would explain why the E distribution is similar to the Apo condition instead of Vi trapped.

In practice, another possible explanation could also come from the way the experiments are carried out. Vanadate actually requires precaution since it reacts with enzymes such as those used for ATPase activity assay or for oxygen-scavenger cocktails. The usual procedure consists in adding vanadate before ATP so that BmrA inhibition occurs at the first cycle of the protein. The protocol used is the following: after the liposomes containing BmrA are immobilized on the surface, a solution at 1 mM of vanadate is incubated in the chamber for 5 min. Then the oxygen-scavenger solution additionned with 1 mM of ATP is loaded in the chamber just before the observation. The pre-incubated solution of vanadate could therefore be rinsed out by the second solution, which could prevent from protein inhibition by the vanadate. This procedure can be optimized by incubating first the ATP, followed by injection of vanadate and, after rinsing the chamber, the oxygen-scavenger cocktail could be loaded to observe the sample.

However, we can probably argue that molecules of vanadate are not completely rinsed

out of the chamber, in particular near the surface of the coverslips where the liposomes are bound, since (i) the concentration of vanadate is very high as compared to the amount of proteins that are in the immobilized liposomes, (ii) solutions are gently injected in the channel and mixing between solutions probably occurs and (iii) the speed of the fluid is zero at the glass coverslip and very low close to the bottom of the chamber. We could thus expect that enough vanadate remains to trap the protein in closed conformation.

No explanation for this result is fully satisfying and another hypothesis will be presented in detail in part 6.4.

6.1.5 ATP BmrA

BmrA is incorporated in nucleotide-free conformation (i.e. apo) in liposomes and the protein is expected to cycle when ATP is added. Figure 6.6 shows the FRET distributions obtained for ATP BmrA according to liposomes size (same distributions as presented in part 5.4). Surprisingly, for the three liposomes conditions, similar distribution to Apo BmrA was found. The FRET efficiency distribution exhibits a clear peak around $E = 0,2$ and with a very long tail towards the high values of E. This indicates, as in parts 6.1.2 and 6.1.4, that a majority of proteins are in open conformation with NBDs separation around 67 Å while a non-negligible amount have their NBDs closer together. This result comes together with the observation that no clear dynamical signature is visible on the time traces (see part 5.4.1). Protein cycling between inward-facing and outward-facing conformations would have resulted in anti-correlated Donor and Acceptor signals.

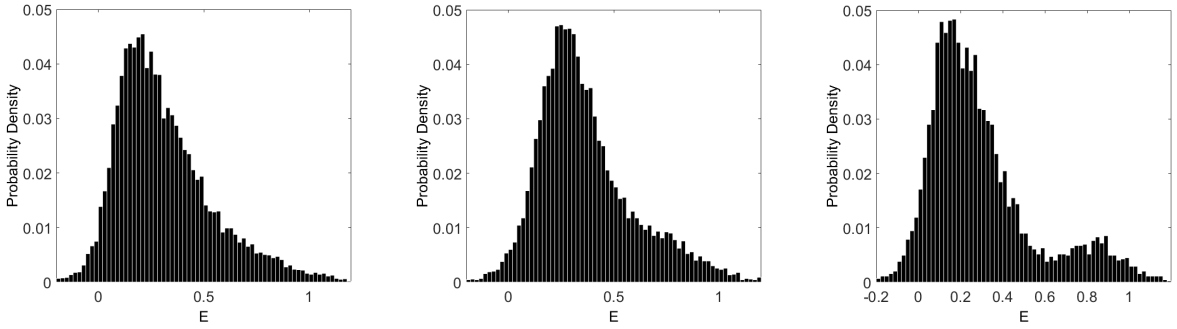

(a) Liposomes ∅ 140 nm (EPC/bPS 20^o). **(b)** Liposomes ∅ 60 nm (*E.coli*). **(c)** Liposomes ∅ 40 nm (EPC/bPS 4^o).

Figure 6.6: FRET distributions of ATP BmrA. E distributions plotted for ATP BmrA (ATP Ver for *E.coli*) reconstituted in three different liposomes populations. Only particles exhibiting FRET signal are plotted.

One possible explanation is that ATP hydrolysis leading to conformational change are rare events. As mentionned in part 5.4.1, the 50 ms exposure time was chosen to optimize the single-molecule observation and to be compatible with BmrA activity measurements. At 37^{o}C, one ATP per 250 ms is hydrolysed and therefore it should be less at 20^{o}C. With 50 ms exposure time over 5 s total observation time, we expected to detect a reasonable number of closure steps, if the life time of the closed state was long enough. However ATP cycles are rare events and, in general, ABC transporters are considered as not very efficient "machines".

The time necessary for a full cycle can be estimated from activity measurement but it is unknown how it distributes between the inward-facing (low FRET) and the outward-facing (high FRET) conformations. If the protein spends less than 100 or 150 ms in the outward-facing conformation (to allow two or three data points being recorded at high FRET), the NBD bound-state cannot be detected. DEER study on P-gp also shows that the protein is mostly in inward-facing conformation upon addition of ATP, with NBDs separation distance found similar as compared to apo (Verhalen et al. [2017], see part 6.3). Similarly, EM observation of MsbA by Moeller et al. [2015] shows that NBDs distance distribution is similar in ATP-bound state and in apo (see figure 6.3D). It suggests that BmrA, and other ABC transporters, promptly returns to the inward-facing conformation after hydrolysis and that the life-time of the outward-facing state is very short.

Finally, the orientation issues mentionned for the ATP Vi BmrA (see part6.1.4) remain valid for addition of ATP: if the NBDs are not accessible to nucleotides, the protein does not cycle.

6.2 Analysis of the fluctuations

The E histograms observed in Apo, ATP Vi and ATP conditions exhibit a peculiar distribution: it is not a single gaussian and the long tail at high FRET values indicates the existence of various intermediate conformations. Distribution of time average E_{mean} confirms this behavior. Several questions arise: can we extract further information from the fluctuations of E over time? Is the measurement of the standard deviation σ_E suitable to discuss the conformational flexibility of BmrA?

For each particle exhibiting FRET signal, in the time interval out of any blinking or bleaching events, we measure the standard deviation of E, σ_E and the time averaged E_{mean}. The DNA experiments are taken as a reference, since they contain the signal

fluctuations due to background noise and photostability of the Donor and Acceptor fluorophores. Figure 6.7a shows the box plots of σ_E for the three DNA samples with interdye distances 19, 12 and 7 bp. Fluctuations at 7 bp are surprisingly high but this is in agreement with the large E distribution we observed but could not fully understand. Given the mean positions $\langle E \rangle$ of FRET efficiency distributions for BmrA, the samples 19 and 12 bp are more relevant and their σ_E will be taken as a reference.

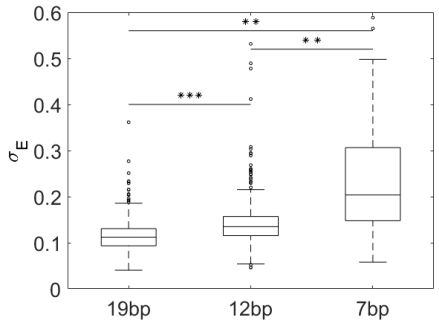

(a) DNA samples (respectively 712, 1030 and 258 data points).

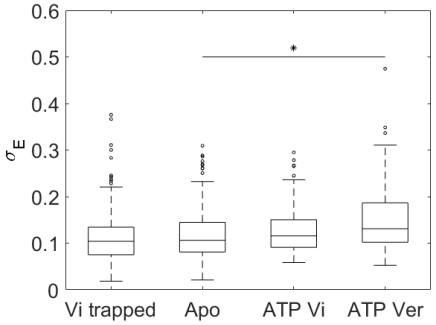

(b) *E.coli* liposomes (respectively 301, 164, 182 and 157 data points).

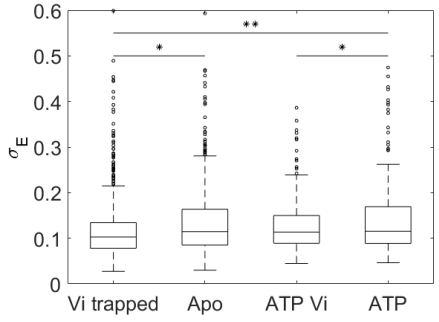

(c) EPC/bPS 20^{o}C liposomes (respectively 894, 566, 191 and 223 data points).

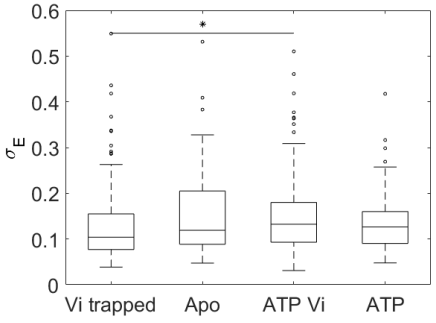

(d) EPC/bPS 4^{o}C liposomes (respectively 197, 79, 142 and 80 data points).

Figure 6.7: Fluctuations of the FRET efficiency for DNA and BmrA samples. For particles exhibiting a clear FRET signature, the standard deviation of the FRET efficiency σ_E is measured. Their distribution is depicted as a box plot. The box lower edge represents the first quartile, the upper edge is the third quartile, and the middle line is the median. 50% of the total data is contained in this box and $99,3\%$ is contained within the whiskers. p values were calculated between conditions indicated by: $\star$ for $p \leq 0.05$, $\star\star$ for $p \leq 0.01$, $\star\star\star$ for $p \leq 0.001$. When no star is indicated between two boxes, their relative p value is higher than 0.04 and corresponds to non significant difference.

Plotting σ_E could provide further informations on the dynamics of the protein, even though no cycling dynamics signature was visible on time traces in the presence of ATP, possibly due to the short life time of the closed conformation as compared to the exposure

time. A flexible protein in apo, or a cycling protein upon addition of ATP, i.e. exploring a larger space of conformations, would be expected to exhibit a higher standard deviation σ_E as compared to static (blocked) proteins inhibited by vanadate.

Figures 6.7b, 6.7c and 6.7d show the σ_E box plots for *E.coli*, EPC/bPS 20^{o}C and EPC/bPS 4^{o}C liposomes respectively. In general, the whiskers of the boxes are widder for BmrA than for the DNA samples, indicating intrinsic fluctuations to the protein. However, it is hard to identify a clear trend between the different conditions. On figures 6.7b and 6.7c, the ATP Ver and ATP condition provides slightly higher values of σ_E, coherent with a cycling protein. However this is not observed for EPC/bPS 4^{o}C liposomes (6.7d), where the apo BmrA seems to undergo more fluctuations.

Since, in general, we did not detect any change of the mean FRET value for each protein over the time course of our recording, we were wondering if the fluctuations depend on the mean conformation of the protein.To address this point, the standard deviation σ_E is plotted versus E_{mean} for the different conditions on figure 6.8. DNA samples serve as a reference. 7 bp sample exhibits higher values of σ_E corresponding to high FRET efficiencies, as reported before and in agreement with the large E distribution observed. 19 bp and 12 bp samples exhibit similar values of σ_E independently on the FRET efficiency. Data with BmrA in EPC/bPS 20^{o}C liposomes are shown on figure 6.8. No trend of σ_E is observable as a function of E_{mean} values. At high FRET, the fluctuations are higher as observed on DNA 7 bp. No difference is visible in the presence of ATP (figure 6.8g) as compared to the apo condition (6.8d).

Currently, FRET efficiency fluctuations are rarely used to analyse single-molecule dynamics. Hohlbein and collaborators propose methods to systematically analyse the distribution heterogeneity. For solution-based measurements (i.e. FCS), they propose a burst variance analysis (BVA) to discriminate static versus dynamic molecules (Torella et al. [2011]). For surface-immobilized molecules (observed with TIRF microscopy), the same group proposes an analytic expression to calculate σ_E accounting for background noise and shot noise (Holden et al. [2010]). σ_E reads

$$\sigma_E = \sqrt{\frac{f_G^2 E_{mean}(1 - E_{mean})}{D + A} + \frac{4\pi}{a^2(D + A)^4}(A^2 s_D^2 b_D^2 + D^2 s_A^2 b_A^2)}, \tag{6.2}$$

where E_{mean} is the mean apparent FRET value; s_D and s_A are the widths of the point spread function (PSF) in the donor and acceptor channels; b_D and b_A are the observed standard deviation (photons per pixel) of the background noise in each channel; D and

A are the photon counts for the entire PSF, in the donor and acceptor channels; a is the pixel size; and f_G is the excess noise factor accounting for noise introduced by the camera ($\sim 0,2$ for emCCD).

Using a DNA loop sample, Farooq and Hohlbein [2015] found σ_E higher than 0,2 for dynamic molecules while static particles exhibit $\sigma_E \simeq 0,1$. Discrimination between static and dynamic molecules can therefore be made by σ_E values selection.

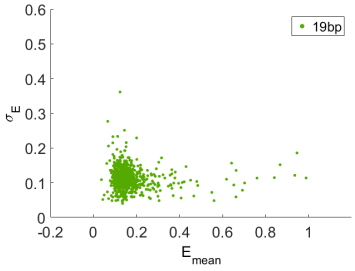

(a) 19 bp DNA (712 data points).

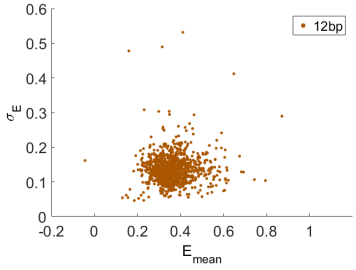

(b) 12 bp DNA (1030 data points).

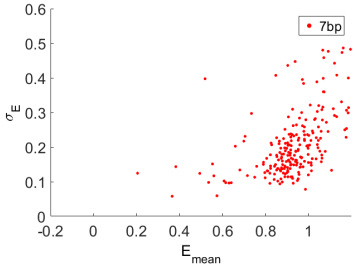

(c) 7 bp (258 data points).

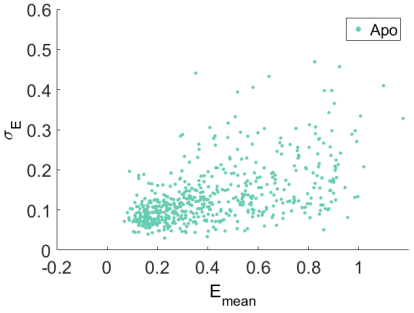

(d) Apo (566 data points).

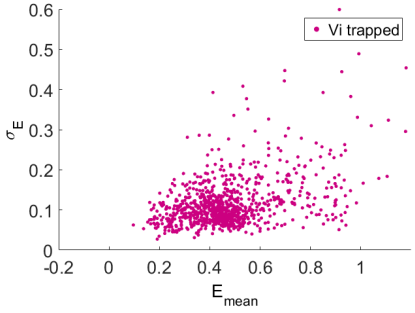

(e) Vi trapped (894 data points).

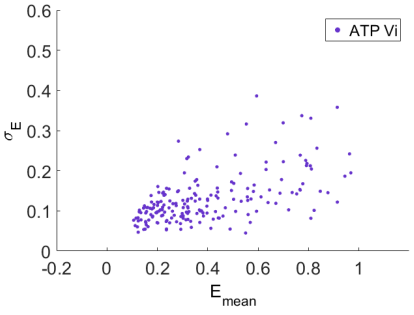

(f) ATP Vi (191 data points).

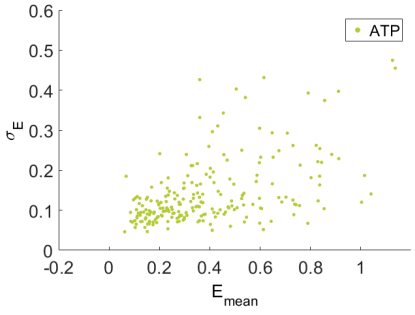

(g) ATP (223 data points).

Figure 6.8: Fluctuations of the FRET efficiency for DNA and BmrA in EPC/bPS 20^{o}C liposomes. For particles exhibiting FRET signature, the standard deviation of the FRET efficiency σ_E is plotted according to the time averaged efficiency E_{mean} for each protein. Data are shown for (a), (b), (c) 19 bp, 12 bp, 7 bp DNA samples respectively, and for BmrA in EPC/bPS 20^{o}C liposomes (d), (e), (f), (g) Apo, Vi trapped, ATP Vi and ATP respectively.

Our analyses of the distribution and of the fluctuations are very preliminary trials to

analyze the conformation fluctuations of BmrA in liposomes and are certainly oversimplified. Further analysis, that could not be achieved considering the limited duration of PhD, will be performed inspired by these studies.

6.3 Comparison with other ABC exporter studies

Very few studies have been released about distance change in ABC exporters conformations. The most studied have been the bacterial MsbA and human P-gp, that share high homology with BmrA. Some of these studies were introduced in part 3.1.3 but are now detailed in order to compare them with the present work.

Figure 6.9 summarizes distance measurements on the NBDs of MsbA (6.9a) and of P-gp (6.9b) using LRET or DEER methods. In general, two distances are found, corresponding to large and small NBD separation, i.e. to open and closed conformation respectively.

For MsbA in nanodiscs, Zoghbi and collaborators found that both populations were equally populated independently on the condition (apo, ATP-bound, MgATP, or MgATP vanadate) (Zoghbi and Altenberg [2018]). This indicates that, in a lipid bilayer, 50% of apo proteins have their NBDs close together, which is coherent with the long tail distribution obtained in Apo BmrA. In their study, addition of Mg^{2+} ATP (resulting in cycling proteins) leads to a visible effect with distribution flattening between the two peaks at 36 Å and 47 Å, as shown on figure 6.9a.B.

Studies on P-gp also show two populations corresponding to large and small NBD separation. LRET measurements by Zoghbi et al. [2017] on P-gp in nanodiscs show an increasing population at 33 Å upon successive addition of Verapamil, ATP, magnesium and vanadate, as depicted on figure 6.9b.B. They were able to detect an effect of ATP cycling and of protein inhibition. This is not the case in DEER study by Verhalen et al. [2017], where a distance change was found only in ATP and vanadate condition (see figure 6.9b.D). Addition of substrate (verapamil), ATP, AMP-PNP or ATP-vanadate leads to a distance distribution similar to apo. Our results are in agreement with this study since we observed a distribution change only in Vi trapped condition.

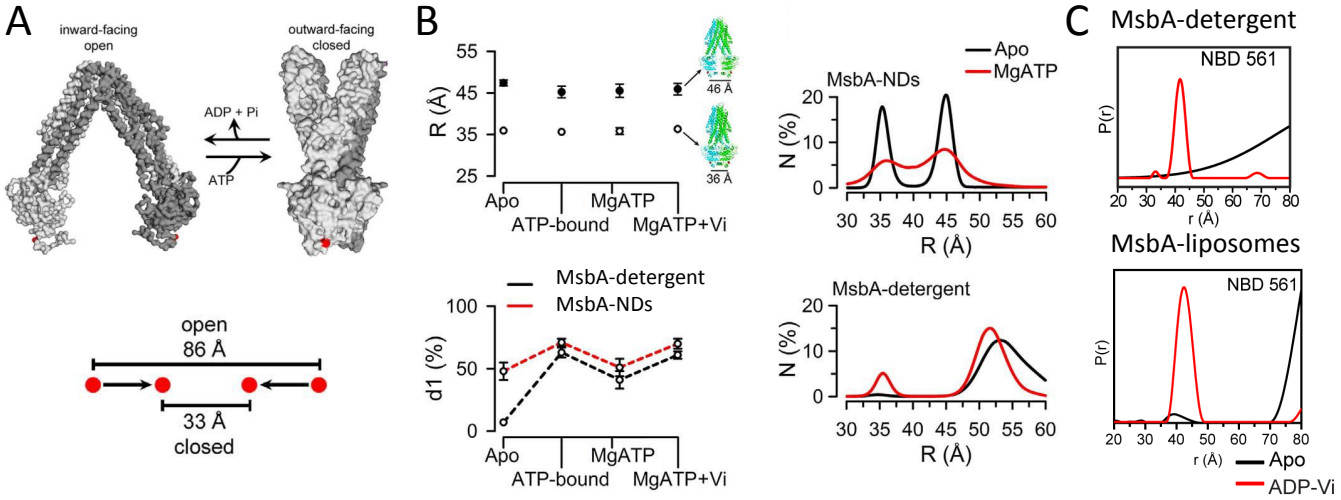

(a) LRET and DEER studies on MsbA (adapter from Zoghbi and Altenberg [2018] and Zou et al. [2009] respectively). (A) Model of MsbA based on crystal structure, in apo and post-hydrolytic conformations. The red dots show the labelled position 561, with the separation expected in both conformations. (B) LRET study of MsbA in detergent and nanodiscs (NDs). Two populations are systematically observed. d1 is the population fraction at $R = 36$ Å. (C) DEER study of MsbA in detergent and liposomes.

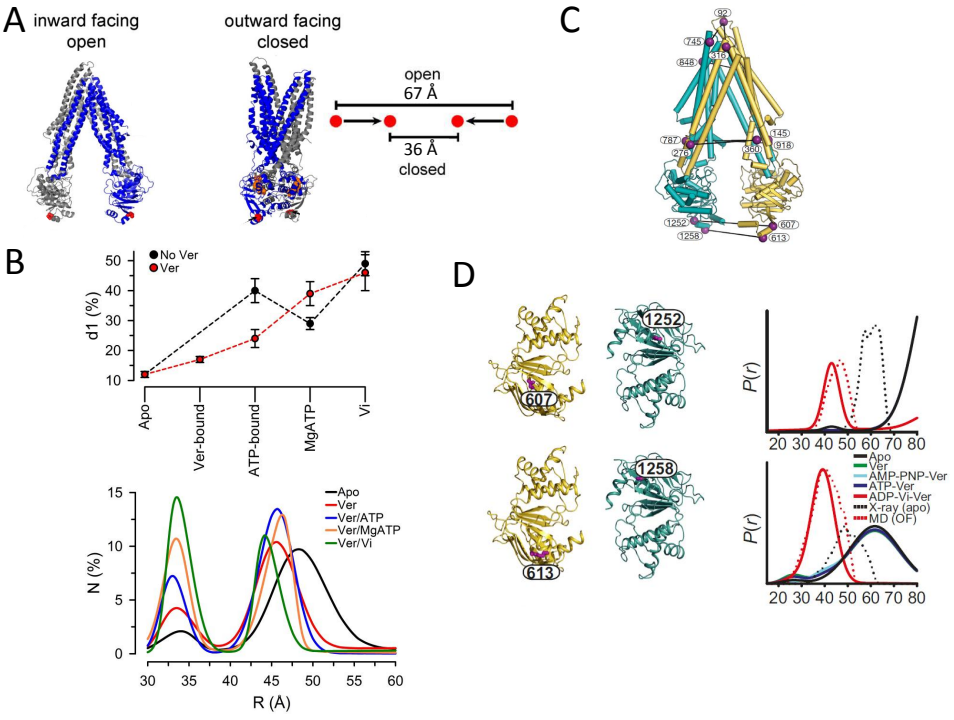

(b) LRET and DEER studies on P-gp (adapter from Zoghbi et al. [2017] and Verhalen et al. [2017] respectively). (A): Model of P-gp based on crystal structure, in apo and post-hydrolytic conformations. The red dots show the labelled positions 607 and 1252 for LRET, with the separation expected in both conformations. (B) LRET study of P-gp in nanodiscs (NDs). Two populations are systematically observed. d1 is the population fraction at $R = 33$ Å. (C) Model of apo P-gp. Purple dots show the successive labelled positions. (D) DEER study of P-gp in detergent. Black dotted lines correspond to X-ray apo structure, red dotted lines correspond to the outward-facing model.

Figure 6.9: LRET and DEER studies on MsbA and P-gp.

Concerning the distance measured for bound NBD-state, the results found by Zoghbi and Altenberg [2018] on MsbA, Zoghbi et al. [2017] on P-gp and Verhalen et al. [2017] on P-gp, are in good agreement with the distance provided by the respective models (based on crystal structures). Zoghbi and collaborators found 36 Å and 33 Å for MsbA and P-gp respectively, as compared to 33 Å and 36 Å from the model. Figure 6.9b.D shows that the ATP-vanadate measurement (red line) is in good agreement with the model (dashed red line). However, these three studies were done in detergent (Verhalen et al. [2017]) or in nanodiscs (Zoghbi et al. [2017]; Zoghbi and Altenberg [2018]). In a DEER study on MsbA in liposomes, Zou et al. [2009], the value 42 Å was measured in ATP Vi condition, indicating that the NBDs are not in their more compact form. This echoes back to our result with Vi trapped BmrA for the three liposome conditions, where the experimental distance was found higher than that given by the model (47 Å measured versus 40 Å expected). The different results obtained in detergent, nanodiscs and finally liposomes show that the lipid bilayer has an impact on the protein conformational space.

Protein	Protein environment	Method used	References
P-gp	Micelles lipids/detergent	DEER	Verhalen et al. [2017]
	Nanodiscs	LRET	Zoghbi et al. [2017]
	Liposomes	FRET (spectroscopy)	Verhalen et al. [2012]
MsbA	Detergent and nanodiscs	LRET	Cooper and Altenberg [2013]
			Zoghbi et al. [2016]
			Zoghbi and Altenberg [2018]
	Detergent and liposomes	DEER	Zou et al. [2009]
	Detergent and liposomes	DEER	Borbat et al. [2007]
McjD	Detergent and liposomes	smFRET	Husada et al. [2018]
BmrCD	Detergent and nanodiscs	DEER	Mishra et al. [2014]

Table 6.1: Some studies about ABC exporters. This is a non-exhaustive list of distance measurement studies about a few ABC exporters, indicating the environment of the protein (detergent, nanodiscs or liposomes) and the method used (DEER, LRET or smFRET).

Only a few studies were published about measuring distances in ABC exporter conformations and most of the measurements were performed in ensemble. Table 6.1 shows

a non-exhaustive list of both ensemble and single-molecule studies. Most of them were done in detergent or in nanodiscs and yet, some results proves that there is an effect of the membrane on the protein conformation. NBDs separation of MsbA was found smaller for the protein incorporated in nanodiscs and in liposomes as compared to detergent, as shown on figure 6.9aB and C (Zoghbi and Altenberg [2018]; Zou et al. [2009]). Distance measurements on three positions of single ABC exporter McjD (two in the TMDs and one in NBDs), both in detergent and reconstituted into proteo-liposomes, showed that the presence of a lipid bilayer impacts the overall conformation of the protein (Husada et al. [2018]). The interplay between ABC conformations and membrane environment is a new field that is to be investigated at the scale of single proteins. Our study proposes to fill these two gaps: a systematic study of the effect of membrane curvature on an ABC exporter at the single-molecule level. This interplay is discussed in detail in next part.

6.4 Interplay between BmrA and membrane mechanical properties

The present work was motivated by previous experimental data on BmrA (Fribourg et al. [2014]; Paik [2018]). First, electron-microscopy observation of BmrA reconstituted in liposomes showed that apo BmrA has a large opening and organizes in ring-shape structure, i.e. structures with a high curvature, suggesting a distance between the NBDs equal to 9 nm (total width at the NBDs level). Addition of ATP and vanadate, leading to outward-facing conformation, results in membrane flattening with a drastic reduction of the curvature. Secondly, ATPase activity measured at 37^oC (see figure 3.10) showed that (i) protein activity is higher in *E.coli* liposomes than in EPC based vesicles, indicating an effect of lipid composition, and (ii) for the same lipid composition (EPC/bPS), activity is twice higher in large liposomes (diameter ⌀ 140 nm) as compared to small liposomes (⌀ 40 nm), indicating an effect of membrane curvature. This study aimed at investigating further the impact of membrane curvature on the protein conformational space.

Protein spontaneous curvature.

Mechanical stresses applied by the membrane could perturb the conformational changes or fluctuations of the protein. In this study, I have investigated the effect of curvature. Small liposomes with a high curvature should perturb more the conformation of BmrA than larger liposomes that should result in lower stresses. Nevertheless, the stress experienced by the protein will depend on its relative orientation in the liposomes, since BmrA can be oriented with outward- or inward-facing NBDs. At the single-molecule level, there

might be a competition between the conformation and orientation of BmrA incorporated in liposomes and the membrane bending of the corresponding liposome. Indeed, based on structural data on P-gp and MsbA and on unpublished data in our group on BmrA (Mahalka et al., in preparation), the spontaneous curvature of the transmembrane domains of ABC transporters switches sign (positive to negative) when the protein changes conformation from apo to post-hydrolytic. Figure 6.10 represents the possible situations that BmrA experiences depending on its orientation and conformation, when it is incorporated into small proteo-liposomes. Two situations are energetically favourable in term of spontaneous curvature: open protein with outward-facing NBDs or closed protein with inward-facing NBDs. In the two other cases, the protein does impose a negative curvature to the neighbouring lipids. Such a deformation has an extra energetic cost as compared to the favourable cases, which might bias the conformational distribution of the proteins.

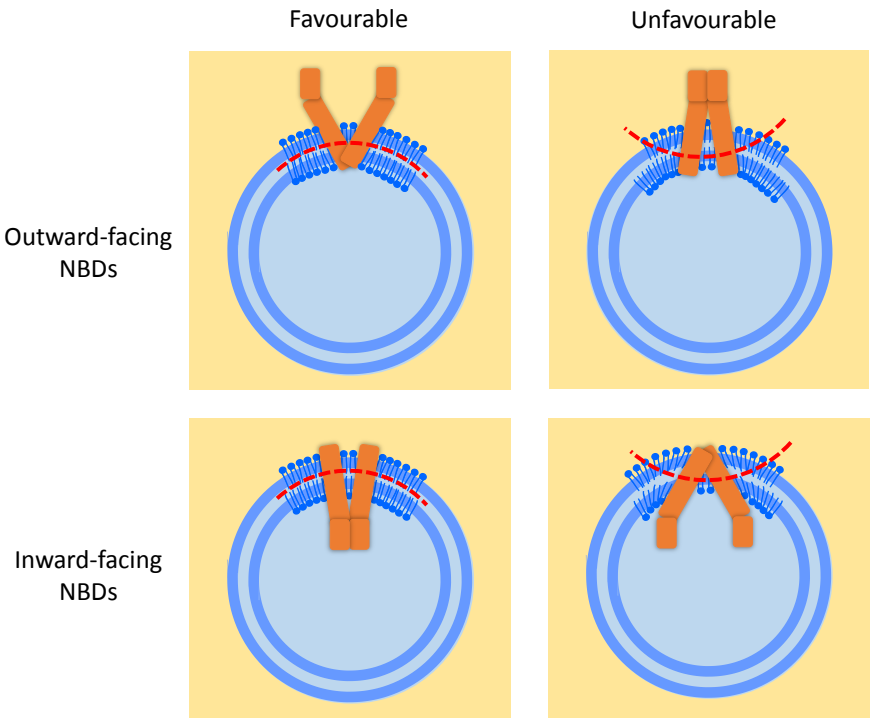

Figure 6.10: Conformation and orientation of BmrA in liposomes versus membrane bending. Scheme of BmrA (orange) incorporated into proteo-SUVs. Lipid bilayer is depicted as a blue double circle, the protein neighbouring lipids are represented to show their orientation. Blue solution inside the liposome is the reconstitution buffer, yellow solution is the observation buffer that may contain ATP or ATP-vanadate. ATP (and inhibitor) can access hydrolysis sites only when the protein is oriented with outward-facing NBDs. Dashed red lines represent the spontaneous curvature of BmrA in both conformations open and closed. Favourable (respectively unfavourable) designates a state where the protein conformation and orientation do not (resp. do) impose an opposite bending to the lipid bilayer.

Effect of liposome size.

Several results in this study are in favor of this hypothesis. First, the fluctuations mean level observed with BmrA in the different conditions is very similar to that of DNA samples (although the fluctuation distribution of the protein are a bit larger than for the DNA samples, see figure 6.7), indicating mostly static protein conformations. In addition, the distributions of time-averaged E_{mean} were found similar to E distributions, with similar widths in particular, for all conditions. Therefore, BmrA might access a large conformational space with different NBD separations, but each conformation is static, indicating that the conformation (in terms of NBD separation distance) would be fully determined by the size of the corresponding liposome and does not change after incorporation. If this hypothesis is correct, the large E distribution of apo BmrA would result from the distribution of liposomes' size. To address this hypothesis, the method developed in the lab of Dimitrios Stamou (Lohr et al. [2009]; Hatzakis et al. [2009]), which consists in measuring the size of individual liposomes by fluorescence, could be used here.

Interestingly, we observed similar behaviors for *E.coli* and EPC/bPS 20^{o}C liposomes (⌀ 60 and 140 nm respectively). In contrast, apo BmrA in small liposomes EPC/bPS 4^{o}C (⌀ 40 nm) exhibits a very different E distribution, potentially indicating a threshold in curvature between 1/30 and 1/20. The E distribution was large and flat, with no maximum at low FRET.

Additionnally, relatively less FRET data points were collected for apo BmrA in EPC/bPS 4^{o}C vesicles, as compared to *E.coli* and EPC/bPS 20^{o}C liposomes (the fraction of FRET data points were 6,5%, 12,8% and 10,4% respectively). This corresponds to 79 FRET data points observed in this small liposomes. Future experiments will aim at increasing the number of data points for this condition. Nevertheless, this result might suggest that most of the proteins have a larger opening in small liposomes, with larger NBD separation resulting in increased distance between Donor and Acceptor fluorophores, and therefore do not exhibit any FRET signal. This result is in agreement with our hypothesis: mechanical stresses arising from membrane curvature experienced by the protein result in a larger NBDs separation.

Orientation of BmrA in the liposomes.

In Vi trapped condition, the protein is incorporated in its closed conformation. Considering the spontaneous curvature of the transmembrane domain, proteins could be potentially oriented with inward-facing NBDs since it is energetically favourable (figure 6.10). However, the distance measured for Vi trapped proteins is of the order of 47 Å according

to our calibration, which is higher than the distance calculated with BmrA model, 40 Å. Thus, the more compact form of BmrA is not reached on average. This could be due to a fraction of proteins with outward-facing NBDs, that undergo a mechanical stress from the membrane bending, leading to a higher NBD separation than that predicted.

For ATP Vi and ATP conditions, the E distributions are similar to apo BmrA, indicating no conformation change towards NBD bound-state. The orientation of the protein in vesicles is crucial here, since ATP and inhibitor are added in the observation buffer and require accessible NBDs to be effective. Only the outward-facing NBDs orientation is impacted by addition of reagents. Nevertheless, if ATP binds and induces a conformation change, the initial (positive) curvature of the membrane might inhibit such a change towards a conformation with a negative curvature, or might decrease the life-time of the closed conformation.

Future experiments should aim at determining the orientation of BmrA in the liposomes. This can be achieved by digesting NBDs with trypsin (see part 4.2.3). Outward-facing NBDs are digested with trypsin, resulting in a loss of fluorescence since the dyes are located on the NBDs, whereas inward-facing proteins do not get affected by trypsin addition. Effects of BmrA orientation and conformation will then be investigated.

Energetic considerations.

Figure 6.11 proposes a very schematic energy profile of BmrA conformational change. We propose that there is an energy barrier between the apo and the closed conformation. The main energies implied are: (i) the thermal fluctuations that, due to the flexibility of the BmrA apo structure, can allow to sample different NBDs separations, and (ii) the energy from ATP hydrolysis that is high enough to release BmrA in closed back to open conformation. Adding bending energy from a lipid membrane can modify this profile: either helping or preventing closing depending on the orientation of the protein in the liposomes. We propose that there is a competition between the energy required to change the protein conformation and the mechanical energy of the membrane.

Other studies carried-out about ABC transporters do not account for membrane mechanical properties and most of the experiments have been performed on proteins (i) in detergent, where no mechanical stress is applied to the proteins, and (ii) in nanodiscs, where the membrane environment exerts a compression on the protein but no bending or stretching (see table 6.1 for a non exhaustive list of ABC studies). Our study proposes a new vision on ABC exporters in lipidic environment, and no testing of our hypothesis is

possible by comparing with another ABC exporter study in similar conditions.

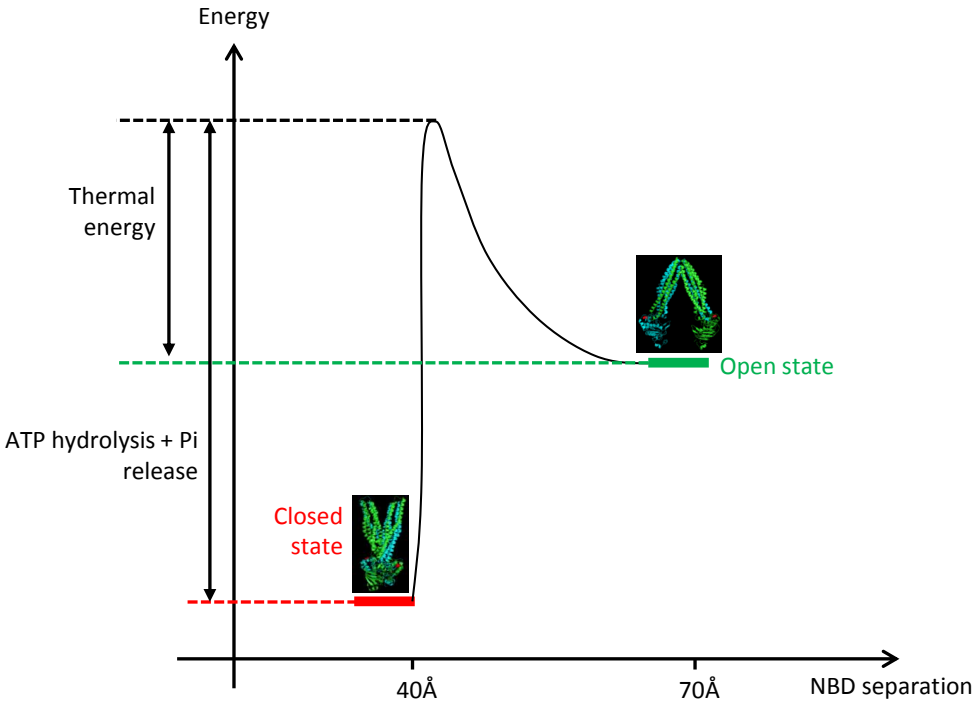

Figure 6.11: Possible energy profile of BmrA conformational change. Open state has a certain flexibility and different NBD distance are accessible thanks to thermal fluctuations. In theory, ATP binding leads to dimerization of NBDs and to closed state protein. Cycling back to open conformation requires energy from ATP hydrolysis and phosphate release. This energy profile can be modified if the protein is incorporated in a membrane since it adds a bending energy that is favourable to one conformation depending on protein orientation (see figure 6.10).

Chapter 7

Conclusions and perspectives

In this study, we proposed a robust protocol to study single-molecule ABC transporter BmrA in three well characterized liposomes conditions, in terms of lamellarity, size and single-molecule protein incorporation. The NBDs separation in the different conditions (Apo, Vi trapped, ATP Vi and ATP) was probed by single-molecule FRET. Some experimental potential improvements were suggested all along the results discussion, and a summary is proposed here, as well as short and long-term perspectives of this project.

7.1 Conclusions and short-term perspectives

- We showed that BmrA can explore a large conformational space, in agreement with previous studies on MsbA and P-gp (Moeller et al. [2015]). Large E distribution were found (with long tails) in all conditions with efficiencies values up to 0,9. From this large conformational space, two states are more populated depending on the condition. In Apo, ATP Vi and ATP (or ATP Ver), a state at $E \simeq 0,2$ is more populated, corresponding to an open conformation with NBD separation of the order of 67 Å(the long tail of the distributions indicates other accessible conformations with closer NBDs). In Vi trapped, the highest probability was found at $E \simeq 0,4$, corresponding to a closed conformation with NBD separation of the order of 47 Å.

  A refined analysis of the distributions, in particular of the long tails, could inform us more precisely on the structural flexibility of the protein and on how ATP hydrolysis changes it, or not.

- Addition of ATP does not lead to a clear population change in terms of FRET efficiency, at least for the largest EPC/bPS 20^{o}C liposomes and in *E.coli*. This was surprizing in this last case, since a twice higher activity was measured with the

enzymatic assay. One possible explanation is that our total acquisition time of 5 seconds is too short to observe BmrA cycling, since a full cycle is expected to last over 1s at 20^{o}C. It might also be that BmrA promptly returns to the inward-facing conformation after hydrolysis and that the life-time of the outward-facing state is very short, as suggested for P-gp in Verhalen et al. [2017].

In order to investigate BmrA dynamics, we propose the two following approaches. The first simply consists in increasing the acquisition time, in order to test the first hypothesis. The second, that has already been initiated and presented in part 6.2, consists in studying the fluctuations of the FRET efficiency signal (Holden et al. [2010]) and to extract information about the state of the protein. Investigating fluctuations allows to discriminate static from dynamic molecules (Farooq and Hohlbein [2015]).

- Closed state BmrA, with a normal distribution peaked at $E \simeq 0,4$, was observed only in one condition, when BmrA is trapped by ATP and vanadate in NBD-bound state before to be incorporated in liposomes. This is in agreement with previously reported results on P-gp (Verhalen et al. [2017]). The value of the FRET efficiency is in agreement with the expected distance between NBDs, from the structure predicted by analogy with MsbA and P-gp, of the order of 40 Å. However, the results obtained when ATP Vi is added a posteriori to the apo form are puzzling, since no conformation change was observed. It could be due to an experimental issue (loading of vanadate is done prior to addition of ATP, see part 6.1.4). It might also result from mechanical stresses applied to the protein by the membrane and preventing from NBDs dimerization.

  One obvious way to address this issue is to try a different strategy for loading ATP and vanadate in the observation chamber. Testing our second hypothesis requires a reference for BmrA behaviors when not incorporated in a lipid bilayer (or in a membrane without mechanical stress (floppy GUV)).

- In addition, accounting for all our observations, we suggest that bending energy in proteo-SUVs (with a size $\leqslant$ 150 nm) is high as compared to the energy required to bring the NBDs in close contact. Membrane curvature might hinder protein closing and bias the life-time of open and closed conformations. In our experiments, we suggest that two parameters might affect protein conformations and turnover in presence of ATP: membrane curvature and protein orientation.

In order to address this hypothesis, a reference with a non-curved membrane is required either in a flat membrane or in detergent. Ensemble FRET measurement can be done with protein incorporated in GUVs, and smFRET measurements can be performed with BmrA in micelles detergent/lipids, immobilized on a surface and observed with TIRF microscopy.

Doing experiment in detergent/lipids is interesting for two different reasons: (i) single-molecule results can be compared with what has been previously reported about other ABC transporters in detergent (see table 6.1 for the references), and (ii) it allows to circumvent the issue of protein orientation and NBDs accessibility to reagents such as ATP and vanadate. The strategy for single protein immobilisation was already optimized, based on previously reported method by Dyla et al. [2017]. The protocol, raw images and preliminary characterization of proteins attachment are available in appendix C.

- If our hypothesis is true that membrane curvature has an impact on protein conformational space and dynamics cycle, our long-term objective is to characterize more precisely this effect. In our work, currently, three populations of liposomes are used with a certain distribution of sizes and only the average diameter of each population is considered. Precise investigation of membrane curvature effect would require a fine measurement of liposomes' individual size. Work from Dimitrios Stamou and collaborators shows that it is possible to measure the diameter of each single immobilized liposomes by using fluorescent lipids (Tonnesen et al. [2014]). In the present study, this requires to add a third fluorophore on top of Donor and Acceptor dyes, and to check carefully for possible leakage and cross-talk in the channels used for FRET measurements. This provides a system to address precisely our hypothesis, to probe finely the conformation of BmrA according to membrane curvature and to find the limit value of curvature that prevents from protein cycling.

7.2 Long-term perspectives for BmrA study

The effect of another membrane mechanical property can be investigated. The effect of membrane tension on BmrA conformations could be addressed by smFRET measurements in GUVs, where tension is controlled via pipette aspiration (Evans and Rawicz [1990]). These experiments will be technically more challenging, since the proteins will be free to diffuse in the GUV membrane, and will escape rapidly the field of view (Quemeneur

et al. [2014]).

Finally, not only the conformation of ABC transporters can be affected by membrane mechanical properties, but also their diffusive behaviour in GUVs, as introduced in part 2.2.6. Long-term perspective on BmrA project is to measure the diffusion coefficient of the protein according to membrane tension, both in open and closed conformation. It was shown that cylindrical-shaped proteins diffusion is not affected by membrane tension while conical-shaped proteins diffusion coefficient decreases with membrane tension (Quemeneur et al. [2014]). BmrA conformations have a distinct shape, apo has a V-shape with large opening and positive spontaneous curvature, and closed conformation has a slightly negative spontaneous curvature. A signature of BmrA conformation should be observed in their diffusive behaviour on a GUV. A long-term objective, although quite difficult, would be to measure simultaneously the diffusion coefficient and the conformation of the protein with smFRET and single particle tracking at high spatial and time resolution.

Appendices

Appendix A

BmrA purification, labelling and characterization

The expression, purification and labelling of BmrA (WT and mutants) was optipmized by Su-Jin Paik and John Manzi, adapting the previously reported method (Steinfels et al. [2004, 2002]; Wiseman et al. [2014]).

A.1 Purification of BmrA

The expression of BmrA in E.Coli and the membrane fraction preparation were carried out by John Manzi from plasmids provided by Jean-Michel Jault (IBCP, Lyon). Most of the protein batches used during this thesis were purified and labelled by Su-Jin Paik. BmrA purification was done using the histidine tag present at its C-terminal and in detergent DDM at $0,05\%$ (weight).

The DDM solution at 10% is prepared fresh each time in ultra pure water. 25 mg of membrane fraction are added to 25 mL of solubilization buffer A (for all the buffers compositions see A.1). The solubilization is allowed for 1 h at 4^oC under stirring (on a spinning wheel). The solution is centrifuged at 50000 rpm for 30 min in a 70TI rotor at 4^oC. After centrifugation, the non solubilized pellet forms a brown stain at the bottom of the tube and the solubilized protein remains in solution. The supernatant is added to 1 mL of pre-washed Ni-NTA agarose beads (the washing steps are done using batch method with 50 mL of water, then with 10 mL of buffer B, centrifuged at 1000 g for 3 min). The solution is incubated for 2 h at 4^oC under stirring and the histidine tag allows BmrA proteins to bind selectively on the beads. We remove the supernatant (it is kept until we are sure the protein anchored on the Ni-NTA resin) and we wash the beads using batch-method with 5 mL of buffer B. The resin is loaded on a column and washed with 4 mL of buffer C to eliminate β-mercaptoethanol. 250 mL fractions of elution buffer D are added successively to the column and the fractions containing the protein are collected in different tubes. Each step of the purification process is analyzed on a 12 or 15% SDS-Page (see an example on figure 4.3). The concentration of the protein fractions is measured by Bradford method.

At this step, the protein can be frozen in small aliquots (5 to 10 μL) in liquid nitrogen and stored at -80^oC. For this project, the protein is systematically labelled in order to perform FRET experiments. Purification of non-labelled protein can be done at pH 8.0 (Tris and Imidazole in buffers C and D are

then at pH 8.0) but in this case the protein is eluted at pH 7.0 where the labelling is more efficient afterwards.

	Tris	NaCl	Imidazole	DDM	Glycerol		
Buffer A *Solubilization*	100 mM pH 8.0	200 mM	20 mM pH 8.0	1%	10%	1 mM PMFS	1 Protease inhibitor tablet
Buffer B	100 mM pH 8.0	100 mM	20 mM pH 8.0	0,05%	10%	5 mM βme	
Buffer C	100 mM pH 7.0	100 mM	20 mM pH 7.0	0,05%	10%		
Buffer D *Elution*	50 mM pH 7.0	100 mM	250 mM pH 7.0	0,05%	10%		
Buffer E	100 mM pH 8.0	100 mM	0	0,05%	10%		
Buffer F	100 mM pH 8.0	100 mM	20 mM pH 8.0	0,05%	10%		
Buffer G *Elution*	50 mM pH 8.0	100 mM	250 mM pH 8.0	0,05%	10%		

Table A.1: Purification buffers. Composition of the buffers used for protein purification (A to D) and labelling (E to G).

A.2 Protein labelling with fluorescent probes

Each NBD carries a single cystein residue C436, that are labelled with fluorescent maleimide dyes. The labelling step is performed on the purified protein in detergent at pH 7.0 (in order to avoid non specific labelling of other residues such as lysines and arginines). The unbound dyes are eliminated using the specific affinity of BmrA histidine tag to Ni-NTA beads (at pH 8.0) just as before.

The fluorescent dyes are dissolved in DMSO to 10 mM, aliquoted and stored under argon gas at -20^{o}C. The dyes used are summarized in table A.2.

Dye	Donor or Acceptor	Molar extinction coefficient ϵ ($cm^{-1}.M^{-1}$)	Maximum Exc/Em wavelength (nm)	MW ($g.mol^{-1}$)	Company
Alexa Fluor 488 C5 Maleimide (Alexa488)	Donor	72000	493/516	720.7	Sigma
sulfo-Cyanine 3 Maleimide (sCy3)	Donor	162000	548/563	777	Lumiprobe
sulfo-Cyanine 5 Maleimide (sCy5)	Acceptor	271000	646/662	803	Lumiprobe

Table A.2: Fluorescent dyes. The following dyes are used in my project to perform FRET experiments.

The purification of the protein is performed as in section A.1. The pure protein is obtained in fractions of buffer D at pH 7.0. The most concentrated fractions (from fraction 2 to 4 or 5 generally) are combined (around 1 mL total) and we measure the concentration by Bradford assay. The fluorescent dyes are added at ratio 1 : 10 : 10 mol/mol/mol for Protein: Donor: Acceptor and incubated over night at 4^{o}C on the spinning wheel. The protein sample is diluted in 15 mL of buffer E to bring the imidazole concentration lower than 20 mM. 0,5 mL of pre-washed Ni-NTA agarose beads are added (the washing steps are done using batch method with 25 mL of water, then with 5 mL of buffer E, centrifuged at 1000 g for 3 min). The solution is incubated for 4 h at 4^{o}C on the spinning wheel. This step allows to separate the protein-bound from the unbound dyes (see on figure 4.3 in column 8 the white arrow indicates the free dyes that remain in the beads supernatant). The Ni-NTA resin is washed in batch with 1 mL of buffer F and then over the column with 5 mL of buffer F. 100 mL fractions of elution buffer G are added successively to the column and the fractions containing the protein are collected in different tubes. Each step of the purification process is analyzed on a 12 or 15% SDS-Page by fluorescence (see an example on figure 4.3, in column 10 after the labelling we see a band at 65 kDa for BmrA which is also visible by fluorescence).

The concentration of the protein fractions is measured by Bradford method. The concentration of fluorescent dyes is measured by absorbance. The rate of labelling is the ratio between dyes and protein concentrations. The protein is frozen in small aliquots (5 to 10 μL) in liquid nitrogen and stored at -80^{o}C. The protein is kept in detergent as the last elution buffer G contains $0,05\%$ of DDM.

A.3 Protein activity measurement

The ATPase protein activity is measured with an enzymatic assay using the difference of absorbance of the reduced and oxidized form of Nicotinamide adenine dinucleotide (NADH/NAD^+) at 340 nm as

shown on figure A.1.A. This assay was optimized by Su-Jin Paik during her thesis. The principle is summarized on figure A.1.B. The drop of NADH absorbance is inversely proportional to the quantity of ATP hydrolysed by the protein.

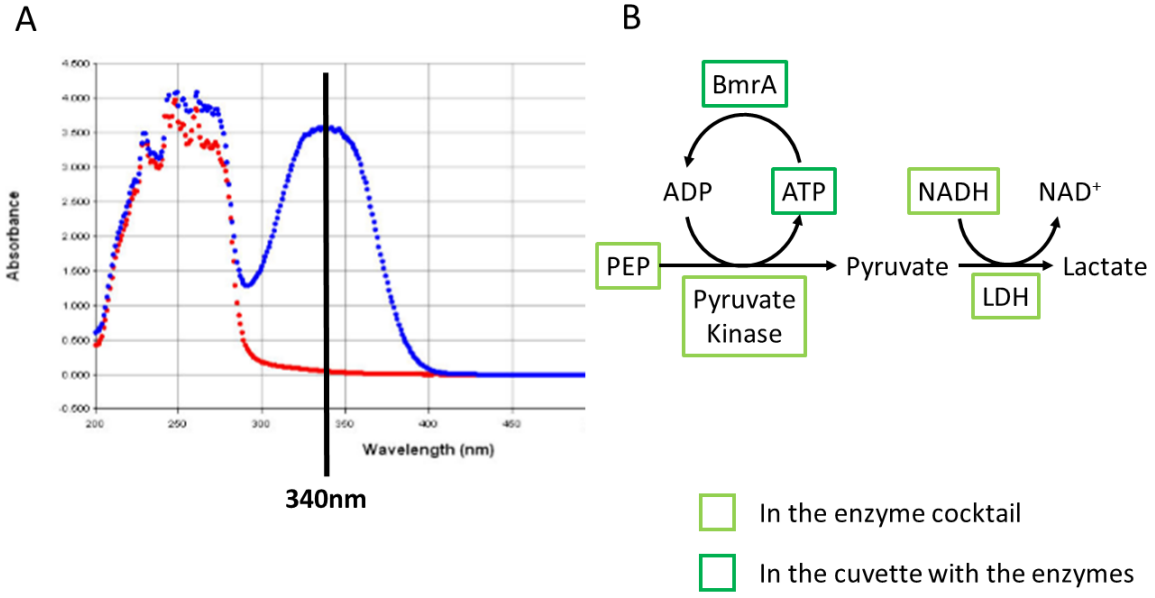

Figure A.1: ATPase activity assay. A. Absorbance spectra of NADH and NAD^+. At 340 nm, NADH (in blue) absorbs while NAD^+ (in red) doesn't. *Ref. https : //www.biotek.com/resources/docs/NADH_AppNote.pdf*. **B.** Enzyme reaction to measure the consumption of ATP by BmrA.

Preparation of 5× enzymes cocktail.

The solution is prepared in buffer (50 mM MOPS pH 7.5, 150 mM NaCl) just before the measurement and is kept on ice in the dark. The final quantities in 200 μL total are : 2 mmoles of NADH, 100 units/mL of LDH (L-Lactate dehydrogenase), 500 units/mL of PK (Pyruvate kinase), 2,5 mM of PEP (Phosphoenolpyruvate). (All products are purchased from Sigma.)

Activity measurement.

The absorbance of NADH is measured with a spectrometer (Cary Win 60 UV-Vis, Agilent Technologies) at 340 nm every 15 seconds for 4 min, in a quartz cuvette (Hellma Analytics, 3×3 mm). A controller allows to keep the sample at 20 or 37°C. 100 μL are prepared in buffer (50 mM MOPS pH 7.5, 150 mM NaCl, 10 mM $MgCl_2$) with 1× enzyme cocktail and 0.5 μg of protein. We check the quality of the enzyme cocktail by adding ADP before to start the measurement : we observe a drop of absorbance indicating that the enzyme reaction works. ATP is added to a final concentration of 10 mM and the absorbance drop is recorded for 4 min. The activity is calculated from the slope between 1 and 4 min (first minute is ignored to avoid taking into account the dilution-related drop). The inhibition rate can also be calculated by adding an inhibitor to the cuvette.

Samples summary.

In this work mainly two batches of BmrA were used, labelled with different dyes to form two FRET

couples : Alexa488/sCy5 et sCy3/sCy5. The characteristics of these batches are summarized on table A.3.

Couple	Rate of labelling (%)	Percentage of doubly labelled	Activity conservation compared to unlabelled WT (%)
Alexa488/sCy5	36,4/52,6	38,3	76
sCy3/sCy5	31,5/38,7	24,4	79,8

Table A.3: Summary of protein batches.

Appendix B

Supplementary figures and results

B.1 Surface cleaning

Raw images taken at different excitation wavelengths show the quality of coverslips cleaning protocol.

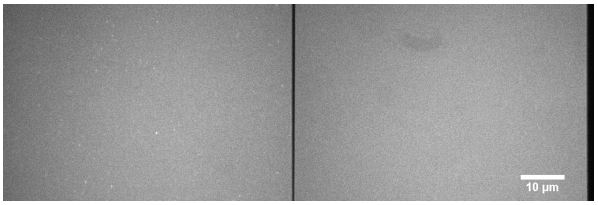

(a) Background at 488 nm taken with laser power 4/5 at 250 ms exposure time with the filter set for the FRET couple Alexa488/sCy5 (see table 4.4)

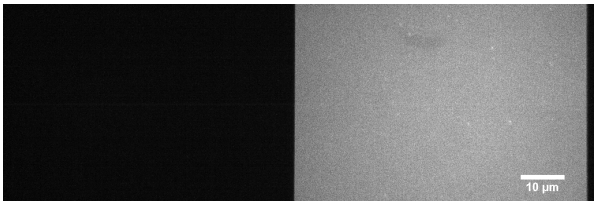

(b) Background at 638 nm taken with laser power 4/5 at 250 ms exposure time with the filter set for the FRET couple Alexa488/sCy5 (see table 4.4).

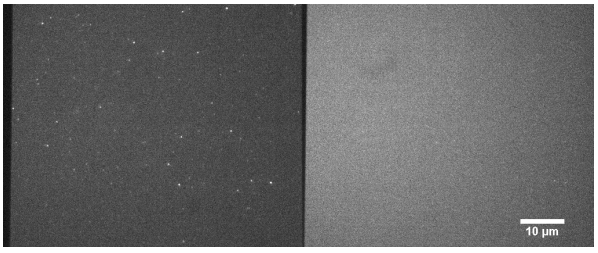

(c) Background at 532 nm taken with laser power 3/5 at 150 ms exposure time with the filter set for the FRET couple sCy3/sCy5 (see table 4.4)

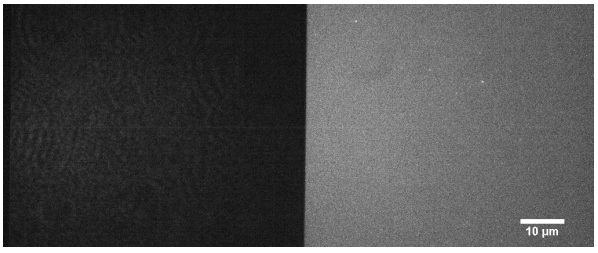

(d) Background at 638 nm taken with laser power 3/5 at 150 ms exposure time with the filter set for the FRET couple sCy3/sCy5 (see table 4.4).

Figure B.1: Surface cleaning evaluation. An empty chamber is observed after all the steps of surface treatment.

B.2 Single molecule observation of DNA samples

Raw images of DNA samples with interdye distances 19, 12 and 7 bp show an increasing FRET signal (middle channel) with decreasing distance.

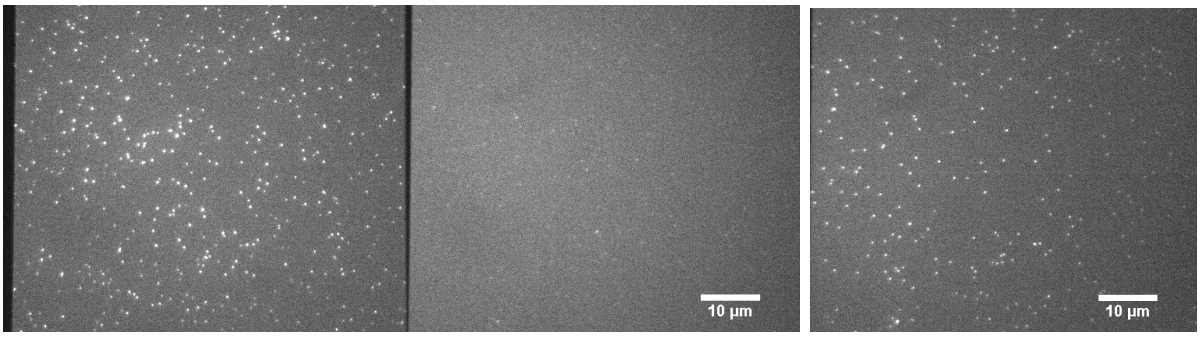

(a) Distance of 19 bp between Donor and Acceptor.

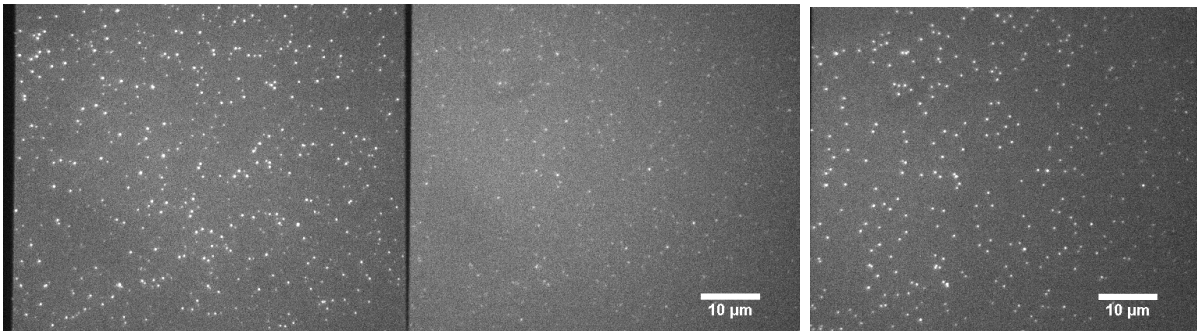

(b) Distance of 12 bp between Donor and Acceptor.

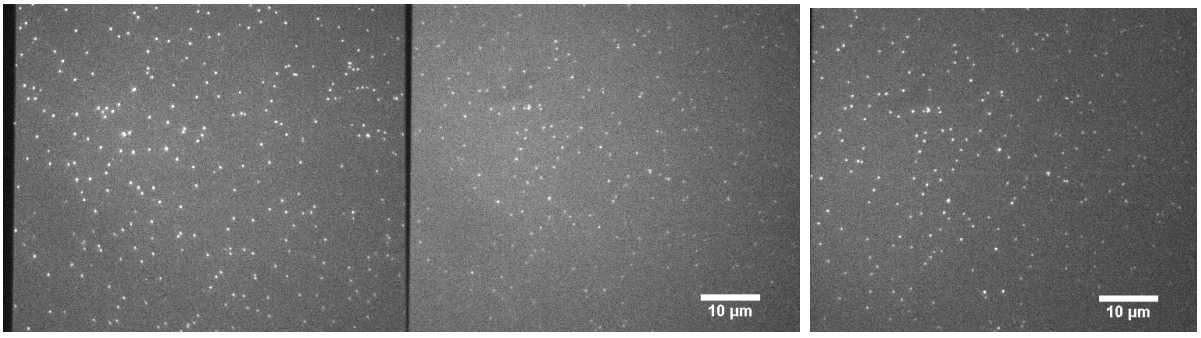

(c) Distance of 7 bp between Donor and Acceptor.

Figure B.2: smFRET images of double stranded DNA labelled with sCy3/sCy5. Left: Dual View image at excitation 532 nm (left is the Donor channel, right is the FRET channel). Right: Image at excitation 638 nm (only Acceptor channel is shown from the Dual View image). The FRET signal (in the middle) increases when the interdye distance decreases: we observe minimum signal at 19 bp, intermediate at 12 bp and maximum for 7 bp.

B.3 Single-molecule FRET results in three different conditions

Supplementary figures show E and E_{mean} distribution (see main text for definitions) for:

- "snapshots" and "movies" data,
- all data points or limited to data points exhibiting FRET.

B.3.1 Liposomes EPC/bPS of 140 nm diameter

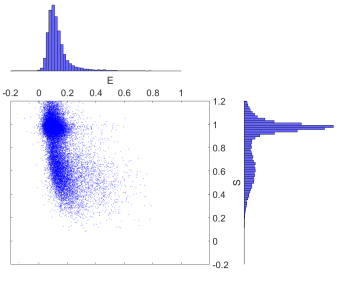

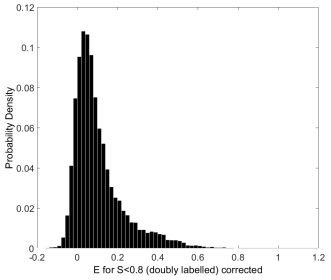

(a) Apo (27868 data points). **(b)** Apo (8117), $\alpha = 0,116$.

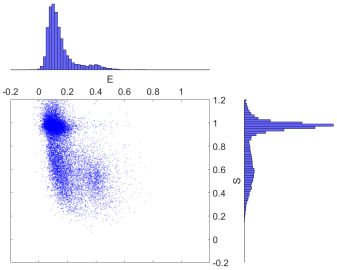

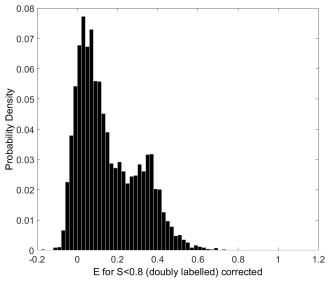

(c) Vi trapped (20876). **(d)** Vi trapped (6509), $\alpha = 0,122$.

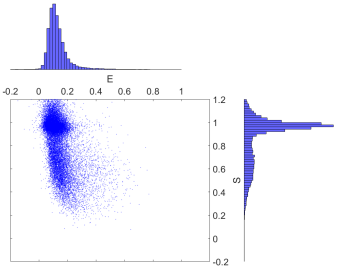

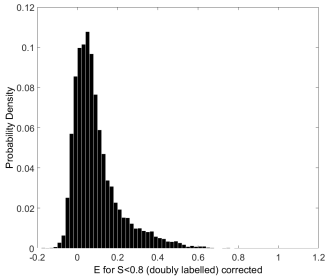

(e) ATP Vi (24764 data points). **(f)** ATP Vi (6977), $\alpha = 0,123$.

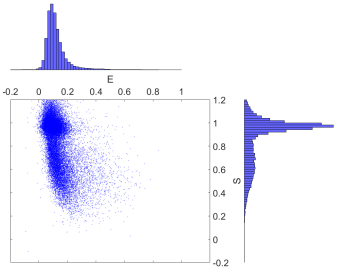

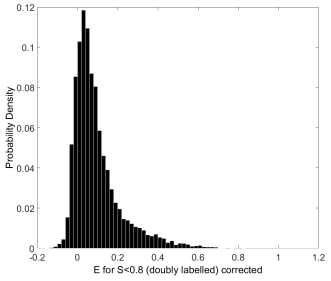

(g) ATP (31827 data points). **(h)** ATP (9117), $\alpha = 0,108$.

Figure B.3: FRET efficiency and stochiometry histograms for BmrA in EPC/bPS 20^{o}C liposomes from "snapshots" data. The left figures are 2D histograms with E (top) and S (right). The right figures show the E histogram for doubly labelled population ($S < 0,8$). Efficiency E is corrected from Donor leakage (factor α is indicated for each). The number of proteins is indicated between brackets, this corresponds to 100 images analyzed.

On figures B.4a, B.4d and B.4g (results from "movies" data) we observe same result as for the "snapshots" data. We observe a first main peak that is here a mixture of "Donor only" population and of low FRET peak, as its mean value was very close to the one of the "Donor only" peak. The only condition for which we observe a high FRET population is the Vi trapped BmrA. This is confirmed by the histograms of E_{mean} where we see a population at $E_{mean} \simeq 0,4$ for Vi trapped condition (figure B.4e).

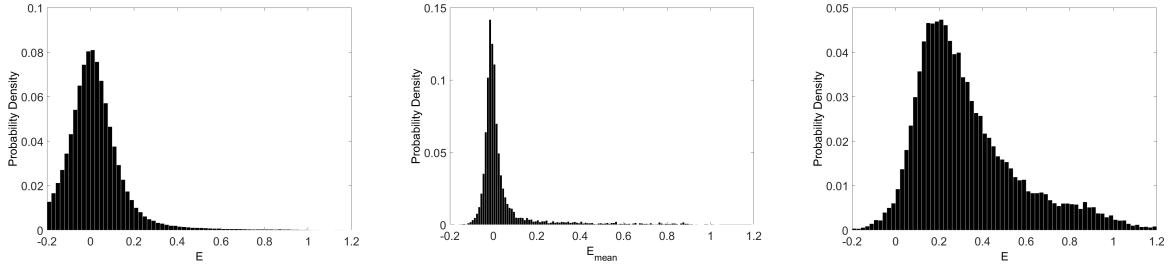

(a) Apo (411198 data points). **(b)** Apo (5466 data points). **(c)** Apo (26594 data points).

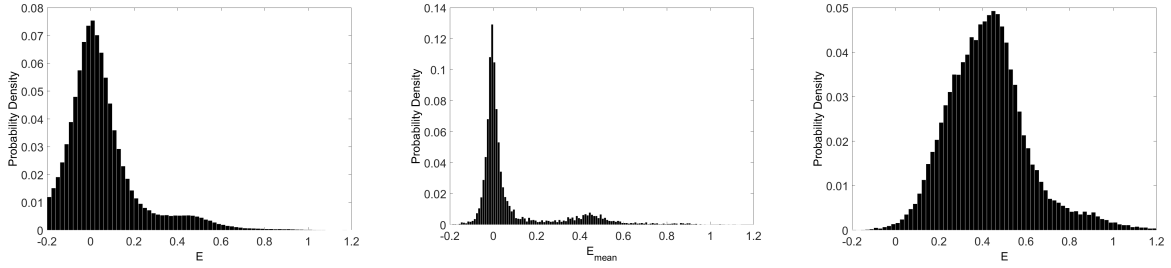

(d) Vi trapped (385556 data points). **(e)** Vi trapped (5074 data points). **(f)** Vi trapped (40274 data points).

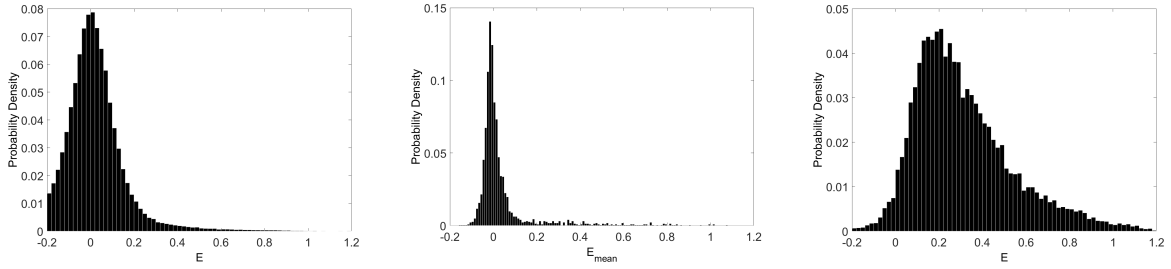

(g) ATP (173805 data points). **(h)** ATP (2226 data points). **(i)** ATP (11917 data points).

Figure B.4: FRET efficiency histograms for BmrA in EPC/bPS 20^{o}C liposomes from "movies" data. The left figures are E histograms with all time data points for all particles. The middle figures are E_{mean} histograms for all particles. The right figures show the E histograms for doubly labelled population (data points with a clear FRET signature). FRET efficiency was corrected from Donor leakage with $\alpha = 0,0469$. The number of data points is indicated between brackets, this corresponds to 30 to 50 movies analyzed.

B.3.2 Liposomes *E.coli* of 60 nm diameter

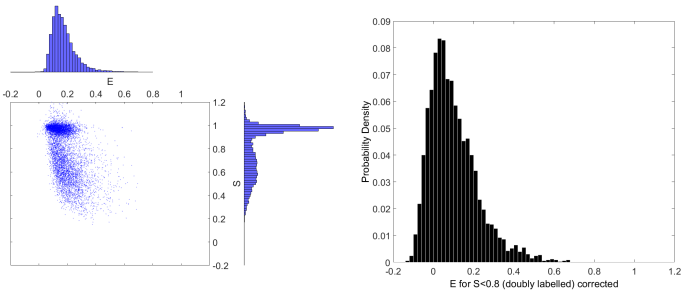

(a) Apo (7913 data points). **(b)** Apo (3246), $\alpha = 0,166$.

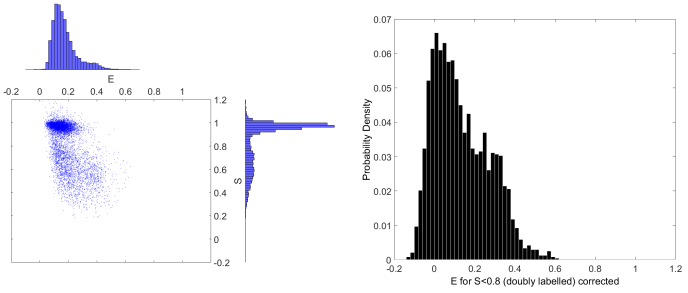

(c) Vi trapped (7632 data points). **(d)** Vi trapped (2379), $\alpha = 0,168$.

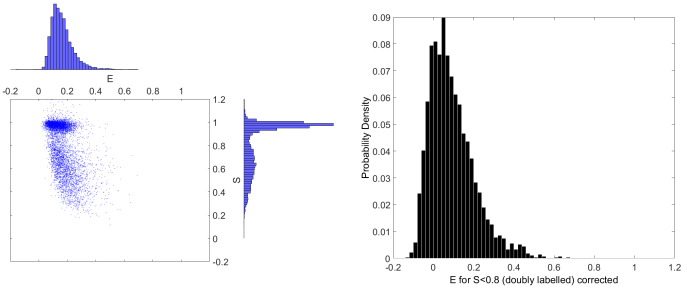

(e) ATP Vi (6795 data points). **(f)** ATP Vi (2682), $\alpha = 0,160$.

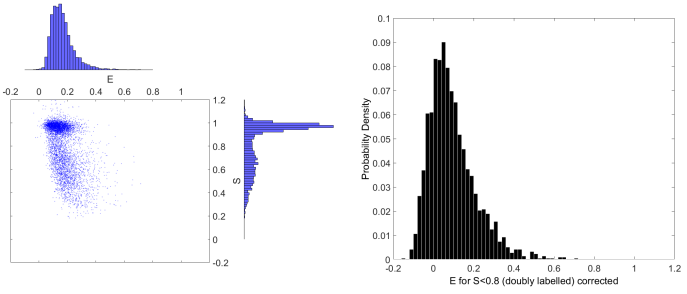

(g) ATP Ver (5824 data points). **(h)** ATP Ver (2166), $\alpha = 0,160$.

Figure B.5: FRET efficiency and stochiometry histograms for BmrA in *E.coli* liposomes from "snapshots" data. The left figures are 2D histograms with E (top) and S (right). The right figures show the E histogram for doubly labelled population ($S < 0,8$). FRET efficiency E was corrected from Donor leakage (the factor α is indicated for each). The number of proteins is indicated between brackets, this corresponds to 100 images analyzed.

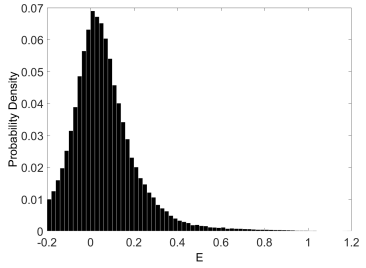

(a) Apo (89584 data points).

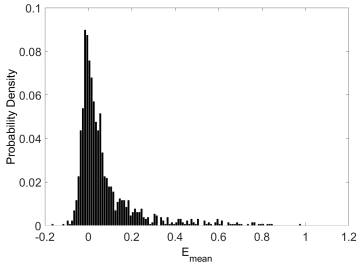

(b) Apo (1279 data points).

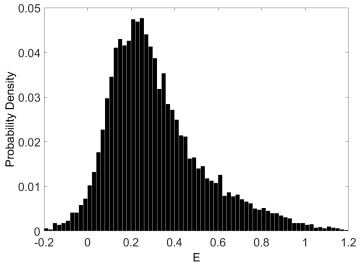

(c) Apo (7691 data points).

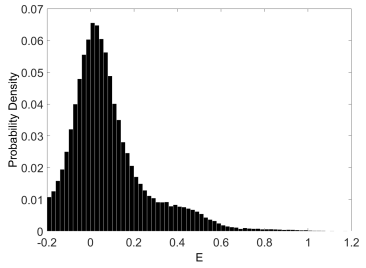

(d) Vi trapped (106335 data points).

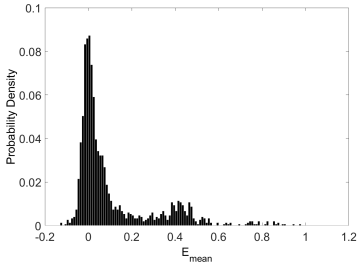

(e) Vi trapped (1489 data points).

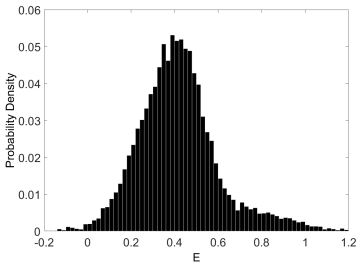

(f) Vi trapped (13587 data points).

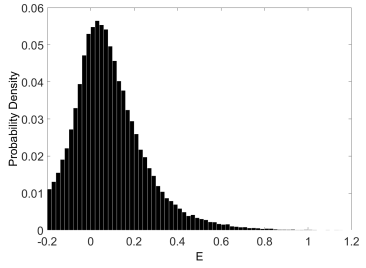

(g) ATP Vi (94470 data points).

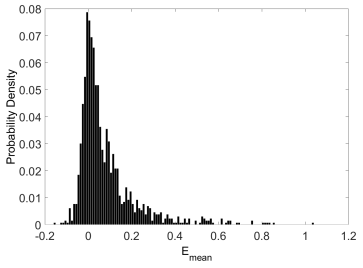

(h) ATP Vi (1295 data points).

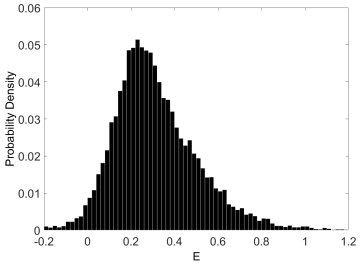

(i) ATP Vi (12561 data points).

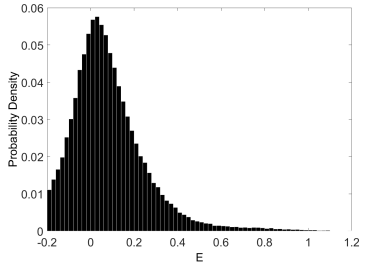

(j) ATP Ver (87586 data points).

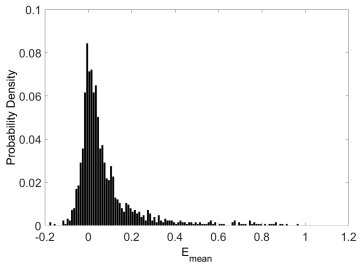

(k) ATP Ver (1232 data points).

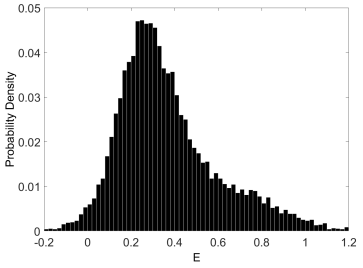

(l) ATP Ver (8997 data points).

Figure B.6: FRET efficiency histograms for BmrA in *E.coli* liposomes from "movies" data. The left figures are E histograms with all time data points for all particles. The middle figures are E_{mean} histograms for all particles. The right figures show the E histograms for doubly labelled population (data points with a clear FRET signature). FRET efficiency was corrected from Donor leakage with $\alpha = 0,0469$. The number of data points is indicated between brackets, this corresponds to 50 movies analyzed.

B.3.3 Liposomes EPC/bPS of 40 nm diameter

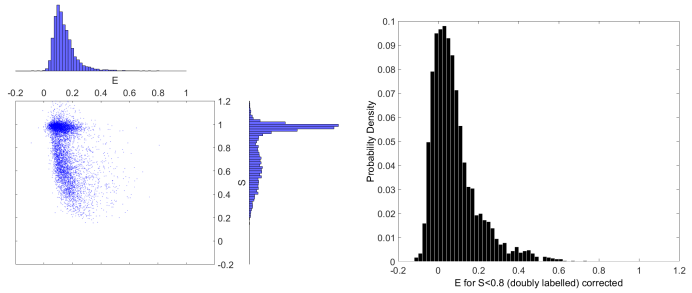

(a) Apo (7459 data points). **(b)** Apo (2961), $\alpha = 0,135$.

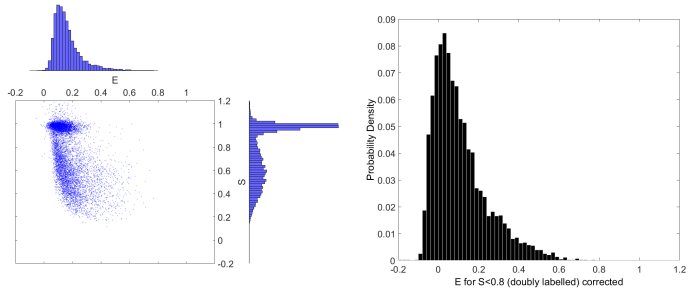

(c) Vi trapped (8923 data points). **(d)** Vi trapped (4341), $\alpha = 0,140$.

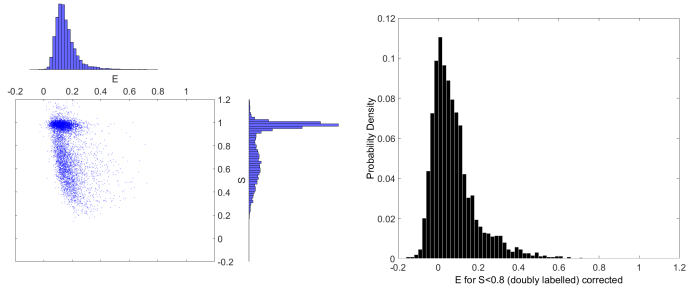

(e) ATP Vi (6725 data points). **(f)** ATP Vi (2634), $\alpha = 0,151$.

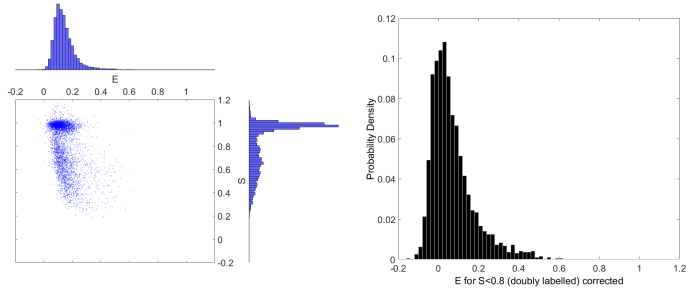

(g) ATP (4868 data points). **(h)** ATP (1923), $\alpha = 0,137$.

Figure B.7: FRET efficiency and stochiometry histograms for BmrA in EPC/bPS 4^{o}C liposomes from "snapshots" data. The left figures are 2D histograms with E (top) and S (right). The right figures show the E histogram for doubly labelled population ($S < 0,8$). FRET efficiency E was corrected from Donor leakage (the factor α is indicated for each). The number of proteins is indicated between brackets, this corresponds to 100 images analyzed.

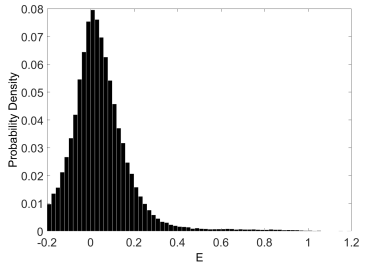

(a) Apo (80856 data points).

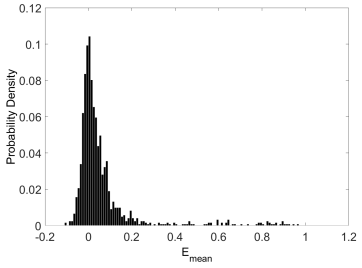

(b) Apo (1208 data points).

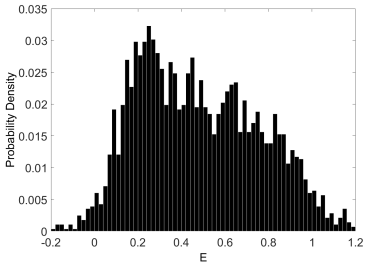

(c) Apo (2817 data points).

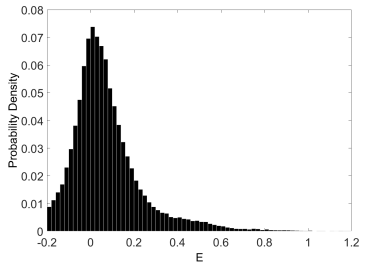

(d) Vi trapped (91937 data points).

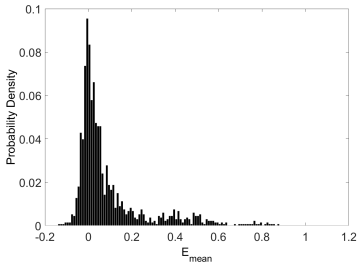

(e) Vi trapped (1329 data points).

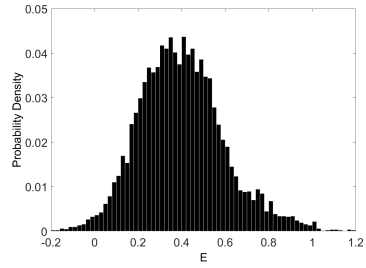

(f) Vi trapped (8259 data points).

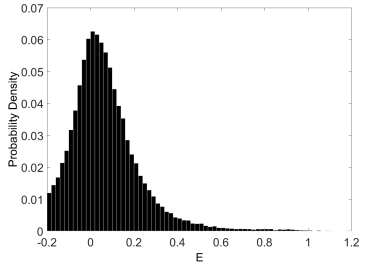

(g) ATP Vi (69631 data points).

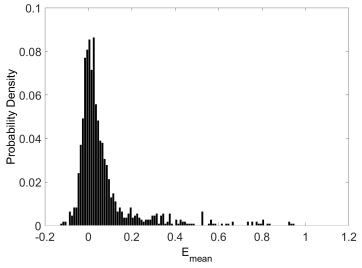

(h) ATP Vi (1076 data points).

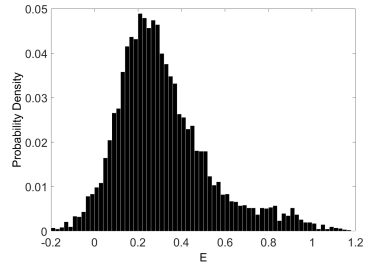

(i) ATP Vi (8012 data points).

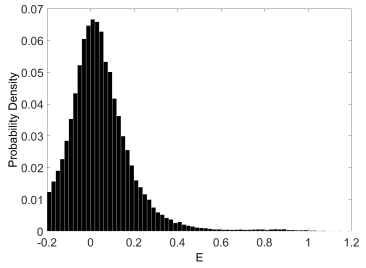

(j) ATP (60682 data points).

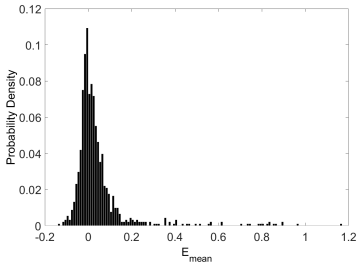

(k) ATP (905 data points).

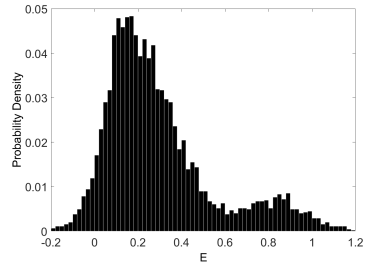

(l) ATP (4447 data points).

Figure B.8: FRET efficiency histograms for BmrA in EPC/bPS 4^{o}C liposomes from "movies" data. The left figures are E histograms with all time data points for all particles. The middle figures are E_{mean} histograms for all particles. The right figures show the E histograms for doubly labelled population (data points with a clear FRET signature). FRET efficiency was corrected from Donor leakage with $\alpha = 0,0469$. The number of data points is indicated between brackets, this corresponds to 50 movies analyzed.

B.4 Results from gaussian fits

B.4.1 Fitting distribution from "snapshots" data for DNA calibration.

From "shapshots" data, the E distributions for the DNA samples, used for calibration, have been fitted with a double gaussian. The fit parameters p_1, μ_1, σ_1, p_2, μ_2, σ_2 are defined by the following equation:

$$p_1 e^{-\frac{(E-\mu_1)^2}{2\sigma_1^2}} + p_2 e^{-\frac{(E-\mu_2)^2}{2\sigma_2^2}} \tag{B.1}$$

Sample		Data points	R^2	p_1 (%)	μ_1	σ_1	p_2 (%)	μ_2	σ_2
DNA	19 bp	23863	0,9986	66,7	0,001	0,029	33,3	0,124	0,086
	12 bp	19682	0,9833	59,8	0,001	0,035	40,2	0,346	0,077
	7 bp	25695	0,9884	69,2	0,001	0,045	30,8	0,614	0,094

Table B.1: Parameters of E distribution with single or double gaussian fit, for "shapshots" data. For each conditions, we indicate the total number of particles analyzed. The parameters of the fit, p_1, μ_1, σ_1, p_2, μ_2, σ_2 are defined in equation (B.1).

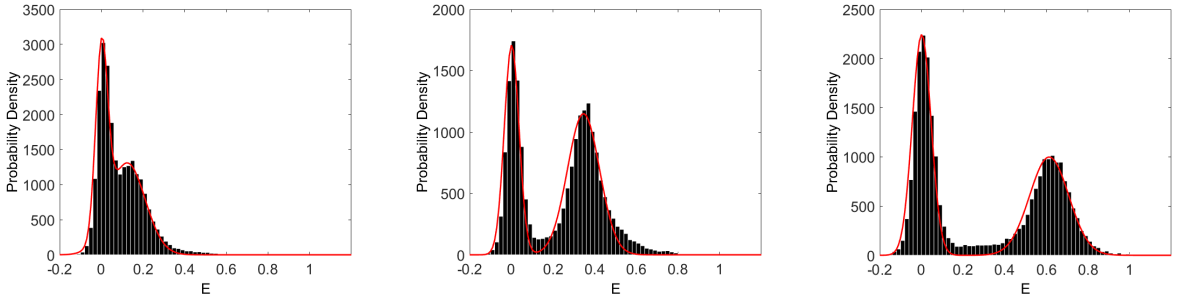

(a) 19 bp **(b)** 12 bp **(c)** 7 bp

Figure B.9: Gaussian fit on E distribution for "snapshots" data with DNA samples.

B.4.2 Fitting distribution from "movies" data.

From "movies" data, the E distributions limited to particles exhibiting FRET, both for the calibration DNA samples and for BmrA incorporated in liposomes, have been fitted with either a single gaussian or double gaussian (indicated). The fit parameters p_1, μ_1, σ_1, p_2, μ_2, σ_2 are defined by equation (B.1).

Sample		Gaussians 1 or 2	Data points	R^2	p_1 (%)	μ_1	σ_1	p_2 (%)	μ_2	σ_2
DNA	19 bp	1	69022	0,9961		0,148	0,114			
	12 bp	1	95940	0,999		0,356	0,141			
	7 bp	1	25024	0,989		0,894	0,172			
BmrA in	Apo	2	26594	0,9866	74,1	0,189	0,111	25,9	0,447	0,249
EPC/bPS	Vi trapped	2	40274	0,9926	16,8	0,468	0,047	83,2	0,387	0,166
20^{o}C	ATP Vi	2	10410	0,9877	80,8	0,216	0,127	19,2	0,480	0,235
	ATP	2	11917	0,9853	63,4	0,167	0,109	36,6	0,382	0,217
BmrA in	Apo	2	7691	0,9897	75,3	0,201	0,122	24,7	0,454	0,237
E.coli	Vi trapped	2	13587	0,9925	90,1	0,383	0,132	9,9	0,494	0,360
	ATP Vi	2	12561	0,9973	57,7	0,213	0,099	42,3	0,353	0,203
	ATP Ver	2	8997	0,9922	77,0	0,252	0,121	23,0	0,519	0,266
BmrA in	Apo	2	2817	0,9401	50,5	0,208	0,107	49,5	0,580	0,274
EPC/bPS	Vi trapped	1	8259	0,9867		0,371	0,182			
4^{o}C	ATP Vi	2	8012	0,9882	81,2	0,223	0,129	18,8	0,471	0,261
	ATP	2	4447	0,9709	87,0	0,174	0,133	13,0	0,638	0,297

Table B.2: Parameters of E distribution with single or double gaussian fit, for "movies" data. For each conditions, we indicate the total number of particles analyzed, and if single or double gaussian fit was applied. The parameters of the fit, p_1, μ_1, σ_1, p_2, μ_2, σ_2 are defined in equation (B.1).

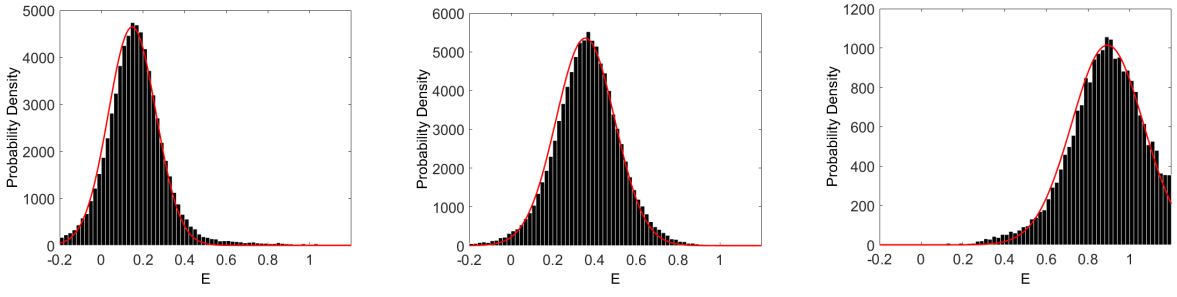

(a) 19 bp, E distribution **(b)** 12 bp, E distribution **(c)** 7 bp, E distribution

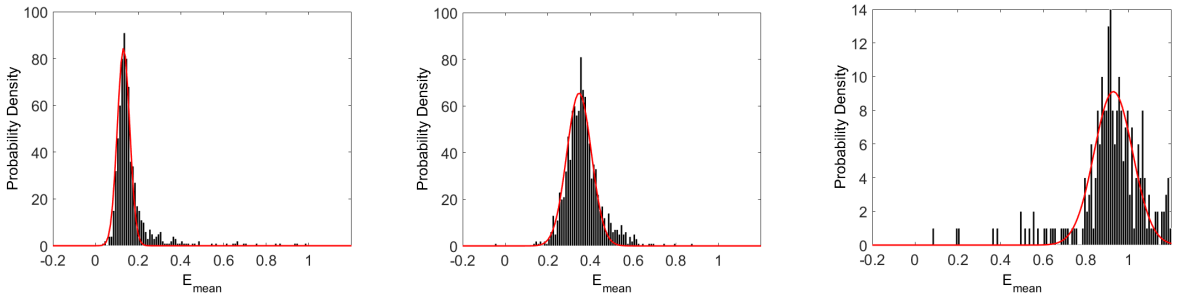

(d) 19 bp, E_{mean} distribution **(e)** 12 bp, E_{mean} distribution **(f)** 7 bp, E_{mean} distribution

Figure B.10: Gaussian fit on E and E_{mean} distributions for "movies" data with DNA samples.

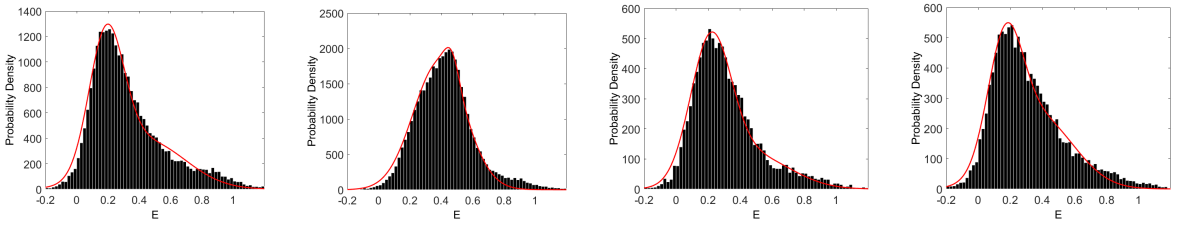

(a) EPC/bPS 20^{o}C, Apo **(b)** EPC/bPS 20^{o}C, Vi trapped **(c)** EPC/bPS 20^{o}C, ATP Vi **(d)** EPC/bPS 20^{o}C, ATP

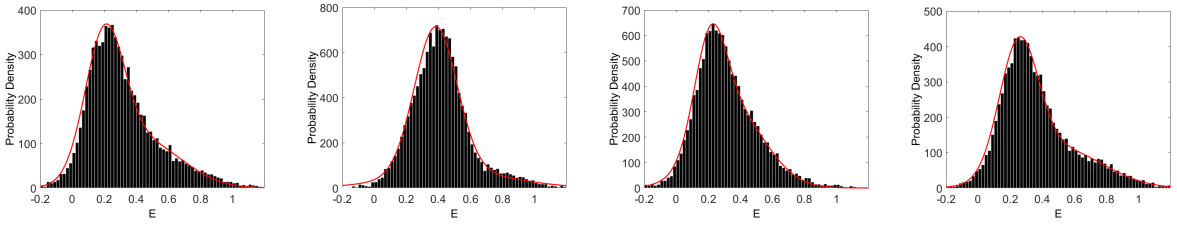

(e) *E.coli*, Apo **(f)** *E.coli*, Vi trapped **(g)** *E.coli*, ATP Vi **(h)** *E.coli*, ATP Ver

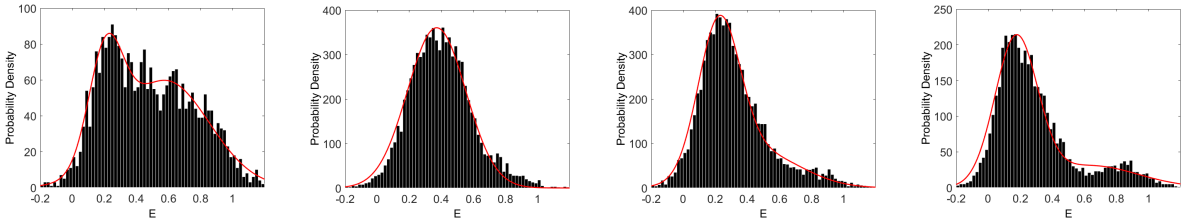

(i) EPC/bPS 4^{o}C, Apo **(j)** EPC/bPS 4^{o}C, Vi trapped **(k)** EPC/bPS 4^{o}C, ATP Vi **(l)** EPC/bPS 4^{o}C, ATP

Figure B.11: Gaussian fit on E distribution for "movies" data with BmrA samples.

Appendix C

BmrA study in micelles detergent/lipids

C.1 Protocol for protein immobilization

Some experiments have been done with protein solubilized in a solution at 0,05% of detergent TX and 50 μg/mL of lipids (EPC or *E.coli*). BmrA proteins are in micelles of detergent and lipids as depicted on figure C.1.A: they do not undergo the same stress as in liposomes. The lipids in solution aim at preventing the detergent from depleting the proteins of its structural lipids. We have to use a different strategy, previously reported in Dyla et al. [2017], to attach the protein in a mixture of detergent and lipids. BmrA is not labelled with a biotin. Therefore we attach it via the histidine-tag (that is used for the purification of the protein) by coating the surface with Biotin-TrisNTA.

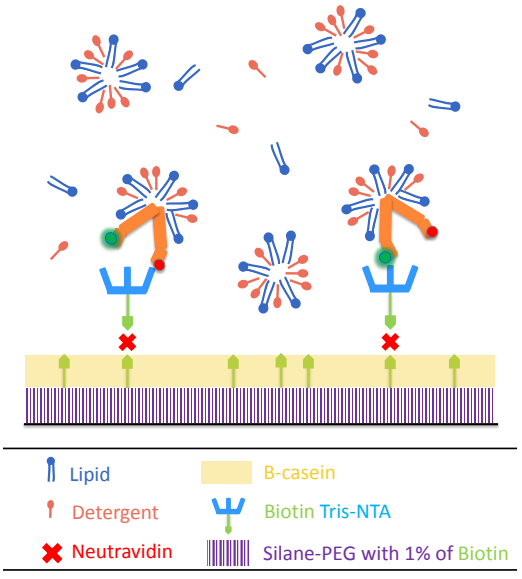

Figure C.1: Surface treatment for BmrA in detergent. BmrA is in a mix of detergent and lipids, that form micelles in the solution.

The steps with Silane-PEG/Silane-PEG-Biotin, neutravidin and β-casein remain the same as previously. Then, a solution at 5 nM of Biotin-TrisNTA is incubated for 1 min and rinsed with 100 μL of buffer A. A 100 μL of buffer A at 0,05% TX and 50 μg/mL of lipids is loaded in the chamber (buffer exchange step). The protein sample is added at 100 pM in the same buffer and incubated for 5 min just before observing. The chamber is rinsed with 100 μL of this buffer. As before, at this step extra reagents can be loaded in the chamber. The strategy is summarized on figure C.1.A.

C.2 Attachment specificity of proteins in detergent

Binding of proteins diluted in detergent/lipids is not a 100% specific. This is on figure C.2 where sCy5 labelled BmrA anchoring is observed. Many dots remain when the surface is not coated with neutravidin. We take several images all over the chambers in both case with or without neutravidin. The average number of dots per image (averaged on 10 images) is: 54 with neutravidin and 14 without neutravidin. It represents 26% of non-specific attachment on the surface, which is high. This can be explained by the presence of detergent in the observation buffer. Detergent can solubilize coating molecules such as β-casein, and therefore partly destroy the protecting layer and allow molecules to stick non-specifically on glass.

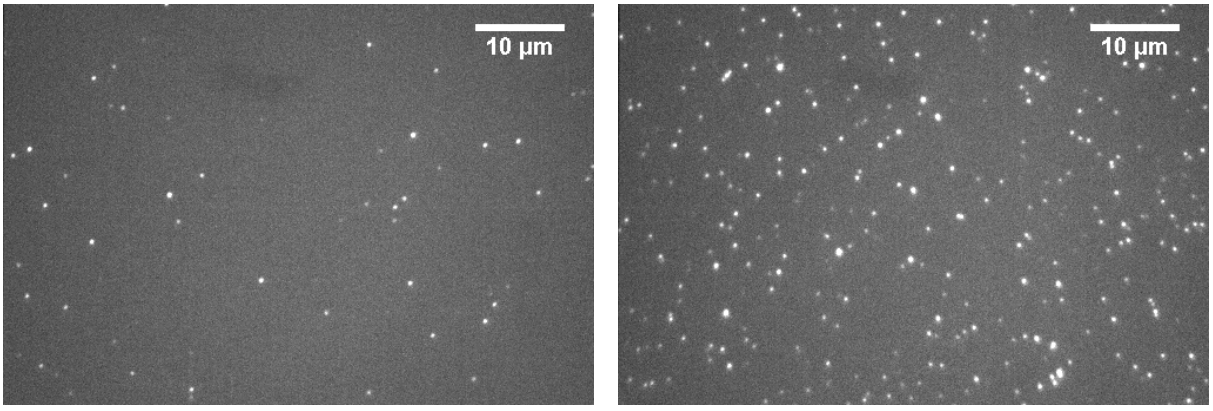

(a) Surface without neutravidin incubated with 100 pM of BmrA and rinsed.

(b) Surface with neutravidin incubated with 100 pM of BmrA and rinsed.

Figure C.2: Protein in detergent specific attachment. The protein sample used here is BmrA Mutant 3 labelled with Alexa488/sCy5. The protein is in a buffer with detergent (0.05% TX) and 50 μ/mL of *E.coli* lipids. Images are taken with laser 638 nm power 4/5 at 250 ms exposure time with the filter set for the FRET couple Alexa488/sCy5 (see table 4.4).

C.3 Observation of BmrA in micelles of detergent/lipids

We first managed to observe FRET signal in single molecule regime with BmrA mutant 3 labelled with Alexa488/sCy5. We chose the mutant 3 because the fluorophores are closer to each other than on the WT as shown on figure 4.1. It was a good candidate to see whether we were able to observe FRET signal on BmrA, before to try to detect dynamics and to resolve the signal in time. The choice of the

dyes couple was purely due to chronology as I synchronized my experiments with the biochemistry work done by Su Jin Paik: Alexa488/sCy5 BmrA was purified first and had a good activity conservation. For the reasons mentioned above in part 5.3.1 we use sCy3/sCy5 WT BmrA for the rest of the study.

Figure C.3 shows smFRET images of Alexa488/sCy5 M3 BmrA in a buffer containing detergent Triton X at 0.05% and *E.coli* lipids at 50 μg/mL. The protein is diluted to 100 pM and the amount of detergent is therefore very high. Lipids are added to the detergent so that the structural lipids, that interact strongly with the protein even in the presence of detergent, do not get depleted. We make sure not to perturb too much the structure and function of the protein in detergent.

We observe a lot of Donor and Acceptor data points respectively in the left and right channels, and we are able to detect good FRET signal in the middle one. This indicates we are able to detect smFRET signal on BmrA immobilized on a coverslip in detergent.

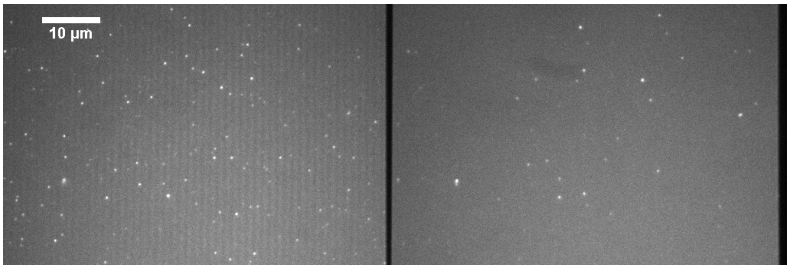

(a) Dual View image at excitation 488 nm: Donor channel on the left, FRET channel on the right.

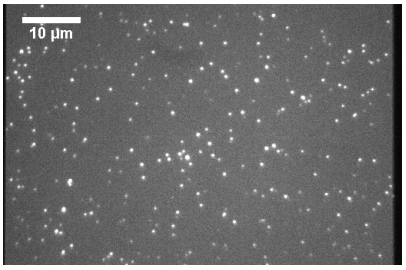

(b) Image at excitation 638 nm: Acceptor channel.

Figure C.3: smFRET image of BmrA in a mixture of detergent and lipids. Images acquired at 250 ms exposure time, with laser power 4/5 both at 488 and 638 nm excitation. M3 BmrA labelled with Alexa488/sCy5 was diluted to 100 pM in a buffer containing 0.05% of Triton X-100 (TX) and 50 μg/mL of *E.coli* lipids.

Bibliography

Elio A. Abbondanzieri, Gregory Bokinsky, Jason W. Rausch, Jennifer X. Zhang, Stuart F.J. Le Grice, and Xiaowei Zhuang. Dynamic binding orientations direct activity of HIV reverse transcriptase. *Nature*, 453:184–189, 2008. doi: 10.1038/nature06941.

Sophie Aimon, Andrew Callan-Jones, Alice Berthaud, Mathieu Pinot, Gilman E.S. Toombes, and Patricia Bassereau. Membrane Shape Modulates Transmembrane Protein Distribution. *Developmental Cell*, 28:212–218, 2014. doi: 10.1016/j.devcel.2013.12.012.

Colin Echeverría Aitken, R. Andrew Marshall, and Joseph D. Puglisi. An oxygen scavenging system for improvement of dye stability in single-molecule fluorescence experiments. *Biophysical Journal*, 94:1826–1835, 2008. doi: 10.1529/biophysj.107.117689.

Nurunisa Akyuz, Elka R Georgieva, Zhou Zhou, Sebastian Stolzenberg, Michel A Cuendet, George Khelashvili, Roger B Altman, Daniel S Terry, Jack H Freed, Harel Weinstein, Olga Boudker, and Scott C Blanchard. Transport domain unlocking sets the uptake rate of an aspartate transporter. *Nature*, 518:68–73, 2015. doi: 10.1038/nature14158.

Bruce Alberts, Alexander Johnson, Julian Lewis, David Morgan, Martin Raff, Keith Roberts, and Peter Walter. *Molecular Biology of the Cell*. Garland sc edition, 2017. doi: 10.1201/9781315735368.

Olaf S. Andersen and Roger E. Koeppe. Bilayer thickness and membrane protein function: An energetic perspective. *Annual Review of Biophysics and Biomolecular Structure*, 36: 107–130, 2007. doi: 10.1146/annurev.biophys.36.040306.132643.

Luis Bagatolli and P. B. Sunil Kumar. Phase behavior of multicomponent membranes: Experimental and computational techniques. *Soft Matter*, 5:3234–3248, 2009. doi: 10.1039/b901866b.

Estefania Barreto-Ojeda, Valentina Corradi, Ruo Xu Gu, and D. Peter Tieleman. Coarse-grained molecular dynamics simulations reveal lipid access pathways in P-glycoprotein. *Journal of General Physiology*, 150(3):417–429, 2018. doi: 10.1085/jgp.201711907.

Chérine Bechara, Anne Nöll, Nina Morgner, Matteo T. Degiacomi, Robert Tampé, and Carol V. Robinson. A subset of annular lipids is linked to the flippase activity of an ABC transporter. *Nature Chemistry*, 7:255–262, 2015. doi: 10.1038/nchem.2172.

A. L. Bernard, M. A. Guedeau-Boudeville, L. Jullien, and J. M. Di Meglio. Strong adhesion of giant vesicles on surfaces: dynamics and permeability. *Langmuir*, 16(17): 6809–6820, 2000. doi: 10.1021/la991341x.

Manuela D. Bienert, Stephanie E.G. Siegmund, Anna Drozak, Tomasz Trombik, Alain Bultreys, Ian T. Baldwin, and Marc Boutry. A pleiotropic drug resistance transporter in Nicotiana tabacum is involved in defense against the herbivore Manduca sexta. *Plant Journal*, 72:745–757, 2012. doi: 10.1111/j.1365-313X.2012.05108.x.

Mikhail Bogdanov, Philip Heacock, Ziqiang Guan, and William Dowhan. Plasticity of lipid-protein interactions in the function and topogenesis of the membrane protein lactose permease from Escherichia coli. *Proceedings of the National Academy of Sciences of the United States of America*, 107(34):15057–15062, 2010. doi: 10.1073/pnas.1006286107.

Peter P. Borbat, Kavitha Surendhran, Marco Bortolus, Ping Zou, Jack H. Freed, and Hassane S. Mchaourab. Conformational motion of the ABC transporter MsbA induced by ATP hydrolysis. *PLoS Biology*, 5(10):2211–2219, 2007. doi: 10.1371/journal.pbio.0050271.

Christoph Bräuchle, Don C. Lamb, and Jens Michaelis. *Single Particle Tracking and Single Molecule Energy Transfer*. 2009. doi: 10.1002/9783527628360.

Michael F. Brown. Curvature forces in membrane lipid-protein interactions. *Biochemistry*, 51(49):9782–9795, 2012. doi: 10.1021/bi301332v.

Wolfgang Busch and Milton H. Saier. The Transporter Classification (TC) system, 2002. *Critical Reviews in Biochemistry and Molecular Biology*, 37(5):287–337, 2002. doi: 10.1080/10409230290771528.

Andrew Callan-Jones and Patricia Bassereau. Curvature-driven membrane lipid and protein distribution. *Current Opinion in Solid State and Materials Science*, 17(4):143–150, 2013. doi: 10.1016/j.cossms.2013.08.004.

Andrew Callan-Jones, Benoit Sorre, and Patricia Bassereau. Curvature-driven lipid sorting in biomembranes. *Cold Spring Harbor Perspectives in Biology*, 3(2), 2011. doi: 10.1101/cshperspect.a004648.

Felix Campelo, Harvey T. McMahon, and Michael M. Kozlov. The hydrophobic insertion mechanism of membrane curvature generation by proteins. *Biophysical Journal*, 95: 2325–2339, 2008. doi: 10.1529/biophysj.108.133173.

P. B. Canham. The minimum energy of bending as a possible explanation of the biconcave shape of the human red blood cell. *Journal of Theoretical Biology*, 26(1):61–76, 1970. doi: 10.1016/S0022-5193(70)80032-7.

Mohamed Chami, Emmanuelle Steinfels, Cédric Orelle, Jean Michel Jault, Attilio Di Pietro, Jean Louis Rigaud, and Sergio Marco. Three-dimensional structure by cryo-electron microscopy of YvcC, an homodimeric ATP-binding cassette transporter from Bacillus subtilis. *Journal of Molecular Biology*, 315:1075–1085, 2002. doi: 10.1006/jmbi.2001.5309.

Rebecca S. Cooper and Guillermo A. Altenberg. Association/dissociation of the nucleotide-binding domains of the atp-binding cassette protein MSBA measured during continuous hydrolysis. *Journal of Biological Chemistry*, 288(29):20785–20796, 2013. doi: 10.1074/jbc.M113.477976.

Valentina Corradi, Eduardo Mendez-Villuendas, Helgi I. Ingólfsson, Ruo Xu Gu, Iwona Siuda, Manuel N. Melo, Anastassiia Moussatova, Lucien J. Degagné, Besian I. Sejdiu, Gurpreet Singh, Tsjerk A. Wassenaar, Karelia Delgado Magnero, Siewert J. Marrink, and D. Peter Tieleman. Lipid-Protein Interactions Are Unique Fingerprints for Membrane Proteins. *ACS Central Science*, 4:709–717, 2018. doi: 10.1021/acscentsci.8b00143.

Pieter R. Cullis, Michael J. Hope, and Colin P.S. Tilcock. Lipid polymorphism and the roles of lipids in membranes. *Chemistry and Physics of Lipids*, 40:127–144, 1986. doi: 10.1016/0009-3084(86)90067-8.

Olivier Dalmas, Marie Ange Do Cao, Miguel R. Lugo, Frances J. Sharom, Attilio Di Pietro, and Jean Michel Jault. Time-resolved fluorescence resonance energy transfer shows that the bacterial multidrug ABC half-transporter BmrA functions as a homodimer. *Biochemistry*, 44(11):4312–4321, 2005. doi: 10.1021/bi0482809.

A. L. Davidson, E. Dassa, C. Orelle, and J. Chen. Structure, Function, and Evolution of Bacterial ATP-Binding Cassette Systems. *Microbiology and Molecular Biology Reviews*, 72(2):317–364, 2008. doi: 10.1128/mmbr.00031-07.

Roger J.P. Dawson and Kaspar P. Locher. Structure of a bacterial multidrug ABC transporter. *Nature*, 443:180–185, 2006. doi: 10.1038/nature05155.

Michael Dean, Tito Fojo, and Susan Bates. Tumour stem cells and drug resistance. *Nature Reviews Cancer*, 5:275–284, 2005. doi: 10.1038/nrc1590.

A A Deniz, M Dahan, J R Grunwell, T Ha, A E Faulhaber, D S Chemla, S Weiss, and P G Schultz. Single-pair fluorescence resonance energy transfer on freely diffusing molecules: observation of Förster distance dependence and subpopulations. *Proceedings of the National Academy of Sciences of the United States of America*, 96(7):3670–5, 1999. doi: 10.1073/pnas.96.7.3670.

D M Dolino, S S Ramaswamy, and V Jayaraman. Luminescence resonance energy transfer to study conformational changes in membrane proteins expressed in mammalian cells. *Journal of Visualized Experiments*, (91), 2014. doi: 10.3791/51895.

Mateusz Dyla, Daniel S. Terry, Magnus Kjaergaard, Thomas L.M. Sørensen, Jacob Lauwring Andersen, Jens Peter Andersen, Charlotte Rohde Knudsen, Roger B. Altman, Poul Nissen, and Scott C. Blanchard. Dynamics of P-type ATPase transport revealed by single-molecule FRET. *Nature*, 551(7680):346–351, 2017. doi: 10.1038/nature24296.

Paul D.W. Eckford and Frances J. Sharom. Interaction of the P-glycoprotein multidrug efflux pump with cholesterol: Effects on ATPase activity, drug binding and transport. *Biochemistry*, 47(51):13686–13698, 2008. doi: 10.1021/bi801409r.

Guus B Erkens, Inga Hänelt, Joris M H Goudsmits, Dirk Jan Slotboom, and Antoine M van Oijen. Unsynchronised subunit motion in single trimeric sodium-coupled aspartate transporters. *Nature*, 502:119–23, 2013. doi: 10.1038/nature12538.

E. Evans and W. Rawicz. Entropy-driven tension and bending elasticity in condensed-fluid membranes. *Physical Review Letters*, 64(17):2094–2097, 1990. doi: 10.1103/PhysRevLett.64.2094.

Shazia Farooq and Johannes Hohlbein. Camera-based single-molecule FRET detection with improved time resolution. *Physical Chemistry Chemical Physics*, 17:27862—-27872, 2015. doi: 10.1039/c5cp04137f.

Jamie I Fletcher, Michelle Haber, Michelle J Henderson, and Murray D Norris. ABC transporters in cancer: more than just drug efflux pumps. *Nature reviews. Cancer*, 10 (2):147–156, 2010. doi: 10.1038/nrc2789.

Th. Förster. Transfer Mechanisms of Electronic Excitation Energy. *Radiation Research Supplement*, 2:326–339, 1960. doi: 10.2307/3583604.

Pierre Frederic Fribourg, Mohamed Chami, Carlos Oscar S. Sorzano, Francesca Gubellini, Roberto Marabini, Sergio Marco, Jean Michel Jault, and Daniel Lévy. 3D cryo-electron reconstruction of BmrA, a bacterial multidrug ABC transporter in an inward-facing conformation and in a lipidic environment. *Journal of Molecular Biology*, 426:2059–2069, 2014. doi: 10.1016/j.jmb.2014.03.002.

Matthias Garten, Sophie Aimon, Patricia Bassereau, and Gilman E. S. Toombes. Reconstitution of a Transmembrane Protein, the Voltage-gated Ion Channel, KvAP, into Giant Unilamellar Vesicles for Microscopy and Patch Clamp Studies. *Journal of Visualized Experiments*, (95), 2015. doi: 10.3791/52281.

Rachelle Gaudet and Don C. Wiley. Structure of the ABC ATPase domain of human TAP1, the transporter associated with antigen processing. *EMBO Journal*, 20(17): 4964–4972, 2001. doi: 10.1093/emboj/20.17.4964.

Andreas Gietl, Phil Holzmeister, Fabian Blombach, Sarah Schulz, Lena Voith Von Voithenberg, Don C. Lamb, Finn Werner, Philip Tinnefeld, and Dina Grohmann. Eukaryotic and archaeal TBP and TFB/TF(II)B follow different promoter DNA bending pathways. *Nucleic Acids Research*, 42(10):6219–6231, 2014. doi: 10.1093/nar/gku273.

Michael M. Gottesman, Tito Fojo, and Susan E. Bates. Multidrug resistance in cancer: Role of ATP-dependent transporters. *Nature Reviews Cancer*, 2:48–58, 2002. doi: 10.1038/nrc706.

Joris M.H. Goudsmits, Dirk Jan Slotboom, and Antoine M. Van Oijen. Single-molecule visualization of conformational changes and substrate transport in the Vitamin B12ABC importer BtuCD-F. *Nature Communications*, 8(1):1652, 2017. doi: 10.1038/s41467-017-01815-7.

Alexander Gust, Adrian Zander, Andreas Gietl, Phil Holzmeister, Sarah Schulz, Birka Lalkens, Philip Tinnefeld, and Dina Grohmann. A starting point for fluorescence-based single-molecule measurements in biomolecular research. *Molecules*, 19:15824–15865, 2014. doi: 10.3390/molecules191015824.

Adelin Gustot, Smriti, Jean Marie Ruysschaert, Hassane Mchaourab, and Cédric Govaerts. Lipid composition regulates the orientation of transmembrane helices in HorA, an ABC multidrug transporter. *Journal of Biological Chemistry*, 285(19):14144–14151, 2010. doi: 10.1074/jbc.M109.079673.

T. Ha, Th Enderle, D. F. Ogletree, D. S. Chemla, P. R. Selvin, and S. Weiss. Probing the interaction between two single molecules: Fluorescence resonance energy transfer

between a single donor and a single acceptor. *Proceedings of the National Academy of Sciences of the United States of America*, 93:6264–6268, 1996. doi: 10.1073/pnas.93.13.6264.

Pierre Hakizimana, Matthieu Masureel, Bénédicte Gbaguidi, Jean-Marie Ruysschaert, and Cédric Govaerts. Interactions between Phosphatidylethanolamine Headgroup and LmrP, a Multidrug Transporter. *Journal of Biological Chemistry*, 283(14):9369–9376, 2008. doi: 10.1074/jbc.m708427200.

Nikos S. Hatzakis, Vikram K. Bhatia, Jannik Larsen, Kenneth L. Madsen, Pierre Yves Bolinger, Andreas H. Kunding, John Castillo, Ulrik Gether, Per Hedegård, and Dimitrios Stamou. How curved membranes recruit amphipathic helices and protein anchoring motifs. *Nature Chemical Biology*, 5:835–841, 2009. doi: 10.1038/nchembio.213.

W. Helfrich. Elastic Properties of Lipid Bilayers: Theory and Possible Experiments. *Zeitschrift fur Naturforschung - Section C Journal of Biosciences*, 28:693–703, 1973. doi: 10.1515/znc-1973-11-1209.

Björn Hellenkamp, Sonja Schmid, Olga Doroshenko, Oleg Opanasyuk, Ralf Kühnemuth, Soheila Rezaei Adariani, Benjamin Ambrose, Mikayel Aznauryan, Anders Barth, Victoria Birkedal, Mark E. Bowen, Hongtao Chen, Thorben Cordes, Tobias Eilert, Carel Fijen, Christian Gebhardt, Markus Götz, Giorgos Gouridis, Enrico Gratton, Taekjip Ha, Pengyu Hao, Christian A. Hanke, Andreas Hartmann, Jelle Hendrix, Lasse L. Hildebrandt, Verena Hirschfeld, Johannes Hohlbein, Boyang Hua, Christian G. Hübner, Eleni Kallis, Achillefs N. Kapanidis, Jae Yeol Kim, Georg Krainer, Don C. Lamb, Nam Ki Lee, Edward A. Lemke, Brié Levesque, Marcia Levitus, James J. McCann, Nikolaus Naredi-Rainer, Daniel Nettels, Thuy Ngo, Ruoyi Qiu, Nicole C. Robb, Carlheinz Röcker, Hugo Sanabria, Michael Schlierf, Tim Schröder, Benjamin Schuler, Henning Seidel, Lisa Streit, Johann Thurn, Philip Tinnefeld, Swati Tyagi, Niels Vandenberk, Andrés Manuel Vera, Keith R. Weninger, Bettina Wünsch, Inna S. Yanez-Orozco, Jens Michaelis, Claus A.M. Seidel, Timothy D. Craggs, and Thorsten Hugel. Precision and accuracy of single-molecule FRET measurements—a multi-laboratory benchmark study. *Nature Methods*, 15:669–676, 2018. doi: 10.1038/s41592-018-0085-0.

Christopher F. Higgins and Kenneth J. Linton. The ATP switch model for ABC transporters. *Nature Structural and Molecular Biology*, 11(10):918–926, 2004. doi: 10.1038/nsmb836.

Lasse L. Hildebrandt, Søren Preus, and Victoria Birkedal. Quantitative single molecule FRET efficiencies using TIRF microscopy. *Faraday Discussions*, 184, 2015. doi: 10.1039/c5fd00100e.

Susanne Hofmann, Dovile Januliene, Ahmad R. Mehdipour, Christoph Thomas, Erich Stefan, Stefan Brüchert, Benedikt T. Kuhn, Eric R. Geertsma, Gerhard Hummer, Robert Tampé, and Arne Moeller. Conformation space of a heterodimeric ABC exporter under turnover conditions. *Nature*, 571:580–583, 2019. doi: 10.1038/s41586-019-1391-0.

Seamus J. Holden, Stephan Uphoff, Johannes Hohlbein, David Yadin, Ludovic Le Reste, Oliver J. Britton, and Achillefs N. Kapanidis. Defining the limits of single-molecule FRET resolution in TIRF microscopy. *Biophysical Journal*, 99(9):3102–3111, 2010. doi: 10.1016/j.bpj.2010.09.005.

Florence Husada, Kiran Bountra, Konstantinos Tassis, Marijn Boer, Maria Romano, Sylvie Rebuffat, Konstantinos Beis, and Thorben Cordes. Conformational dynamics of the ABC transporter McjD seen by single-molecule FRET. *The EMBO Journal*, 37: e100056, 2018. doi: 10.15252/embj.2018100056.

Jae Ung Hwang, Won Yong Song, Daewoong Hong, Donghwi Ko, Yasuyo Yamaoka, Sunghoon Jang, Sojeong Yim, Eunjung Lee, Deepa Khare, Kyungyoon Kim, Michael Palmgren, Hwan Su Yoon, Enrico Martinoia, and Youngsook Lee. Plant ABC Transporters Enable Many Unique Aspects of a Terrestrial Plant's Lifestyle. *Molecular Plant*, 9:338–355, 2016. doi: 10.1016/j.molp.2016.02.003.

J.N. Israelachvili. *Intermolecular and surface forces*. Academic Press, 1992.

Peter M. Jones and Anthony M. George. Mechanism of the ABC transporter ATPase domains: Catalytic models and the biochemical and biophysical record. *Critical Reviews in Biochemistry and Molecular Biology*, 48(1):39–50, 2013. doi: 10.3109/10409238.2012.735644.

Achillefs N Kapanidis, Nam Ki Lee, Ted A Laurence, Sören Doose, Emmanuel Margeat, and Shimon Weiss. Fluorescence-aided molecule sorting: analysis of structure and interactions by alternating-laser excitation of single molecules. *Proceedings of the National Academy of Sciences of the United States of America*, 101(24):8936–41, 2004. doi: 10.1073/pnas.0401690101.

C. A. Keller, K. Glasmästar, V. P. Zhdanov, and B. Kasemo. Formation of Supported Membranes from Vesicles. *Physical Review Letters*, 84(23):5443, 2000. doi: 10.1103/PhysRevLett.84.5443.

Ambalika S. Khadria and Alessandro Senes. Fluorophores, environments, and quantification techniques in the analysis of transmembrane helix interaction using FRET. *Biopolymers*, 104(4):247–264, 2015. doi: 10.1002/bip.22667.

Norbert Kučerka, Mu Ping Nieh, and John Katsaras. Fluid phase lipid areas and bilayer thicknesses of commonly used phosphatidylcholines as a function of temperature. *Biochimica et Biophysica Acta - Biomembranes*, 1808(11):2761–2771, 2011. doi: 10.1016/j.bbamem.2011.07.022.

Akihiro Kusumi, Takahiro K. Fujiwara, Rahul Chadda, Min Xie, Taka A. Tsunoyama, Ziya Kalay, Rinshi S. Kasai, and Kenichi G.N. Suzuki. Dynamic Organizing Principles of the Plasma Membrane that Regulate Signal Transduction: Commemorating the Fortieth Anniversary of Singer and Nicolson's Fluid-Mosaic Model. *Annual Review of Cell and Developmental Biology*, 28:215–250, 2012. doi: 10.1146/annurev-cellbio-100809-151736.

Arthur Laganowsky, Eamonn Reading, Timothy M. Allison, Martin B. Ulmschneider, Matteo T. Degiacomi, Andrew J. Baldwin, and Carol V. Robinson. Membrane proteins bind lipids selectively to modulate their structure and function. *Nature*, 510(7503): 172–175, 2014. doi: 10.1038/nature13419.

Ludovic Le Reste, Johannes Hohlbein, Kristofer Gryte, and Achillefs N. Kapanidis. Characterization of dark quencher chromophores as nonfluorescent acceptors for single-molecule FRET. *Biophysical Journal*, 102(11):2658–2668, 2012. doi: 10.1016/j.bpj.2012.04.028.

A. G. Lee. Lipid-protein interactions in biological membranes: A structural perspective. *Biochimica et Biophysica Acta - Biomembranes*, 1612(1):1–40, 2003. doi: 10.1016/S0005-2736(03)00056-7.

S. Leibler. Curvature instability in membranes. *Journal de Physique*, 47(3):507–516, 1986. doi: 10.1051/jphys:01986004703050700.

Daniel Lévy, Aline Bluzat, Michel Seigneuret, and Jean Louis Rigaud. A systematic study of liposome and proteoliposome reconstitution involving Bio-Bead-mediated Triton X-100 removal. *BBA - Biomembranes*, 105(2):179–190, 1990. doi: 10.1016/0005-2736(90)90096-7.

Daniel Lingwood and Kai Simons. Lipid rafts as a membrane-organizing principle. *Science*, 327(5961):46–50, 2010. doi: 10.1126/science.1174621.

R Lipowsky and E Sackmann. *Structure and dynamics of membranes: Generic and specific interactions*. Elsevier, 1995. ISBN 9780080541914.

Kaspar P Locher. Mechanistic diversity in ATP-binding cassette (ABC) transporters. *Nature structural & molecular biology*, 23(6):487–93, 2016. doi: 10.1038/nsmb.3216.

Christina Lohr, Andreas H. Kunding, Vikram K. Bhatia, and Dimitrios Stamou. Constructing Size Distributions of Liposomes from Single-Object Fluorescence Measurements. *Methods in Enzymology*, 465:143–160, 2009. doi: 10.1016/S0076-6879(09)65008-4.

Ioannis Manolaridis, Scott M. Jackson, Nicholas M.I. Taylor, Julia Kowal, Henning Stahlberg, and Kaspar P. Locher. Cryo-EM structures of a human ABCG2 mutant trapped in ATP-bound and substrate-bound states. *Nature*, 563:426–430, 2018. doi: 10.1038/s41586-018-0680-3.

Derek Marsh. Elastic curvature constants of lipid monolayers and bilayers. *Chemistry and Physics of Lipids*, 144(2):146–159, 2006. doi: 10.1016/j.chemphyslip.2006.08.004.

Derek Marsh. Lateral pressure profile, spontaneous curvature frustration, and the incorporation and conformation of proteins in membranes. *Biophysical Journal*, 93(11):3884–3899, 2007. doi: 10.1529/biophysj.107.107938.

Hassane S. McHaourab, P. Ryan Steed, and Kelli Kazmier. Toward the fourth dimension of membrane protein structure: Insight into dynamics from spin-labeling EPR spectroscopy. *Structure*, 19(11):1549–1561, 2011. doi: 10.1016/j.str.2011.10.009.

Harvey T. McMahon and Emmanuel Boucrot. Membrane curvature at a glance. *Journal of Cell Science*, 128:1065–1070, 2015. doi: 10.1242/jcs.114454.

Harvey T. McMahon and Jennifer L. Gallop. Membrane curvature and mechanisms of dynamic cell membrane remodelling. *Nature*, 438:590–596, 2005. doi: 10.1038/nature04396.

Shahid Mehmood, Carmen Domene, Eric Forest, and Jean Michel Jault. Dynamics of a bacterial multidrug ABC transporter in the inward- and outward-facing conformations. *Proceedings of the National Academy of Sciences of the United States of America*, 109(27):10832–10836, 2012. doi: 10.1073/pnas.1204067109.

R. Milo and R. Phillips. *Cell biology by the numbers*. Garland Press, 2016.

Smriti Mishra, Brandy Verhalen, Richard A. Stein, Po Chao Wen, Emad Tajkhorshid, and Hassane S. Mchaourab. Conformational dynamics of the nucleotide binding domains and the power stroke of a heterodimeric ABC transporter. *eLife*, 3:e02740, 2014. doi: 10.7554/eLife.02740.

Arne Moeller, Sung Chang Lee, Houchao Tao, Jeffrey A. Speir, Geoffrey Chang, Ina L. Urbatsch, Clinton S. Potter, Bridget Carragher, and Qinghai Zhang. Distinct Conformational Spectrum of Homologous Multidrug ABC Transporters. *Structure*, 23(3): 450–460, 2015. doi: 10.1016/j.str.2014.12.013.

Jennifer Neumann, Dania Rose-Sperling, and Ute A. Hellmich. Diverse relations between ABC transporters and lipids: An overview. *BBA-Biomembranes*, 1859(4):605–618, 2016. doi: 10.1016/j.bbamem.2016.09.023.

Cédric Orelle, Francesca Gubellini, Anne Durand, Sergio Marco, Daniel Lévy, Philippe Gros, Attilio Di Pietro, and Jean Michel Jault. Conformational change induced by ATP binding in the multidrug ATP-binding cassette transporter BmrA. *Biochemistry*, 47(8): 2404–2412, 2008. doi: 10.1021/bi702303s.

Su Jin Paik. *Interplay between ABC membrane transporter BmrA and its membrane environment*. PhD thesis, 2018.

Camilo Perez, Sabina Gerber, Jérémy Boilevin, Monika Bucher, Tamis Darbre, Markus Aebi, Jean Louis Reymond, and Kaspar P. Locher. Structure and mechanism of an active lipid-linked oligosaccharide flippase. *Nature*, 524:433–438, 2015. doi: 10.1038/nature14953.

Eduardo Perozo, Anna Kloda, D. Marien Cortes, and Boris Martinac. Physical principles underlying the transduction of bilayer deformation forces during mechanosensitive channel gating. *Nature Structural Biology*, 9:696–703, 2002. doi: 10.1038/nsb827.

Rob Phillips, Tristan Ursell, Paul Wiggins, and Pierre Sens. Emerging roles for lipids in shaping membrane-protein function. *Nature*, 459(7245):379–85, 2009. doi: 10.1038/nature08147.

Rob Phillips, Jane Kondev, Julie Theriot, and Hernan G. Garcia. *Physical biology of the cell*. 2013.

Baptiste Pierman, Frédéric Toussaint, Aurélie Bertin, Daniel Lévy, Nicolas Smargiasso, Edwin De Pauw, and Marc Boutry. Activity of the purified plant ABC transporter NtPDR1 is stimulated by diterpenes and sesquiterpenes involved in constitutive and induced defenses. *Journal of Biological Chemistry*, 292(47):19491–19502, 2017. doi: 10.1074/jbc.M117.811935.

María Florencia Pignataro, Martín M. Dodes-Traian, F. Luis González-Flecha, Mauricio Sica, Irene C. Mangialavori, and Juan Pablo F.C. Rossi. Modulation of plasma membrane Ca2+-ATPase by neutral phospholipids: Effect of the micelle-vesicle transition

and the bilayer thickness. *Journal of Biological Chemistry*, 290(10):6179–6190, 2015. doi: 10.1074/jbc.M114.585828.

Euan Pyle, Antreas C. Kalli, Sotiris Amillis, Zoe Hall, Andy M. Lau, Aylin C. Hanyaloglu, George Diallinas, Bernadette Byrne, and Argyris Politis. Structural Lipids Enable the Formation of Functional Oligomers of the Eukaryotic Purine Symporter UapA. *Cell Chemical Biology*, 25(7):840–848, 2018. doi: 10.1016/j.chembiol.2018.03.011.

F. Quemeneur, J. K. Sigurdsson, M. Renner, Paul J Atzberger, P. Bassereau, and D. Lacoste. Shape matters in protein mobility within membranes. *Proceedings of the National Academy of Sciences*, 111(14):5083–5087, 2014. doi: 10.1073/pnas.1321054111.

Ivan Rasnik, Sean A. McKinney, and Taekjip Ha. Nonblinking and long-lasting single-molecule fluorescence imaging. *Nature Methods*, 3(11):891–893, 2006. doi: 10.1038/nmeth934.

W. Rawicz, B. A. Smith, T. J. McIntosh, S. A. Simon, and E. Evans. Elasticity, strength, and water permeability of bilayers that contain raft microdomain-forming lipids. *Biophysical Journal*, 94(12):4725–4736, 2008. doi: 10.1529/biophysj.107.121731.

Jean Louis Rigaud and Daniel Lévy. Reconstitution of Membrane Proteins into Liposomes. *Methods in Enzymology*, 372:65–86, 2003. doi: 10.1016/S0076-6879(03)72004-7.

Jean Louis Rigaud, Bruno Pitard, and Daniel Levy. Reconstitution of membrane proteins into liposomes: application to energy-transducing membrane proteins, 1995.

Robert W. Robey, Kristen M. Pluchino, Matthew D. Hall, Antonio T. Fojo, Susan E. Bates, and Michael M. Gottesman. Revisiting the role of efflux pumps in multidrug-resistant cancer. *Nature Reviews Cancer*, 18(7):452–464, 2018. doi: 10.1038/s41568-018-0005-8.

Kadla R. Rosholm, Natascha Leijnse, Anna Mantsiou, Vadym Tkach, Søren L. Pedersen, Volker F. Wirth, Lene B. Oddershede, Knud J. Jensen, Karen L. Martinez, Nikos S. Hatzakis, Poul Martin Bendix, Andrew Callan-Jones, and DImitrios Stamou. Membrane curvature regulates ligand-specific membrane sorting of GPCRs in living cells. *Nature Chemical Biology*, 13:724–729, 2017. doi: 10.1038/nchembio.2372.

Rahul Roy, Sungchul Hohng, and Taekjip Ha. A practical guide to single-molecule FRET. *Nature Methods*, 5(6):507–516, 2008. doi: 10.1038/nmeth.1208.

Harekrushna Sahoo and Petra Schwille. FRET and FCS - Friends or foes? *ChemPhysChem*, 12:532 – 541, 2011. doi: 10.1002/cphc.201000776.

M. H. Saier, Can V. Tran, and Ravi D. Barabote. TCDB: the Transporter Classification Database for membrane transport protein analyses and information. *Nucleic Acids Research*, 34:D181–D186, 2006. doi: 10.1093/nar/gkj001.

Zuben E. Sauna, In Wha Kim, Krishnamachary Nandigama, Stephan Kopp, Peter Chiba, and Suresh V. Ambudkar. Catalytic cycle of ATP hydrolysis by P-glycoprotein: Evidence for formation of the E·S reaction intermediate with ATP-γ-S, a nonhydrolyzable analogue of ATP. *Biochemistry*, 46(48):13787–13799, 2007. doi: 10.1021/bi701385t.

Daniel Schmidt and Roderick MacKinnon. Voltage-dependent K+ channel gating and voltage sensor toxin sensitivity depend on the mechanical state of the lipid membrane. *Proceedings of the National Academy of Sciences of the United States of America*, 105 (49):19276–19281, 2008. doi: 10.1073/pnas.0810187105.

Daniel Schmidt, Qiu Xing Jiang, and Roderick MacKinnon. Phospholipids and the origin of cationic gating charges in voltage sensors. *Nature*, 444:775–779, 2006. doi: 10.1038/nature05416.

Ulrich Schmidt and Matthias Weiss. Hydrophobic mismatch-induced clustering as a primer for protein sorting in the secretory pathway. *Biophysical Chemistry*, 151(1-2): 34–38, 2010. doi: 10.1016/j.bpc.2010.04.009.

Paul R. Selvin and Taekjip Ha. *Single-molecule Techniques: A Laboratory Manual*. 2008.

Frances J. Sharom. ABC multidrug transporters: Structure, function and role in chemoresistance. *Pharmacogenomics*, 9(1):105–127, 2008. doi: 10.2217/14622416.9.1.105.

Frances Jane Sharom. Complex interplay between the P-glycoprotein multidrug efflux pump and the membrane: Its role in modulating protein function. *Frontiers in Oncology*, 4(41), 2014. doi: 10.3389/fonc.2014.00041.

Alena Siarheyeva, Ronghua Liu, and Frances J. Sharom. Characterization of an asymmetric occluded state of P-glycoprotein with two bound nucleotides: Implications for catalysis. *Journal of Biological Chemistry*, 285(10):7575–7586, 2010. doi: 10.1074/jbc.M109.047290.

Benoit Sorre, Andrew Callan-Jones, Jean Baptiste Manneville, Pierre Nassoy, Jean François Joanny, Jacques Prost, Bruno Goud, and Patricia Bassereau. Curvature-driven lipid sorting needs proximity to a demixing point and is aided by proteins. *Proceedings of the National Academy of Sciences of the United States of America*, 106 (14):5622–5626, 2009. doi: 10.1073/pnas.0811243106.

Ingo H. Stein, Verena Schüller, Philip Böhm, Philip Tinnefeld, and Tim Liedl. Single-molecule FRET ruler based on rigid DNA origami blocks. *ChemPhysChem*, 12(3):689 – 695, 2011. doi: 10.1002/cphc.201000781.

Emmanuelle Steinfels, Cédric Orelle, Olivier Dalmas, François Penin, Bruno Miroux, Attilio Di Pietro, and Jean Michel Jault. Highly efficient over-production in E. coli of YvcC, a multidrug-like ATP-binding cassette transporter from Bacillus subtilis. *Biochimica et Biophysica Acta - Biomembranes*, 1565(1):1–5, 2002. doi: 10.1016/S0005-2736(02)00515-1.

Emmanuelle Steinfels, Cédric Orelle, Jean Raphaël Fantino, Olivier Dalmas, Jean Louis Rigaud, François Denizot, Attilio Di Pietro, and Jean Michel Jault. Characterization of YvcC (BmrA), a multidrug ABC transporter constitutively expressed in Bacillus subtilis. *Biochemistry*, 43(23):7491–7502, 2004. doi: 10.1021/bi0362018.

Timothy J. Stevens and Isaiah T. Arkin. Do more complex organisms have a greater proportion of membrane proteins in their genomes? *Proteins: Structure, Function and Genetics*, 39(4):417–420, 2000. doi: 10.1002/(SICI)1097-0134(20000601)39:4<417::AID-PROT140>3.0.CO;2-Y.

Asger Tonnesen, Sune M. Christensen, Vadym Tkach, and Dimitrios Stamou. Geometrical membrane curvature as an allosteric regulator of membrane protein structure and function. *Biophysical Journal*, 106(1):201–209, 2014. doi: 10.1016/j.bpj.2013.11.023.

Joseph P. Torella, Seamus J. Holden, Yusdi Santoso, Johannes Hohlbein, and Achillefs N. Kapanidis. Identifying molecular dynamics in single-molecule fret experiments with burst variance analysis. *Biophysical Journal*, 100(6):1568–1577, 2011. doi: 10.1016/j.bpj.2011.01.066.

Els Van Den Brink-Van Der Laan, J. Antoinette Killian, and Ben De Kruijff. Nonbilayer lipids affect peripheral and integral membrane proteins via changes in the lateral pressure profile. *Biochimica et Biophysica Acta - Biomembranes*, 1666(1-2):275–288, 2004. doi: 10.1016/j.bbamem.2004.06.010.

Gerrit Van Meer and Anton I.P.M. De Kroon. Lipid map of the mammalian cell. *Journal of Cell Science*, 124:5–8, 2011. doi: 10.1242/jcs.071233.

Gerrit Van Meer, Dennis R. Voelker, and Gerald W. Feigenson. Membrane lipids: Where they are and how they behave. *Nature Reviews Molecular Cell Biology*, 9:112–124, 2008. doi: 10.1038/nrm2330.

Vasilis Vasiliou, Konstandinos Vasiliou, and Daniel W. Nebert. Human ATP-binding cassette (ABC) transporter family. *Human genomics*, 3(3):281–290, 2009. doi: 10.1186/1479-7364-3-3-281.

Brandy Verhalen and Stephan Wilkens. P-glycoprotein retains drug-stimulated ATpase activity upon covalent linkage of the two nucleotide binding domains at their C-terminal ends. *Journal of Biological Chemistry*, 286(12):10476–10482, 2011. doi: 10.1074/jbc.M110.193151.

Brandy Verhalen, Stefan Ernst, Michael Börsch, and Stephan Wilkens. Dynamic ligand-induced conformational rearrangements in P-glycoprotein as probed by fluorescence resonance energy transfer spectroscopy. *Journal of Biological Chemistry*, 287(2):1112–1127, 2012. doi: 10.1074/jbc.M111.301192.

Brandy Verhalen, Reza Dastvan, Sundarapandian Thangapandian, Yelena Peskova, Hanane A. Koteiche, Robert K. Nakamoto, Emad Tajkhorshid, and Hassane S. McHaourab. Energy transduction and alternating access of the mammalian ABC transporter P-glycoprotein. *Nature*, 543:738–741, 2017. doi: 10.1038/nature21414.

Shizhen Wang, Reza Vafabakhsh, William F Borschel, Taekjip Ha, and Colin G Nichols. Structural dynamics of potassium-channel gating revealed by single-molecule FRET. *Nature Structural & Molecular Biology*, 23(1):31–36, 2015. doi: 10.1038/nsmb.3138.

Andrew B. Ward, Paul Szewczyk, Vinciane Grimard, Chang Wook Lee, Lorena Martinez, Rupak Doshi, Alexandra Caya, Mark Villaluz, Els Pardon, Cristina Cregger, Douglas J. Swartz, Pierre Guy Falson, Ina L. Urbatsch, Cedric Govaerts, Jan Steyaert, and Geoffrey Chang. Structures of P-glycoprotein reveal its conformational flexibility and an epitope on the nucleotide-binding domain. *Proceedings of the National Academy of Sciences of the United States of America*, 110(33):13386–13391 |, 2013. doi: 10.1073/pnas.1309275110.

Shimon Weiss. Fluorescence spectroscopy of single biomolecules. *Science*, 283(5408):1676–1683, 1999. doi: 10.1126/science.283.5408.1676.

Stephan Wilkens. Structure and mechanism of ABC transporters. *F1000 Prime reports*, 7(14), 2015. doi: 10.12703/P7-14.

Benjamin Wiseman, Arnaud Kilburg, Vincent Chaptal, Gina Catalina Reyes-Mejia, Jonathan Sarwan, Pierre Falson, and Jean Michel Jault. Stubborn contaminants: Influence of detergents on the purity of the multidrug ABC transporter BmrA. *PLoS ONE*, 9(12):e114864, 2014. doi: 10.1371/journal.pone.0114864.

Min You, Edwin Li, William C. Wimley, and Kalina Hristova. Förster resonance energy transfer in liposomes: Measurements of transmembrane helix dimerization in the native bilayer environment. *Analytical Biochemistry*, 340(1):154–164, 2005. doi: 10.1016/j.ab.2005.01.035.

C. Zander, M. Sauer, K. H. Drexhage, D. S. Ko, A. Schulz, J. Wolfrum, L. Brand, C. Eggeling, and C. A.M. Seidel. Detection and characterization of single molecules in aqueous solution. *Applied Physics B: Lasers and Optics*, 63(5):517–523, 1996. doi: 10.1007/BF01828950.

Nawid Zarrabi, Stefan Ernst, Brandy Verhalen, Stephan Wilkens, and Michael Börsch. Analyzing conformational dynamics of single P-glycoprotein transporters by Förster resonance energy transfer using hidden Markov models. *Methods*, 66(2):168–179, 2014. doi: 10.1016/j.ymeth.2013.07.026.

Yongfang Zhao, Daniel Terry, Lei Shi, Harel Weinstein, Scott C. Blanchard, and Jonathan A. Javitch. Single-molecule dynamics of gating in a neurotransmitter transporter homologue. *Nature*, 465(7295):188–193, 2010. doi: 10.1038/nature09057.

Maria E. Zoghbi and Guillermo A. Altenberg. Luminescence resonance energy transfer spectroscopy of ATP-binding cassette proteins. *Biochimica et Biophysica Acta - Biomembranes*, 1860(4):854–867, 2018. doi: 10.1016/j.bbamem.2017.08.005.

Maria E. Zoghbi, Rebecca S. Cooper, and Guillermo A. Altenberg. The lipid bilayer modulates the structure and function of an ATP-binding cassette exporter. *Journal of Biological Chemistry*, 291(9):4453–4461, 2016. doi: 10.1074/jbc.M115.698498.

Maria E. Zoghbi, Leo Mok, Douglas J. Swartz, Anukriti Singh, Gregory A. Fendley, Ina L. Urbatsch, and Guillermo A. Altenberg. Substrate-induced conformational changes in the nucleotide-binding domains of lipid bilayer-associated P-glycoprotein during ATP hydrolysis. *Journal of Biological Chemistry*, 292:20412–20424, 2017. doi: 10.1074/jbc.M117.814186.

Ping Zou, Marco Bortolus, and Hassane S. Mchaourab. Conformational Cycle of the ABC Transporter MsbA in Liposomes: Detailed Analysis Using Double Electron-Electron Resonance Spectroscopy. *Journal of Molecular Biology*, 393(3):586–597, 2009. doi: 10.1016/j.jmb.2009.08.050.